

## ABSTRACT

JOHNSON, MATTHEW STEPHEN. Understanding the Transport, Chemical Transformation, and Biogeochemical Impact of Mineral Dust. (Under the direction of Dr. Nicholas Meskhidze.)

Mineral dust can influence the Earth's climate by directly absorbing and scattering incoming solar radiation, indirectly influencing the Earth's radiative budget by altering cloud microphysics and lifetime, and its deposition has been suggested to play a controlling role in marine primary productivity which can cause fluxuations in atmospheric carbon dioxide (CO<sub>2</sub>) concentrations. During this dissertation research, synergistic methods were developed in order to study the complex processes controlling mineral dust transport, chemical transformation, and the impact of its deposition on marine ecosystems. To evaluate these processes, we combine calculations made by the three dimensional (3-D) global chemical transport model (CTMs) GEOS-Chem and a dust/biota assessment tool with remotely-sensed data from the Moderate-resolution Imaging Spectroradiometer (MODIS), Multi-Angle Imaging SpectroRadiometer (MISR), and Sea-viewing Wide Field-of-view Sensor (SeaWiFS), and active satellite retrievals from the Cloud-Aerosol Lidar and Infrared Pathfinder Satellite Observation (CALIPSO).

Horizontal and vertical dust transport pathways simulated in GEOS-Chem were compared to remotely-sensed aerosol optical depth (AOD) and aerosol extinction data over the major global dust emission and transport regions ("dusty" regions). The model-satellite intercomparison demonstrates that while GEOS-Chem, MODIS, MISR, and CALIPSO agree in the horizontal and vertical distributions of mineral dust, GEOS-Chem-predicted AOD values display a positive bias in comparison to remotely-sensed data over the majority of "dusty" regions (particularly in the lowest 4 km of the troposphere). This result reveals that

GEOS-Chem may be over predicting mineral dust emissions or contains uncertainties in mineral dust optical properties. The implementation of a new dust mass size distribution scheme systematically reduced mineral dust AOD values and improved model-satellite comparisons. The improved agreement between GEOS-Chem and remotely-sensed AODs was achieved without reducing mineral dust emission rates, which in the past has been common practice in order to improve model-satellite/measurement comparisons.

The influence of Patagonian dust and soluble/bioavailable iron (sol-Fe) deposition on marine primary productivity was evaluated using GEOS-Chem (implemented with a prognostic dust-iron (Fe) dissolution scheme), a dust/biota assessment tool, and remotely-sensed SeaWiFS chlorophyll concentration ([Chl-*a*]) data. General conclusions based on the model simulations of two large Patagonian dust outbreaks reveal that the synoptic meteorological patterns of strong high and low pressure systems control the horizontal and vertical transport pathways over the South Atlantic and Southern Ocean (SAO/SO). The dust outbreaks examined during this study, which are representative of large summertime outflows of mineral dust from South American continental sources, reveal that atmospheric fluxes of mineral dust from Patagonia are not likely to be the major source of bioavailable Fe to oceanic regions characterized by high primary productivity, however, even if these dust events are not causing large visual algal blooms, they may still play a controlling factor in background [Chl-*a*] in the SAO.

Past modeling studies calculating bioavailable nutrient deposition to global remote oceanic regions tend to use simplified parameterizations and numerous a priori assumptions. However, during this research, the most comprehensive dust-nutrient dissolution mechanism to date was developed and implemented into GEOS-Chem in order to produce bioavailable

nutrient deposition datasets for usage in future marine biogeochemical and climate model predictions. Expanding on our past dust-Fe dissolution mechanism (acid-based dissolution), we added: organic ligand-promoted dissolution processes, Fe(II)/Fe(III) photochemical redox cycling, acid-based phosphorus/phosphate ( $\text{PO}_4^{3-}$ ) dissolution, and nitrate ( $\text{NO}_3^-$ ) formation during atmospheric transport. Overall, the model predicted ~0.17, 0.20, and 75 Tg of sol-Fe,  $\text{PO}_4^{3-}$ , and  $\text{NO}_3^-$  were deposited to the global oceans during a yearlong simulation. Our model results agree with in situ measurements/laboratory data in the fact that the bioavailable fractions of these micronutrient, associated with mineral dust, were highly variable both spatially and temporally.

Understanding the Transport, Chemical Transformation, and Biogeochemical Impact of  
Mineral Dust

by  
Matthew Johnson

A dissertation submitted to the Graduate Faculty of  
North Carolina State University  
in partial fulfillment of the  
requirements for the Degree of  
Doctor of Philosophy

Marine, Earth, and Atmospheric Sciences

Raleigh, North Carolina

2012

APPROVED BY:

---

Dr. Nicholas Meskhidze  
Chair of Advisory Committee

---

Dr. Owen Duckworth

---

Dr. Markus Petters

---

Dr. Santiago Gassó

## BIOGRAPHY

Matthew Johnson is a Doctoral Candidate at North Carolina State University conducting research under the advisement of Dr. Nicholas Meskhidze. He was raised in Kill Devil Hills, NC where he acquired the love and appreciation for his surrounding natural environment. He graduated from Manteo High School and moved to Raleigh, NC to study Meteorology at North Carolina State University. He obtained his Bachelor of Science degree in 2007 and began his graduate research in Atmospheric Science working with Dr. Nicholas Meskhidze. Matthew Johnson received his Master of Science degree in Atmospheric Sciences during the spring of 2009 and continued his graduate research at North Carolina State University. Upon graduation Matthew Johnson has accepted a permanent/civilian position at the NASA Ames Research Center and will be working on various topics in climate science.

## ACKNOWLEDGMENTS

First of all, I would like to thank my committee members: Dr. Markus Petters, Dr. Owen Duckworth, Dr. Santiago Gassó, and Dr. Nicholas Meskhidze. I am especially grateful to Dr. Meskhidze for providing the opportunity to conduct research under his advisement and for giving me unlimited opportunities for academic growth throughout my masters and doctoral research. Thanks are also due to my collaborators and co-authors on my presentation and publications: Dr. Santiago Gassó, Goddard Earth Sciences and Technology Center; Dr. Fabien Solmon, Laboratoire d'Aérodologie, CNRS, Université de Toulouse; Velayudhan Praju Kiliyanpilakkil, North Carolina State University, and Brett Gantt, North Carolina State University. Extended thanks go out to those at Harvard University, who have provided me assistance in the compilation and application of the GEOS-Chem model: Dr. Daniel Jacob, model scientist; Bob Yantosca, model engineer, and many more for answering my numerous questions throughout my graduate research. I am also thankful to Dr. Gary Howell and Dr. Eric Sills for their assistance and acquired knowledge of computational parallel processing. I also wish to thank those that funded my research: the National Science Foundation (NSF) Grant No. 0826117 and the NASA North Carolina Space Grant Graduate Research Fellowship Program.

I wish to extend special thanks to all my colleagues/friends from Jordan Hall and my research group. They have provided guidance and assistance during my tenure at North Carolina State University, and our friendships have made all the long days in the office much more tolerable. Extra thanks go to Brett Gantt, whom kept me company throughout my time

in Jordan Hall and equally understands the enduring and everlasting tasks provided throughout graduate school for the past 5 years.

The most important thanks are given to my parents, Stephen and Joyce Johnson, to which all this would have never been possible. You have been behind me through everything and have given me never ending support and encouragement, and I would not be where I am today without it. To my friends and family, you have seen me through each stage that led me to this point, and I am forever grateful to each of you. To those whom I have forgotten you know I give you all the thanks deserved.

## TABLE OF CONTENTS

LIST OF TABLES.....		viii
LIST OF FIGURES.....		ix
ACRONYMS.....		xv
1. SUMMARY.....		1
2. LITERATURE REVIEW.....		8
2.1 Potential climatic impact of mineral dust.....		8
2.2 Bioavailable nutrients in mineral dust.....		10
2.2.1 Bioavailable Fe.....		10
2.2.2 Bioavailable P and N.....		16
2.3 Simulating mineral dust processes.....		19
2.3.1 Mineral dust emissions.....		20
2.3.2 Dust transport and deposition.....		24
2.3.3 Mineral dust optical properties.....		28
2.4 GEOS-Chem.....		30
2.5 Objectives.....		34
3. A GLOBAL COMPARISON OF GEOS-CHEM-PREDICTED AND REMOTELY-SENSED MINERAL DUST AEROSOL OPTICAL DEPTH AND EXTINCTION PROFILES.....		55
3.1 Introduction.....		59
3.2 Methods.....		63
3.2.1 GEOS-Chem simulations.....		63
3.2.2 Satellite retrievals of aerosol optical depth.....		65
3.2.3 Comparison between GEOS-Chem and satellite data.....		68
3.3 Results.....		69
3.3.1 Global distribution of AOD values.....		69
3.3.2 Yearly-averaged vertical profiles of mineral dust extinction.....		72

3.3.3	Seasonally-averaged dust extinction profiles.....	74
3.3.4	Mineral dust size distribution.....	76
3.3.5	Statistical analysis of AOD values.....	78
3.4	Conclusions.....	80
4.	UNDERSTANDING THE TRANSPORT OF PATAGONIAN DUST AND ITS INFLUENCE ON MARINE BIOLOGICAL ACTIVITY IN THE SOUTH ATLANTIC OCEAN.....	104
4.1	Introduction.....	109
4.2	Methods.....	112
4.2.1	GEOS-Chem/DFeS.....	112
4.2.2	Liabile Fe and the ocean productivity.....	114
4.2.3	Satellite data.....	115
4.3	Results.....	117
4.3.1	Mineral dust transport from Patagonia.....	117
4.3.2	Response of marine biological productivity to mineral dust deposition.....	123
4.3.3	Sensitivity analysis.....	126
4.4	Conclusions.....	127
5.	UPDATES DUST-NUTRIENT DISSOLUTION MECHANISM IN GEOS- CHEM.....	151
5.1	Introduction.....	156
5.2	Methods.....	162
5.2.1	GEOS-Chem.....	162
5.2.2	Model developments.....	164
5.2.2.1	Dust mineralogical composition.....	164
5.2.2.2	Model-predicted oxalate concentrations.....	165
5.2.2.3	Mineral dissolution kinetics.....	167
5.2.2.4	Kinetic modeling of Fe photochemistry/chemistry.....	170
5.2.2.5	Acid-based bioavailable P production and N formation.....	172
5.3	Results.....	174
5.3.1	Atmospheric concentrations of oxalic acid.....	174

5.3.2 Sol-Fe deposition.....	175
5.3.2.1 Total sol-Fe deposition.....	175
5.3.2.2 Sol-Fe(II) deposition.....	177
5.3.2.3 Organic ligand-promoted Fe dissolution.....	179
5.3.2.4 Fe-containing mineral speciation.....	180
5.3.3 PO <sub>4</sub> <sup>3-</sup> deposition.....	181
5.3.4 NO <sub>3</sub> <sup>-</sup> deposition.....	182
5.3.5 Potential biogeochemical impact.....	183
5.3.6 Potential error due to a priori assumptions.....	185
5.4 Conclusions.....	186
6. SUMMARY AND FUTURE WORK.....	219
6.1 Introduction.....	219
6.2 Main results.....	219
6.3 Suggestions for future work.....	223

## LIST OF TABLES

Table 2.1	Baseline GEOS-Chem model configuration.....	50
Table 2.2	Anthropogenic emission inventories available in GEOS-Chem.....	51
Table 3.1	GEOS-Chem-predicted global annual dust sources and sinks.....	92
Table 3.2	Monthly-averaged GEOS-Chem-predicted AOD in comparison to MODIS and MISR data between March 2009 and February 2010.....	93
Table 4.1	Variables with corresponding values and (uncertainties) used in Eq. (2)...	140
Table 5.1	Tracers implemented into GEOS-Chem/DFeS and chemical forms allowed.....	200
Table 5.2	Coefficients used to derive oxalate-promoted Fe dissolution.....	201
Table 5.3	Kinetic and photochemical reactions implemented into SMV-GEAR II...	202
Table 5.4	Aqueous-phase reactions and equilibrium constants.....	203
Table 5.5	Set of differential equations used in the model.....	204

## LIST OF FIGURES

Figure 2.1	Natural and anthropogenic radiative forcing components and their estimated impact, as determined by the IPCC in 2007.....	52
Figure 2.2	This figure shows oceanic $[\text{NO}_3^-]$ in the global oceans. HNLC oceanic regions are assumed to be the surface waters with elevated $[\text{NO}_3^-]$ (bright colors). The HNLC regions of the subarctic North Pacific, equatorial Pacific, and the Southern Ocean comprising ~30% of the global oceans (data from the World Ocean Atlas 1994).....	53
Figure 2.3	Model-predicted total dust emissions ( $\text{g m}^{-2}$ ) during a) March-April, b) June-August, c) September-November, and d) December-February during the simulation time period of March 2009 to February 2010.....	54
Figure 3.1	GEOS-Chem-predicted percent contribution of mineral dust AOD to total AOD between March 2009 and February 2010. The white boxes covering the “dusty” regions of 1) Saharan dust source region, 2) Saharan dust outflow (N. Atlantic Ocean), 3) Asian dust source region, 4) Middle Eastern dust source region, 5) Australian dust source region, and 6) Patagonian dust source region used for the comparison of model-predicted and remotely-sensed dust AOD/extinction values.....	94
Figure 3.2	GEOS-Chem-predicted daily-averaged dust column burden ( $\mu\text{g m}^{-2}$ ) during a) March-April (MAM), b) June-August (JJA), c) September-November (SON), and d) December-February (DJF).....	95
Figure 3.3	Seasonally-averaged percent differences for GEOS-Chem-predicted and MODIS (left column) and MISR (right column) retrieved AOD values...	96
Figure 3.4	Annually-averaged CALIPSO-retrieved (blue line) and GEOS-Chem-simulated (standard version - red line, <i>Kok</i> [2011] scheme - green line) vertical profiles of mineral dust extinction ( $\text{km}^{-1}$ ) for a) Saharan dust source region, b) Saharan dust outflow region, c) Asian dust source region, d) Middle Eastern dust source region, e) Australian dust source region and f) Patagonian dust source region. Height (m) indicates the elevation above sea level for the center of the model grid. Figure insert shows regionally-averaged AOD values from MODIS, MISR, and	

Figure 3.5 Seasonally-averaged CALIPSO-retrieved (blue line) and GEOS-Chem simulated (standard version - red line, *Kok* [2011] scheme - green line) vertical profiles of mineral dust extinction ( $\text{km}^{-1}$ ) for the a) Saharan dust source region, b) Saharan dust outflow region, c) Asian dust source region, d) Middle Eastern dust source region, e) Australian dust source region and f) Patagonian dust source region. Height (m) indicates the elevation above sea level for the center of the model grid..... 98

Figure 3.6 Seasonally-averaged percent differences for GEOS-Chem-predicted and MODIS (left column) and MISR (right column) AOD values. GEOS-Chem dust AODs are calculated using the size distribution parameterization of *Kok* [2011]..... 99

Figure S3.1 GEOS-Chem-predicted total dust emissions ( $\text{g m}^{-2}$ ) during a) March-April, b) June-August, c) September-November, and d) December-February..... 100

Figure S3.2 Seasonally-averaged AOD (on a logarithmic scale) predicted by GEOS-Chem (left column) and remotely-sensed by MODIS (middle column) and MISR (right column)..... 101

Figure S3.3 Scatter plots of CALIPSO-retrieved dust aerosol extinction ( $\text{km}^{-1}$ ) against GEOS-Chem simulations for the a) Saharan dust source region, b) Saharan dust outflow region, c) Asian dust source region, d) Middle Eastern dust source region, e) Australian dust source region and f) Patagonian dust source region. The solid black line is the 1:1 line, and the two dashed lines are the 1:2 and 2:1 lines. Height (m) indicates the elevation above sea level for the center of the model grid..... 102

Figure S3.4 Scatter plots of CALIPSO-retrieved dust extinction ( $\text{km}^{-1}$ ) against GEOS-Chem simulations using the dust size distribution scheme of *Kok* [2011] for the a) Saharan dust source region, b) Saharan dust outflow region, c) Asian dust source region, d) Middle Eastern dust source region, e) Australian dust source region and f) Patagonian dust source region. The solid black line is the 1:1 line, and the two dashed lines are the 1:2 and 2:1 lines. Height (m) indicates the elevation above sea level for the center of the model

grid..... 103

Figure 4.1 *Aqua* MODIS real-time imagery at a) 18:40 UTC 23 January 2009 and b) 18:35 UTC 17 February 2009 and GEOS-Chem-predicted daily-averaged vertically-integrated dust concentration ( $\mu\text{g m}^{-2}$ ) of Patagonian dust plumes advecting off the coast of South America on c) 23 January 2009 and d) 17 February 2009, respectively. The black square indicates the location of San Antonio Oeste ( $40.8^{\circ}\text{S}$ ,  $65.1^{\circ}\text{W}$ )..... 141

Figure 4.2 GEOS-Chem-predicted daily dust burden ( $\text{g m}^{-2}$ ) (contour lines) and sea level pressure anomalies (SLPAs) (mb) over the SAO for a) 23 January, b) 24 January, and c) 25 January 2009. Cold colors indicate negative SLPA (low pressure systems) and warm colors display high pressure systems..... 142

Figure 4.3 The GEOS-Chem-predicted dust burden ( $\text{g m}^{-2}$ ) for 23 January 2009 (the background image) with overlaid vertical swaths of a) CALIPSO retrievals of dust aerosol layers, b) model-predicted vertical cross-section of dust concentration ( $\mu\text{g m}^{-3}$ ) along the CALIPSO orbit track and c) CALIPSO dust layer AOD at 532 nm. Modeled vertical cross-section calculations are conducted along the CALIPSO orbital track beginning at 4:28:59 UTC on 23 January 2009 (V3-01.2009-01-23T04-28-59Z)..... 143

Figure 4.4 Same as Fig. 4.3 but for 24 January 2009 and the CALIPSO orbital track beginning at 3:33:27 UTC (V3-01.2009-01-24T03-33-27Z)..... 144

Figure 4.5 The background images are the GEOS-Chem-predicted dust burden ( $\text{g m}^{-2}$ ) on 25 January 2009 overlaid with vertical swaths of the CALIPSO orbital track beginning at 2:37:55 UTC (V3-01.2009-01-25T02-37-55Z) (left column) and 0:59:00 UTC (V3-01.2009-01-25T00-59-00Z) (right column) displaying the a), d) CALIPSO retrievals of dust aerosol layers, b), e) CALIPSO dust layer AOD at 532 nm, and c), f) model-predicted vertical cross-section of dust concentration ( $\mu\text{g m}^{-3}$ ) along the CALIPSO orbit tracks..... 145

Figure 4.6 GEOS-Chem-predicted dust burden ( $\text{g m}^{-2}$ ) (contour lines) and sea level pressure anomalies (SLPAs) (mb) over the SAO for a-c) 23-25 January 2009 and d-f) 13-15 February 2009. Arrows are for the visual aid for

the general transport pathway of Patagonian dust. Low and high pressure anomalies are shown by symbols of L and H, respectively.....	146
Figure 4.7 The 8-day averaged GEOS-Chem-predicted percent contributions of Patagonian dust sources to total mineral dust deposition in the HNLC waters of the SO for the a) J23 and b) F11 dust episodes.....	147
Figure 4.8 GEOS-Chem/DFeS-simulated total sol-Fe fluxes ( $\mu\text{g m}^{-2}$ ) (contour lines) and predicted $[\text{Chl-}a]$ increases ( $\Delta[\text{Chl-}a]_{\text{pred}}$ ) ( $\text{mg m}^{-3}$ ) for the a) J23 and b) F11 dust episodes.....	148
Figure 4.9 Differences in SeaWiFS remotely-sensed 8-day averaged $[\text{Chl-}a]$ ( $\Delta[\text{Chl-}a]_{\text{obs}}$ ) ( $\text{mg m}^{-3}$ ) and the percent ratio of $\Delta[\text{Chl-}a]_{\text{pred}}/\Delta[\text{Chl-}a]_{\text{obs}}$ for the a), c) J23 and b), d) F11 dust episodes, respectively. The $\Delta[\text{Chl-}a]_{\text{obs}}$ for J23 and F11 episodes are calculated by subtracting 23-30 January averages from 15-22 January 2009 and 11-18 February averages from 3-10 February 2009, respectively.....	149
Figure 4.10 Percent ratio of $\Delta[\text{Chl-}a]_{\text{pred}}/\Delta[\text{Chl-}a]_{\text{obs}}$ for the grid cells with positive values of remotely-sensed 8-day averaged $[\text{Chl-}a]$ differences (after the storm minus before) for the a) J23 and b) F11 dust episodes. Black dots depict the grid cells located in the HNLC regions of the SAO.....	150
Figure 5.1 Fe-containing mineral dissolution rates used within GEOS-Chem/DFeS simulations for hematite (red line), goethite (blue line), and illite (green line) at 298°K. Organic ligand-promoted Fe dissolution rates are shown at oxalic acid concentrations of 0 $\mu\text{M}$ (solid lines), 10 $\mu\text{M}$ (dashed lines) and 20 $\mu\text{M}$ (dotted lines) for each individual Fe-containing mineral.....	205
Figure 5.2 GEOS-Chem-predicted surface level oxalic acid concentrations (using model-predicted $\text{SO}_4^{2-}$ concentrations as a proxy, Eq. 1) in comparison to a global data-set of measured oxalic acid concentrations. Urban, rural, and remote oceanic measurements are indicated by red, green, and blue dots, respectively. Observed surface level oxalic acid concentrations are taken from the study of <i>Myriokefalitakis et al.</i> [2011] and references within. The solid black line represents the 1:1 comparison of model-predicted and measured oxalic acid and the two dashed lines are the 1:2 and 2:1 comparison	

lines.....	206
Figure 5.3 GEOS-Chem-predicted seasonally-averaged sol-Fe deposition ( $\mu\text{g m}^{-2}$ day $^{-1}$ ) to the surface oceans between a) March-April (MAM), b) June-August (JJA), c) September-November (SON), and d) December-February (DJF).....	207
Figure 5.4 GEOS-Chem-predicted seasonally-averaged DIF values (%) in mineral dust deposited to the surface oceans between a) March-April (MAM), b) June-August (JJA), c) September-November (SON), and d) December-February (DJF).....	208
Figure 5.5 GEOS-Chem-predicted seasonally-averaged sol-Fe(II) deposition ( $\mu\text{g m}^{-2}$ day $^{-1}$ ) to the surface oceans between a) March-April (MAM), b) June-August (JJA), c) September-November (SON), and d) December-February (DJF).....	209
Figure 5.6 GEOS-Chem-predicted seasonally-averaged sol-Fe(II)% in deposited dust ( $\mu\text{g m}^{-2}$ day $^{-1}$ ) to the surface oceans between a) March-April (MAM), b) June-August (JJA), c) September-November (SON), and d) December-February (DJF).....	210
Figure 5.7 GEOS-Chem-predicted percent change in seasonally-averaged sol-Fe deposition rates to the surface oceans due to organic ligand-promoted Fe dissolution for a) March-April (MAM), b) June-August (JJA), c) September-November (SON), and d) December-February (DJF).....	211
Figure 5.8 GEOS-Chem/DFeS-predicted monthly-averaged sol-Fe deposition ( $\mu\text{g m}^{-2}$ day $^{-1}$ ) for July 2009 when Fe mobilization is calculated using a) hematite, b) goethite, and c) illite.....	212
Figure 5.9 GEOS-Chem-predicted daily-averaged $\text{PO}_4^{3-}$ deposition ( $\mu\text{g m}^{-2}$ ) to the surface oceans between a) March-April (MAM), b) June-August (JJA), c) September-November (SON), and d) December-February (DJF).....	213
Figure 5.10 GEOS-Chem-predicted daily-averaged $\text{NO}_3^-$ deposition ( $\mu\text{g m}^{-2}$ ) to the surface oceans between a) March-April (MAM), b) June-August (JJA), c) September-November (SON), and d) December-February (DJF).....	214

Figure 5.11 GEOS-Chem-predicted daily-averaged a) sol-Fe, b) PO <sub>4</sub> <sup>3-</sup> , and c) NO <sub>3</sub> <sup>-</sup> deposition rates (μg m <sup>-2</sup> ) to the surface oceans which have primary productivity limited by each individual micronutrient during the entire simulation period (March 2009 - February 2010).....	215
Figure 5.12 GEOS-Chem-predicted percent difference between sol-Fe deposition when assuming a constant 1% DIF and explicitly model-predicted DIF during the yearlong simulation period.....	216
Figure S5.1 GEOS-Chem-predicted daily-averaged oxalic acid surface level concentrations (μg m <sup>-3</sup> ) during a) March-April (MAM), b) June-August (JJA), c) September-November (SON), and d) December-February (DJF).....	217
Figure S5.2 GEOS-Chem/DFeS-predicted total sol-Fe (green line), Fe(II) (blue line), and Fe(III) (redline) at the surface of the model grid cell encompassing the dust measurement sites on the island of Barbados (13.17°N, 59.43°W). This figure illustrates the model-predicted diurnal cycle of Fe(II)/Fe(III) redox cycling (2 hour resolution) during the Barbados Dust Deposition Experiment (BarDEx) [ <i>Trapp et al.</i> , 2010].....	218

## ACROYNMS

<u>Acronym</u>	<u>Definition</u>
3-D	Three dimensional
ACC	Antarctic Circumpolar Current
Al <sup>+</sup>	Aluminum
ALD2	Acetaldehyde
ALK4	Alkanes
AOD	Aerosol optical depth
Apatite	Ca <sub>5</sub> (PO <sub>4</sub> ) <sub>3</sub> (OH)
BC	Black carbon
BRAVO	Big Bend Regional Aerosol and Visibility Observational Observatory
C <sub>2</sub> H <sub>6</sub>	Ethane
C <sub>3</sub> H <sub>8</sub>	Propane
Ca <sup>+</sup>	Calcium
CAD	Cloud-aerosol discrimination
CaCO <sub>3</sub>	Calcite/Calcium carbonate
CALIOP	Cloud-Aerosol Lidar with Orthogonal Polarization
CALIPSO	Cloud-Aerosol Lidar and Infrared Pathfinder Satellite Observation
CaSO <sub>4</sub>	Gypsum
CCN	Cloud condensation nuclei
CF	Cloud fraction
CH <sub>2</sub> O	Formaldehyde
Chl- <i>a</i>	Chlorophyll concentration
Cl <sup>-</sup>	Chlorine
CO	Carbon monoxide

CO <sub>2</sub>	Carbon dioxide
(COOH) <sub>2</sub>	Oxalic acid
CTM	Chemical transport model
DEAD	Dust Entrainment and Deposition
DFe	Dissolved iron
DFeS	Dust-Fe dissolution module
DIF	Dissolved iron fraction
DMS	Dimethyl sulfide
EDGAR	European Monitoring and Evaluation Programme
EMEP	Environmental Protection Agency and National Emission Inventory
EPA/NEI	Environmental Protection Agency and National Emission Inventory non-methane
ESMF	Earth System Modeling Framework
Fe	Iron
Fe(III)	Ferric iron
Fe(II)	Ferrous iron
Fe <sub>2</sub> O <sub>3</sub>	Hematite
FeO(OH)	Goethite
GADS	Global Aerosol Data Set
GCM	Global Climate Model
GEOS	Goddard Earth Observing System Model
GEIA	Global Emission Inventory Activity
GMAO	Global Modeling and Assimilation Office
GOCART	Goddard Chemistry Aerosol Radiation and Transport
GSI	Grid-point Statistical Interpolator
H <sub>2</sub> O <sub>2</sub>	Hydrogen peroxide

H <sub>2</sub> SO <sub>4</sub>	Sulfuric acid
HNO <sub>3</sub>	Nitric acid
HNLC	High-nitrate low-chlorophyll
HO <sub>2</sub>	Hydroperoxyl radical
IC	Inorganic carbon
IN	Ice nuclei
IPCC	Intergovernmental Panel on Climate Change
K <sup>+</sup>	Potassium
Mg <sup>2+</sup>	Magnesium
MEGAN	Model of Emissions of Gases and Aerosols from Nature
MEK	Methyl ethyl ketone
MISR	Multi-Angle Imaging SpectroRadiometer
MODIS	Moderate Resolution Imaging Spectroradiometer
MODIS-DB	MODIS Deep Blue
N	Nitrogen
Na <sup>+</sup>	Sodium
NASA	National Aeronautics and Space Administration
NH <sub>3</sub>	Ammonia
NH <sub>4</sub> <sup>+</sup>	Ammonium
NMB	Normalized mean bias
NO <sub>2</sub>	Nitrogen dioxide
NO <sub>3</sub> <sup>-</sup>	Nitrate
NO <sub>x</sub>	NO+NO <sub>2</sub>
NSF	National Science Foundation
O <sub>3</sub>	Ozone
OC	Organic carbon

ODE	Ordinary differential equation
OH	Hydroxyl radical
P	Phosphorus
PBL	Planetary boundary layer
$\text{PO}_4^{3-}$	Phosphate
PRPE	Propene
QA	Quality Assured
R	Correlation coefficient
RMSE	Root mean square error
SAO	South Atlantic Ocean
SeaWiFs	Sea-viewing Wide Field-of-view Sensor
SLPA	Sea level pressure anomaly
SMVGEAR	Sparse matrix vectorized gear
$\text{SO}_2$	Sulfur dioxide
$\text{SO}_4^{2-}$	Sulfate
SO	Southern Ocean
Sol-Fe	Soluble iron
TOMS	Total Ozone Mapping Spectrometer

# 1. Summary

The deposition of essential micronutrients (iron (Fe), phosphorus (P), and nitrogen (N)) associated with mineral dust has been suggested as a major atmospheric supply pathway of these nutrients needed in photosynthetic processes driving biogeochemistry in remote marine ecosystems. These fluxes of essential micronutrients can drive marine primary productivity and carbon cycling in the global oceans which can have a direct impact on atmospheric carbon dioxide (CO<sub>2</sub>) concentrations and overall climate. The amount of nutrients, provided by mineral dust deposition, able to be utilized in marine ecosystem processes is complicated by the fact these dust-nutrients must be in a bioavailable form. For example, in order for mineral-Fe to be utilized by phytoplankton (bioavailable), it must be in a soluble/aqueous, colloidal, or nano-particulate form. Additionally, the bioavailable portions of atmospheric P and N are considered to be in the form of phosphate (PO<sub>4</sub><sup>3-</sup>) and nitrate (NO<sub>3</sub><sup>-</sup>), respectively. Past measurement and modeling studies have demonstrated that the bioavailable fraction (fraction of the total nutrient concentration considered to be bioavailable) of these micronutrients in mineral dust are highly variable both spatially and temporally. For example, the in situ measurement study of *Baker et al.* [2006] showed that the soluble/bioavailable portion of Fe and P range from less than 1% to greater than 80%. In general, measurement and modeling studies demonstrate that nutrient solubilities tend to increase during atmospheric transport [e.g., *Baker and Jickells, 2006; Baker et al., 2006*]. These results support the hypothesis that atmospheric chemical/physical processing is a

major contributor to bioavailable nutrient formation within mineral dust during atmospheric transport.

In this dissertation research, synergistic methods were developed through a combination of modeled and remotely-sensed data to evaluate mineral dust transport dynamics, chemical transformation, and the influence of nutrient deposition on primary productivity in the global oceans. Model simulations using the state-of-the-art 3-D global chemical transport model (CTMs) GEOS-Chem were applied during this study, in conjunction with passive space-borne data from the Moderate-resolution Imaging Spectroradiometer (MODIS), Multi-Angle Imaging SpectroRadiometer (MISR), and Sea-viewing Wide Field-of-view Sensor (SeaWiFS), and active satellite data from the Cloud-Aerosol Lidar and Infrared Pathfinder Satellite Observation (CALIPSO).

The first step in my dissertation research was to evaluate the ability of GEOS-Chem to accurately simulate mineral dust emissions and transport pathways. In order to achieve this, model-predicted and remotely-sensed AOD/aerosol extinction profiles are compared over six regions where aerosol abundances are dominated by mineral dust (“dusty” regions). Calculations indicate that over the “dusty” regions examined in this study (with the exception of the Middle Eastern dust sources) GEOS-Chem demonstrates a positive bias in AOD values compared to MODIS and MISR. The positive bias is particularly pronounced over the Saharan dust source regions, where model-predicted AOD values can be greater than a factor of 2 higher. When comparing model outputs to CALIPSO-derived dust aerosol extinction

profiles it was revealed that the model overestimations of dust abundances over the study regions primarily occur below ~4 km. This suggests excessive emission rates of mineral dust and/or uncertainties in dust optical properties. The implementation of a new dust size distribution scheme into GEOS-Chem reduced the yearly-mean positive bias in model-predicted AOD values over the study regions without having to reduce global dust emission rates. The results were most noticeable over the Saharan dust source regions where the differences between model-predicted and MODIS/MISR retrieved AOD values were reduced from 0.22 and 0.17 to 0.02 and -0.04, respectively. Our results also show that positive/negative biases between satellite and model-predicted aerosol extinction values at different altitudes can sometimes even out, giving a false impression for the agreement between remotely-sensed and model-predicted column-integrated AOD data.

Additionally, during this research, GEOS-Chem results and remotely-sensed data are analyzed to examine the horizontal and vertical transport pathways of Patagonian dust and quantify the effect of Fe-laden mineral dust deposition on marine biological productivity in the surface waters of the South Atlantic Ocean (SAO). Model simulations for the atmospheric transport and deposition of mineral dust and bioavailable Fe are carried out for two large dust outbreaks originated at the source regions of northern Patagonia during the austral summer of 2009. Simulations indicate that the synoptic meteorological patterns of high and low pressure systems are largely accountable for dust transport trajectories over the SAO. According to model results and satellite retrievals from CALIPSO, synoptic flows caused by opposing pressure systems (a high pressure system located to the east or north-east

of a low pressure system) elevate the South American dust plumes well above the marine boundary layer. Under such conditions, the bulk concentration of mineral dust can quickly be transported around the low pressure system in a clockwise manner, follow the southeasterly advection pathway, and reach the high-nitrate low-chlorophyll (HNLC) waters of the SAO and Antarctica in ~3-4 days after emission from the source regions of northern Patagonia.

Two different mechanisms for Fe mobilization into a bioavailable form are considered in this study. GEOS-Chem, implemented with an Fe dissolution scheme, is employed to estimate the atmospheric fluxes of soluble Fe (sol-Fe), while a dust/biota assessment tool [Boyd *et al.*, 2010] is applied to evaluate the amount of bioavailable Fe formed through the slow and sustained leaching of dust in the ocean mixed layer. The effect of Fe-laden mineral dust supply on surface ocean biomass is investigated by comparing predicted surface chlorophyll-*a* concentration ([Chl-*a*]) to remotely-sensed data. As the two dust transport episodes examined here represent large summertime outflows of mineral dust from South American continental sources, this study suggests that (1) atmospheric fluxes of mineral dust from Patagonia are not likely to be the major source of bioavailable Fe to ocean regions characterized by large visual diatom blooms, however, (2) even if Patagonian dust plumes may not cause visible algae blooms, they could still be a contributor to background sol-Fe (in conjunction with marine supply pathways (e.g., upwelling and shelf runoff)) and [Chl-*a*] in the South Atlantic sector of the Southern Ocean (SO).

Many global remote oceanic regions have marine primary productivity limited by essential micronutrients which can be supplied by mineral dust deposition. During my dissertation research, mineral dust and micronutrient deposition rates are predicted for March 2009 to February 2010 using the 3-D CTM GEOS-Chem implemented with an updated dust-nutrient dissolution scheme. This comprehensive nutrient dissolution scheme simulates sol-Fe production taking into account acid-based and organic ligand-promoted dissolution processes, ferrous/ferric Fe (Fe(II)/Fe(III)) photochemical redox cycling, acid-based  $\text{PO}_4^{3-}$  dissolution, and  $\text{NO}_3^-$  formation during atmospheric transport. During the yearlong simulation  $\sim 0.17$ ,  $0.20$ , and  $75$  Tg ( $1 \text{ Tg} = 10^{12} \text{ g}$ ) of sol-Fe,  $\text{PO}_4^{3-}$ , and  $\text{NO}_3^-$  was deposited to global oceanic regions, respectively. The addition of organic ligand-promoted Fe dissolution proved to be significant as annual model-predicted sol-Fe deposition to global oceanic regions increased by  $\sim 20\%$  when compared to simulations only taking into account acid-based Fe dissolution. Additionally, the mineralogy of Fe-containing compounds (i.e., hematite, goethite, illite) largely influenced the magnitude of oceanic sol-Fe fluxes due to differing dissolution rates. Marine ecosystems with primary productivity limited by sol-Fe, such as the subarctic North Pacific and Southern Oceans, are predicted to receive biogeochemically important sol-Fe fluxes from Asian, Patagonian, and Australian dust source regions with seasonally-averaged deposition rates exceeding  $1.0 \mu\text{g m}^{-2} \text{ day}^{-1}$  during times of maximum sol-Fe deposition. Furthermore, the explicit calculations of Fe(II) deposition rates are presented with maximum daily-averaged values exceeding  $1.0 \mu\text{g m}^{-2}$  in oceanic regions influenced by organic acids and substantial incoming solar radiation.

Surface oceans assumed to be limited by the essential micronutrients  $\text{PO}_4^{3-}$  and  $\text{NO}_3^-$  are simulated to receive seasonally-averaged deposition rates exceeding 10 and 100  $\mu\text{g m}^{-2} \text{day}^{-1}$ , respectively. Overall during this study, the most comprehensive dataset of essential micronutrient deposition rates are presented and provide a unique opportunity for usage in global ocean biogeochemistry and climate model predictions.

## References

- Baker, A. R., and T. D. Jickells (2006), Mineral particle size as a control on aerosol iron solubility, *Geophys. Res. Lett.*, 33, L17608, doi:10.1029/2006GL026557.
- Baker, A.R., Jickells, T.D., Witt, M. and Ligne, K.L. (2006) Trends in the solubility of iron, aluminium, manganese and phosphorus in aerosol collected over the Atlantic Ocean. *Marine Chemistry*, 98(1), 43-58.
- Boyd, P. W., D. S. Mackie, and K. A. Hunter (2010), Aerosol iron deposition to the surface ocean: Modes of iron supply and biological responses, *Mar. Chem.*, 120, 128-143, doi:10.1016/j.marchem.2009.01.008.

## 2. Literature Review

### 2.1 Potential climatic impact of mineral dust

Mineral dust particles are one of the most abundant aerosols in the Earth's atmosphere (by mass). With global emission rates  $\sim 2150 \text{ Tg yr}^{-1}$  ( $1 \text{ Tg} = 10^{12} \text{ g}$ ) mineral dust makes up  $\sim 40\%$  of the global annual mass of aerosols emitted from the Earth [IPCC, 2001]. These natural aerosols can directly impact radiative forcing by altering incoming solar radiation in the atmosphere through scattering and absorption [Tegen *et al.*, 1997; Haywood and Boucher, 2000] and indirectly by changing cloud microphysics and optical properties by acting as cloud condensation (CCN) and/or ice nuclei (IN) [Wurzler *et al.*, 2000; Sassen *et al.*, 2003; DeMott *et al.*, 2003; Solomos *et al.*, 2011]. Presently, there remains considerable uncertainty in both the sign and magnitude of the net direct radiative forcing by mineral dust, ranging from  $-0.56$  to  $+0.4 \text{ W m}^{-2}$  [Forster *et al.*, 2007]. General circulation models also simulate a wide variety of estimates for the indirect radiative forcing by dust particles acting as IN with an estimated range from  $-1.0$  to  $-2.1 \text{ W m}^{-2}$  [Lohmann and Diehl, 2006]. Figure 2.1 shows the estimate of the radiative forcing (and uncertainty) of both anthropogenic and natural aerosols determined by the Intergovernmental Panel on Climate Change (IPCC). This IPCC report suggests that the direct and indirect forcing of aerosols in the Earth's atmosphere has a medium to low level of scientific understanding.

In addition to the direct and indirect radiative effect of mineral dust, these natural aerosols have a long-term indirect effect on the Earth's climate. This long-term effect is due

to the fact that the atmospheric deposition of aeolian dust is recognized as an important supply pathway of nutrients (i.e., Fe, P, and N) to the surface waters of global oceans [Martin and Fitzwater, 1988; Jickells et al., 2005; Meskhidze et al., 2005; Duce et al., 2008; Mahowald et al., 2008; Nenes et al., 2011]. These deposition fluxes may exert control on the dynamics of plankton growth, which in turn affects the biogeochemical cycles of carbon, nitrogen, silicon, sulfur, and can ultimately influence the Earth's climate [e.g., Boyd et al., 2007; Duce et al., 2008; Mahowald et al., 2008; Nenes et al., 2011; Nickovic et al., 2011; Mahowald, 2011]. For example, mesoscale Fe enrichment experiments have shown that the supply of bioavailable iron to Fe-depleted surface waters (also known as HNLC regions (shown in Fig. 2.2)) directly impact phytoplankton dynamics and possibly influence atmospheric CO<sub>2</sub> concentrations. In the recent publication by Mahowald [2011], it was estimated that the long-term indirect effect of sol-Fe deposition to the global oceans equated to a radiative forcing of  $-0.07 \pm 0.07 \text{ W m}^{-2}$ . Finally, uncertainties in the radiative forcing of natural background aerosols, such as mineral dust, can strongly influence the model-predicted extent of human induced climate change and our ability to predict future climate. Therefore, the improved quantification of mineral dust emission rates, transport dynamics, particle-size distributions, mixing state, chemical transformations in the atmosphere, oceanic nutrient supply, and CCN and IN properties are some of the main motivations of present-day scientific research [e.g., Mahowald, 2011].

## 2.2 Bioavailable nutrients in mineral dust

### 2.2.1 Bioavailable Fe

One of the main foci of my dissertation research is the quantification of aeolian dust deposition and its supply of bioavailable Fe to remote global surface oceans and the potential impact on biogeochemical cycling [Martin and Fitzwater, 1988; Coale et al., 1996; Boyd et al., 2000; Fung et al., 2000]. Fe is one of the main nutrient elements needed for utilization by phytoplankton in order to carry out photosynthetic processes. Although Fe is the fourth most abundant element in the Earth's crust, Fe is in short supply in most near-surface remote oceanic waters (i.e., subarctic north Pacific, east equatorial Pacific, and the Southern Ocean (Figure 2.2)). Concentrations of Fe are particularly low in the HNLC oceanic regions, where the availability of the micronutrient Fe has been shown to be a limiting factor for marine primary productivity [Martin and Fitzwater, 1988; Martin, 1990]. HNLC oceanic regions comprise ~30% of the global oceans, with the Southern Ocean (SO) suggested to be the most biogeochemically significant due to its large spatial extent and considerable influence on the global carbon cycle [Martin, 1990; Watson et al., 2000; Boyd et al., 2000; Sarmiento et al., 2004]. The climatic importance of this region is reflected in a hypothesis that the glacial-interglacial changes in atmospheric CO<sub>2</sub> can be attributed to changes in the atmospheric dust-Fe supply to the SO [Martin and Fitzwater, 1988]; although recent studies have also pointed out that marine processes play a key role in the biogeochemical cycling of Fe in the SO [Meskhidze et al., 2007; Blain et al., 2007; Wagener et al., 2008].

The role of aeolian Fe deposition in marine ecosystem productivity is complicated by the fact that in order for Fe to be utilized by phytoplankton in photosynthetic processes (bioavailable Fe) it must be in an aqueous, colloidal, or nanoparticulate form [*Jickells et al.*, 2005; *Raiswell and Canfield*, 2012]. The majority of the Fe mass found in the atmosphere is contained within mineral dust aerosols emitted from continental sources. Fe in atmospheric mineral dust particles is primarily in the form of Fe-(oxyhydr)oxides, such as hematite ( $\alpha$ -Fe<sub>2</sub>O<sub>3</sub>) and goethite ( $\alpha$ -FeO(OH)), ferric Fe (Fe(III)) substituted into aluminosilicate minerals [*Dedik and Hoffmann*, 1992; *Hoffmann et al.*, 1996; *Arimoto et al.*, 2002], and ferrihydrite [*Shi et al.*, 2009, 2012]. The soluble/dissolved iron fraction (DIF) ( $DIF(\%) = \frac{sol-Fe}{total\ Fe} \times 100$ ) of Fe-containing minerals, commonly found in freshly emitted dust particles, are typically small (< 1%), however, in situ measurements suggest downwind from the dust source regions increased (> 10%) and spatially variable DIFs [e.g., *Baker and Jickells*, 2006; *Baker et al.*, 2006]. These measurements support the hypothesis that atmospheric processing of mineral dust, by anthropogenic and natural pollutants, may be an important process in mobilizing Fe and increasing the atmospheric bioavailable Fe supply for oceanic primary productivity.

Several past research studies have suggested that the majority of sol-Fe within mineral dust is derived from atmospheric processing during long-range transport [e.g., *Jickells and Spokes*, 2001; *Mahowald et al.*, 2005]. Therefore, an important goal in present day climate research is to better understand how physical and chemical processes affect the

formation of sol-Fe in mineral dust during atmospheric transport. Fe in mineral dust particles can be mobilized through three different mechanisms: proton-promoted, ligand-promoted, and reductive dissolution [Schwertmann, 1991]. Fe dissolution in acidic environments (low pH) commonly occurs due to high proton concentrations destabilizing Fe-oxygen bonds in the crystal lattice of Fe-(oxyhydr)oxides and aluminosilicates [Wiederhold *et al.*, 2006; Journet *et al.*, 2008]. During ligand-promoted Fe dissolution, Fe in the crystal lattice structuring is complexed by organic ligand molecules and is more readily detached in atmospheric and oceanic waters, resulting in a soluble form of Fe(III) [Wiederhold *et al.*, 2006]. The third process is known as reductive dissolution which involves an electron transfer to Fe(III) resulting in ferrous iron (Fe(II)) formation which is readily released into solution [Larsen and Postma, 2001; Fu *et al.*, 2010].

The dissolution of Fe containing minerals is extremely slow at neutral pH values commonly encountered in desert top-soils and oceanic surface waters [Stumm and Morgan, 1996; Fung *et al.*, 2000; Hand *et al.*, 2004; Bonnet and Guieu, 2004; Jickells *et al.*, 2005], therefore, it has been proposed that the acidification of mineral dust aerosols during atmospheric transport increases the amount of bioavailable Fe production before deposition [Duce and Tindale, 1991; Zhu *et al.*, 1992; Zhuang *et al.*, 1992a, 1992b; Zhu *et al.*, 1993, 1997; Meskhidze *et al.*, 2003, 2005]. Past modeling studies, focused on predicting Fe mobilization within mineral dust, have primarily concentrated on acidity/pH dependent dissolution processes [e.g., Meskhidze *et al.*, 2003, 2005; Cwiertny *et al.*, 2008; Solmon *et al.*, 2009]. During atmospheric transport, alkaline mineral dust particles chemically react with

acidic trace gases (e.g., sulfur dioxide (SO<sub>2</sub>) and NO<sub>x</sub>) and accumulate oxidation products such as sulfate (SO<sub>4</sub><sup>2-</sup>) and nitrate (NO<sub>3</sub><sup>-</sup>). The acidity/pH of the aqueous solution surrounding mineral dust aerosol is controlled by the ionic balance between these acidic species and the main alkaline buffering agent calcite/calcium carbonate (CaCO<sub>3</sub>) and ammonium (NH<sub>4</sub><sup>+</sup>). If the concentration of the acidic species becomes abundant enough to overcome the alkalinity of mineral dust, the pH of the aqueous solution surrounding the dust particle will decrease and Fe can be effectively mobilized from the particle through proton-promoted dissolution processes [Meskhidze *et al.*, 2003, 2005]. Modeling studies incorporating acid-mobilization of Fe, resulting from the mixing of mineral dust with anthropogenic acidic gases, have predicted considerable increases in sol-Fe as a result of this mixing process [Meskhidze *et al.*, 2005; Fan *et al.*, 2006; Solmon *et al.*, 2009].

Due to the large buffering capacity of CaCO<sub>3</sub>, on average mineral dust particles do not easily become acidic. Therefore, when deliquesced mineral dust particles have near neutral pH values, additional chemical processes have been suggested as important sources of sol-Fe production within mineral dust. For example, dicarboxylic acids commonly found in atmospheric waters (e.g., oxalic acid) [Kawamura and Kaplan, 1989, Zuo and Holgné, 1992] have been shown to increase Fe dissolution rates through organic ligand-promoted dissolution [e.g., Martin, 2005; Paris *et al.*, 2011]. Among the major organic compounds found in the atmosphere, oxalic acid ((COOH)<sub>2</sub>) has been extensively measured and suggested to be one of the most abundant and highly effective Fe complexing ligands [Cornell and Schindler, 1987]. Oxalic acid has been suggested to have both anthropogenic

and natural terrestrial sources of its precursor gases [e.g., *Fu et al.*, 2008; *Myriokefalitakis et al.*, 2008; *Sinreich et al.*, 2010; *Volkamer et al.*, 2010; *Rinaldi et al.*, 2011]. The impact of oxalic acid/oxalate concentrations on Fe dissolution rates are studied in depth in Chapter 5.

Past laboratory studies have demonstrated that when Fe dissolution experiments are conducted in the absence of UV/visible radiation, minimal amounts of Fe(II) are produced and the majority of sol-Fe is in the form of Fe(III) [e.g., *Cwiertny et al.*, 2009]. However, in the presence of organic Fe-complexing ligands and incoming solar radiation, it has been shown that a higher fraction of sol-Fe can exist in the Fe(II) form [*Zuo and Holgné*, 1992; *Cornell and Schwertmann*, 1996]. Organically complexed Fe(III) (i.e., Fe(III)-oxalate species), produced during the atmospheric transport of mineral dust, strongly absorb UV/visible incoming solar radiation and photochemically react to form Fe(II) in the presence of light with wavelengths between 290-570 nm [*Zuo and Holgné*, 1992]. The photochemical reduction of Fe(III)-organic species results in Fe(II) which increases the bioavailability of Fe in seawater and has been demonstrated to more effectively enhance diatom growth in comparison to soluble Fe(III) [*Barbeau et al.*, 2001; *Chen and Siefert*, 2003]. In surface ocean and aerosol waters, Fe(II) tends to be rapidly oxidized into the Fe(III) form by oxidants such as hydrogen peroxide ( $\text{H}_2\text{O}_2$ ), hydroperoxyl radical ( $\text{HO}_2$ ), hydroxyl radical ( $\text{OH}$ ), superoxide ( $\text{O}_2^-$ ), and ozone ( $\text{O}_3$ ). However, in the presence of organic ligands, Fe(II) may be stabilized in environments with elevated oxidant concentrations, significantly increasing the lifetime of Fe(II) under oxic conditions. Therefore, the organic complexing of Fe-laden dust is suggested to have a major impact on the formation and redox cycling of sol-Fe.

In addition to chemical transformations, the preferential deposition of larger particles during the long-range transport of mineral dust influences bulk mineralogy. Gravitational settling will cause a shift from larger (predominantly quartz) to smaller (clay/aluminosilicate minerals) sized dust particles downwind from the emission source region. In previous research, it has commonly been assumed that Fe-(oxyhydr)oxides are the major forms of Fe solubilized during atmospheric processes and available for biological utilization [Meskhidze *et al.*, 2005; Luo *et al.*, 2005; Fan *et al.*, 2006; Solmon *et al.*, 2009]. However, it has recently been observed that greater solubilities of Fe resulted from clays (~4%) in comparison to Fe-(oxyhydr)oxides (< 1%) after simulated atmospheric transport (pH < 5) [Journet *et al.*, 2008]. Journet *et al.* [2008] suggested that Fe solubility could be greatest in clay minerals where Fe is often found as amorphous impurities, compared to the (oxyhydr) oxides where Fe is bound by ionic/covalent bonds in the crystalline lattice. Complementary analyses using Mössbauer spectroscopy and scanning electron microscopy with energy dispersive X-ray analysis (CCSEM/EDX) suggests that solid phases responsible for sol-Fe generation may be Fe(II)-substituted clay/aluminosilicates [Cwiertny *et al.*, 2008]. Additionally, recent laboratory studies have demonstrated the importance of readily soluble forms of Fe, such as ferrihydrite nano-particles, which are suggested to provide an important source of bioavailable Fe upon deposition to oceanic surface waters [Shi *et al.*, 2009; Raiswell and Canfield, 2012]. These past laboratory and modeling studies have demonstrated how the mineralogical composition/Fe-containing mineral speciation of dust particles can significantly influence the amount of Fe mobilized during atmospheric transport.

Physical characteristics of dust plumes and single dust particles have also been suggested to influence Fe mobilization. Several past studies have shown an inverse relationship between atmospheric dust concentrations and the solubility fraction of Fe [*Chen and Siefert, 2004; Baker and Jickells, 2006; Meskhidze et al., 2005; Solmon et al., 2009*]. The reduced concentrations of mineral dust, during long-range transport, allows for acidic trace gases to overcome the alkalinity buffer of CaCO<sub>3</sub> and lower pH values of the deliquesced dust particle, thus having a better chance of initiating Fe dissolution. Additionally, due to the preferential removal of particles with larger diameters by gravitational settling [*Seinfeld and Pandis, 1998*], dust plumes will have an increasing number of particles with smaller diameters during long-range transport. Dust plumes containing small particles, which have high surface area to volume ratios, have a large collective surface area in comparison to a dust plume with more coarse mode particles. The larger surface areas expose a maximum amount of Fe contained within the dust particle to acidic deliquesced solutions and trace gases in the atmosphere. These two physically-based characteristics can have a large impact on the magnitude of bioavailable Fe deposition to remote global oceanic regions.

### **2.2.2 Bioavailable P and N**

Mineral dust deposition is an important atmospheric source of P and N to remote oceanic surface waters, and has been suggested to play a controlling role in marine ecosystem processes in oligotrophic nutrient depleted surface oceans outside of the global HNLC regions [*Elser et al., 2007; Krishnamurthy et al., 2007; Duce et al., 2008; Mahowald*

*et al.*, 2008; *Okin et al.*, 2011]. Similar to Fe, mineral dust particles contain the majority of P mass found in the atmosphere [*Mahowald et al.*, 2008]. Soil-derived-P is primarily found in the apatite mineral group ( $\text{Ca}_5(\text{PO}_4)_3(\text{OH}, \text{F}, \text{Cl})$ ) and adsorbed onto Fe-(oxyhydr)oxides [*Graham and Duce*, 1979; *Palmer*, 1985; *Singer et al.*, 2004]. In general, the soluble/bioavailable fraction of P (sol-P) within mineral dust is considered to be  $\text{PO}_4^{3-}$  [*Mahowald et al.*, 2008; *Nenes et al.*, 2011]. The soluble fraction of P-containing minerals, within freshly emitted dust particles, is typically small (< 10%), however, downwind from the dust source regions previous modeling/laboratory studies and in situ measurements suggest much higher and spatially variable sol-P fractions (> 90%) [e.g., *Baker et al.*, 2006; *Mahowald et al.*, 2008; *Nenes et al.*, 2011].

The atmospheric processing of mineral-P has been studied much less thoroughly compared to Fe laden dust. However, past laboratory and measurement studies have determined that P solubility is minimal (~10%) in seawater (primarily polyphosphates [*Benitez-Nelson*, 2000]) [*Lepple*, 1975; *Graham and Duce*, 1979; *Herut et al.*, 1999; *Izquierdo et al.*, 2012] compared to aerosol samples in lower pH environments (22-73%) [*Herut et al.*, 2002, 2005; *Carbo et al.*, 2005]. Similar to mineral-Fe, *Ridame and Guieu* [2002] measured that the solubility of P in Saharan dust was inversely proportional to particle concentrations. These studies have led to the conclusion that the solubility percentages of P increase with decreasing pH, suggesting that desorption and acidity driven dissolution may be a controlling factor of mineral-P bioavailability [*Ridame and Guieu*, 2002; *Markaki et al.*, 2003; *Jones and Jacobsen*, 2005].

With such limited information on the processes controlling mineral-P dissolution, recent studies have calculated bioavailable P deposition assuming a priori and constant solubility fractions. For example, *Mahowald et al.* [2008] estimated that 17% of mineral-P was water soluble in order to predict bioavailable  $\text{PO}_4^{3-}$  fluxes to the global oceans. The problem with using a constant fraction of P solubility is that this does not agree with measurements that observe a gradient in P solubility in transported mineral dust (ranging between 7 and 100%) [e.g., *Baker et al.*, 2006]. In order to reproduce the pattern of increasing P solubility during the atmospheric transport of mineral dust, studies such as *Nenes et al.* [2011] performed laboratory and modeling experiments to evaluate the impact of acidity driven dissolution processes on  $\text{PO}_4^{3-}$  formation. This study showed that the acidity driven dissolution of Saharan dust particles caused an increase in the sol-P fraction by a factor of 10 - 40 (up to 96%). Expanding on these findings, *Nenes et al.* [2011] suggested that, similar to the acid mobilization of mineral Fe, anthropogenic  $\text{SO}_2$  and  $\text{NO}_x$  absorption onto mineral dust will increase the solubility fraction of P during atmospheric transport. Overall, due to P limiting and co-limiting marine primary productivity in many remote oceanic regions [e.g., *Elser et al.*, 2007], it is important to understand the atmospheric processes producing bioavailable P within mineral dust particles.

The majority of N in oceanic environments is present as  $\text{N}_2$  and is available only to marine organisms known as diazotrophs. The usage of  $\text{N}_2$  is restricted to this group of microorganisms due to the fact they can fix  $\text{N}_2$ . The availability of fixed  $\text{N}_2$  limits marine primary production and the conversion of inorganic carbon (IC) to organic carbon (OC) in

many remote oligotrophic surface oceans outside of HNLC regions. Bioavailable N can be supplied to oceanic surface waters by riverine discharge, N<sub>2</sub> fixation, and atmospheric deposition of aerosol NO<sub>3</sub><sup>-</sup> [Moore *et al.*, 2001; Mills *et al.*, 2004; Duce *et al.*, 2008]. In situ measurements of the chemical composition of dust particles have shown that NO<sub>3</sub><sup>-</sup> is frequently formed on coarse mode mineral dust aerosols during atmospheric transport [e.g., Zhuang *et al.*, 1999; Parmar, 2001; Artiñano *et al.*, 2003; Henning *et al.*, 2003; Park *et al.*, 2004; Cousin *et al.*, 2005; Dentener *et al.*, 2006; Sullivan *et al.*, 2007]. The major formation pathways of NO<sub>3</sub><sup>-</sup> on mineral dust are the heterogeneous uptake of nitric acid (HNO<sub>3</sub>) and nitrogen dioxide (NO<sub>2</sub>) [Dentener *et al.*, 2006; Usher *et al.*, 2003]. It has been suggested that, on a global scale, the atmospheric deposition of aerosol NO<sub>3</sub><sup>-</sup> is an important supply pathway of bioavailable N to remote oceanic regions [i.e., Paerl and Whittall, 1999; Duce *et al.*, 2008;]. However, the deposition of NO<sub>3</sub><sup>-</sup> laden dust particles is an atmospheric supply pathway of bioavailable N that has not been a major focus in previous research evaluating atmospheric nutrient deposition.

### **2.3 Simulating mineral dust processes**

With the growing interest in dust-nutrient deposition and its impact on marine primary productivity, improving dust aerosol modeling is an increasingly important topic. Due to the limited number of mineral dust and total aerosol Fe concentration measurements, aerosol transport models are applied on a global scale in order to fill the spatial and temporal gaps. Global and regional aerosol models treating dust particles are commonly applied in order to study aspects ranging from dust emission fluxes to the climatic impact of dust

particles [e.g., *Marticorena and Bergametti*, 1995; *Mahowald et al.*, 1999, 2006; *Werner et al.*, 2002; *Tegen et al.*, 2002]. Although progress has been made in the treatment of mineral dust in aerosol transport models, the recent work by *Huneus et al.* [2011] evaluated 15 global dust transport models and determined that dust emission fluxes, surface level concentrations, total atmospheric burdens, and aerosol optical depth (AOD) calculations differed largely between models. In the following section an overview is presented on past and present modeling studies helping to better constrain mineral dust in global/regional models.

### **2.3.1 Mineral dust emissions**

Past research studies applying global models, in situ measurements, and remotely-sensed data have been beneficial in constraining global mineral dust emission source locations and strengths [e.g. *Marticorena and Bergametti*, 1995; *Fung et al.*, 2000; *Ginoux et al.*, 2001, 2003; *Tegen et al.*, 2002; *Prospero et al.*, 2002; *Zender et al.*, 2003; *Mahowald et al.*, 2003, 2005, 2008; *Fairlie et al.*, 2007; *Li et al.*, 2008; *Johnson et al.*, 2010, 2012]. These past studies have shown that the dominant sources of mineral dust in the Northern Hemisphere are the arid desert regions of North Africa, the Middle East, and Asia. In addition, studies conducted to quantify dust emissions in the Southern Hemisphere seem to agree that the arid and semi-arid regions of South America and Australia are the major source regions. The process of predicting dust emission source regions and strength is highly complex with dependence on various meteorological and soil/ground surface characteristics. Specifically, mineral dust emission schemes are highly dependent on surface wind speed, soil

moisture, top-soil size distribution, soil crustiness, roughness length, vegetation cover, and snow cover [e.g., *Ginoux et al.*, 2001; *Zender et al.*, 2003].

An important aspect in predicting mineral dust emissions, explained in *Zender et al.* [2003], is a process known as “saltation” bombardment. Dust particles with small diameters are necessary for long-range transport, however, due to the large cohesion force of smaller dust particles (clay size particles ( $< 2 \mu\text{m}$ )) they are not prone to atmospheric entrainment. As larger dust particles (sand ( $> 50 \mu\text{m}$ ) and silt ( $2 - 50 \mu\text{m}$ )) are advected, they will impact clusters of smaller/clay sized particles and reduce the cohesion force allowing for smaller particles to be entrained into the overlying atmosphere (“saltation” effect). The initiation of this process is highly dependent on surface wind speeds. In the dust emission scheme applied during this study (Dust Entrainment and Deposition (DEAD)), the saltation flux is calculated using Eq. (1):

$$Q_s = \frac{c_s \rho u_*^3}{g} \left(1 - \frac{u_{*t}}{u_*}\right) \left(1 + \frac{u_{*t}}{u_*}\right) \quad (1)$$

where  $c_s = 2.61$ ,  $\rho$  is the density of air,  $u_*$  represents the wind friction speed,  $g$  is gravity, and  $u_{*t}$  is the threshold wind friction speed. Eq. 1 is suggested to be valid for the atmospherically transportable size range of mineral dust commonly simulated in global aerosol transport models (i.e.,  $0.1$  to  $10 \mu\text{m}$ ) [*Zender et al.*, 2003]

Total model-predicted annual global dust emissions demonstrate large variability between different models with emission fluxes ranging between  $\sim 500 - 4000 \text{ Tg yr}^{-1}$  [*Huneus et al.*, 2011 and references within]. These differences are likely to be associated

with the fact that a large variety of emission parameterization schemes and input data are applied to calculate dust emission fluxes [Ginoux *et al.*, 2001; Tegen *et al.*, 2002; Zender *et al.*, 2003; Stier *et al.*, 2005; Pringle *et al.*, 2010]. In addition, many models and emission parameterizations are tuned to match available in situ measurement and remotely sensed data, often at long distances from the dust source regions. This fact makes it difficult to compare mineral dust emission schemes, when used in individual global models, due to model specific tuning factors being applied. Numerous emission schemes have been developed in order to estimate dust fluxes with varying ranges of comprehensiveness [e.g., Marticorena and Bergametti, 1995; Marticorena *et al.*, 1997; Shao *et al.*, 1993, 2004, 2011; Alfaro and Gomes, 2001; Nickovic *et al.*, 2001; Ginoux *et al.*, 2001; Tegen *et al.*, 2002; Zender *et al.*, 2003; Balkanski *et al.*, 2004]. An example of these emission parameterizations is the DEAD scheme (used predominantly during this study) which allows for the online calculation of the vertical dust flux (dust emissions) using the input data of boundary layer wind speeds, soil texture and hydrology, leaf and stem area index, solar and thermal radiative fluxes (to determine stability), and local topography. Using these inputs, the model calculates the saltation mass flux ( $Q_s$ , Eq. (1)) and the size-dependant vertical dust entrainment flux  $F_{d,j}$  using Eq. (2) derived from Zender *et al.* [2003]:

$$F_{d,j} = TA_m S \propto Q_s \sum_{i=1}^l Mi,j \quad (2)$$

where  $T$  is a globally uniform tuning factor,  $A_m$  is the fraction of bare soil exposed in a gridcell,  $\alpha$  is the saltation and blasting mass efficiency, and  $M_{i,j}$  is the mass fraction of each size mode  $i$  carried in each transport bin  $j$ .

As previously stated, mineral dust emissions predominantly occur in arid and semi-arid regions which contain fine/loose sediment, with low surface roughness values [Gillette, 1999; Ginoux *et al.*, 2001; Prospero *et al.*, 2002; Zender *et al.*, 2003]. In our study, we use the source function from the Goddard Chemistry Aerosol Radiation and Transport (GOCART) model in order to determine the geographical positioning of mineral dust emissions. Principal dust emission source regions predicted by this parameterization are deserts or dry lakes and streambeds where alluvial deposits have accumulated [Ginoux *et al.*, 2001]. Ginoux *et al.* [2001] scaled global dust emissions to topographic depressions in dry/un-vegetated regions in order to simulate areas that potentially contain sediments from dried lakes/streams shown by Eq. (3):

$$S = \left( \frac{z_{max} - z_i}{z_{max} - z_{min}} \right)^5 \quad (3)$$

where  $S$  is the probability of having accumulated sediment in a given model grid cell,  $z_i$  is the model grid elevation, and  $z_{max}$  and  $z_{min}$  are the maximum and minimum elevation of the surrounding  $10^\circ \times 10^\circ$  topography, respectively. The resulting dust emission fluxes from combining Eq. (1) – (3) in GEOS-Chem are shown in Fig. 2.3.

The direct measurement of mineral dust emission fluxes has proven to be difficult and has resulted in a limited database of dust emission locations/rates. A good example of a way

to study dust emission source regions without using dust emission measurements was demonstrated in the work by *Prospero et al.* [2002]. This study applied Total Ozone Mapping Spectrometry (TOMS) satellite data in order to determine dust emission sources and temporal variability on a global scale. While it was well known before this study that arid and semi-arid desert regions were the major sources of dust emissions, this study determined that the action of water in the past can form ephemeral streams, rivers, lakes, and playas which evolve into major dust emission locations. This further indicated that major global dust sources have in the past been intermittently flooded as evidenced by deep alluvial deposits. In addition to past hydrological cycles influencing dust source regions, presently many dust sources are associated with human/anthropogenic activity demonstrating that humans can largely influence global dust emissions through increased desertification [*Ginoux et al.*, 2012].

### **2.3.2 Dust transport and deposition**

Due to larger aerosols being prone to gravitational settling, only dust particles with diameters  $< \sim 10 \mu\text{m}$  are typically considered for long-range transport [*Seinfeld and Pandis*, 1998; *Reid et al.*, 2003]. Once emitted from the Earth's surface, simulated atmospheric lifetime and horizontal/vertical transport pathways of mineral dust are highly dependent on model specific meteorological fields (e.g., wind speed/direction and precipitation). For example, aerosols transported above the boundary layer are less affected by wet deposition processes, and therefore, particle lifetimes tend to increase with advection altitude [e.g., *Tegen et al.*, 1996]. Additionally, wind speed and wind shear increase with height and

aerosols that are transported in the free troposphere tend to be carried longer distances than dust that remains in the boundary layer [*Prospero et al.*, 1981; *Li et al.*, 2008]. In global models, which apply coarse grid spacing to simulate mineral dust transport, generally rely heavily on large scale synoptic meteorological conditions to predict mineral dust transport. However, these coarse grid models have been shown to be unable to capture small-scale processes, such as squall lines, which have a large influence on mineral dust emission and transport in regions such as the Sahel region of North Africa [e.g., *Sommeria and Testud*, 1984]. Past studies have shown that the absence of these small-scale processes may lead to an underestimation of the long-range transport of dust in global models.

The atmospheric lifetime of mineral dust simulated within global dust models is highly dependent on deposition process. Typically, dust removal from the atmosphere occurs through dry deposition processes such as gravitational settling [*Seinfeld and Pandis*, 1998] and turbulent dry transfer of particles to the surface [*Zhang et al.*, 2001]. In addition to dry deposition, dust removal from the atmosphere is initiated by wet deposition processes which includes both convective up draft scavenging and rainout/washout from large-scale precipitation [*Liu et al.*, 2001]. The ratio of dry and wet deposition fluxes are highly model dependant [*Huneeus et al.*, 2011]. However, in general, close to the dust source regions, gravitational sedimentation controls the majority of dust deposition. Further downwind from the dust emission regions, wet deposition fluxes are the controlling factor in dust aerosol atmospheric lifetime. Overall, atmospheric lifetimes of dust particles generally differ with aerosol size. For example, past studies have shown that dust particles with diameters  $> 10$

$\mu\text{m}$  tend to be deposited in a few hours, however, sub-micron dust particles can have atmospheric lifetimes well over a week [Tegen and Fung, 1994; Tegen and Lacis, 1996; Mahowald et al., 1999; Ginoux et al., 2001].

Dry deposition ( $D_d$ ) parameterizations (Eq. (4)) in global dust models focus on 1) gravitational settling ( $v_g$ ) and 2) mixing to the surface from the first atmospheric layer by turbulent air motions ( $v_t$ ) [Tegen et al., 2003].

$$D_d = v_g + v_t \quad (4)$$

For example, in the DEAD scheme dust particles are assumed to gravitationally settle at terminal velocity ( $v_g$ ) shown in Eq. (5):

$$v_g = \left( \frac{4gDC_c\rho_p}{3C_D\rho} \right)^{\frac{1}{2}} \quad (5)$$

where  $g$  is gravity,  $D$  represents the dust particle diameter,  $C_c$  is the slip correction factor,  $\rho_p$  stands for the particle density, and  $\rho$  is the atmospheric density. Turbulent deposition velocities ( $v_t$ ) are the second factor used to calculate dry deposition rates and is predicted using Eq. (6):

$$v_t = \frac{1}{r_a + r_b + r_a r_b v_g} \quad (6)$$

where  $r_a$  is the aerodynamic resistance constant and accounts for local stability effects and  $r_b$  is the quasi-laminar resistance (dependant on Schmidt number and wind friction velocity). From sensitivity studies performed in Zender et al. [2003] it was determined that the dry

deposition limiting resistance for turbulent mix out of accumulation mode dust particles (diameter  $< 2 \mu\text{m}$ ) is  $r_b$  at all wind speeds. For larger dust particles, at low wind speeds ( $< 5 \text{ m s}^{-1}$ ),  $r_b$  is the deposition limiting resistance, however, when wind speeds are  $> 5 \text{ m s}^{-1}$   $r_a$  becomes the limiting resistance.

Wet deposition of mineral dust occurs through sub- and below-cloud scavenging by precipitation and in some models by in-cloud removal processes (in the cases when dust is effective for ice cloud formation). Model-predicted wet deposition fluxes of mineral dust are still highly uncertain due to the lack of knowledge of dust-cloud-precipitation interactions. In the majority of models, wet scavenging processes are treated with mass mean and path-normalized scavenging ratios,  $r_m$  ( $\text{m}^2 \text{ kg}^{-1}$ ), as shown in Eq. (7):

$$\frac{dM_p}{dt} = AP_M r_m M_p \quad (7)$$

where  $A$  is the fraction of the model grid cell in which precipitation is occurring,  $P_M$  represents the rate of collision between mineral dust and scavenging precipitation droplets,  $r_m$  is the scavenging ratio, and  $M_p$  is grid cell aerosol concentration. Sub-cloud and below-cloud scavenging is generally not calculated explicitly but applies a “scavenging ratio” ( $r_m$ ). This value is the ratio of the dust concentration that is scavenged by rainwater and the concentration that remains in the ambient air. Past studies [e.g., *Buat-Menard and Duce, 1986; Duce et al., 1991*] have measured widely varying values of the scavenging ratio for differing regions of the world. The overall uncertainty in simulated wet deposition fluxes

stems from the fact that the majority of global models apply a single/constant scavenging ratio to calculate wet deposition fluxes of mineral dust.

Although dust deposition measurement datasets are limited, they have been applied to evaluate simulated dust deposition rates. In general, modeling studies [e.g., *Luo et al.*, 2003, 2005, 2008; *Mahowald et al.*, 2003; *Hand et al.*, 2004] show that terrestrial in situ measurements have better correlation with model outputs than when compared to marine based measurements. This fact may point to the uncertainty in modeling wet deposition processes. Additionally, the difficulty in evaluating predicted dust concentrations and deposition rates may be due to the fact that dust events are highly episodic in nature. Large dust outbreaks occur only a few days annually, and these events contribute the dominant magnitude of both dust concentration and depositions [*Loye-Pilot et al.*, 1986]. It is unlikely that any individual observation station will be temporally and spatially correlated with these large dust plumes in order to record data on the few days each year they occur. This problem with model-measurement intercomparison is further magnified due to global dust models using larger grid resolutions. These issues have caused for the comparison of model-predicted dust concentrations and observations to result in model-measurement differences ranging between 50 to over 1000% [*Mahowald et al.*, 2008].

### **2.3.3 Mineral dust optical properties**

Due to the lack of in situ measurements of mineral dust concentrations, many global models calculate aerosol optical depth (AOD), which can be compared to remotely-sensed

AOD data during model evaluations. Many mineral dust properties can influence model-predicted dust AOD values such as: mass loading, refractive indexes, and hygroscopic properties of aerosols. Typically, global dust models relate mineral dust AOD and total column mass concentrations using a mass loading based parameterization similar to that described in *Tegen and Lacis* [1996] shown in Eq. (8):

$$M = \frac{4}{3} \rho r \tau Q_{ext}^{-1} \quad (8)$$

where  $M$  is the column mass burden of a specific size range of mineral dust (defined by the effective radius ( $r$ )),  $\rho$  represents mineral dust density,  $\tau$  is the mineral dust AOD value, and  $Q_{ext}$  is the Mie scattering efficiency. This mass loading based parameterization can be applied to numerous size bins of mineral dust where each size range will have specific  $\rho$ ,  $r$ , and  $Q_{ext}$  values. Model-predicted AOD values also depend on transport and removal processes, which can be influenced by the dust advection altitude [*Tegen et al.*, 1996; *Chin et al.*, 2002], as well as particle size distribution [*Tegen and Lacis*, 1996; *Kok*, 2011]. As explained previously, the long-range transport of mineral dust reduces the median size of the aerosol size distribution. Dust particles with median radii  $\sim 1 \mu\text{m}$  or less scatter the majority of incident solar radiation, although, larger particles close to the dust source region ( $> 10 \mu\text{m}$ ) are more absorbing of both incoming short-wave and outgoing long-wave radiation [*Duce*, 1995; *Schuetz et al.*, 1981; *Tegen and Lacis*, 1996; *Liao and Sienfeld*, 1998]. These studies show the importance of being able to accurately simulate mineral dust size distributions in order to calculate dust AOD values (studied in detail in Chapter 3).

In general, global climate models (GCMs) predict higher fractions of clay aerosols in emitted dust by a factor of ~2-8 in comparison to in situ measurement data. This overestimation has large implications for model-predicted spatial distributions, radiative forcing, and dust emission rates [Kok, 2011]. A major uncertainty caused by this overestimation of clay sized dust particles is the optical efficiency ( $Q_{ext}$ ) of mineral dust in the sub-micron range is much larger compared to coarse mode aerosols and therefore, this overestimation of the clay sized dust particles will lead to a positive bias in model-predicted AOD values. The study by Kok [2011] suggested that the emission of mineral dust is a scale-invariant process and offered a simple theoretical expression for the power law size distribution of emitted dust aerosols (applicable for all size ranges of mineral dust that are assumed to be prone to atmospheric transport). It was suggested, that when implemented in regional and global climate models, the proposed parameterization may resolve the substantial overestimation of the emitted clay size fraction of dust commonly occurring in these models [Kok, 2011]. Therefore, a full understanding of mineral dust size distributions is necessary to constrain mineral dust mass and AOD values in global dust models. The influence of mineral dust mass size distributions on model-predicted AOD values is evaluated in Chapter 3.

## **2.4 GEOS-Chem**

The state-of-the-art 3-D global CTM GEOS-Chem has been widely-used for the evaluation of atmospheric chemical composition, aerosol transport, AOD, and sol-Fe deposition to the global oceans [e.g., Bey *et al.*, 2001; Heald *et al.*, 2006; van Donkelaar *et*

*al.*, 2006; *Solmon et al.*, 2009; *Johnson et al.*, 2010, 2011, 2012]. GEOS-Chem can also be used in combination with other GCMs to study past and future climate [e.g., *Wu et al.*, 2007, 2008]. The model was first described and evaluated with observations in the study by *Bey et al.* [2001] and includes detailed emission schemes for both natural and anthropogenic sources, explicit chemistry, aerosol processes, long-range transport of gas and aerosol species, troposphere-stratosphere exchanges, and more. GEOS-Chem comprises H<sub>2</sub>SO<sub>4</sub>-HNO<sub>3</sub>-NH<sub>3</sub> aerosol thermodynamics coupled to an O<sub>3</sub>-NO<sub>x</sub>-hydrocarbon-aerosol chemical mechanism [*Bey et al.*, 2001; *Park et al.*, 2004]. Sulfur compounds, carbonaceous aerosols, and sea-salt emission and chemistry are accounted for and described by *Park et al.* [2004], *Heald et al.* [2004], and *Alexander et al.* [2005]. Our in house version of GEOS-Chem, implemented with our improved nutrient dissolution scheme (described in Chapter 5), was applied to quantify global mineral dust emissions, transport, deposition, and bioavailable nutrient formation (general model configuration shown in Table 2.1).

The standard GEOS-Chem tropospheric chemical mechanism consists of over 100 species and 300 reactions integrated using the stiff-ordinary first order differential equation solver Sparse Matrix Vectorized GEAR II (SMVGEAR II) [*Jacobson and Turco*, 1994; *Jacobson*, 1995, 1998]. Using these sparse matrix operations has been proven to be computationally efficient while displaying a high order of accuracy in 3-D models. The GEOS-Chem model calculates photolysis frequencies using the Fast-J radiative transfer algorithm of *Wild et al.* [2000], which uses a seven-wavelength quadrature scheme that accurately predicts Rayleigh scattering as well as aerosol and cloud Mie scattering. In order

to simulate the diurnal variations of photochemical processes, photolysis calculations are performed every hour in the model. The Fast-J scheme is highly accurate as it calculates photolysis frequencies generally within 3% and predicts values comparable to past photolysis schemes [Wild *et al.*, 2000]

The baseline GEOS-Chem model allows for the application of several different anthropogenic emission inventories: the Global Emission Inventory Activity (GEIA), which is the default inventory to account for global anthropogenic emissions, Big Bend Regional Aerosol and Visibility Observational (BRAVO) [Kuhns *et al.*, 2003], Emissions Database for Global Atmospheric Research (EDGAR) [Olivier *et al.*, 2001], European Monitoring and Evaluation Programme (EMEP) [Vestreng and Klein, 2002], Streets 2000 [Streets *et al.*, 2003], and the Environmental Protection Agency and National Emission Inventory non-methane (EPA/NEI99). Table 2.2 illustrates the anthropogenic emission inventories that are available for GEOS-Chem (v8-01-01) in the full chemistry configuration. Biomass burning emissions in the model are derived from the GFED database which includes emission factors for gas-phase species ( $\text{CO}_2$ ,  $\text{NO}_x$ , sulfur dioxide ( $\text{SO}_2$ ), ammonia ( $\text{NH}_3$ ), carbon monoxide ( $\text{CO}$ ), alkanes (ALK4), acetone (ACET), methyl ethyl ketone (MEK), acetaldehyde (ALD2), propene (PRPE), propane ( $\text{C}_3\text{H}_8$ ), formaldehyde ( $\text{CH}_2\text{O}$ ), ethane ( $\text{C}_2\text{H}_6$ )) and aerosol species (black carbon (BC), organic carbon (OC)) [Van der Werf *et al.*, 2010]. Natural pollutant emission inventories, pertaining to this research, include volcanic  $\text{SO}_2$  and oceanic dimethylsulfide (DMS) emissions. The volcanic  $\text{SO}_2$  emissions are derived from GEIA emissions inventory and TOMS remotely-sensed data. Monthly-averaged oceanic DMS

emissions were developed by Dr. Meinrat Andreae. GEOS-Chem uses the Model of Emissions of Gases and Aerosols from Nature (MEGAN) [Guenther *et al.*, 2006] to derive terrestrial biogenic emissions, such as isoprene, in GEOS-Chem. MEGAN computes emissions for varying plant types as a function of temperature, solar radiation, leaf area index, and leaf age. Finally, sea-salt emissions are predicted using the surface wind speed dependant Gong [2003] parameterization.

Importantly, for my dissertation research, GEOS-Chem simulates dust mobilization by combining the DEAD scheme [Zender *et al.*, 2003] with the source function used in the GOCART model [Ginoux *et al.*, 2001; Chin *et al.*, 2002]. Principal source regions are deserts or dry lakes and streambeds where alluvial deposits have accumulated. Once mineral dust is mobilized from the surface, the model uses four standard dust bins with diameter boundaries of 0.2 - 2.0, 2.0 - 3.6, 3.6 - 6.0 and 6.0 - 12.0  $\mu\text{m}$  to simulate global dust transport and deposition [Fairlie *et al.*, 2007]. Dust removal from the atmosphere occurs through dry deposition processes such as gravitational settling [Seinfeld and Pandis, 1998] and turbulent dry transfer of particles to the surface [Zhang *et al.*, 2001]. Dust removal by wet deposition processes includes both convective up draft scavenging and rainout/washout from large-scale precipitation [Liu *et al.*, 2001]. Table 2.1 gives a complete list of chemical species transported during our base model simulations (tracers are assigned to species with lifetimes long enough for transport between grid cells).

Assimilated meteorological fields from the Goddard Earth Observing System (GEOS) of the NASA Global Modeling Assimilation Office (GMAO) are used to drive GEOS-Chem

[*Bey et al.*, 2001; *Park et al.*, 2004]. Our version of the model uses the newest GEOS-5 meteorological fields at a  $2^\circ \times 2.5^\circ$  (latitude-longitude) grid resolution and 47 vertical levels ([http://wiki.seas.harvard.edu/geos-chem/index.php/List\\_of\\_GEOS-5\\_met\\_fields](http://wiki.seas.harvard.edu/geos-chem/index.php/List_of_GEOS-5_met_fields)). GEOS-5 meteorological fields are available every 3 and 6 hr and have a native horizontal resolution of  $0.5^\circ \times 0.67^\circ$  and vertical resolution of 72 hybrid eta levels, extending from the surface to 0.01 hPa. The first 31 levels from the surface upward are pure sigma levels and the rest are fixed pressure levels. These meteorological fields are then re-gridded to the desired vertical and horizontal resolution, used in specific GEOS-Chem model simulations, and applied during calculations of aerosol emission, transport, chemistry, and deposition.

## **2.5 Objectives**

During this research, synergistic methods were applied by combining passive and active remotely-sensed data with model-predictions to evaluate the following interdisciplinary atmospheric/oceanic processes:

(1) Global dust mobilization source regions and emission rates, transport pathways and dynamics, and deposition processes.

(2) Compare GEOS-Chem-predicted AOD and dust aerosol extinction profiles to passive and active satellite data to evaluate global horizontal and vertical dust transport pathways.

(3) Determine the possible impact of mineral dust/sol-Fe deposition on marine primary productivity and biogeochemistry in the HNLC regions of the South Atlantic sector of the Southern Ocean.

(4) Improve our dust-nutrient dissolution scheme through the following model developments:

- a) Implementation of organic acids
- b) Organic ligand-promoted Fe dissolution
- c) Photochemical Fe(II)/Fe(III) redox cycling
- d) Acid-based  $\text{PO}_4^{3-}$  dissolution
- e) Dust- $\text{NO}_3^-$  formation
- f) Heterogeneous global dust mineralogy datasets
- g) Source specific mineral dust and bioavailable nutrient treatment

(5) Simulate and create the most comprehensive global dataset of bioavailable nutrient concentrations and deposition for future application in global ocean biogeochemistry and climate model predictions.

## References

- Alexander, B., R. J. Park, D. J. Jacob, Q. B. Li, R. M. Yantosca, J. Savarino, C. C. W. Lee, and M. H. Thiemens (2005), Sulfate formation in sea-salt aerosols: Constraints from oxygen isotopes, *J. Geophys. Res.*, *110*, doi:10.1029/2004JD005659.
- Alfaro S. C., and L. Gomes (2001), Modeling mineral aerosol production by wind erosion: Emission intensities and aerosol distributions in source areas, *J. Geophys. Res.*, *106*, 18075-18084.
- Arimoto, R., W. Balsam, and C. Schloesslin (2002), Visible spectroscopy of aerosol particles collected on filters: Iron-oxide minerals, *Atmos. Env.*, *36*, 89-96.
- Artiñano, B., P. Salvador, D. G. Alonso, X. Querol, and A. Alastuey (2003), Anthropogenic and natural influence on the PM10 and PM2.5 aerosol in Madrid (Spain). Analysis of high concentration episodes, *Environ. Pollut.*, *125*(3), 453–465, doi:10.1016/S0269-7491(03)00078-2.
- Baker, A. R., and T. D. Jickells (2006), Mineral particle size as a control on aerosol iron solubility, *Geophys. Res. Lett.*, *33*, L17608, doi:10.1029/2006GL026557.
- Baker, A. R., T. D. Jickells, M. Witt, and K. L. Ligne (2006), Trends in the solubility of iron, aluminium, manganese and phosphorus in aerosol collected over the Atlantic Ocean, *Marine Chemistry*, *98*(1), 43-58.
- Balkanski, Y., M. Schulz, T. Claquin, C. Moulin, and P. Ginoux (2004), Emission Of Atmospheric Trace Compounds, chap. Global emissions of mineral aerosol: formulation and validation using satellite imagery, pp. 239-267, Ed. Kluwer.
- Barbeau, K., E. L. Rue, K. W. Bruland, and A. Butler (2001), Photochemical cycling of iron in the surface ocean mediated by microbial iron(III)-binding ligands, *Nature*, *413*, 409-413.
- Benitez-Nelson, C. R., (2000), The biogeochemical cycling of phosphorus in marine systems, *Earth-Science Reviews*, *51*, 109-135.
- Bey, I., D. J. Jacob, R. M. Yantosca, J. A. Logan, B. Field, A. M. Fiore, Q. Li, H. Liu, L. J. Mickley, and M. Schultz (2001), Global modeling of tropospheric chemistry with assimilated meteorology: Model description and evaluation, *J. Geophys. Res.*, *106*(D19), 23073-23095.

- Blain, S. et al. (2007), Effect of natural iron fertilization on carbon sequestration in the Southern Ocean, *Nature*, 446, doi: 10.1038/nature05700.
- Bonnet, S., and C. Guieu (2004), Dissolution of atmospheric iron in seawater, *Geophys. Res. Lett.*, 31, doi:10.1029/2003GL018423.
- Buat-Menard, P., and R. A. Duce (1986), Precipitation scavenging of aerosol particles over remote marine regions, *Nature*, 321, 508–510.
- Boyd, P. W., et al. (2000), A mesoscale phytoplankton bloom in the polar Southern Ocean stimulated by iron fertilization, *Nature*, 407, 695-702.
- Boyd, P. W., et al. (2007), Mesoscale iron enrichment experiments 1993-2005: Synthesis and future directions, *Science*, 315, 612-617.
- Carbo, P., M. D. Krom, W. B. Homoky, L. G. Benning, and B. Herut (2005), Impact of atmospheric deposition on N and P geochemistry in the southeastern Levantine basin, *Deep-Sea Research II*, 52, 3041e3053.
- Chen, Y., and R. L. Siefert (2003), Determination of various types of labile atmospheric iron over remote oceans, *J. Geophys. Res.*, 108(D24), 4774, doi:10.1029/2003JD003515.
- Chin, M., P. Ginoux, S. Kinne, O. Torres, B. Holben, B. Duncan, R. Martin, J. Logan, A. Higurashi, and T. Nakajima (2002), Tropospheric aerosol optical thickness from the GOCART model and comparisons with satellite and sunphotometer measurements, *J. Atmos. Sci.*, 59, 461-483.
- Chen, Y. and R. L. Seifert (2004), Seasonal and spatial distributions of atmospheric total and labile iron over the Tropical and sub-tropical North Atlantic Ocean, *J. Geophys. Res.*, 109, doi:10.1029/2003JD003958.
- Coale, K. H., et al. (1996), A massive phytoplankton bloom induced by an ecosystem-scale iron fertilization experiment in the equatorial Pacific Ocean, *Nature*, 383, 495-501, doi:10.1038/383495a0.
- Cornell, R. M., and U. Schwertmann (1996), *The Iron Oxides, Structure, Properties, Reactions, Occurrence and Uses*, 573 pp., John Wiley, Hoboken, N. J.
- Cornell R. M., and P. W. Schindler (1987), Photochemical dissolution of goethite in acid/oxalate solution, *Clays Clay Miner.*, 35, 347-352.

- Cousin, F., C. Liousse, H. Cachier, B. Bessagnet, B. Guillaume, and R. Rosset (2005), Aerosol modelling and validation during ESCOMPTE 2001, *Atmos. Environ.*, *39*(8), 1539-1550.
- Cwiertny, D. M., J. Baltusaitis, G. J. Hunter, A. Laskin, M. M. Scherer, and V. H. Grassian (2008), Characterization and acid-mobilization study of iron-containing mineral dust source materials, *J. Geophys. Res.*, *113*, D05202, doi:10.1029/2007JD009332.
- Cwiertny, D. M., G. J. Hunter, J. M. Pettibone, M. M. Scherer, and V. H. Grassian (2009), Surface Chemistry and Dissolution of  $\alpha$ -FeOOH Nanorods and Microrods: Environmental Implications of Size-Dependent Interactions with Oxalate, *J. Phys. Chem.*, *113*, 2175-2186.
- Dedik, A. N., and P. Hoffmann (1992), Chemical characterization of iron in atmospheric aerosols, *Atmos. Env.*, *26*, 2545-2548.
- DeMott, P. J., K. Sassen, M. R. Poellet, D. Baumgardner, D. C. Rogers, S. D. Brooks, A. J. Prenni, and S. M. Kreidenweis (2003), African dust aerosols as atmospheric ice nuclei, *Geophys. Res. Lett.*, *30*, 1732, doi:10.1029/2003GL017410.
- Dentener, F., et al. (2006), Nitrogen and sulfur deposition on regional and global scales: A multimodel evaluation, *Global Biogeochem. Cycles*, *20*, GB4003, doi:10.1029/2005GB002672.
- Duce, R. A. (1995), Sources, distributions, and fluxes of mineral aerosols and their relationship to climate. In: Charlson, R., Heintzenberg, J. (Eds.), *Aerosol Forcing of Climate*, Wiley, New York, pp. 43-72.
- Duce, R. A., and N. W. Tindale (1991), Atmospheric transport of iron and its deposition in the ocean, *Limnol. Oceanogr.*, *36*, 1715-1726.
- Duce, R. A., et al. (2008), Impacts of atmospheric anthropogenic nitrogen on the open ocean, *Science*, *320*(5878), 893-897, doi:10.1126/science. 1150369.
- Elser, J. J., M. E. S. Bracken, E. E. Cleland, D. S. Gruner, W. S. Harpole, H. Hillebrand, J. T. Ngai, E. W. Seabloom, J. B. Shurin, and J. E. Smith (2007), Global analysis of nitrogen and phosphorus limitation of primary producers in freshwater, marine and terrestrial ecosystems, *Ecol. Lett.*, *10*, 1135-1142.
- Fan, S.-M., W. J. Moxim, and H. Levy II (2006), Aeolian input of bioavailable iron to the ocean, *Geophys. Res. Lett.*, *33*, doi:10.1029/2005GL024852.

- Forster, P., et al. (2007), Changes in atmospheric constituents and radiative forcing, in: *Climate Change 2007: The Physical Science Basis, contribution of Working Group I to the Fourth Assessment Report of the Intergovernmental Panel on Climate Change*, in the *Fourth Assessment Report of the Intergovernmental Panel on Climate Change*, edited by S. Solomon et al., chap. 2, pp. 131–234, Cambridge Univ. Press, Cambridge, U. K.
- Fu, H., D. M. Cwiertny, G. R. Carmichael, M. M. Scherer, and V. H. Grassian (2010), Photoreductive dissolution of Fe-containing mineral dust particles in acidic media, *J. Geophys. Res.*, *115*, D11304, doi:10.1029/2009JD012702.
- Fu, T. -M., D. J. Jacob, F. Wittrock, J. P. Burrows, M. Vrekoussis, and D. Henze (2008), Global budgets of atmospheric glyoxal and methylglyoxal, and implications for formation of secondary organic aerosols, *J. Geophys. Res.*, *113*, D15303, doi:10.1029/2007JD009505.
- Fung, I. Y., S. K. Meyu, I. Tegen, S. C. Doney, J. G. John, and J. K. B. Bishop (2000), Iron supply and demand in the upper ocean, *Global Biogeochem. Cycles*, *14*, 281-295.
- Gillette, D. A. (1999), A qualitative geophysical explanation for “hot spot” dust emitting source regions, *Contributions to Atmospheric Physics*, *72*, 67-77.
- Ginoux, P. A., J. M. Prospero, T. E. Gill, C. Hsu, and M. Zhao (2012), Global scale attribution of anthropogenic and natural dust sources and their emission rates based on MODIS Deep Blue aerosol products, *Rev. Geophys.*, doi:10.1029/2012RG000388, in press.
- Gong, S. L. (2003), A parameterization of sea-salt aerosol source function for sub- and supermicron particles, *Global Biogeochem. Cycles*, *17*(4), 1097, doi:10.1029/2003GB002079.
- Graham, W. F., and R. A. Duce (1979), Atmospheric pathways of the phosphorus cycle, *Geochimica et Cosmochimica Acta*, *43*, 1195-1208.
- Guenther, A., T. Karl, P. Harley, C. Wiedinmyer, P. I. Palmer, and C. Geron (2006), Estimates of global terrestrial isoprene emissions using MEGAN (Model of Emissions of Gases and Aerosols from Nature), *Atmos. Chem. Phys.*, *6*, 3181-3210, doi:10.5194/acp-6-3181-2006.
- Hand, J. L., N. M. Mahowald, Y. Chen, R. L. Siefert, C. Luo, A. Subramaniam, and I. Fung (2004), Estimates of atmospheric-processed soluble iron from observations and a global mineral aerosol model: Biogeochemical implications, *J. Geophys. Res.*, *109*, doi:10.1029/2004JD004574.

- Haywood, J., and O. Boucher (2000), Estimates of the direct and indirect radiative forcing due to tropospheric aerosols, *Rev. Geophys.*, *38*, 513-543.
- Heald, C. L., D. J. Jacob, D. B. A. Jones, P. I. Palmer, J. A. Logan, D. G. Streets, G. W. Sachse, J. C. Gille, R. N. Hoffman, and T. Nehrkorn (2004), Comparative inverse analysis of satellite (MOPITT) and aircraft (TRACE-P) observations to estimate Asian sources of carbon monoxide, *J. Geophys. Res.*, *109*, doi:10.1029/2004JD005185.
- Heald, C. L., D. J. Jacob, R. J. Park, B. Alexander, T. D. Fairlie, R. M. Yantosca, and D. A. Chu (2006), Transpacific transport of Asian anthropogenic aerosols and its impact on surface air quality in the United States, *J. Geophys. Res.*, *111*, D14310, doi:10.1029/2005JD006847.
- Henning, S., E. Weingartner, M. Schwikowski, H. W. Gaggeler, R. Gehrig, K.-P. Hinz, A. Trimborn, B. Spengler, and U. Baltensperger (2003), Seasonal variation of water-soluble ions of the aerosol at the high-alpine site Jungfraujoch (3580 m asl), *J. Geophys. Res.*, *108*(D1), 4030, doi:10.1029/2002JD002439.
- Herut, B., R. Collier, and M. D. Krom (2002), The role of dust in supplying nitrogen and phosphorus to the Southeast Mediterranean, *Limnology and Oceanography*, *47*, 870e878.
- Herut, B., et al. (2005), Response of East Mediterranean surface water to Sahara dust: on-board microcosm experiment and field observations, *Deep-Sea Research II*, *52*, 3024e3040.
- Herut, B., M. D. Krom, G. Pan, and R. Mortimer (1999), Atmospheric input of nitrogen and phosphorus to the Southeast Mediterranean: sources, fluxes, and possible impact, *Limnology and Oceanography*, *44*, 1683e1692.
- Hoffmann, P., A. N. Dedik, J. Ensling, S. Weinbruch, S. Weber, T. Sinner, P. Gutlich, and H. M. Ornter (1996), Speciation of iron in atmospheric aerosol samples, *J. Aerosol Sci.*, *27*, 325-337.
- Huneus, N., et al. (2011), Global dust model intercomparison in AeroCom phase I, *Atmos. Chem. Phys.*, *11*, 7781-7816, doi:10.5194/acpd-10-23781-2010.
- IPCC, 2007: *Climate Change 2007: The Physical Science Basis. Contribution of Working Group I to the Fourth Assessment Report of the Intergovernmental Panel on Climate Change* [Solomon, S., D. Qin, M. Manning, Z. Chen, M. Marquis, K.B. Averyt, M. Tignor and H.L. Miller (eds.)]. Cambridge University Press, Cambridge, United Kingdom and New York, NY, USA.

- Jacobson, M. Z. (1995), Computation of global photochemistry with SMVGEARII, *Atmos. Environ.*, 29A, 2541-2546.
- Jacobson, M. Z. (1998), Improvement of SMVGEARII on vector and scalar machines through absolute error tolerance control, *Atmos. Environ.*, 32, 791-796.
- Jacobson, M. Z., and R. P. Turco (1994), SMVGEAR: A Sparse-Matrix, Vectorized Gear Code for Atmospheric Models, *Atmos. Env.*, 2, 273-284.
- Jickells, T. D., and L. J. Spokes (2001), Atmospheric iron inputs to the ocean, in: *Biogeochemistry of Iron in Seawater* (Eds. D. Turner and K.A. Hunter), John Wiley and Sons.
- Jickells, T. D., et al. (2005), Global iron connections between desert dust, ocean biogeochemistry, and climate, *Science*, 308, 67-71.
- Johnson, M. S., N. Meskhidze, F. Solmon, S. Gassó, P. Y. Chuang, D. M. Gaiero, R. M. Yantosca, S. Wu, Y. Wang, and C. Carouge (2010), Modeling dust and soluble iron deposition to the South Atlantic Ocean, *J. Geophys. Res.*, 115, D15202, doi:10.1029/2009JD013311.
- Johnson, M. S., N. Meskhidze, V. P. Kiliyanpilakkil, and S. Gassó (2011), Understanding the transport of Patagonian dust and its influence on marine biological activity in the South Atlantic Ocean, *Atmos. Chem. Phys.*, 11, 2487-2502, doi:10.5194/acp-11-2487-2011.
- Johnson, M. S., N. Meskhidze, and K. V. Praju (2012), A global comparison of GEOS-Chem-predicted and remotely-sensed mineral dust aerosol optical depth and extinction profiles, *J. Adv. Model. Earth Syst.*, doi:10.1029/2011MS000109.
- Jones, C., and J. Jacobsen (2005), Phosphorus Cycling, Testing and Fertilizer Recommendations, *Nutrient Management Module*, 4.
- Journet, E., K. V. Desboeufs, S. Caquineau, and J.-L. Colin (2008), Mineralogy as a critical factor of dust iron solubility, *Geophys. Res. Lett.*, 35, L07805, doi:10.1029/2007GL031589.
- Kawamura, K., and I. R. Kaplan (1989), Organic compounds in rainwater. In: Hansen, L.D., Eatough, D.J. (Eds.), *Organic Compounds in Rainwater*, second ed. CRC Press, Boston, 33-284.
- Kok, J. F (2011), A scaling theory for the size distribution of emitted dust aerosols suggests climate models underestimate the size of the global dust cycle, *PNAS*, 108(3), 1016-1021.

- Krishnamurthy, A., J. K. Moore, C. S. Zender, and C. Luo (2007), Effects of atmospheric inorganic nitrogen deposition on ocean biogeochemistry, *J. Geophys. Res.*, *112*, G02019, doi:10.1029/2006JG000334.
- Kuhns, H., M. Green, and V. Etyemezian (2003), Big Bend Regional Aerosol and Visibility Observational (BRAVO) Study Emissions Inventory, *Open File Rep*, 1-56, Desert Research Institute, Las Vegas, NV.
- Larsen, O., and D. Postma (2001), Kinetics of reductive bulk dissolution of lepidocrocite, ferrihydrite, and goethite, *Geochim. Cosmochim. Acta*, *65*(9), 1367-1379, doi:10.1016/S0016-7037(00)00623-2.
- Lepple, F.K. (1975), Eolian dust over the North Atlantic Ocean, PhD Thesis, University of Delaware.
- Liao, H., and J. H. Seinfeld (1998), Radiative forcing by mineral dust aerosols: sensitivity to key variables, *J. Geophys. Res.*, *103*, 31637-31645.
- Lohmann, U., and K. Diehl (2006), Sensitivity studies of the importance of dust ice nuclei for the indirect aerosol effect on stratiform mixed-phase clouds, *J. Atmos. Sci.*, *63*, 968-982.
- Loye-Pilot M., J. Martin, and J. Morellit (1986), Influence of Saharan dust on the rain acidity and atmospheric input to the Mediterranean, *Nature*, *321*, 427-428.
- Liu, H., D. J. Jacob, I. Bey, and R. M. Yantosca (2001), Constraints from <sup>210</sup>Pb and <sup>7</sup>Be on wet deposition and transport in a global three-dimensional chemical tracer model driven by assimilated meteorological fields, *J. Geophys. Res.*, *106*(D11), 12109-12128.
- Luo, C., N. Mahowald, and J. Corral (2003), Sensitivity study of meteorological 29 parameters on mineral aerosol mobilization, transport and distribution, *J. Geophys. Res.*, *108*, D15, 4447, 10.1029/2003JD0003483.
- Luo, C., N. M. Mahowald, N. Meskhidze, Y. Chen, R. L. Siefert, A. R. Baker, and A. M. Johansen (2005), Estimation of iron solubility from observations and a global aerosol model, *J. Geophys. Res.*, *110*, doi:10.1029/2005JD006059.
- Luo, C., N. Mahowald, T. Bond, P. Y. Chuang, P. Artaxo, R. Siefert, Y. Chen, and J. Schauer (2008), Combustion iron distribution and deposition, *Global Biogeochem. Cycles*, *22*, doi:10.1029/2007GB002964.
- Mahowald, N. (2011), Aerosol Indirect Effect on Biogeochemical Cycles and Climate, *Science*, *334*, doi:10.1126/science.1207374.

- Mahowald, N., K. E. Kohfeld, M. Hansson, Y. Balkanski, S. P. Harrison, I. C. Prentice, M. Schulz, and H. Rohde (1999), Dust sources and deposition during the Last Glacial Maximum and current climate: a comparison of model results with paleodata from ice cores and marine sediments, *J. Geophys. Res.*, *104*, 15895-16436.
- Mahowald, N., C. Luo, J. D. Corral, and C. Zender (2003), Interannual variability in atmospheric mineral aerosols from a 22-year model simulation and observational data, *J. Geophys. Res.*, *108*, 4352.
- Mahowald, N., A. Baker, G. Bergametti, N. Brooks, R. Duce, T. Jickells, N. Kubilay, J. Prospero, and I. Tegen (2005), Atmospheric global dust cycle and iron inputs to the ocean, *Global Biogeochem. Cycles*, *19*, 10.1029/2004GB002402.
- Mahowald, N., D. Muhs, S. Levis, P. Rasch, M. Yoshioka, and C. Zender (2006), Change in atmospheric mineral aerosols in response to climate: last glacial period, preindustrial, modern and doubled-carbon dioxide climates, *J. Geophys. Res.*, *111*, D10202.
- Mahowald, N., et al. (2008), Global distribution of atmospheric phosphorus sources, concentrations and deposition rates, and anthropogenic impacts, *Global Biogeochem. Cy.*, *22*, GB4026, doi:10.1029/2008GB003240.
- Mahowald, N., et al. (2009), Atmospheric Iron Deposition: Global Distribution, Variability, and Human Perturbations, *Annu. Rev. Mar. Sci.*, 245-278.
- Markaki, Z., K. Oikonomou, M. Koçak, G. Kouvrakis, A. Chaniotaki, N. Kubilay, and N. Mihalopoulos (2003), Atmospheric deposition of inorganic phosphorus in the Levantine Basin, Eastern Mediterranean: spatial and temporal variability and its role in seawater productivity, *Limnology and Oceanography*, *48*, 1557e1568.
- Marticorena, B., and G. Bergametti (1995), Modeling the atmospheric dust cycle: 1. Design of a soil-derived dust emission scheme, *J. Geophys. Res.*, *100*, 16415-16430.
- Marticorena, B., G. Bergametti, B. Aumont, Y. Callot, C. N'Doume, and M. Legrand (1997), Modeling the atmospheric dust cycle: 2. Simulation of Saharan dust sources, *J. Geophys. Res.*, *102*, 4387-4404.
- Martin, J. H. (1990), Glacial-interglacial CO<sub>2</sub> change: The Iron Hypothesis, *Paleoceanography*, *5*, 1-13.
- Martin, S. T. (2005), Precipitation and dissolution of iron and manganese oxides. In: Grassian, V.H. (Ed.), *Environmental Catalysis*, Marcel-Dekker CRC Press, Boca Raton, 61-81.

- Martin, J. H., and S. E. Fitzwater (1988), Iron-deficiency limits phytoplankton growth in the northeast pacific subarctic, *Nature*, 331, 341-343.
- Meskhidze, N., W. L. Chameides, A. Nenes, and G. Chen (2003), Iron mobilization in mineral dust: Can anthropogenic SO<sub>2</sub> emissions affect ocean productivity?, *Geophys. Res. Lett.*, 30, doi:10.1029/2003GL018035.
- Meskhidze, N., W. L. Chameides, and A. Nenes (2005), Dust and pollution: A recipe for enhanced ocean fertilization?, *J. Geophys. Res.*, 110, D03301, doi:10.1029/2004JD005082.
- Meskhidze, N., A. Nenes, W. L. Chameides, C. Luo, and N. Mahowald (2007), Atlantic Southern Ocean productivity: Fertilization from above or below?, *Global Biogeochem. Cycles*, 21, GB2006, doi: 10.1029/2006GB002711.
- Mills, M. M., C. Ridame, M. Davey, J. La Roche, and J. G. Geider (2004), Iron and phosphorous co-limit nitrogen fixation in the eastern tropical North Atlantic, *Nature*, 429, 292e294.
- Moore, J. K., S. Doney, J. Kleypas, D. Glover, and I. Fung (2001), An intermediate complexity marine ecosystem model for the global domain, *Deep Sea Res. Part II*, 49, 403-462, doi:10.1016/S0967-0645(01)00108-4.
- Myriokefalitakis, S., M. Vrekoussis, K. Tsigaridis, F. Wittrock, A. Richter, C. Bruhl, R. Volkamer, J. P. Burrows, and M. Kanakidou (2008), The influence of natural and anthropogenic secondary sources on the glyoxal global distribution, *Atmos. Chem. Phys.*, 8, 4965-4981, doi:10.5194/acp-8-4965-2008.
- Nenes, A., M. D. Krom, N. Mihalopoulos, P. Van Cappellen, Z. Shi, A. Bougiatioti, P. Zampas, and B. Herut (2011), Atmospheric acidification of mineral aerosols: a source of bioavailable phosphorus for the oceans, *Atmos. Chem. Phys.*, 11, 6252-6272.
- Nickovic, S. (2001), A model for prediction of desert dust cycle in the atmosphere, *J. Geophys. Res.*, 106, 18113-18129.
- Okin, G. S., et al. (2011), Impacts of atmospheric nutrient deposition on marine productivity: Roles of nitrogen, phosphorus, and iron, *Global Biogeochem. Cycles*, 25, GB2022, doi:10.1029/2010GB003858.
- Olivier, J. G. J. and J. J. M. Berdowski (2001), Global emissions sources and sinks, *The Climate System*, 33-78, Lisse, The Netherlands.

- Paerl, H. W., and D. R. Whittall (1999), Anthropogenically-derived atmospheric nitrogen deposition, marine eutrophication and harmful algal bloom expansion: Is there a link?, *Ambio*, 28, 307-311.
- Palmer, M. R., (1985), Rare earth elements in foraminifera tests, *Earth and Planetary Science Letters*, 73, 285-298.
- Paris, R., K. V. Desboeufs, and E. Journet (2011), Variability of dust iron solubility in atmospheric waters: Investigation of the role of oxalate organic complexation, *Atmos. Environ.*, 45, 6510-6517.
- Park, R. J., D. J. Jacob, B. D. Field, R. M. Yantosca, and M. Chin (2004), Natural and transboundary pollution influences on sulfate nitrate-ammonium aerosols in the United States: Implications for policy, *J. Geophys. Res.*, 109, D15204, doi:10.1029/2003JD004473.
- Park, S. H., C. B. Song, M. C. Kim, S. B. Kon, and K. W. Lee (2004), Study on size distribution of total aerosol and water-soluble ions during an Asian dust storm event at Jegu Island, Korea, *Environment Monitoring and Assessment*, 93, 157-183.
- Parmar, R. S. (2001), Study on the chemistry of fog and dew in Agra. Ph.D. Thesis, Dayalbagh Educational Institute, Dayalbagh, Agra, India.
- Pringle, K. J., H. Tost, S. Message, B. Steil, D. Giannadaki, A. Nenes, C. Fountoukis, P. Stier, E. Vignati, and J. Lelieveld (2010), Description and evaluation of GMXe: a new aerosol submodel for global simulations (v1), *Geosci. Model Dev.*, 3, 391-412, doi:10.5194/gmd-3-391-2010.
- Prospero, J. M., R. A. Glaccum, and R. T. Nees (1981), Atmospheric transport of soil dust from Africa to South America, *Nature*, 289, 570-572.
- Prospero, J. M., P. Ginoux, O. Torres, and S. E. Nicholson (2002), Environmental characterization of global sources of atmospheric soil dust identified with the Nimbus 7 Total Ozone Mapping Spectrometer (TOMS) absorbing aerosol product, *Rev. Geophys.*, 40(3), 1002, doi:10.1029/2000RG000095.
- Raiswell, R., and D. E. Canfield (2012), The Iron Biogeochemical Cycle Past and Present, *Geochem. Perspect.*, 1, 1-220.
- Reid, J. S., et al. (2003), Analysis of measurements of Saharan dust by airborne and ground-based remote sensing methods during the Puerto Rico Dust Experiment (PRIDE), *J. Geophys. Res.*, 108, 8586, doi:10.1029/2002JD002493.

- Ridame, C., and C. Guieu (2002), Saharan input of phosphate to the oligotrophic water of the open western Mediterranean Sea, *Limnology and Oceanography*, *47*, 856e869.
- Rinaldi, M., et al. (2011), Evidence of a natural marine source of oxalic acid and a possible link to glyoxal, *J. Geophys. Res.*, *116*, D16204, doi:10.1029/2011JD015659.
- Sassen, K., P. J. DeMott, J. M. Prospero, and M. R. Poellot (2003), Saharan dust storms and indirect aerosol effects on clouds: CRYSTAL-FACE results, *Geophys. Res. Lett.*, *30*, doi:10.1029/2003GL017371.
- Sarmiento, J. L., N. Gruber, M. A. Brzezinski, and J. P. Dunne (2004), High-latitude controls of thermocline nutrients and low latitude biological productivity, *Nature*, *427*(6969), 56-60, doi:10.1038/nature02127.
- Schuetz, L., R. Jaenicke, and H. Pietrek (1981), Saharan dust transport over the North Atlantic Ocean, *Geological Society of America, Special Papers*, *186*, 87-100.
- Schwertmann, U. (1991), Solubility and dissolution of iron oxides, *Plant and Soil*, *130*, 1-25.
- Seinfeld, J. H., and S. N. Pandis (1998), *Atmospheric Chemistry and Physics: From Air Pollution to Climate Change*, Wiley, New York.
- Shao, Y., M. R. Raupach, and P. A. Findlater (1993), Effect of saltation bombardment on the entrainment of dust by wind, *J. Geophys. Res.*, *98*, 12719-12726.
- Shao, Y. P. et al. (2004), Simplification of a dust emission scheme and comparison with data, *J. Geophys. Res.*, *109*(D10), D10202, doi: 10.1029/2003JD004372.
- Shao, Y. P., M. Ishizuka, M. Mikami, and J. F. Leys (2011), Parameterization of Size-resolved Dust Emission and Validation with Measurements, *J. Geophys. Res.*, *116*, D08203, doi:10.1029/2010JD014527.
- Shi, Z., M. D. Krom, S. Bonneville, A. R. Baker, T. D. Jickells, and L. G. Benning (2009), Formation of Iron Nanoparticles and Increase in Iron Reactivity in Mineral Dust during Simulated Cloud Processing, *Environ. Sci. Technol.*, *43*, 6592-6596.
- Singer, A., S. Dultz, and E. Argaman (2004), Properties of the nonsoluble fractions of suspended dust over the Dead Sea, *Atmos. Environ.*, *38*, 1745-1753.
- Sinreich, R., S. Coburn, B. Dix, and R. Volkamer (2010), Ship-based detection of glyoxal over the remote tropical Pacific Ocean, *Atmos. Chem. Phys.*, *10*, 11359-11371, doi:10.5194/acp-10-11359-2010.

- Solmon, F., P. Y. Chuang, N. Meskhidze, and Y. Chen (2009), Acidic processing of mineral dust iron by anthropogenic compounds over the north Pacific Ocean, *J. Geophys. Res.*, *114*, D02305, doi:10.1029/2008JD010417.
- Solomos, S., G. Kallos, J. Kushta, M. Astitha, C. Tremback, A. Nenes, and Z. Levin (2011), An integrated modeling study on the effects of mineral dust and sea salt particles on clouds and precipitation, *Atmos. Chem. Phys.*, *11*, 873-892, doi:10.5194/acp-11-873-2011.
- Sommeria, G., and J. Testud (1984), COPT81: a field experiment designed for the study of dynamics and electrical conductivity of deep convection in continental tropical regions, *Bulletin of the American Meteorological Society*, *65*, 4-10.
- Stier, P., et al. (2005), The aerosol-climate model ECHAM5-HAM, *Atmos. Chem. Phys.*, *5*, 1125-1156.
- Stumm, W., and J. J. Morgan (1981), *Aquatic Chemistry: An Introduction Emphasizing Chemical Equilibria in Natural Waters*, 780, John Wiley, Hoboken, N. J.
- Sullivan, R. C., S. A. Guazzotti, D. A. Sodeman, and K. A. Prather (2007), Direct observations of the atmospheric processing of Asian mineral dust, *Atmos. Chem. Phys.*, *7*, 1213-1236.
- Tegen, I., and I. Fung (1994), Modeling of mineral dust in the atmosphere: sources, transport, and optical thickness, *J. Geophys. Res.*, *99*, 22897-22914.
- Tegen, I., and I. Fung (1995), Contribution to the mineral aerosol load from land surface modification, *J. Geophys. Res.*, *100*, 18707-18726.
- Tegen, I., and A. A. Lacis (1996), Modeling of particle size distribution and its influence on the radiative properties of mineral dust aerosol, *J. Geophys. Res.*, *101*, 19237-19244.
- Tegen, I., P. Hollrig, M. Chin, I. Fung, D. Jacob, and J. Penner (1997), Contribution of different aerosol species to the global aerosol extinction optical thickness: Estimates from model results, *J. Geophys. Res.*, *102*(D20), 23,895-23,915, doi:10.1029/97JD01864.
- Tegen, I., A. Lacis, and I. Fung (1996), The influence of mineral aerosol from disturbed soils on the global radiation budget, *Nature*, *380*, 419-422.
- Tegen, I., S. P. Harrison, K. E. Kohfeld, I. C. Prentice, M. C. Coe, and M. Heimann (2002), The impact of vegetation and preferential source areas on global dust aerosol: results from a model study, *J. Geophys. Res.*, *107*, doi:10.1029/2001JD000963.

- Usher, C. R., A. E. Michel, and V. H. Grassian (2003), Reactions on mineral dust, *Chem. Rev.*, *103*, 4883-4939.
- van Donkelaar, A., R. V. Martin, and R. J. Park (2006), Estimating ground-level PM<sub>2.5</sub> using aerosol optical depth determined from satellite remote sensing, *J. Geophys. Res.*, *111*, D21201, doi:10.1029/2005JD006996.
- Vestreng, V., and H. Klein (2002), Emission data reported to UNECE/EMEP: Quality assurance and trend analysis & Presentation of WebDab, MSC-W Status Report 2002, Norwegian Meteorological Institute, Oslo Norway, July 2002.
- Volkamer, R., S. C. Coburn, B. K. Dix, and R. Sinreich (2010), The Eastern Pacific Ocean is a source for short lived atmospheric gases: glyoxal and iodine oxide, *CLIVAR Exchanges*, *15*, 30-33.
- Wagner, T., C. Guieu, R. Losno, S. Bonnet, and N. Mahowald (2008), Revisiting atmospheric dust export to the Southern Hemisphere ocean: Biogeochemical implications, *Global Biogeochem. Cycles*, *22*, GB2006, doi:10.1029/2007GB002984.
- Watson, A. J., D. C. E. Bakker, A. J. Ridgwell, P. W. Boyd and C. S. Law (2000), Effect of iron supply on Southern Ocean CO<sub>2</sub> uptake and implications for glacial atmospheric CO<sub>2</sub>, *Nature*, *407*, 730-733.
- Werner, M., I. Tegen, S. P. Harrison, K. E. Kohfeld, I. C. Prentice, Y. Balkanski, H. Rodhe, and C. Roelandt (2002), Seasonal and interannual variability of the mineral dust cycle under present and glacial climate conditions, *J. Geophys. Res.*, *107*, doi:10.1029/2002JD002365.
- Wiederhold, J. G., et al. (2006), Iron isotope fractionation during proton-promoted, ligand-controlled, and reductive dissolution of goethite, *Environ. Sci. Technol.*, *40*(12), 3787-3793, doi:10.1021/es052228y.
- Wild, O., Q. Zhu, and M. J. Prather (2000), Fast-J: Accurate simulation of in- and below-cloud photolysis in global chemical models, *J. Atmos. Chem.*, *37*, 245-282.
- Wu, S., L. J. Mickley, D. J. Jacob, J. A. Logan, R. M. Yantosca, and D. Rind (2007), Why are there large differences between models in global budgets of tropospheric ozone?, *J. Geophys. Res.*, *112*, D05302, doi:10.1029/2006JD007801.
- Wu, S., L. J. Mickley, E. M. Leibensperger, D. J. Jacob, D. Rind, and D. G. Streets (2008), Effects of 2000–2050 global change on ozone air quality in the United States, *J. Geophys. Res.*, *113*, D06302, doi:10.1029/2007JD008917.

- Wurzler, S., T. G. Reisin, and Z. Levin (2000), Modification of mineral dust particles by cloud processing and subsequent effects on drop size distributions, *J. Geophys. Res.*, *105*, 4501-4512.
- Zhang, L., S. L- Gong, J. Padro, and L. Barrie (2001), A Size-segregated Particle Dry Deposition Scheme for an Atmospheric Aerosol Module, *Atmos. Environ.*, *35*(3), 549-560.
- Zhu, X., J. M. Prospero, F. J. Millero, D. L. Savoie, and G. W. Brass (1992), The solubility of ferric ion in marine mineral aerosol solutions at ambient relative humidities, *Mar. Chem.*, *38*, 91-107.
- Zhu, X., J. M. Prospero, D. L. Savoie, F. J. Millero, R. G. Zika, and E. S. Saltzman (1993), Photoreduction of iron (III) in marine mineral aerosol solutions, *J. Geophys. Res.*, *98*, 9039-9046.
- Zhu, X. R., J. M. Prospero, and F. J. Millero (1997), Diel variability of soluble Fe(II) and soluble total Fe in North African dust in the trade winds at Barbados, *J. Geophys. Res.*, *102*, 21297-21305.
- Zhuang, G., Z. Yi, R. A. Duce, and P. R. Brown (1992a), Link between iron and sulphur cycles suggested by detection of Fe(II) in remote marine aerosols, *Nature*, *355*, 537-539.
- Zhuang, G., Z. Yi, R. A. Duce, and P. R. Brown (1992b), Chemistry of iron in marine aerosols, *Global Biogeochemical Cycles*, *6*, 161-173.
- Zhuang, H., C.K. Chan, M. Fang, and A. S. Wexler (1999), Size distributions of particulate sulfate, nitrate, and ammonium at a coastal site in Hong Kong, *Atmos. Environ.*, *33*, 843-853.
- Zuo, Y., and J. Holgné (1992), Formation of hydrogen peroxide and depletion of oxalic acid in atmospheric water by photolysis of iron(III)-oxalato complexes, *Environ. Sci. Technol.*, *26*, 1014-1022.

## Tables

Table 2.1 Baseline GEOS-Chem model configuration

Scientific Option	Configuration
Model Version	v8-01-01
Horizontal Resolution	2° x 2.5°
Vertical Resolution	47 layers
Time Step	15 minutes
Meteorological Fields	GEOS-5 (offline)
Chemical Tracers	NO <sub>x</sub> , O <sub>x</sub> , PAN, CO, ALK <sub>4</sub> , ISOP, HNO <sub>3</sub> , H <sub>2</sub> O <sub>2</sub> , ACET, MEK, ALD, RCHO, MVK, MACR, PMN, PPN, R <sub>4</sub> N <sub>2</sub> , PRPE, C <sub>3</sub> H <sub>8</sub> , CH <sub>2</sub> O, C <sub>2</sub> H <sub>4</sub> , N <sub>2</sub> O <sub>5</sub> , HNO <sub>4</sub> , MP, DMS, SO <sub>2</sub> , SO <sub>4</sub> , SO <sub>4</sub> s, MSA, NH <sub>3</sub> , NH <sub>4</sub> , NIT, Ns, BCPI, OCPI, BCPO, OCPO, DST1, DST2, DST3, DST4, SALA, SAC, FEDI, ALDI, NADI, SILDI, KDI, MGDI, CADI, SO <sub>4</sub> DI, NH <sub>4</sub> DI, CASO <sub>4</sub> , CACO <sub>3</sub>
Chemical Mechanism	SMVGEAR II [Jacobson et al, 1997], using over 100 chemical species, approximately 300 kinetic reactions and 51 photolysis reactions.
Photolysis Mechanism	FAST-J algorithm [Wild et al, 2000]
SOA Formation	Chung and Seinfeld, [2002]
Aerosol Thermodynamics Module	ISORROPIA
Anthropogenic Emissions	Global Emissions Inventory Activity (GEIA)
Dry Deposition	Dry deposition accounts for gravitational settling [Seinfeld and Pandis, 1998] and turbulent dry transfer of particles to the surface [Zhang et al., 2001].
Wet Deposition	Wet deposition uses the scheme of Liu et al. [2001], including scavenging in convective updrafts, rainout and washout from large-scale precipitation and convective anvils.

Table 2.2 Anthropogenic emission inventories available in GEOS-Chem

	Inventory	Base Year	Region	NO <sub>x</sub>	CO	PRPE	C <sub>3</sub> H <sub>8</sub>	ALK4	C <sub>2</sub> H <sub>6</sub>	ACET	MEK	ALD2	CH <sub>2</sub> O	SO <sub>2</sub>	SO <sub>4</sub>	NH <sub>3</sub>	BC/OC
Global	GEIA	1985	global	X	X	X	X	X	X	X	X			X	X	X	
	EDGAR	2000	global	X	X									X			
	BOND	1996	global														X
Regional	CAC	2002, 2005	Canada	X	X									X		X	
	EMEP	1980-2005	Europe	X	X	X		X	X		X	X		X			X
	EPA	1999 (2004)	USA	X	X	X	X	X	X	X	X		X	X	X	X	
	VISTAS	2002	USA	X													
	BRAVO	1999	Mexico	X	X									X		X	
	STREETS	2004	Asia	X	X	X	X	X	X	X	X	X	X	X		X	
	COOKE	1996	N. America														X

\* Yellow highlights indicate the default emission setup during GEOS-Chem full chemistry simulations.

Figures

## Radiative Forcing Components

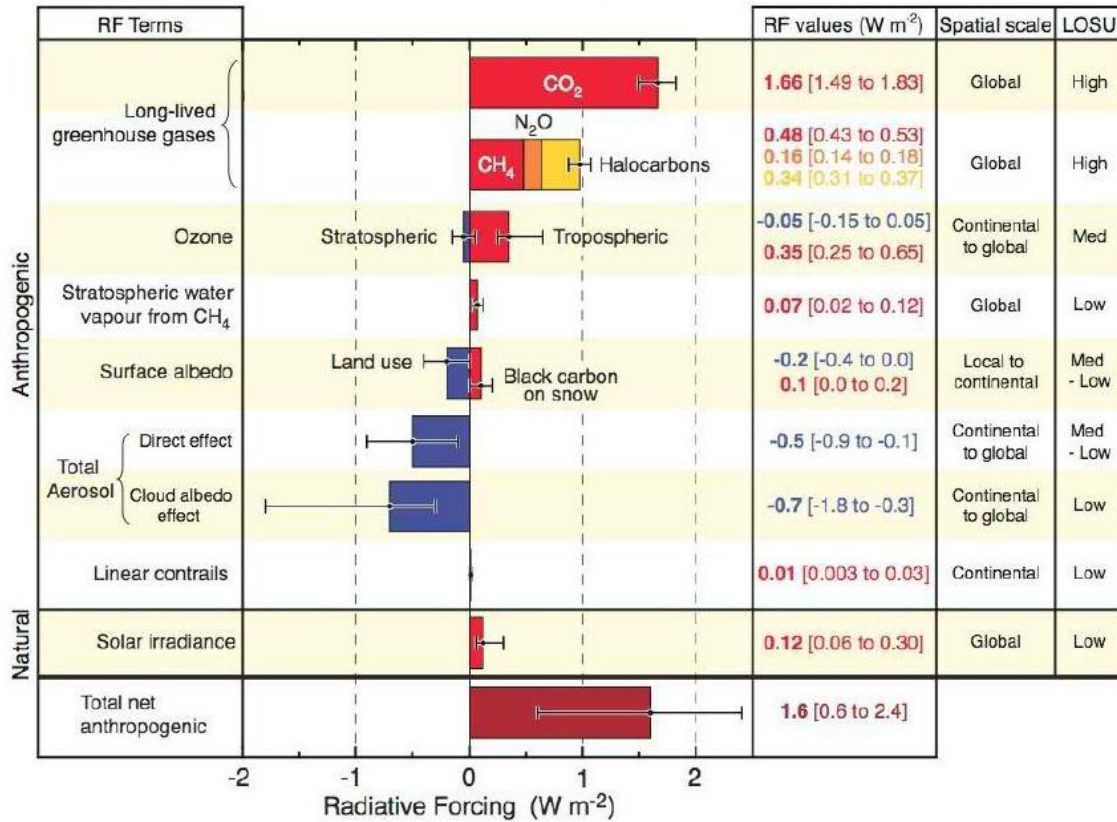
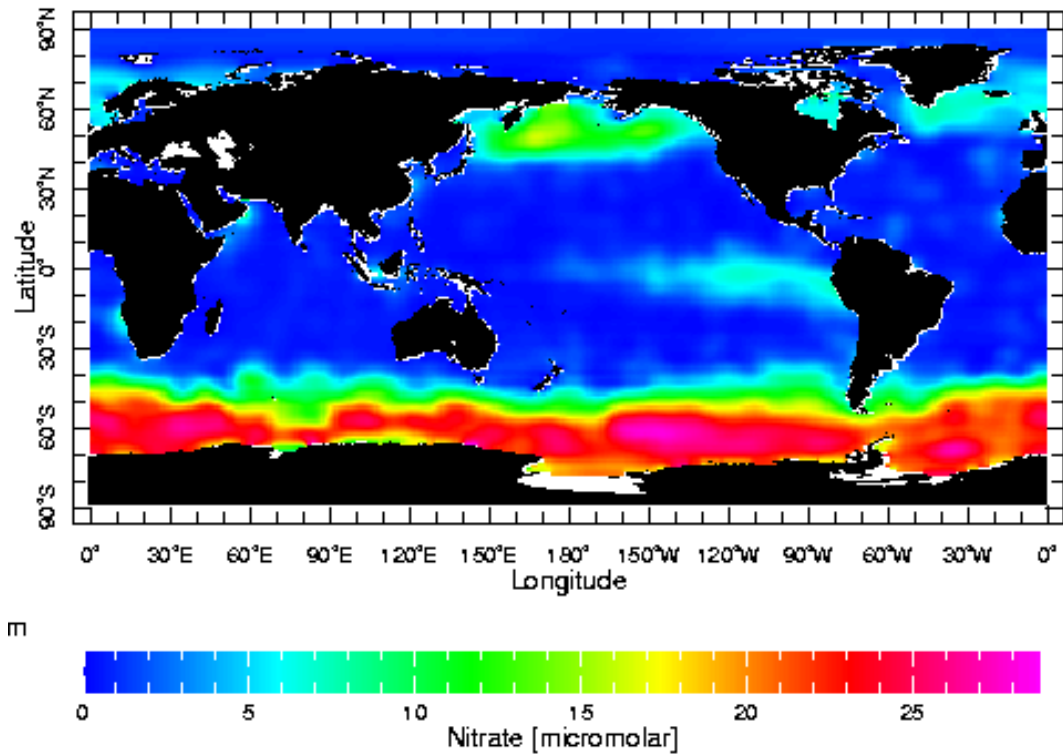
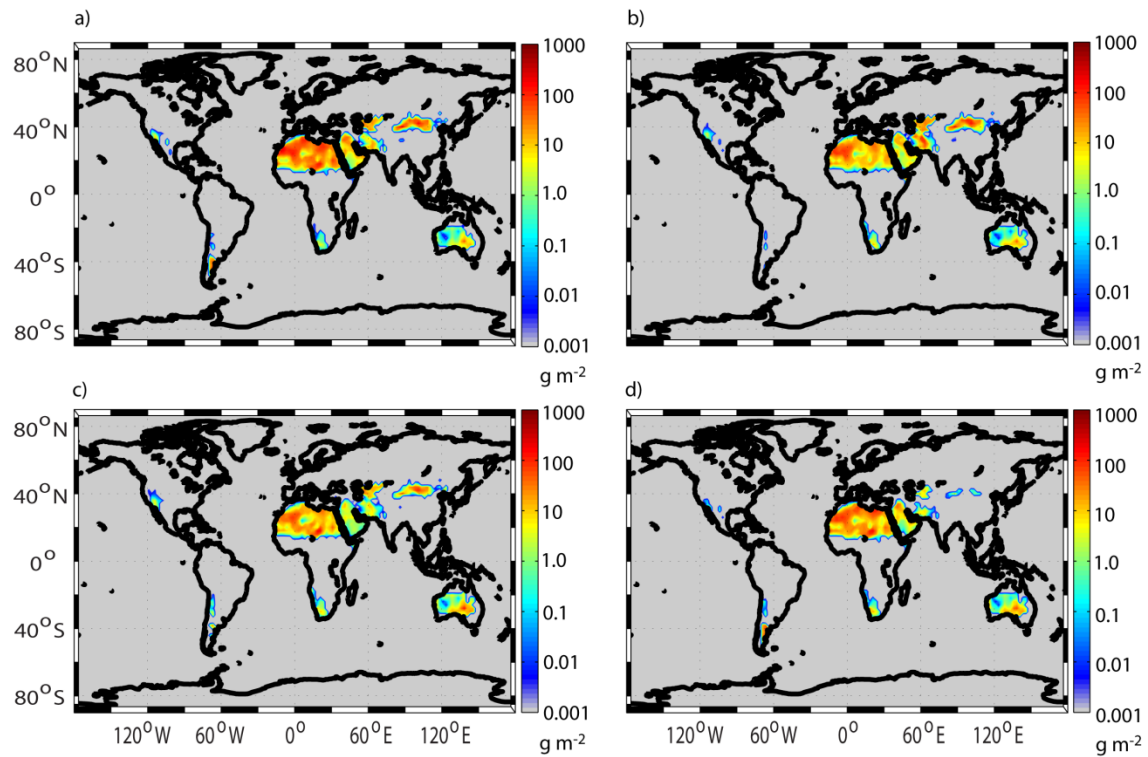


Figure 2.1. Natural and anthropogenic radiative forcing components and their estimated impact, as determined by the IPCC in 2007.



**Figure 2.2.** This figure shows oceanic  $[\text{NO}_3^-]$  in the global oceans. HNLC oceanic regions are assumed to be the surface waters with elevated  $[\text{NO}_3^-]$  (bright colors). The HNLC regions of the subarctic North Pacific, equatorial Pacific, and the Southern Ocean comprising ~30% of the global oceans (data from the World Ocean Atlas 1994).



**Figure 2.3.** Model-predicted total dust emissions ( $\text{g m}^{-2}$ ) during a) March-April, b) June-August, c) September-November, and d) December-February during the simulation time period of March 2009 to February 2010.

### **3. A Global Comparison of GEOS-Chem-predicted and Remotely-sensed Mineral Dust Aerosol Optical Depth and Extinction Profiles**

#### Preface

The state-of-the-art 3-D CTM GEOS-Chem is widely-used in radiative budget calculations and for the evaluation of atmospheric chemical composition, aerosol transport, and AOD [e.g., *Bey et al.*, 2001; *Heald et al.*, 2006; *van Donkelaar et al.*, 2006]. A major objective of my dissertation research was to simulate bioavailable nutrient supplies, associated with mineral dust, to the remote global surface oceans. Therefore, it is important to evaluate the ability of GEOS-Chem to replicate mineral dust emissions, transport, and deposition to remote oceanic surface waters. In previous studies large discrepancies between GEOS-Chem-predicted mineral dust concentrations/AODs in comparison to measurement and remotely-sensed data have been reported [*Generoso et al.*, 2008; *Fairlie et al.*, 2010]. For example, based on the differences between model-predicted dust concentrations/AOD values and in situ measurement/remotely-sensed data, it was suggested that when GEOS-Chem is run with GEOS-4 meteorology, global emission rates of mineral dust should be reduced [*Generoso et al.*, 2008; *Fairlie et al.*, 2010]. These over-predictions in mineral dust concentrations and AOD values were suggested to be due to the higher surface winds in GEOS-4 datasets compared to reanalysis data. Surface winds in the newest GEOS-5 meteorological data have been shown to compare more closely to reanalysis data, therefore, it is important to evaluate simulated mineral dust processes within GEOS-Chem when driven

by these newest set of meteorological data. In this work, for the first time, we apply a synergistic approach in order to evaluate global horizontal and vertical distributions of mineral dust predicted by GEOS-Chem (driven by GEOS-5 meteorology) using remotely-sensed AOD values collected by MODIS and MISR and vertical profiles of dust aerosol extinction retrieved by CALIPSO.

This chapter of my dissertation has been published in the Journal of Advances in Modeling Earth Systems (JAMES).

**A global comparison of GEOS-Chem-predicted and remotely-sensed  
mineral dust aerosol optical depth and extinction profiles**

**Matthew S. Johnson, Nicholas Meskhidze, Velayudhan Praju Kiliyanpilakkil**

Marine Earth and Atmospheric Science, North Carolina State University, Raleigh, NC, USA

*Correspondence to:* Nicholas Meskhidze  
(nmeskhidze@ncsu.edu)

## **Abstract**

Dust AOD and vertical distribution of aerosol extinction predicted by a global chemical transport model (GEOS-Chem) are compared to space-borne data from MODIS, MISR, and CALIPSO for March 2009 to February 2010. Model-predicted and remotely-sensed AOD/aerosol extinction profiles are compared over six regions where aerosol abundances are dominated by mineral dust. Calculations indicate that over the regions examined in this study (with the exception of Middle Eastern dust sources) GEOS-Chem predicts higher AOD values compared to MODIS and MISR. The positive bias is particularly pronounced over the Saharan dust source regions, where model-predicted AOD values are a factor of 2 to 3 higher. The comparison with CALIPSO-derived dust aerosol extinction profiles revealed that the model overestimations of dust abundances over the study regions primarily occur below ~4 km, suggesting excessive emissions of mineral dust and/or uncertainties in dust optical properties. The implementation of a new dust size distribution scheme into GEOS-Chem reduced the yearly-mean positive bias in model-predicted AOD values over the study regions. The results were most noticeable over the Saharan dust source regions where the differences between model-predicted and MODIS/MISR retrieved AOD values were reduced from 0.22 and 0.17 to 0.02 and -0.04, respectively. Our results suggest that positive/negative biases between satellite and model-predicted aerosol extinction values at different altitudes can sometimes even out, giving a false impression for the agreement between remotely-sensed and model-predicted column-integrated AOD data.

### 3.1. Introduction

Mineral dust particles are one of the most abundant aerosols in the Earth's atmosphere. With global emission rates  $\sim 2150 \text{ Tg yr}^{-1}$  (1 Tg =  $10^{12}$  g) mineral dust makes up  $\sim 40\%$  of the global annual mass of aerosols emitted from the Earth [Forster *et al.*, 2007]. These natural aerosols can directly impact radiative forcing by altering incoming solar radiation in the atmosphere through scattering and absorption [Tegen *et al.*, 1997; Haywood and Boucher, 2000] and indirectly by changing cloud microphysics and optical properties by acting as CCN and/or IN [Wurzler *et al.*, 2000; Sassen *et al.*, 2003; DeMott *et al.*, 2003; Solomos *et al.*, 2011]. Presently, there remains considerable uncertainty in both the sign and magnitude of the net direct radiative forcing by mineral dust, ranging from  $-0.56$  to  $+0.4 \text{ W m}^{-2}$  [Forster *et al.*, 2007]. General circulation models also provide a wide variety of estimates for the indirect radiative forcing by dust particles acting as IN with an estimated range from  $-1.0$  to  $-2.1 \text{ W m}^{-2}$  [Lohmann and Diehl, 2006]. Additionally, mineral dust can influence marine biogeochemical processes as the atmospheric deposition of aeolian dust is recognized as an important natural pathway for nutrient (i.e., Fe and P) deposition to the surface waters of the oceans [Martin and Fitzwater, 1988; Jickells *et al.*, 2005; Meskhidze *et al.*, 2005]. Mesoscale Fe enrichment experiments have shown that the supply of bioavailable iron to Fe-depleted surface waters (also known as HNLC regions) exerts control on the dynamics of plankton growth, which in turn affects the biogeochemical cycles of carbon, nitrogen, silicon, sulfur, and can ultimately influence the Earth's climate [e.g., Boyd *et al.*, 2007]. Large uncertainties in the radiative forcing of mineral dust aerosols can strongly

affect the model-predicted extent of human induced climate change and our ability to predict future climate. Therefore, the improved quantification of mineral dust emission rates, particle-size distributions, mixing state, chemical transformations in the atmosphere, and its CCN and IN properties are some of the main motivations of present-day research.

Global atmospheric distributions of mineral dust used in radiative budget calculations and height-dependant remote sensing algorithms (i.e., UV remote sensing) are often determined using CTMs such as GEOS-Chem [Torres *et al.*, 1998, 2007; Hu *et al.*, 2009]. This state-of-the-art model is widely-used for the evaluation of atmospheric chemical composition, aerosol transport, AOD, and nutrient deposition to the oceans [e.g., Bey *et al.*, 2001; Heald *et al.*, 2006; van Donkelaar *et al.*, 2006; Solomon *et al.*, 2009; Johnson *et al.*, 2010, 2011]. GEOS-Chem can also be used in combination with GCMs to study past and future climate [e.g., Wu *et al.*, 2007, 2008]. However, recent studies have reported large discrepancies between GEOS-Chem-predicted mineral dust concentrations/AODs in comparison to measurement and remotely-sensed data [Generoso *et al.*, 2008; Fairlie *et al.*, 2010]. For example, based on the differences between model results and measurements of Asian dust concentrations, it was suggested that when GEOS-Chem is run with GEOS-4 meteorology global emission rates of mineral dust should be reduced by a factor of two [Fairlie *et al.*, 2010]. A factor of three reduction in dust emission rates was recommended for the Saharan dust sources based on the comparison of model-predicted AOD and remotely-sensed data [Generoso *et al.*, 2008]. Such large uncertainties for different dust producing regions are believed to be caused by the fact that the GEOS-Chem dust

mobilization scheme was developed and implemented for GEOS-3 meteorological fields. GEOS-Chem-predicted dust emissions are being driven by the “saltation” process, which is dependent to the third power of 10 m wind speed [*Zender et al.*, 2003]. Therefore, small variations in surface wind speeds can lead to significant discrepancies in dust emission fluxes and total column concentrations. Higher surface winds in GEOS-4 datasets (with a global positive wind bias of  $0.2 \text{ m s}^{-1}$  between GEOS-4 and the National Centers for Environmental Prediction (NCEP) reanalysis [*Jaeglé et al.*, 2011]) were suggested to cause the over-prediction of mineral dust emissions and total column concentrations in comparison to observational data [*Generoso et al.*, 2008; *Fairlie et al.*, 2010].

Now that GEOS-Chem is run with GEOS-5 meteorological fields it is particularly important to evaluate GEOS-Chem-predicted mineral dust AOD/extinction values on a global scale for these new sets of meteorological data. A recent study by *Jaeglé et al.* [2011] showed good agreement between GEOS-5 and NCEP surface wind speed values, with a globally averaged annual bias of  $+0.03 \text{ m s}^{-1}$  (GEOS-5 minus NCEP). In addition to improved representation of surface wind speeds, GEOS-5 is also a better choice for simulating aerosol vertical profiles. Due to the greater vertical resolution between the surface and 2 km (5 model layers in GEOS-4 compared to 14 in GEOS-5) and accurate representation of planetary boundary layer (PBL) mixing under all possible meteorological conditions [*Lin and McElroy*, 2010], GEOS-5 meteorological fields are expected to yield a more realistic representation of the vertical structure of mineral dust in GEOS-Chem.

Past studies evaluating the spatial and temporal abundances and variations of mineral dust aerosols in GEOS-Chem, have recommended scaling model emission fluxes by comparing model results with remotely-sensed data over and downwind from the source regions using a column-integrated AOD. However, in addition to mass loading, refractive indexes, and hygroscopic properties of aerosols, model-predicted AOD values also depend on transport and removal processes which can be influenced by the dust advection altitude [Tegen *et al.*, 1996; Chin *et al.*, 2002], as well as particle size distribution [Tegen and Lacis, 1996; Kok, 2011]. As aerosols above the boundary layer are less affected by wet deposition processes, particle lifetimes tend to increase with altitude [e.g., Tegen *et al.*, 1996]. Due to the increase in wind speed and wind shear with height, aerosols that are transported in the free troposphere also tend to be carried longer distances than dust that remains in the boundary layer [Prospero *et al.*, 1981; Li *et al.*, 2008]. In addition to atmospheric transport and depositional processes, mineral dust size distribution can also affect particle single scattering albedo, extinction coefficient, and total mass of emitted aerosols, influencing aerosol optical properties [e.g., Sokolik and Toon, 1996; Tegen and Lacis, 1996; Shell and Somerville, 2007; Kok, 2011]. Therefore, good/poor agreement between model-predicted and measured/remotely-sensed AOD values cannot always be used as a base for proposed changes to the emissions scheme/rates, especially, when model-predicted and measured AOD values are compared downwind from the source regions.

In this work, for the first time, we evaluate global horizontal and vertical distributions of mineral dust predicted by GEOS-Chem (driven by GEOS-5 meteorology) using remotely-

sensed AOD values collected by MODIS and MISR and vertical profiles of dust aerosol extinction retrieved by CALIPSO. Such a synergistic approach to the evaluation of model-predicted mineral dust AOD/extinction calculations helps to better constrain total column burdens of mineral dust as well as aerosol vertical distribution.

## **3.2. Methods**

### **3.2.1 GEOS-Chem simulations**

The global chemical transport model GEOS-Chem (v8-01-01) was applied to quantify the atmospheric transport of mineral dust and associated AOD/extinction values. Assimilated meteorological fields from the GEOS of the NASA GMAO are used to drive GEOS-Chem [Bey *et al.*, 2001; Park *et al.*, 2004]. The model uses GEOS-5 meteorological fields at a  $2^\circ \times 2.5^\circ$  (latitude-longitude) grid resolution and 47 vertical levels. To simulate dust mobilization, GEOS-Chem combines the DEAD scheme [Zender *et al.*, 2003] with the source function used in the GOCART model [Ginoux *et al.*, 2001; Chin *et al.*, 2004]. Principal source regions are deserts or dry lakes and streambeds where alluvial deposits have accumulated. Mineral dust mobilization occurs when turbulent drag forces of the atmosphere overcome gravitational inertia and inter-particle cohesion. Once mineral dust is mobilized from the surface, the model uses four standard dust bins with diameter boundaries of 0.2 - 2.0, 2.0 - 3.6, 3.6 - 6.0 and 6.0 - 12.0  $\mu\text{m}$  to simulate global dust transport and deposition [Fairlie *et al.*, 2007]. Dust removal from the atmosphere occurs through dry deposition processes such as gravitational settling [Seinfeld and Pandis, 1998] and turbulent dry transfer

of particles to the surface [Zhang *et al.*, 2001]. Dust removal by wet deposition processes includes both convective up draft scavenging and rainout/washout from large-scale precipitation [Liu *et al.*, 2001]. An in-house version of GEOS-Chem, with a prognostic dust-Fe dissolution scheme, is also available and has been applied to simulate bioavailable Fe formation within mineral dust during atmospheric transport and deposition to the oceans [Solmon *et al.*, 2009; Johnson *et al.*, 2010, 2011].

Simulated 3-D profiles of aerosols influencing the magnitude and spatial distribution of AOD include mineral dust, sulfate, sea salt, and organic and black carbon. AODs at 550 nm are derived online from simulated aerosol mass concentrations and assumed lognormal size distributions of externally mixed aerosols of different types [Martin *et al.*, 2003]. Aerosol type dependent hygroscopic growth factors and refractive indices in GEOS-Chem are taken from the Global Aerosol Data Set (GADS) [Koepke *et al.*, 1997], with updated aerosol size and optical properties from Drury *et al.* [2010]. Hygroscopic growth is calculated using GEOS-5 relative humidity fields. A standard Mie code is used to calculate optical properties for each aerosol type. Total AOD values for each vertical model layer are generated assuming an external mixture of aerosols and summed over all aerosol types [Drury *et al.*, 2008]. In the baseline GEOS-Chem model, mineral dust AOD values are calculated using seven separate dust bins with each size range having size specific optical properties. The dust mass in the smallest/sub-micron size transport bin (diameter 0.2 - 2.0  $\mu\text{m}$ ) is separated into four additional bins with effective radii of 0.15, 0.25, 0.4, and 0.8  $\mu\text{m}$ .

The predicted dust mass is then evenly distributed into these four sub-micron size bins and used for dust AOD calculations.

Recently, *Kok* [2011] suggested that the emission of mineral dust is a scale-invariant process and offered a simple theoretical expression for the power law size distribution of emitted dust aerosols. It was suggested, that when implemented in regional and global climate models, the proposed parameterization may resolve the substantial overestimation of the emitted clay size fraction of dust commonly occurring in these models [*Kok*, 2011]. Since GEOS-Chem-predicted mineral dust AOD/concentrations have previously been found to be higher compared to remotely-sensed/measurement data [*Generoso et al.*, 2008; *Fairlie et al.*, 2010], we have carried out AOD and extinction profile calculations in GEOS-Chem by reallocating model-predicted mineral dust emissions in all dust bins using the *Kok* [2011] dust aerosol size distribution parameterization. The new size distribution predicted by the *Kok* [2011] scheme is then used during transport, deposition, and AOD calculations. In section 3.4 and 3.5 we present sensitivity calculations to assess how results from this new dust size distribution scheme compare to AOD/aerosol extinction values retrieved by satellites. All model simulations were conducted from March 2009 to February 2010.

### **3.2.2 Satellite retrievals of aerosol optical depth**

GEOS-Chem-predicted AOD values were compared to remotely-sensed data derived by *Terra* MISR (at 555 nm wavelength) and *Aqua* MODIS (at 550 nm wavelength) satellites. *Aqua* MODIS Deep-Blue (MODIS-DB) (550 nm) data were combined with *Aqua* MODIS

data in order to retrieve AOD values over bright surfaces (i.e., desert regions) [Hsu *et al.*, 2004, 2006]. Both MISR [Martonchik *et al.*, 2004; Kahn *et al.*, 2005] and MODIS [Remer *et al.*, 2005; Hsu *et al.*, 2006; Levy *et al.*, 2007a, 2007b] remotely-sensed data have been extensively evaluated and described in past literature [e.g., Martonchik *et al.*, 1998, 2002; Kaufman *et al.*, 1997; Tanré *et al.*, 1997]. In this study we use global daily gridded quality assured (QA) AOD data from MODIS and MODIS-DB Collection 5 Level-3 at  $1^\circ \times 1^\circ$  resolution and MISR Collection 4 Level-3 at  $0.5^\circ \times 0.5^\circ$  resolution.

While passive sensors retrieve column-integrated optical extinction for all aerosols (i.e., AOD), active sensors such as the Cloud-Aerosol Lidar with Orthogonal Polarization (CALIOP) onboard the CALIPSO satellite can explicitly separate desert dust aerosols and associated optical extinction from that produced by other aerosol subtypes remotely-sensed by CALIPSO (i.e., smoke, polluted continental, polluted dust, clean continental, and clean marine). CALIPSO can further retrieve vertically resolved aerosol type and extinction profiles and therefore, can be used to evaluate GEOS-Chem-predicted vertical distributions of mineral dust. To determine the aerosol subtypes the CALIPSO algorithm uses volume depolarization ratio, integrated attenuated backscatter, the earth surface types (land/ocean), and altitude information [Omar *et al.*, 2009; Young and Vaughan, 2009]. Using a cloud-aerosol discrimination (CAD) algorithm, CALIOP identified features are classified into aerosol and cloud by providing a CAD score for each vertical layer [Liu *et al.*, 2009]. The standard CAD scores for the level of confidence in the aerosol-cloud classification range from -100 to 0 for aerosols and +100 to 0 for clouds. A larger absolute value of the CAD

score indicates higher confidence of the feature classification. To extract relatively high confidence cloud free data, in this study desert dust aerosols and the corresponding extinction values are extracted using CAD scores of -70 to -100 [Liu *et al.*, 2009; Vaughan *et al.*, 2004; Kiliyanpilakkil and Meskhidze, 2011] for the condition when initial lidar ratio (selected based on type and subtype of the layer) is equal to the final lidar ratio (derived by applying transmittance correction to the extinction processing) ([http://eosweb.larc.nasa.gov/PRODOCS/calipso/Quality\\_Summaries/](http://eosweb.larc.nasa.gov/PRODOCS/calipso/Quality_Summaries/)). Polluted dust aerosols were not included in mineral dust aerosol extinction calculations due to potential contamination by smoke and sea salt (A. H. Omar, personal communications, 2011). In this study we use CALIPSO Level 2 (v3.01) profile data at a 5 km resolution.

Uncertainties in CALIPSO retrievals of specific aerosol subtypes and extinction values have been previously recognized [Winker *et al.*, 2009, Yu *et al.*, 2010]. For example, the algorithm that separates specific aerosol types assumes a constant lidar ratio. In reality, lidar ratios within a given aerosol subtype can vary over 30% [Winker *et al.*, 2009; Yu *et al.*, 2010]. Such uncertainty can cause for the misclassification of aerosol subtypes and errors in aerosol extinction retrievals, particularly for strongly attenuating layers, where retrieval errors tend to accumulate toward the base of the layer [Yu *et al.*, 2010]. Additional details regarding the uncertainties in CALIPSO lidar measurements of aerosol vertical distributions can be found in Winker *et al.* [2009] and Yu *et al.* [2010].

### 3.2.3 Comparison between GEOS-Chem and satellite data

Remotely-sensed AOD data from MODIS and MISR were re-gridded to a  $2^\circ \times 2.5^\circ$  grid resolution for direct comparison to the model-predicted AODs. Vertical profiles of model-predicted mineral dust aerosol extinction values were estimated by dividing daily-averaged dust AOD output by the layer height of each one of the 47 vertical levels of GEOS-Chem. To minimize the uncertainty of satellite AOD retrievals in the vicinity of clouds where hydrated aerosols occur frequently [Zhang *et al.*, 2005; Wen *et al.*, 2006, 2007; Koren *et al.*, 2007], satellite retrievals for monthly mean AOD are weighted by the number of cloud-free pixels within a grid square. To be consistent with the satellite data, model-predicted monthly mean AOD data was weighted by the modeled grid column averaged cloud fraction ( $CF$ ) as:  $AOD = \frac{1}{1-CF} \sum_{i=1}^n (1 - CF_i) AOD_i$ , where  $i$  represents individual days. The basic statistical parameters used during this study include the correlation coefficient ( $R$ ), total bias, root mean square error (RMSE), and normalized mean bias (NMB). In order to evaluate GEOS-Chem-predicted intermittent temporal (monthly/seasonal) patterns of mineral dust emission and transport from different regions, time-series analyses have been applied to monthly satellite and modeled AOD data. To minimize potential error in satellite-model inter-comparison associated with aerosols other than mineral dust, statistical analyses between GEOS-Chem-predicted and MODIS/MISR retrieved AODs were carried out over the regions where aerosol abundances are dominated by mineral dust. These areas (shown on Fig. 3.1 and hereinafter referred to as “dusty” regions) are the regions where model-predicted mineral dust aerosols contributed  $> 75\%$  of total annually-averaged AOD values. Such a

percentage was chosen to considerably lessen model-predicted biases in AOD calculations caused by uncertainties in simulated aerosol species other than mineral dust.

Nighttime CALIPSO dust aerosol extinction retrievals are compared directly to model-predicted dust aerosol extinction outputs when CALIPSO data are available within a GEOS-Chem grid cell. CALIPSO nighttime data are used during this study because it has been shown to have higher accuracy than that collected during the daytime [Omar *et al.*, 2009]. CALIPSO data are re-gridded vertically to match the 47 vertical levels used by GEOS-Chem. Due to CALIPSO's narrow swath, near-nadir view (~70 m), and a 16-day repeating cycle, the lidar data was seasonally- and annually-averaged to acquire a global view of aerosol distribution [Yu *et al.*, 2010]. To evaluate model-predicted dust transport heights, seasonally- and annually-averaged GEOS-Chem-simulated vertical profiles of dust aerosol extinction over each “dusty” region are compared to CALIPSO-retrieved data. CALIPSO dust aerosol extinction profiles were calculated by averaging remotely-sensed dust aerosol extinction coefficients within each vertical layer of the model.

### **3.3. Results**

#### **3.3.1 Global distribution of AOD values**

GEOS-Chem-predicted global dust emission source regions (see Supplementary Fig. S3.1) are consistent with previous studies [e.g., Tegen *et al.*, 2002; Prospero *et al.*, 2002]. The total global annual dust emission predicted during the yearlong simulation of the current study was ~1630 Tg. This magnitude of emitted dust is within the range of dust emission

fluxes predicted by global dust models considered in the recent study by *Huneeus et al.* [2011]. Figure 3.2 shows there are large seasonal variations in the magnitude and transport pathways of mineral dust during the simulated time period. According to this figure dust column burdens over the Sahara Desert are large year-round, with the highest concentrations associated with the deserts of north-western Sahara and the Bodélé Depression. This figure also shows that Asian dust column concentrations are particularly large during the spring season (MAM) and represent the second largest source of mineral dust globally. Dust burdens over Asia are mainly associated with the source regions of the Taklimakan and Gobi Deserts. Figure 3.2 shows that there is year-round dust activity over the majority of the Middle East. Total column dust concentrations over the Middle Eastern dust sources are at a maximum during the spring and summer (JJA) and a minimum during fall (SON). In the Southern Hemisphere, the largest mineral dust column concentrations are simulated over the dust source regions of Australia and South America (see Fig. 3.2). According to model simulations, the largest activity for Australian dust (with the source region near Lake Eyre) occurs during austral spring and summer, while South American dust sources (the Patagonia and Atacama Desert) are most active during austral summer and fall.

Table 3.1 shows the size-resolved global emission and deposition fluxes of mineral dust predicted by the baseline GEOS-Chem model when driven by the GEOS-5 meteorological fields. According to Table 3.1, the major fraction of the model-predicted global dust mass is removed from the atmosphere through dry deposition processes. However, Table 3.1 also shows that dust particles between 0.2 to 3.6  $\mu\text{m}$  in diameter, prone

to long-range transport, are mainly removed by wet deposition processes. Overall, the GEOS-Chem-predicted global annual dust source and sink budget shown in Table 3.1 is comparable to past modeling studies summarized in the AeroCom phase I project [Huneus *et al.*, 2011].

In general, MODIS, MISR, and GEOS-Chem give similar spatial patterns and seasonal variations of AOD values over the major global dust source regions and transport pathways (see Supplementary Fig. S3.2). However, Fig. 3.3 shows that the model tends to predict higher AOD values compared to the remotely-sensed data over these “dusty” regions. This is particularly true over the northern Sahara Desert where, according to Fig. 3.3, GEOS-Chem-predicted AOD values are more than a factor of 2 higher compared to both MODIS and MISR retrievals. The difference is most pronounced during MAM, one of the largest dust activity seasons for the Saharan dust sources. Over the Saharan dust outflow region of the N. Atlantic Ocean, Fig. 3.3 shows a positive bias in model-predicted AOD values just off the coast of the continent and then a transition from warm to cool colors as the dust moves westward, suggesting that downwind from the Saharan dust source regions GEOS-Chem-predicted AOD values are lower compared to the remotely-sensed data. This result is consistent with the study of *Generoso et al.* [2008], who noticed that in the model too little dust reached the Caribbean region and suggested this transition from a positive to negative bias in model-predicted AOD values could be due to the under prediction of the westward transport of mineral dust over the N. Atlantic Ocean or the over prediction of depositional fluxes [*Generoso et al.*, 2008]. Figure 3.3 also shows some discrepancies between model-

predicted and remotely-sensed AODs over the Asian dust sources, where GEOS-Chem simulated AOD values are higher in all seasons except the winter months. The positive bias in the model is most noticeable during MAM when model-predicted emission rates are at a maximum. However, unlike the Saharan dust source region, where the model shows a systematic overestimation of AOD values over the entire northern Africa, larger values predicted by the model compared to the satellite data are centered just above the Asian dust source regions. Over the dust source region of the Middle East, GEOS-Chem simulates lower AOD values in comparison to MODIS and MISR data. As for the Australian and Patagonian dust source regions, the comparison between model-predicted and remotely-sensed AODs is highly variable both spatially and temporally.

From Fig. 3.3 it is also apparent that GEOS-Chem displays discrepancies in predicted AOD values compared to MODIS and MISR data in regions other than ones dominated by mineral dust. For example, Fig. 3.3 shows a persistent underestimation of AODs over marine regions as well as AOD values retrieved over the biomass burning regions of central Africa and the regions of intensive anthropogenic activities in eastern China.

### **3.3.2 Yearly-averaged vertical profiles of mineral dust extinction**

Figure 3.4 shows that over the “dusty” regions (with the exception of the Middle East), GEOS-Chem-predicted annually-averaged dust extinction profiles display a positive bias compared to CALIPSO retrievals. According to Fig. 3.4 the largest discrepancies between model-predicted and satellite-retrieved dust extinction profile values were observed

below 4 km height. This is particularly true over the Saharan source region, where GEOS-Chem-calculated dust aerosol extinction values are a factor of 2 to 3 higher compared to CALIPSO retrievals. Although, such discrepancies in the lower levels of the atmosphere found over the Saharan sources could be due to the strong attenuation of the CALIPSO signal by large dust plumes biasing satellite retrievals to low values [Yu *et al.*, 2010], such a mechanism is highly unlikely to explain the model-satellite differences over the other “dusty” regions. Moreover, it was shown on Fig. 3.3 that GEOS-Chem predicts higher AOD values over the Saharan dust sources compared to both MODIS and MISR satellites, therefore the model overestimation of dust extinction shown in Fig. 3.4a is likely due to excessive emissions of mineral dust as suggested by *Generoso et al.* [2008] or uncertainties in dust optical properties (i.e., aerosol size distribution) that will be examined in section 3.4. Compared to CALIPSO retrievals GEOS-Chem-predicted dust extinction profiles over the N. Atlantic Ocean were similar to the ones over the Saharan dust source region: up to a factor of ~2 higher below 4 km and slightly lower above that height (see Fig. 3.4b). Over the Asian dust source regions, Fig. 3.4c reveals that the model-predicted dust extinction profile values are higher compared to CALIPSO data, with the largest discrepancy found below 4 km. This figure also reveals a consistent model over estimation of dust extinction values up to 10 km compared to remotely-sensed data. Model-predicted high altitude (above 5 km) entrainment of Asian dust is consistent with previous modeling studies suggesting that dust particles from the Taklimakan Desert can be entrained to an elevation well above 5 km and transported over long distances in the free troposphere [Sun *et al.*, 2001; Yu *et al.*, 2010]. Possible reasons for

the model-satellite differences at higher altitudes over the Asian dust sources could be related to inaccuracies in both the model-predictions and the satellite-retrievals. The possible over prediction of vertical advection of dust in GEOS-Chem combined with elevated dust concentrations over the Asian source regions may cause enhanced dust extinction values at the higher model levels. On the other hand, it is also known that CALIPSO commonly misclassifies mineral dust in the upper troposphere as thin cirrus clouds reducing dust extinction values [Yu *et al.*, 2010]. Figure 3.4d shows that GEOS-Chem can generally reproduce the dust extinction profiles retrieved by CALIPSO in the lower 3 km over the Middle Eastern dust source region but slightly underestimates above this height. As for the Southern Hemisphere, the model predicts higher dust extinction values compared to CALIPSO data over the desert regions of both Australia (see Fig 3.4e) and Patagonia (see Fig. 3.4f) in the lower 3 km of the troposphere and displays a slight negative bias above this height.

### **3.3.3 Seasonally-averaged dust extinction profiles**

Figure 3.5 compares GEOS-Chem-predicted and CALIPSO-retrieved vertically resolved mineral dust extinction profiles for different seasons over each “dusty” region. Further details for the GEOS-Chem to CALIPSO comparison of daily mean dust extinction values for each model horizontal grid resolution and vertical level are given on Fig. S3.3. Fig. 3.5a shows that over the Saharan dust source region GEOS-Chem-predicted mineral dust aerosol extinctions are generally larger in the lower troposphere (< 3 km) by well over a factor of 2. However, the comparisons between model and satellite data are reasonably good

in the middle (between 3 and 6 km) and upper (> 6 km) troposphere. Model-predicted and remotely-sensed dust extinction profiles agree most closely during the summer months when both data sets suggest Saharan dust is advected to the highest altitudes during this time. Figure 3.5b shows that over the N. Atlantic Ocean, downwind from the Saharan dust source region, model-predicted dust extinctions tend to be larger in the lower troposphere compared to CALIPSO. The simulated larger dust aerosol extinction values in this region are evident during all four seasons, but are most pronounced during the spring when model-predicted dust aerosol extinction values are highest.

Figure 3.5c shows that over the Asian dust source regions the model predicts larger dust aerosol extinction values compared to CALIPSO data at the majority of vertical heights during all seasons. During both the winter and spring months the model tends to predict noticeably larger dust extinction values in the upper troposphere compared to remotely-sensed data. A slight negative bias in model-predicted mineral dust extinction values is also found near the surface during winter months when dust emission fluxes are at a minimum. Over the dust source region of the Middle East (see Fig. 3.5d), model-predicted dust aerosol extinctions tend to be lower compared to CALIPSO-retrieved data. The comparison of the two data sets reveals that during spring and winter months GEOS-Chem-calculated dust extinction values are most comparable to satellite data. However, the model demonstrates a negative bias in simulated dust aerosol extinction values at all other heights and seasons. In the Southern Hemisphere, over the Australian dust source region, the model shows a tendency to predict higher values in the lower troposphere and smaller values in the upper

troposphere (see Fig. 3.5e). Over the Patagonian dust source region (see Fig. 3.5f) GEOS-Chem produces larger values of dust aerosol extinction in the lower troposphere and smaller values in the middle and upper troposphere during all seasons when compared to CALIPSO data. Differences between model-predicted and remotely-sensed dust extinction values are most pronounced over the Patagonian dust source region during the active dust season (i.e., the austral summer).

### **3.3.4 Mineral dust size distribution**

In this section, sensitivity calculations are presented to illustrate how GEOS-Chem-predicted AOD values and aerosol extinction profiles change when mineral dust emissions, transport, deposition, and optical properties are calculated using the dust size distribution scheme of *Kok* [2011]. Seasonally-averaged percent differences between model-predicted AOD values (with the dust aerosol size distribution scheme of *Kok* [2011]), and MODIS/MISR satellite retrievals are shown in Fig. 3.6. The comparison of Figs. 3.6 and 3.3 shows that the implementation of the *Kok* [2011] scheme led to the reduction of dust AOD values and improved agreement between model-predicted and remotely-sensed data over most of the dust producing regions. The reduction in model-predicted dust AOD values is likely due to the reallocation of the dust mass from the sub-micron mode bins to the coarse mode bins (see Table 3.1). Since sub-micron size dust particles tend to have higher mass extinction efficiencies, such changes in aerosol mass-size distribution led to reduced AOD values. Table 3.1 also shows that the reallocation of mineral dust mass to the larger transport size bins lead to a decrease in atmospheric dust burden. The smaller magnitude of mineral

dust mass in the atmosphere causes some further reduction in dust AOD values. The decrease in AOD values due to the new dust size distribution scheme did, however, increase the negative bias between GEOS-Chem and remotely-sensed data over the dust source region of the Middle East.

Figure 3.4 shows that the implementation of the *Kok* [2011] dust size distribution scheme also improved the comparison between CALIPSO-derived and GEOS-Chem-predicted dust aerosol extinction profiles. However, this figure also shows that despite considerable improvements, some discrepancies remain between GEOS-Chem-predicted and CALIPSO-retrieved vertical profiles of aerosol extinction. Overall, the implementation of the *Kok* [2011] mineral dust size distribution scheme lead to a systematic reduction in model-predicted dust extinction values at all vertical levels without reducing the overall magnitude of emitted dust (see Fig. 3.4). Such reductions yield considerable improvement between GEOS-Chem and CALIPSO AOD/aerosol extinction data over all the “dusty” regions with the exception of the Middle East. Additional details for the comparison of dust extinction values predicted by GEOS-Chem, with the *Kok* [2011] scheme, to CALIPSO-retrieved data are given on Fig. S3.4. Each individual data point on these scatter plots correspond to a daily mean dust aerosol extinction at a given horizontal grid resolution and vertical level within each “dusty” region. To better quantify the differences in model-predicted and remotely-sensed AOD values for the baseline simulations and the ones conducted using the *Kok* [2011] mineral dust size distribution scheme, a statistical analysis of monthly-averaged column AOD values is carried out in section 3.5.

### 3.3.5 Statistical analysis of AOD values

Table 3.2 shows that when the baseline GEOS-Chem model is compared to MODIS and MISR retrievals, model-predicted regionally-averaged positive biases over the Sahara source region are 0.22 (+70%) and 0.17 (+43%), respectively. Downwind from the Sahara Desert, over the N. Atlantic Ocean, GEOS-Chem also predicts larger AOD values in comparison to MODIS and MISR data. Table 3.2 shows that monthly-averaged AOD values calculated by GEOS-Chem over the Sahara Desert are well correlated with remotely-sensed data with the linear correlation coefficient  $> 0.8$ , suggesting that the model can largely predict the temporal variation of mineral dust emissions from the source region. Model-predicted and remotely-sensed AOD values are also highly correlated over the N. Atlantic Ocean. The implementation of the *Kok* [2011] scheme greatly reduced the bias between model-predicted and remotely-sensed AOD values (0.02 and -0.04 for MODIS and MISR, respectively) over the Sahara Desert (see Table 3.2). The rest of the parameters, such as the RMSE and the NMB have also been improved. Sensitivity calculations show that downwind from the Saharan dust source region the *Kok* [2011] scheme improved the correlation between modeled and MODIS satellite data and reduced the absolute value in model bias, RMSE, and NMB in comparison to MODIS. The comparison of GEOS-Chem-predicted AOD values to MISR-retrievals yield slightly different results. The implementation of the *Kok* [2011] dust size distribution scheme improved model-satellite AOD correlation and RMSE values over the N. Atlantic Ocean, but increased model bias and NMB.

High correlations between baseline model-predicted and remotely-sensed monthly AOD values ( $R = \sim 0.75$  for MODIS and  $R = \sim 0.80$  for MISR) over the dust source regions of Asia (see Table 3.2) also indicate that the model can reproduce the temporal variability of mineral dust emission and transport from the Asian dust sources. However, Table 3.2 shows that GEOS-Chem displays a positive bias in simulated AOD values in comparison to remotely-sensed data, particularly when compared to MISR retrievals (NMB  $\sim 30\%$ ). The implementation of the *Kok* [2011] scheme improved all statistical parameters when comparing GEOS-Chem-predicted AOD values to MISR data. In comparison to MODIS AOD values, the implementation of the new dust size distribution scheme improved the correlation and RMSE, but slightly increased the absolute value of biases and NMB.

Table 3.2 shows that baseline model-predicted AOD values over the dust source region of the Middle East tend to display negative biases in comparison to remotely-sensed data. The possible reason for this negative bias could be the under-prediction of dust emissions from the Middle East, errors in simulated north African dust transport and deposition processes, and errors in anthropogenic emission inventories over this region. As expected the implementation of the *Kok* [2011] scheme reduced mineral dust AOD values even further, producing larger discrepancies between model-predicted and remotely-sensed AOD values. In the Southern Hemisphere, the baseline GEOS-Chem model simulates higher AOD values in comparison to MODIS and MISR data over both the Australian and Patagonian dust source regions. In these regions the implementation of the *Kok* [2011] dust size distribution scheme had a minimal influence on the model-satellite correlation and

resulted in better agreement and improvement in all other statistical parameters in comparison to remotely-sensed data.

### **3.4. Conclusion**

Mineral dust AOD/extinction values predicted by the global 3-D chemical transport model GEOS-Chem were evaluated against space-borne data from MODIS, MISR, and CALIPSO. In order to minimize the contribution from aerosols other than mineral dust, six major dust source regions and transport pathways were identified. Model runs were conducted from March 2009 to February 2010. Spatial and temporal variability of seasonally- and annually-averaged horizontal profiles of AODs predicted by GEOS-Chem were comparable to remotely-sensed data by MODIS and MISR satellites. However, noticeable discrepancies between model-predicted and remotely-sensed AODs were also detected over the majority of “dusty” regions where GEOS-Chem simulates higher AOD values in compared to remotely-sensed data. The discrepancies between model-predicted AOD values and satellite retrievals were particularly pronounced over the Saharan dust source region where GEOS-Chem results were more than a factor of 2 higher compared to MODIS and MISR. The comparison of model-predicted vertical profiles of mineral dust aerosol extinction with CALIPSO retrievals revealed that over all “dusty” regions (with the exception of the Middle East) the model generally predicted larger dust aerosol extinction values compared to CALIPSO data. Furthermore, our analysis showed that discrepancies between model-predicted and remotely-sensed aerosol extinction values depend on seasonality and location. Such analysis shows the great advantage of vertically resolved

aerosol extinction profiles for model evaluation and indicates that the understanding of physical processes influencing spatiotemporal distribution of dust is necessary for improved representation of mineral aerosols in GEOS-Chem. The comparison between model-predicted and remotely-sensed dust AOD/extinctions also indicated that when AOD values are compared, positive/negative biases between satellite and model-predicted aerosol extinction values at different altitudes can sometimes even out, giving a false impression for the agreement between remotely-sensed and model-predicted aerosol data.

Sensitivity calculations suggest that changing the dust mass size distribution according to the *Kok* [2011] scheme greatly reduced model-predicted positive biases in AOD values over the majority of dust source regions, particularly over the Sahara Desert. It is important to note that unlike previous studies that recommended a factor of 2 to 3 reduction of global mineral dust emissions, improvements in model-satellite AOD comparison were achieved with the implementation of the *Kok* [2011] dust mass size distribution scheme. The analysis of GEOS-Chem-predicted and CALIPSO-retrieved dust extinction profiles further showed that the *Kok* [2011] scheme improves the agreement for mineral dust extinctions over the majority of “dusty” regions.

Our analysis shows that the implementation of the *Kok* [2011] dust size distribution scheme yields improved agreement between GEOS-Chem-predicted and CALIPSO-retrieved dust extinction values; however, the degree of improvement differed between “dusty” regions and time periods, suggesting that although the size distribution seems to play a key role in mineral dust AOD/extinction calculations, other factors may also influence mineral dust

optical properties and light extinction. Several factors for the model-satellite discrepancies related to GEOS-Chem are: dust emission rates, deposition fluxes, wind fields, mixing states, surface properties, assumed optical properties (i.e., extinction coefficients), and cloud and precipitation fields. Possible reasons for the discrepancies linked to CALIPSO satellite include misclassification of mineral dust in the upper troposphere as thin cirrus clouds, attenuation of signal by highly concentrated dust plumes, and the 16-day repeating cycle making it possible to obtain a global view of aerosol by averaging cloud-free profiles collected over a period of time (e.g., a season). Some of the uncertainties associated with MODIS and MISR AOD retrievals are related to instrument calibration, cloud-masking of thin cirrus clouds, assumptions of surface reflectance, aerosol shape, and aerosol model selection. Although all these factors can potentially cause model biases in calculating dust AOD/extinction values when compared to the satellite data, our calculations suggest that better representation of mineral dust aerosol optical properties can be achieved in GEOS-Chem by improving the size distribution of emitted dust aerosols.

### **Acknowledgements**

This research was supported by the National Science Foundation through the grant ATM-0826117 and by National Aeronautics & Space Administration (NASA) through grant no NNX11AG72G. The authors would like to thank Dr. Yongxiang Hu and Dr. Ali *Omar* of the NASA Langley Research Center for their help with the processing and application of CALIPSO data. Thanks are also due to Dr. Daniel Jacob and the Harvard University

Atmospheric Chemistry Modeling Group for providing the baseline GEOS-Chem model used during our research.

## References

- Bey, I., D. J. Jacob, R. M. Yantosca, J. A. Logan, B. Field, A. M. Fiore, Q. Li, H. Liu, L. J. Mickley, and M. Schultz (2001), Global modeling of tropospheric chemistry with assimilated meteorology: Model description and evaluation, *J. Geophys. Res.*, *106*(D19), 23,073-23,095.
- Boyd, P. W., et al. (2007), Mesoscale Iron Enrichment Experiments 1993–2005: Synthesis and Future Directions, *Science*, *315*, 612-617.
- Chin, M., P. Ginoux, S. Kinne, O. Torres, B. Holben, B. Duncan, R. Martin, J. Logan, A. Higurashi, and T. Nakajima (2002), Tropospheric aerosol optical thickness from the GOCART model and comparisons with satellite and sunphotometer measurements, *J. Atmos. Sci.*, *59*, 461-483.
- Chin, M., A. Chu, R. Levy, L. Remer, Y. Kaufman, B. Holben, T. Eck, P. Ginoux, and O. Gao (2004), Aerosol distribution in the Northern Hemisphere during ACE-Asia: Results from global model, satellite observations, and Sunphotometer measurements, *J. Geophys. Res.*, *109*, D23S90, doi:10.1029/2004JD004829.
- DeMott, P. J., K. Sassen, M. R. Poellet, D. Baumgardner, D. C. Rogers, S. D. Brooks, A. J. Prenni, and S. M. Kreidenweis (2003), African dust aerosols as atmospheric ice nuclei, *Geophys. Res. Lett.*, *30*, 1732, doi:10.1029/2003GL017410.
- Drury, E., D. J. Jacob, J. Wang, R. J. D. Spurr, and K. Chance (2008), Improved algorithm for MODIS satellite retrievals of aerosol optical depths over land. *J. Geophys. Res.*, *113*, D16204.
- Drury, E., D. J. Jacob, R. J. D. Spurr, J. Wang, Y. Shinozuka, B. E. Anderson, A. D. Clarke, J. Dibb, C. McNaughton, and R. Weber (2010), Synthesis of satellite (MODIS), aircraft (ICARTT), and surface (IMPROVE, EPA-AQS, AERONET) aerosol observations over eastern North America to improve MODIS aerosol retrievals and constrain surface aerosol concentrations and sources, *J. Geophys. Res.*, *115*, D14204, doi:10.1029/2009JD012629.
- Fairlie, T. D., D. J. Jacobs, and R. J. Rokjin (2007), The impact of transpacific transport of mineral dust in the United States, *Atmos. Env.*, *41*, 1251-1266.
- Fairlie, T. D., D. J. Jacob, J. E. Dibb, B. Alexander, M. A. Avery, A. van Donkelaar, and L. Zhang (2010), Impact of mineral dust on nitrate, sulfate, and ozone in transpacific Asian pollution plumes, *Atmos. Chem. Phys.*, *10*, 3999-4012, doi:10.5194/acp-10-3999-2010.

- Forster, P., et al. (2007), Changes in atmospheric constituents and radiative forcing, in: *Climate Change 2007: The Physical Science Basis, contribution of Working Group I to the Fourth Assessment Report of the Intergovernmental Panel on Climate Change*, in the *Fourth Assessment Report of the Intergovernmental Panel on Climate Change*, edited by S. Solomon et al., chap. 2, pp. 131–234, Cambridge Univ. Press, Cambridge, U. K.
- Fung, I. Y., S. K. Meyu, I. Tegen, S. C. Doney, J. G. John, and J. K. B. Bishop (2000), Iron supply and demand in the upper ocean. *Global Biogeochem. Cycles*, *14*, 281–295.
- Generoso, S., I. Bey, M. Labonne, and F. M. Breon (2008) Aerosol vertical distribution in dust outflow over the atlantic: Comparisons between Geos-chem and cloud-aerosol lidar and infrared pathfinder satellite observation (calipso), *J. Geophys. Res.*, *113*, D24209, doi:10.1029/2008jd010154.
- Ginoux, P., M. Chin, I. Tegen, J. M. Prospero, B. Holben, O. Dubovik, and S.-J. Lin (2001), Sources and distributions of dust aerosols simulated with the GOCART model, *J. Geophys. Res.*, *106*, 20,255-20,273.
- Ginoux, P., J. M. Prospero, O. Torres, and M. Chin (2004), Long-term simulation of global dust distribution with the GOCART model: Correlation with North Atlantic Oscillation, *Environmental Modelling and Software*, *19*, 113-128.
- Haywood, J., and O. Boucher (2000), Estimates of the direct and indirect radiative forcing due to tropospheric aerosols, *Rev. Geophys.*, *38*, 513-543.
- Heald, C. L., D. J. Jacob, R. J. Park, B. Alexander, T. D. Fairlie, R. M. Yantosca, and D. A. Chu (2006), Transpacific transport of Asian anthropogenic aerosols and its impact on surface air quality in the United States, *J. Geophys. Res.*, *111*, D14310, doi:10.1029/2005JD006847.
- Hsu, N. C., S. C. Tsay, M. D. King, and J. R. Herman (2004), Aerosol properties over bright-reflecting source regions, *Ieee Trans. Geosci. Remote Sens.*, *42*, 557-569.
- Hsu, N. C., S. C. Tsay, M. D. King, and J. R. Herman (2006), Deep blue retrievals of Asian aerosol properties during ACE-Asia, *Ieee Trans. Geosci. Remote Sens.*, *44*, 3,180-3,195.
- Hu, R.-M., R. S. Sakhi, and B. E. A. Fisher (2009), New algorithms and their application for satellite remote sensing of surface PM<sub>2.5</sub> and aerosol absorption, *J. Aero. Sci.*, *40*, 394-402.
- Huneus, N., et al. (2011), Global dust model intercomparison in AeroCom phase I, *Atmos. Chem. Phys.*, *11*, 7781-7816, doi:10.5194/acpd-10-23781-2010.

- Jaeglé, L., P. K. Quinn, T. Bates, B. Alexander, and J. -T Lin (2011), Global distribution of sea salt aerosols: new constraints from in situ and remote sensing observations, *Atmos. Chem. Phys.*, *10*, 25,687-25,742.
- Jickells, T. D., et al. (2005), Global iron connections between desert dust, ocean biogeochemistry, and climate, *Science*, *308*, 67-71.
- Johnson, M. S., N. Meskhidze, F. Solmon, S. Gassó, P. Y. Chuang, D. M. Gaiero, R. M. Yantosca, S. Wu, Y. Wang, and C. Carouge (2010), Modeling dust and soluble iron deposition to the South Atlantic Ocean, *J. Geophys. Res.*, *115*, D15202, doi:10.1029/2009JD013311.
- Johnson, M. S., N. Meskhidze, V. P. Kiliyanpilakkil, and S. Gassó (2011), Understanding the transport of Patagonian dust and its influence on marine biological activity in the South Atlantic Ocean, *Atmos. Chem. Phys.*, *11*, 2487-2502, doi:10.5194/acp-11-2487-2011.
- Kiliyanpilakkil, V. P., and N. Meskhidze (2011), Deriving the effect of wind speed on clean marine aerosol optical properties using the A-Train satellites, *Atmos. Chem. Phys.*, *11*, 11401-11413, doi:10.5194/acp-11-11401-2011.
- Kaufman, Y. J., D. Tanré, L. A. Remer, E. Vermote, A. Chu, and B. N. Holben (1997) Operational remote sensing of tropospheric aerosol over land from EOS Moderate Resolution Imaging Spectroradiometer, *J. Geophys. Res.*, *102*, 17,051-17,067.
- Kahn, R. A., B. J. Gaitley, J. V. Martonchik, D. J. Diner, K. A. Crean, and B. Holben (2005), Multiangle Imaging Spectroradiometer (MISR) global aerosol optical depth validation based on 2 years of coincident Aerosol Robotic Network (AERONET) observations, *J. Geophys. Res.*, *110*, D10S04, doi:10.1029/2004JD004706.
- Koepke, P., M. Hess, I. Schult, and E. P. Shettle (1997), Global aerosol data set, report, Max-Planck Inst. fur Meteorol., Hamburg, Germany.
- Kok, J. F (2011), A scaling theory for the size distribution of emitted dust aerosols suggests climate models underestimate the size of the global dust cycle, *PNAS*, *108*(3), 1016-1021.
- Koren, I., L. A. Remer, Y. J. Kaufman, Y. Rudich, and J. V. Martins (2007), On the twilight zone between clouds and aerosols, *Geophys. Res. Lett.*, *34*, L08805, doi:10.1029/2007GL029253.
- Levy, R. C., L. A. Remer, and O. Dubovik (2007a), Global aerosol optical properties and application to MODIS aerosol retrieval over land, *J. Geophys. Res.*, *112*, D13210, doi:10.1029/2006JD007815.

- Levy, R. C., L. A. Remer, S. Mattoo, E. Vermote, and Y. J. Kaufman (2007b), Second-generation algorithm for retrieving aerosol properties over land from MODIS spectral reflectance, *J. Geophys. Res.*, *112*, D13211, doi:10.1029/2006JD007811.
- Li, F., P. Ginoux, and V. Ramaswamy (2008), Distribution, transport, and deposition of mineral dust in the Southern Ocean and Antarctica: Contribution of major sources, *J. Geophys. Res.*, *113*, D10207, doi:10.1029/2007JD009190.
- Lin, J. -T., and M. McElroy (2010), Impacts of boundary layer mixing on pollutant vertical profiles in the lower troposphere: Implications to satellite remote sensing, *Atmos. Environ.*, *44*(14), 1726-1739, doi:10.1016/j.atmosenv.2010.02.009.
- Liu, H., D. J. Jacob, I. Bey, and R. M. Yantosca (2001), Constraints from <sup>210</sup>Pb and <sup>7</sup>Be on wet deposition and transport in a global three-dimensional chemical tracer model driven by assimilated meteorological fields, *J. Geophys. Res.*, *106*(D11), 12,109-12,128.
- Liu, Z., M. Vaughan, D. Winker, C. Kittaka, B. Getzewich, R. Kuehn, A. Omar, K. Powell, C. Trepte, and C. Hostetler (2009), The CALIPSO Lidar Cloud and Aerosol Discrimination: Version 2 Algorithm and Initial Assessment of Performance, *J. Atmos. Ocean. Tech.*, *26*, 1198-1213, doi:10.1175/2009JTECHA1229.1.
- Lohmann, U., and K. Diehl (2006), Sensitivity studies of the importance of dust ice nuclei for the indirect aerosol effect on stratiform mixed-phase clouds, *J. Atmos. Sci.*, *63*, 968-982.
- Martin, J. H., and S. E. Fitzwater (1988), Iron-deficiency limits phytoplankton growth in the northeast pacific subarctic, *Nature*, *331*, 341-343.
- Martin, R. V., D. J. Jacob, R. M. Yantosca, M. Chin, and P. Ginoux (2003), Global and regional decreases in tropospheric oxidants from photochemical effects of aerosols, *J. Geophys. Res.*, *108*(D3), 4097, doi:10.1029/2002JD002622.
- Martonchik, J. V., D. J. Diner, R. Kahn, T. P. Ackerman, M. M. Verstraete, B. Pinty, and H. R. Gordon (1998), Techniques for the retrieval of aerosol properties over land and ocean using multi-angle imaging, *IEEE Trans. Geosci. Remote Sens.*, *36*, 1212-1227.
- Martonchik, J. V., D. J. Diner, K. A. Crean, and M. A. Bull (2002), Regional aerosol retrieval results from MISR, *IEEE Trans. Geosci. Remote Sens.*, *7*, 1520-1531.
- Martonchik, J. V., D. J. Diner, R. Kahn, B. Gaitley, and B. N. Holben (2004), Comparison of MISR and AERONET aerosol optical depths over desert sites, *Geophys. Res. Lett.*, *31*, L16102, doi:10.1029/2004GL019807.

- Meskhidze, N., W. L. Chameides, and A. Nenes (2005), Dust and pollution: A recipe for enhanced ocean fertilization?, *J. Geophys. Res.*, *110*, D03301, doi:10.1029/2004JD005082.
- Omar, A., et al. (2009), The CALIPSO Automated Aerosol Classification and Lidar Ratio Selection Algorithm, *J. Atmos. Ocean. Tech.*, *26*, 1994-2014, doi:10.1175/2009JTECHA1231.1.
- Park, R. J., D. J. Jacob, B. D. Field, R. M. Yantosca, and M. Chin (2004), Natural and transboundary pollution influences on sulfate nitrate-ammonium aerosols in the United States: Implications for policy, *J. Geophys. Res.*, *109*, D15204, doi:10.1029/2003JD004473.
- Prospero, J. M., R. A. Glaccum, and R. T. Nees (1981), Atmospheric transport of soil dust from Africa to South America, *Nature*, *289*, 570-572.
- Prospero, J. M., P. Ginoux, O. Torres, and S. E. Nicholson (2002), Environmental characterization of global sources of atmospheric soil dust identified with the Nimbus 7 Total Ozone Mapping Spectrometer (TOMS) absorbing aerosol product, *Rev. Geophys.*, *40*(3), 1002, doi:10.1029/2000RG000095.
- Remer, L. A., et al. (2005), The MODIS algorithm, products and validation, *J. Atmos. Sci.*, *62*, 947-973, doi:10.1175/JAS3385.1.
- Sassen, K., P. J. DeMott, J. M. Prospero, and M. R. Poellot (2003), Saharan dust storms and indirect aerosol effects on clouds: CRYSTAL-FACE results, *Geophys. Res. Lett.*, *30*, doi:10.1029/2003GL017371.
- Seinfeld, J. H., and S. N. Pandis (1998), *Atmospheric Chemistry and Physics: From Air Pollution to Climate Change*, Wiley, New York.
- Shell, K. M., and R. C. J. Someville (2007), Direct radiative effect of mineral dust and volcanic aerosols in a simple aerosol climate model, *J. Geophys. Res.*, *112*, D03205, doi:10.1029/2006JD007197.
- Sokolik, I. N., and O. B. Toon (1996), Direct radiative forcing by anthropogenic airborne mineral aerosols, *Nature*, *381*, 681-683.
- Solmon, F., P. Y. Chuang, N. Meskhidze, and Y. Chen (2009), Acidic processing of mineral dust iron by anthropogenic compounds over the north Pacific Ocean, *J. Geophys. Res.*, *114*, D02305, doi:10.1029/2008JD010417.

- Solomos, S., G. Kallos, J. Kushta, M. Astitha, C. Tremback, A. Nenes, and Z. Levin (2011), An integrated modeling study on the effects of mineral dust and sea salt particles on clouds and precipitation, *Atmos. Chem. Phys.*, *11*, 873-892, doi:10.5194/acp-11-873-2011.
- Sun, J., M. Zhang, and T. Liu (2001), Spatial and temporal characteristics of dust storms in China and its surrounding regions, 1960-1999: Relations to source area and climate, *J. Geophys. Res.*, *106*, 10,325-10,333, doi:10.1029/2000JD900665.
- Tanré, D., Y. J. Kaufman, M. Herman, and S. Mattoo (1997), Remote sensing of aerosol properties over oceans using the MODIS/EOS spectral radiances, *J. Geophys. Res.*, *102*(D14), 16,971-16,988.
- Tegen, I., and A. A. Lacis (1996), Modeling of particle size distribution and its influence on the radiative properties of mineral dust aerosol, *J. Geophys. Res.*, *101*, 19,237-19,244.
- Tegen, I., A. A. Lacis, and I. Fung (1996), The influence of mineral aerosol from disturbed soils on the global radiation budget, *Nature*, *380*, 419-422.
- Tegen, I., P. Hollrig, M. Chin, I. Fung, D. Jacob, and J. Penner (1997), Contribution of different aerosol species to the global aerosol extinction optical thickness: Estimates from model results, *J. Geophys. Res.*, *102*(D20), 23,895-23,915, doi:10.1029/97JD01864.
- Tegen, I., S. P. Harrison, K. Kohfeld, I. C. Prentice, M. Coe, and M. Heimann (2002), Impact of vegetation and preferential source areas on global dust aerosol: Results from a model study, *J. Geophys. Res.*, *107*(D21), 4576, doi:10.1029/2001JD000963.
- Torres, O., P. K. Bhartia, J. R. Herman, and Z. Ahmad (1998), Derivation of aerosol properties from satellite measurements of backscattered ultraviolet radiation: Theoretical basis, *J. Geophys. Res.*, *103*, 17,099-17,110.
- Torres, O., A. Tanskanen, B. Veihelmann, C. Ahn, R. Braak, P. K. Bhartia, P. Veefkind, and P. Levelt (2007), Aerosols and surface UV products from Ozone Monitoring Instrument observations: An overview, *J. Geophys. Res.*, *112*, D24S47, doi:10.1029/2007JD008809.
- van Donkelaar, A., R. V. Martin, and R. J. Park (2006), Estimating ground-level PM<sub>2.5</sub> using aerosol optical depth determined from satellite remote sensing, *J. Geophys. Res.*, *111*, D21201, doi:10.1029/2005JD006996.
- Vaughan, M., S. Young, D. Winker, K. Powell, A. Omar, Z. Liu, Y. Hu, and C. Hostetler (2004), Fully automated analysis of space-based lidar data: An overview of the CALIPSO retrieval algorithms and data products, *Proc. SPIE Int. Soc. Opt. Eng.*, *5575*, 16-30.

- Wen, G. Y., A. Marshak, and R. F. Cahalan (2006), Impact of 3-D clouds on clear-sky reflectance and aerosol retrieval in a biomass burning region of Brazil, *IEEE Trans. Geosci. Remote Sens. Lett.*, 3(1), 169-172.
- Wen, G. Y., A. Marshak, R. F. Cahalan, L. A. Remer, and R. G. Kleidman (2007), 3D Aerosol-cloud radiative interaction observed in collocated MODIS and ASTER images of cumulus cloud fields, *J. Geophys. Res.*, 112, D13204, doi:10.1029/2006JD008267.
- Winker, D. M., M. A. Vaughan, A. Omar, Y. Hu, K. A. Powell, Z. Liu, W. H. Hunt, and S. A. Young (2009), Overview of the CALIPSO mission and CALIOP data processing algorithms, *J. Atmos. Ocean. Technol.*, 26, 2310-2323, doi:10.1175/2009JTECHA1281.1.
- Wu, S., L. J. Mickley, D. J. Jacob, J. A. Logan, R. M. Yantosca, and D. Rind (2007), Why are there large differences between models in global budgets of tropospheric ozone?, *J. Geophys. Res.*, 112, D05302, doi:10.1029/2006JD007801.
- Wu, S., L. J. Mickley, E. M. Leibensperger, D. J. Jacob, D. Rind, and D. G. Streets (2008), Effects of 2000–2050 global change on ozone air quality in the United States, *J. Geophys. Res.*, 113, D06302, doi:10.1029/2007JD008917.
- Wurzler, S., T. G. Reisin, and Z. Levin (2000), Modification of mineral dust particles by cloud processing and subsequent effects on drop size distributions, *J. Geophys. Res.*, 105, 4501-4512.
- Young, S., and M. Vaughan (2009), The retrieval of profiles of particulate extinction from Cloud Aerosol Lidar Infrared Pathfinder Satellite Observation (CALIPSO) data: Algorithm description. *J. Atmos. Ocean. Technol.*, 26, 1105-1119.
- Yu, H., M. Chin, D. M. Winker, A. H. Omar, Z. Liu, C. Kittaka, and T. Diehl (2010), Global view of aerosol vertical distributions from CALIPSO lidar measurements and GOCART simulations: Regional and seasonal variations, *J. Geophys. Res.*, 115, doi:10.1029/2009JD013364.
- Zender, C. S., D. Newman, and O. Torres (2003), Spatial heterogeneity in aeolian erodibility: Uniform, topographic, geomorphic, and hydrologic hypotheses, *J. Geophys. Res.*, 108, doi: 10.1029/2002JD003039.
- Zhang, L., S. L- Gong, J. Padro, and L. Barrie (2001), A Size-segregated Particle Dry Deposition Scheme for an Atmospheric Aerosol Module, *Atmos. Environ.*, 35(3), 549-560.

Zhang, J., J. S. Reid, and B. N. Holben (2005), An analysis of potential cloud artifacts in MODIS over ocean aerosol optical thickness products, *Geophys. Res. Lett.*, 32, L15803, doi:10.1029/2005GL023254.

## Tables

Table 3.1 GEOS-Chem-predicted global annual dust sources and sinks

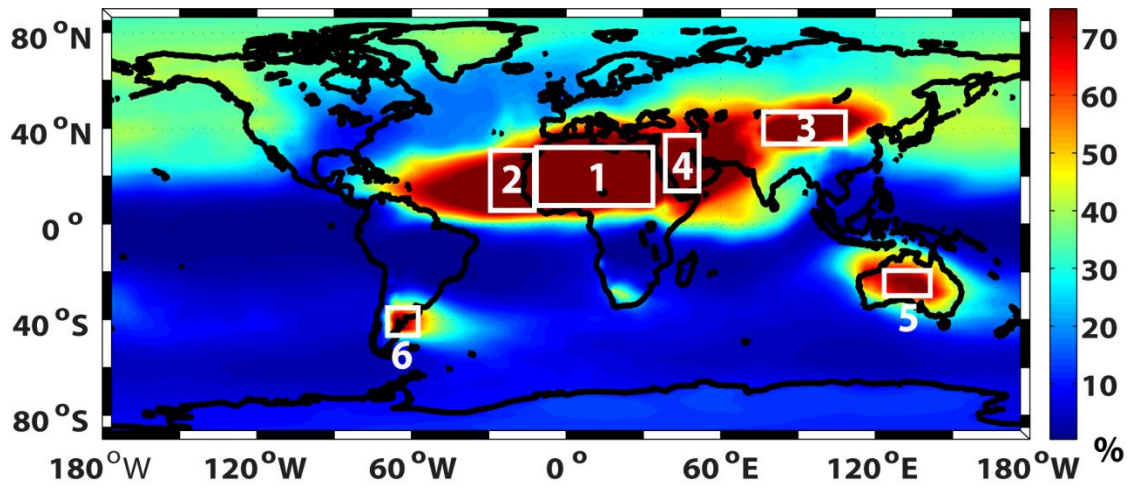
<b>Diameter range (<math>\mu\text{m}</math>)</b>	<b>Emission (Tg yr<sup>-1</sup>)</b>	<b>Dry deposition (Tg yr<sup>-1</sup>)</b>	<b>Wet deposition (Tg yr<sup>-1</sup>)</b>	<b>Burden (Tg)</b>
<b>Baseline model</b>				
0.2 - 2.0	197	57	138	4.1
2.0 - 3.6	422	146	272	7.8
3.6 - 6.0	528	337	189	7.1
6.0 - 12.0	489	447	42	1.6
Total	1636	987	641	20.6
<b>With <i>Kok</i> [2011] scheme</b>				
0.2 - 2.0	51	14	35	1.2
2.0 - 3.6	133	42	90	3.2
3.6 - 6.0	384	263	119	4.9
6.0 - 12.0	1068	994	73	7.2
Total	1636	1313	317	16.5

Table 3.2 Monthly-averaged GEOS-Chem-predicted AOD in comparison to MODIS and MISR data between March 2009 and February 2010

	MODIS				MISR			
<b>Baseline model</b>	R	Bias	RMSE	NMB*	R	Bias	RMSE	NMB*
Sahara Source	0.86	0.22	0.29	70.1	0.88	0.17	0.24	43.2
N. Atlantic Ocean	0.79	0.07	0.15	25.5	0.85	0.04	0.14	12.5
Asian Source	0.75	0.05	0.14	13.3	0.78	0.08	0.17	31.7
Middle East	0.85	-0.12	0.16	-27.3	0.79	-0.11	0.17	-24.2
Australia	0.84	0.02	0.06	18.6	0.77	0.02	0.06	17.3
Patagonia	0.88	0.02	0.08	15.5	0.74	0.03	0.08	30.6
<b>With <i>Kok</i> [2011] scheme</b>								
Sahara Source	0.90	0.02	0.10	4.95	0.85	-0.04	0.10	-11.2
N. Atlantic Ocean	0.84	-0.05	0.11	-17.5	0.90	-0.08	0.10	-24.1
Asian Source	0.82	-0.06	0.11	-17.9	0.80	-0.01	0.10	-0.20
Middle East	0.86	-0.24	0.25	-54.1	0.84	-0.25	0.26	-55.6
Australia	0.87	-0.01	0.04	-13.5	0.79	-0.01	0.04	-14.3
Patagonia	0.87	-0.01	0.05	-11.4	0.75	0.01	0.05	-0.30

\*NMB (normalized mean bias) is in percent.

## Figures



**Figure 3.1.** GEOS-Chem-predicted percent contribution of mineral dust AOD to total AOD between March 2009 and February 2010. The white boxes covering the “dusty” regions of 1) Saharan dust source region, 2) Saharan dust outflow (N. Atlantic Ocean), 3) Asian dust source region, 4) Middle Eastern dust source region, 5) Australian dust source region, and 6) Patagonian dust source region used for the comparison of model-predicted and remotely-sensed dust AOD/extinction values.

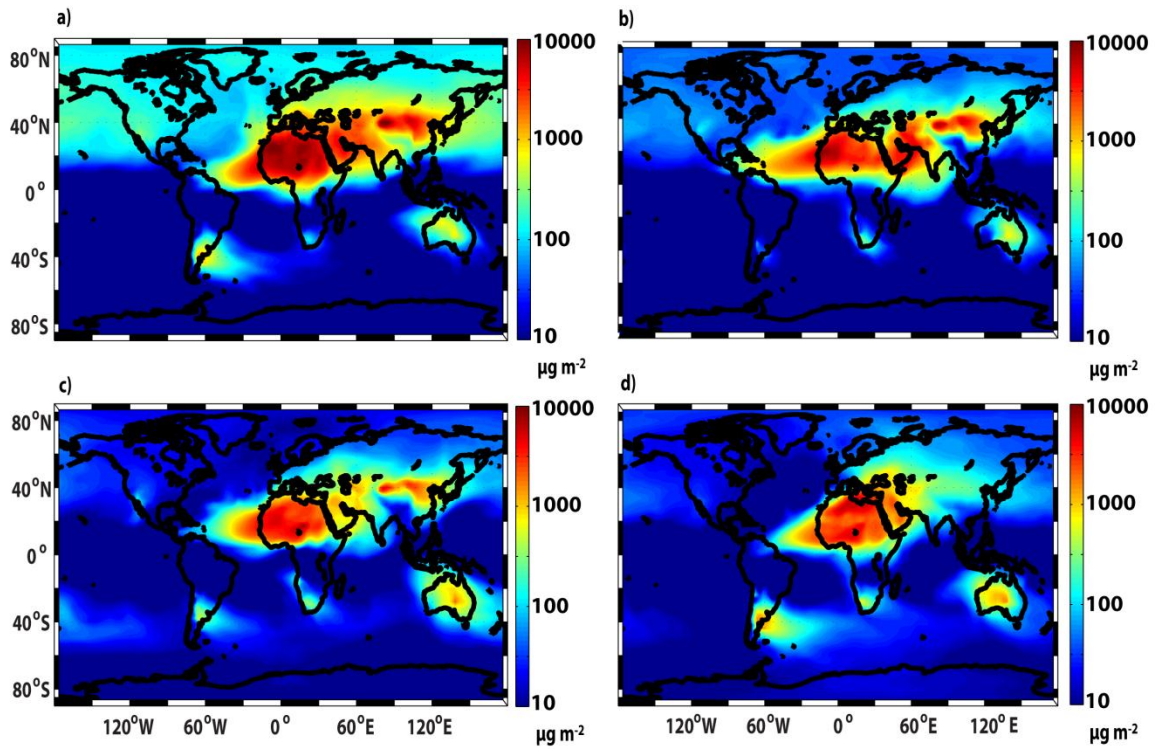


**Figure 3.2.** GEOS-Chem-predicted daily-averaged dust column burden ( $\mu\text{g m}^{-2}$ ) during a) March-April (MAM), b) June-August (JJA), c) September-November (SON), and d) December-February (DJF).

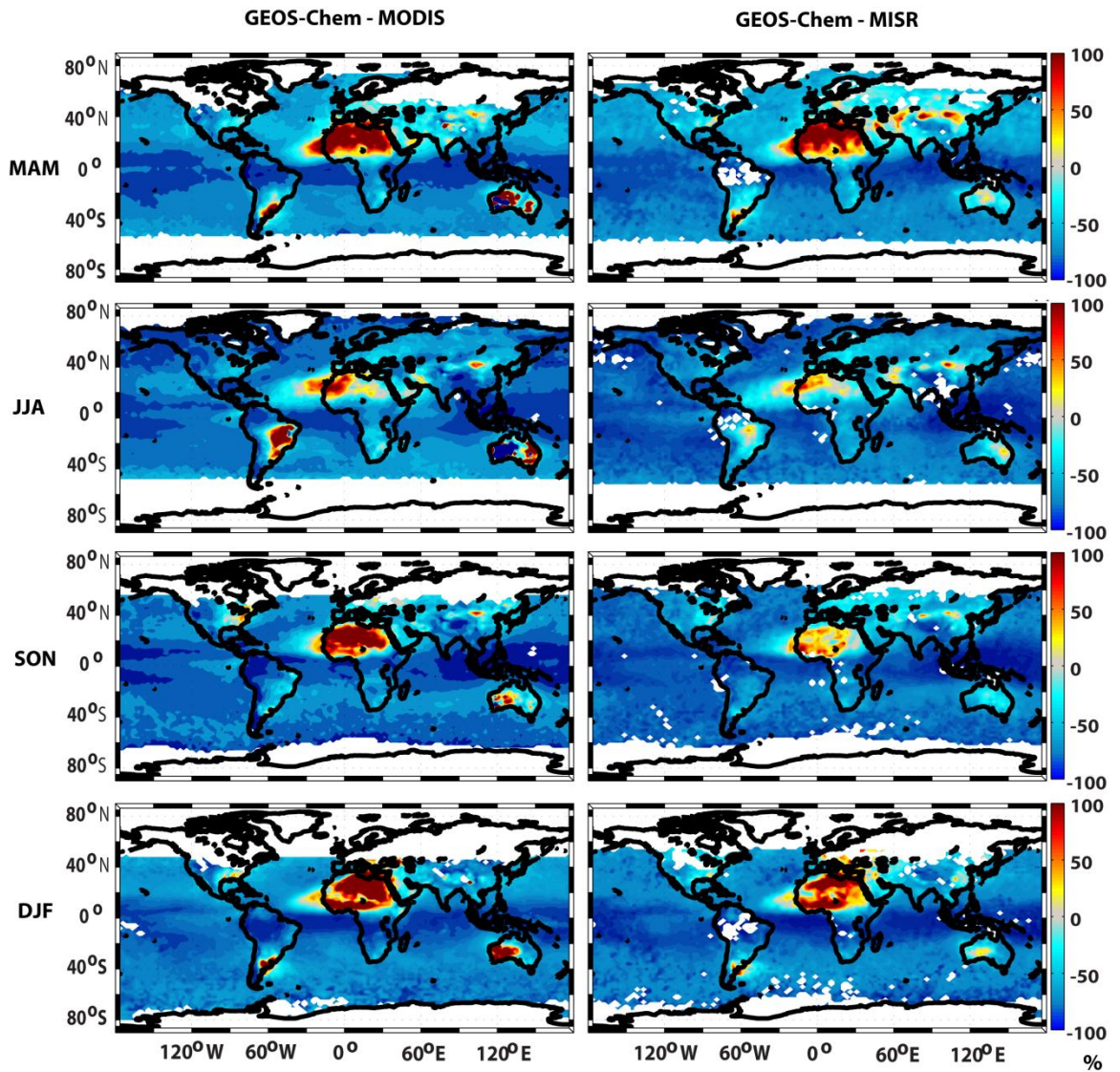


**Figure 3.3.** Seasonally-averaged percent differences for GEOS-Chem-predicted and MODIS (left column) and MISR (right column) retrieved AOD values.

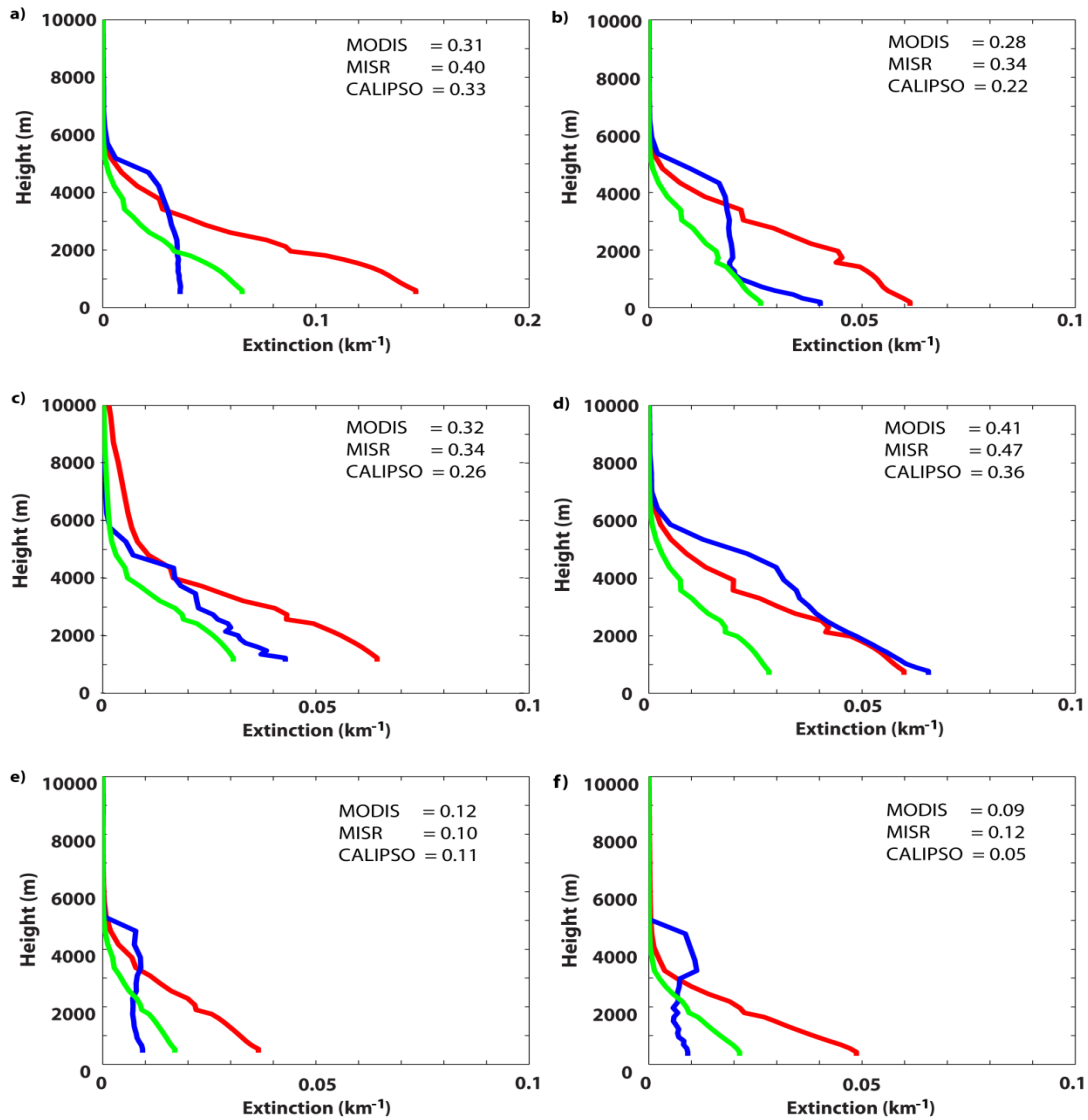


**Figure 3.4.** Annually-averaged CALIPSO-retrieved (blue line) and GEOS-Chem-simulated (standard version - red line, *Kok* [2011] scheme - green line) vertical profiles of mineral dust extinction ( $\text{km}^{-1}$ ) for a) Saharan dust source region, b) Saharan dust outflow region, c) Asian dust source region, d) Middle Eastern dust source region, e) Australian dust source region and f) Patagonian dust source region. Height (m) indicates the elevation above sea level for the center of the model grid. Figure insert shows regionally-averaged AOD values from MODIS, MISR, and CALIPSO.

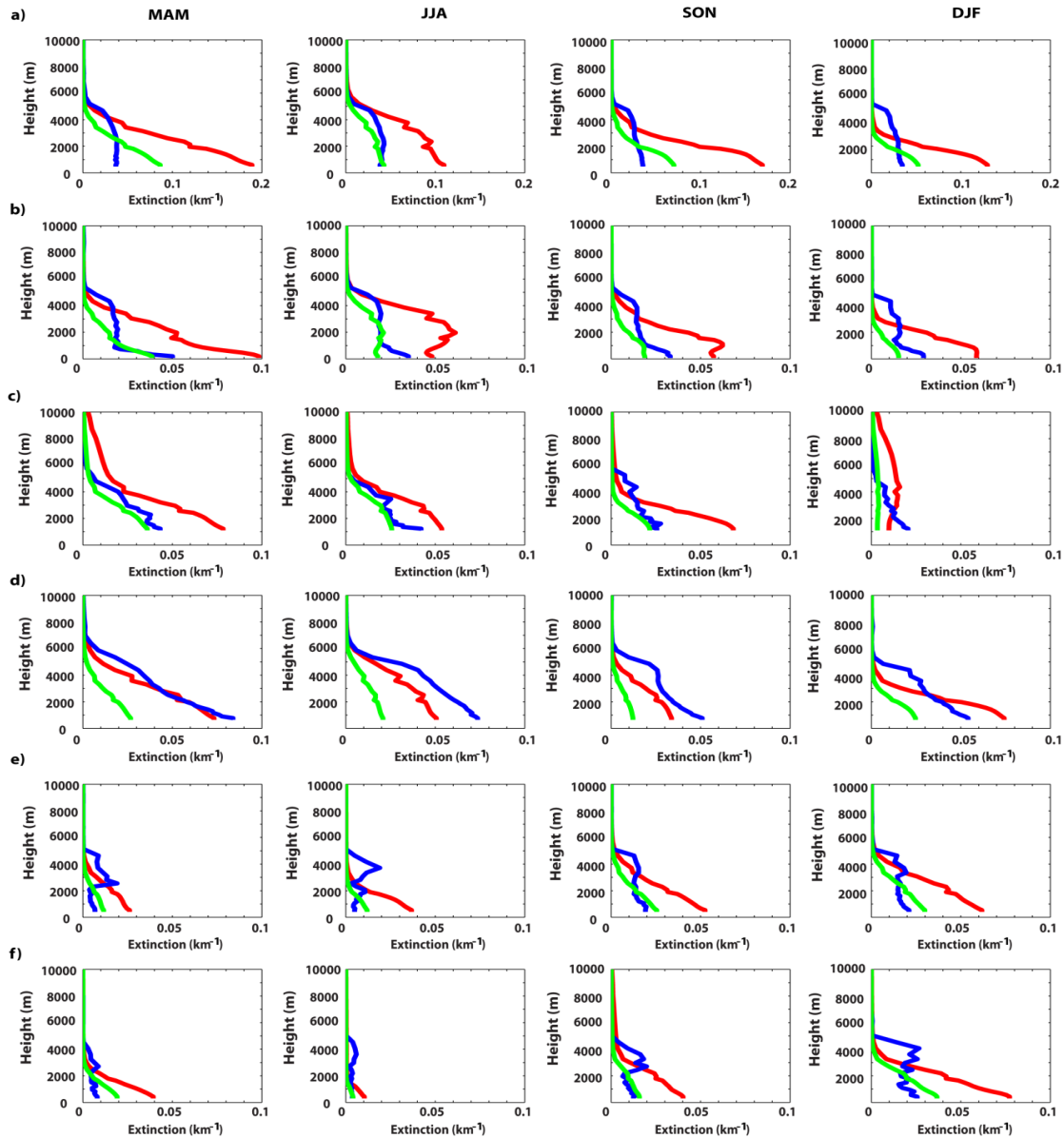


**Figure 3.5.** Seasonally-averaged CALIPSO-retrieved (blue line) and GEOS-Chem simulated (standard version - red line, *Kok* [2011] scheme - green line) vertical profiles of mineral dust extinction ( $\text{km}^{-1}$ ) for the a) Saharan dust source region, b) Saharan dust outflow region, c) Asian dust source region, d) Middle Eastern dust source region, e) Australian dust source region and f) Patagonian dust source region. Height (m) indicates the elevation above sea level for the center of the model grid.

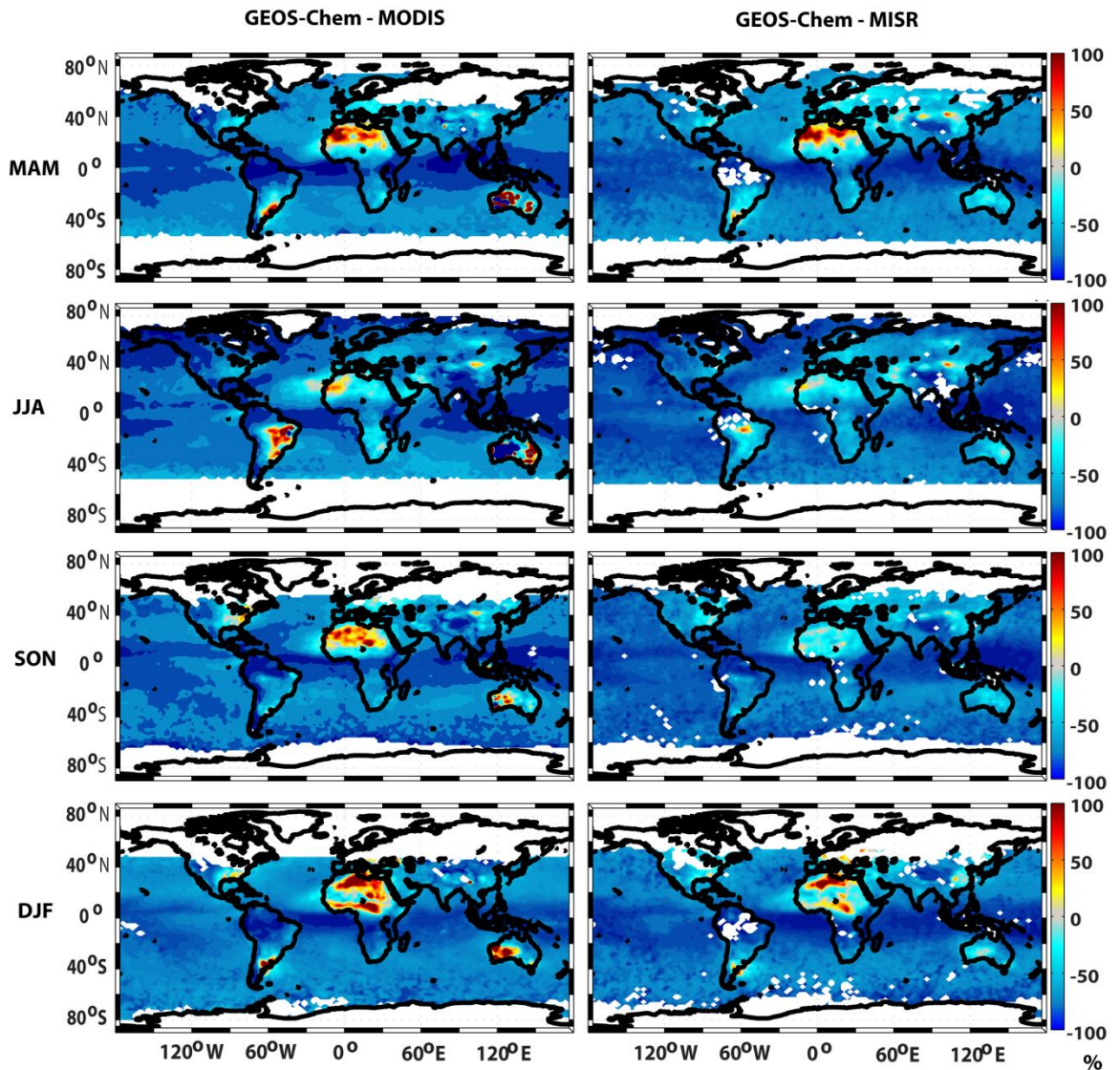


**Figure 3.6.** Seasonally-averaged percent differences for GEOS-Chem-predicted and MODIS (left column) and MISR (right column) AOD values. GEOS-Chem dust AODs are calculated using the size distribution parameterization of *Kok* [2011].

Supplementary online material

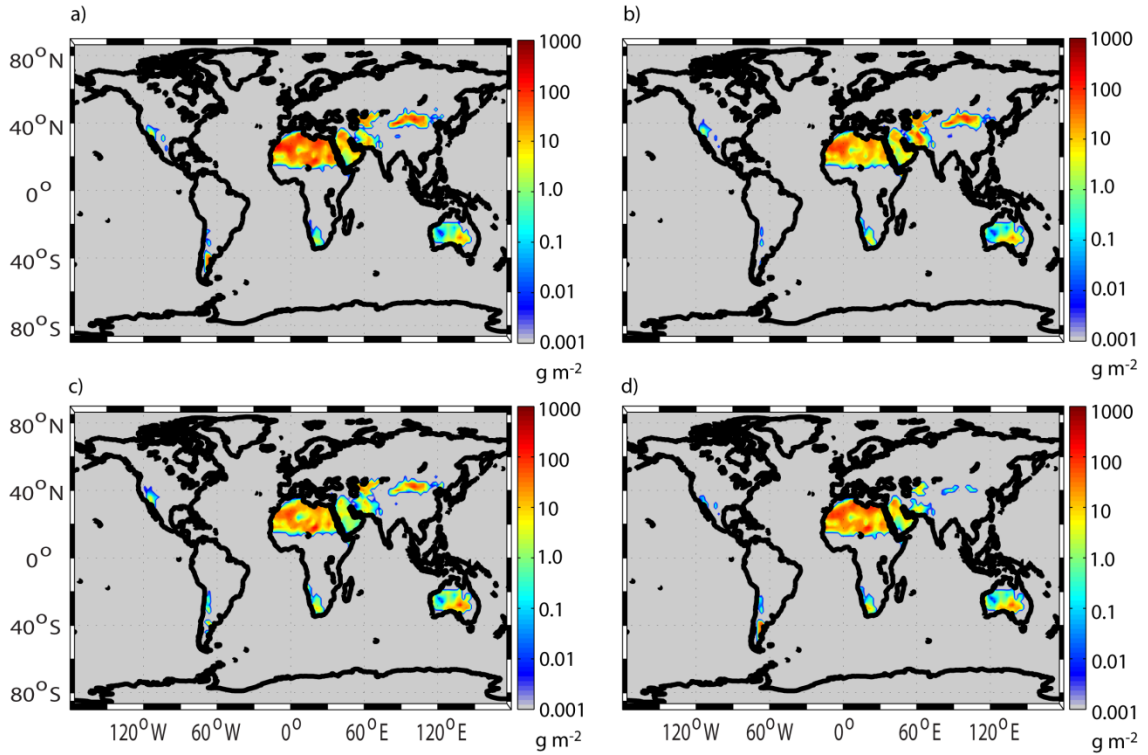


**Figure S3.1.** GEOS-Chem-predicted total dust emissions ( $\text{g m}^{-2}$ ) during a) March-April , b) June-August , c) September-November , and d) December-February.

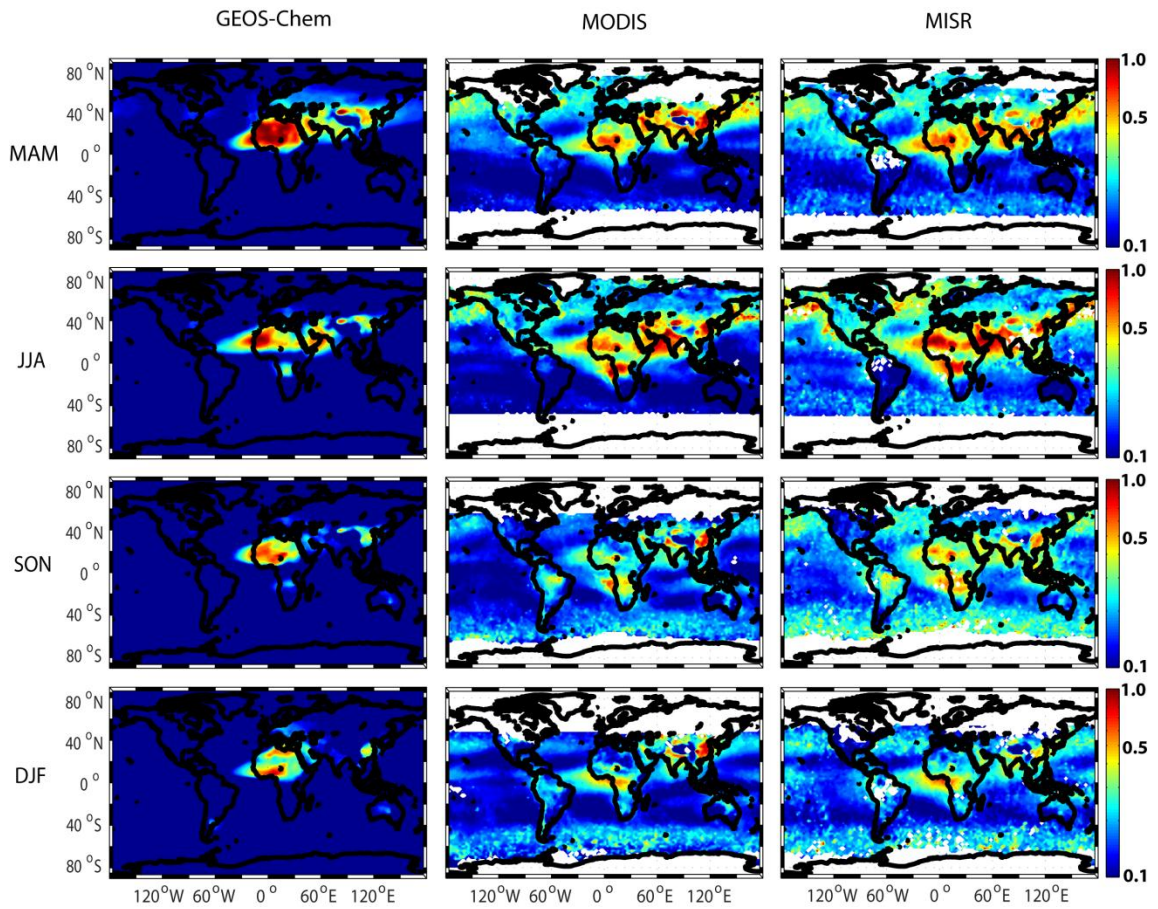


**Figure S3.2.** Seasonally-averaged AOD (on a *logarithmic scale*) predicted by GEOS-Chem (left column) and remotely-sensed by MODIS (middle column) and MISR (right column).

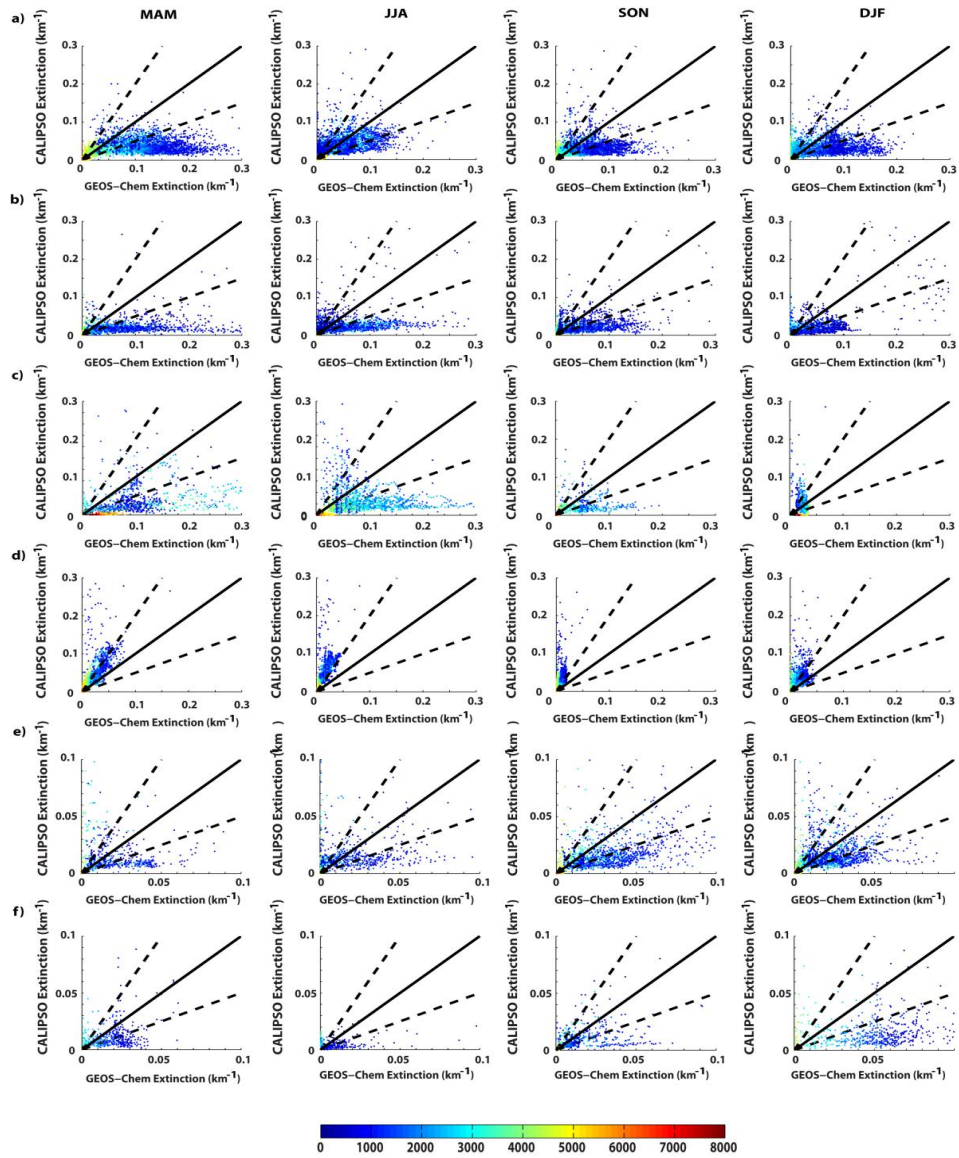


**Figure S3.3.** Scatter plots of CALIPSO-retrieved dust aerosol extinction ( $\text{km}^{-1}$ ) against GEOS-Chem simulations for the a) Saharan dust source region, b) Saharan dust outflow region, c) Asian dust source region, d) Middle Eastern dust source region, e) Australian dust source region and f) Patagonian dust source region. The solid black line is the 1:1 line, and the two dashed lines are the 1:2 and 2:1 lines. Height (m) indicates the elevation above sea level for the center of the model grid.

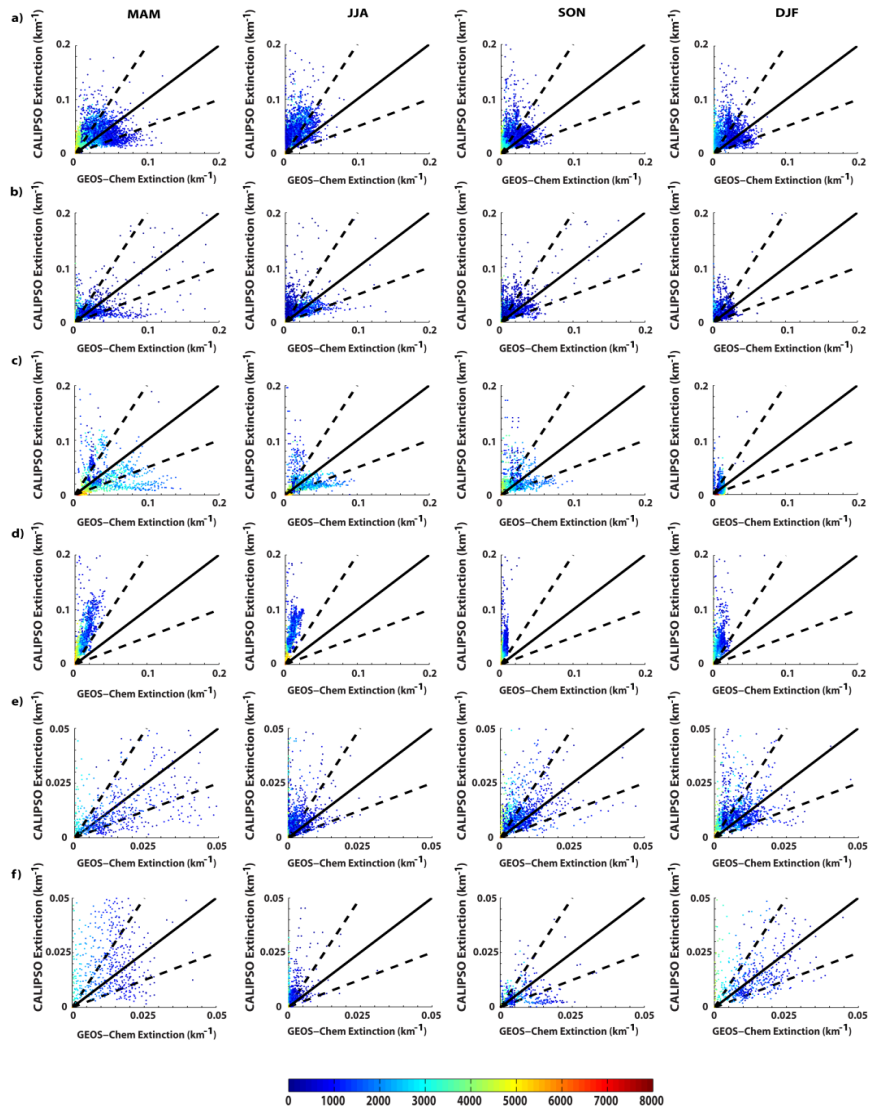


**Figure S3.4.** Scatter plots of CALIPSO-retrieved dust extinction ( $\text{km}^{-1}$ ) against GEOS-Chem simulations using the dust size distribution scheme of *Kok* [2011] for the a) Saharan dust source region, b) Saharan dust outflow region, c) Asian dust source region, d) Middle Eastern dust source region, e) Australian dust source region and f) Patagonian dust source region. The solid black line is the 1:1 line, and the two dashed lines are the 1:2 and 2:1 lines. Height (m) indicates the elevation above sea level for the center of the model grid.

## **4. Understanding the Transport of Patagonian Dust and its Influence on Marine Biological Activity in the South Atlantic Ocean**

### Preface

During a previous yearlong GEOS-Chem simulation, conducted in *Johnson et al.* [2010], 22 Tg of mineral dust and 4 Gg of sol-Fe were quantified to be deposited to the surface waters of the entire SAO. Approximately 30% of the dust and sol-Fe was predicted to be deposited to the HNLC oceanic regions of the SAO between October 2006 and September 2007. Model-predicted DIF values of mineral dust deposited to the SAO were small, on average only accounting for 0.57% of total Fe. Simulations suggest that the primary reason for such a small average DIF value is the low ambient concentrations of acidic trace gases available for mixing with Patagonian dust plumes. Overall, model-predicted concentrations of acidic traces gases absorbed into the deliquesced aerosol solution were not enough to overcome the alkalinity buffer of dust and initiate considerable acid dissolution of mineral-Fe. Sensitivity studies during *Johnson et al.* [2010] demonstrated that the amount of sol-Fe deposited to the HNLC regions of the SAO was, on average, controlled by the initial amount of sol-Fe at the dust source region, with limited contribution from atmospheric chemical processing induced by anthropogenic and natural sources of acidic trace gases.

During this chapter of my dissertation research we evaluate the atmospheric transport dynamics and the potential impact that the deposition of mineral dust and sol-Fe can have on marine primary productivity in the Fe-starved waters of the South Atlantic sector of the Southern Ocean. We focus on model-predictions during two large dust outbreaks originated at the source regions of northern Patagonia during the austral summer of 2009. We chose to focus on large dust outbreaks due to the fact that our previous study shows that minimal amounts of bioavailable Fe are produced by atmospheric chemical processing [*Johnson et al.*, 2010], therefore, highly episodic large dust events may provide the biogeochemically important supplies of sol-Fe.

This chapter of my dissertation has been published in *Atmospheric Chemistry and Physics* (ACP).

# **Understanding the transport of Patagonian dust and its influence on marine biological activity in the South Atlantic Ocean**

**Matthew S. Johnson<sup>1</sup>, Nicholas Meskhidze<sup>1</sup>, Velayudhan Praju Kiliyanpilakkil<sup>1</sup>,  
Santiago Gassó<sup>2</sup>**

<sup>1</sup>Marine Earth and Atmospheric Science, North Carolina State University, Raleigh, NC, USA

<sup>2</sup>Goddard Earth Science and Technology Center, University of Maryland Baltimore County, Baltimore, Maryland, USA

*Correspondence to:* Nicholas Meskhidze

(nmeskhidze@ncsu.edu)

## **Abstract**

The supply of bioavailable Fe to the HNLC waters of the Southern Ocean through atmospheric pathways could stimulate phytoplankton blooms and have major implications for the global carbon cycle. In this study, model results and remotely-sensed data are analyzed to examine the horizontal and vertical transport pathways of Patagonian dust and quantify the effect of Fe-laden mineral dust deposition on marine biological productivity in the surface waters of the SAO. Model simulations for the atmospheric transport and deposition of mineral dust and bioavailable Fe are carried out for two large dust outbreaks originated at the source regions of northern Patagonia during the austral summer of 2009. Model-simulated horizontal and vertical transport pathways of Patagonian dust plumes are in reasonable agreement with remotely-sensed data. Simulations indicate that the synoptic meteorological patterns of high and low pressure systems are largely accountable for dust transport trajectories over the SAO. According to model results and retrievals from CALIPSO, synoptic flows caused by opposing pressure systems (a high pressure system located to the east or north-east of a low pressure system) elevate the South American dust plumes well above the marine boundary layer. Under such conditions, the bulk concentration of mineral dust can quickly be transported around the low pressure system in a clockwise manner, follow the southeasterly advection pathway, and reach the HNLC waters of the SAO and Antarctica in ~3-4 days after emission from the source regions of northern Patagonia. Two different mechanisms for dust-Fe mobilization into a bioavailable form are considered in this study. GEOS-Chem, implemented with an Fe dissolution scheme, is employed to

estimate the atmospheric fluxes of soluble iron, while a dust/biota assessment tool (*Boyd et al.*, 2010) is applied to evaluate the amount of bioavailable Fe formed through the slow and sustained leaching of dust in the ocean mixed layer. The effect of Fe-laden mineral dust supply on surface ocean biomass is investigated by comparing predicted surface chlorophyll-*a* concentration ([Chl-*a*]) to remotely-sensed data. As the dust transport episodes examined here represent large summertime outflows of mineral dust from South American continental sources, this study suggests that (1) atmospheric fluxes of mineral dust from Patagonia are not likely to be the major source of bioavailable iron to ocean regions characterized by high primary productivity; (2) even if Patagonian dust plumes may not cause visible algae blooms, they could still influence background [Chl-*a*] in the South Atlantic sector of the Southern Ocean.

#### 4.1. Introduction

Fe is one of the nutrient elements needed by phytoplankton to carry out photosynthesis. Despite being the fourth most abundant element in the Earth's crust, Fe is in a short supply in most near-surface remote oceanic waters. Concentrations of Fe are particularly low in the so called HNLC oceanic regions, where availability of the micronutrient Fe has been shown to be a limiting factor for marine primary productivity [*Martin and Gordon, 1988; Martin and Fitzwater, 1988; Martin, 1990*]. There are three main HNLC regions (subarctic north Pacific, east equatorial Pacific, and the SO), with the SO suggested to be the most biogeochemically significant due to its large spatial extent and considerable influence on the global carbon cycle [*Martin, 1990; Watson et al., 2000; Boyd et al., 2000; Sarmiento et al., 2004*]. Mesoscale Fe enrichment experiments have unequivocally shown that the Fe supply in the SO exerts control on the dynamics of plankton blooms, which in turn affect the biogeochemical cycles of carbon, nitrogen, silicon, sulfur, and ultimately influences the Earth's climate system [e.g., *Boyd et al., 2007*].

The atmospheric deposition of aeolian dust is one of the natural pathways for the contribution of Fe to the surface waters of the SO. Compared to other Fe-limited regions, the SO is thought to receive the lowest flux of mineral dust [*Duce and Tindale, 1991*] and, as a result, upwelling of deep water, re-suspension of sediments, re-mineralization of sinking material, diffusion from the pore waters, and release of bioavailable Fe from glaciers and icebergs have often been proposed to be the likely suppliers of Fe to this region [*de Baar et al., 1995; Löscher et al., 1997; Watson et al., 2000; Raiswell et al., 2008*]. However, over

the past decade there has been a growing interest for the possible role of mineral dust-Fe in regulating this region's biological productivity, air-sea fluxes of CO<sub>2</sub>, emissions of marine biogenic aerosols and trace gases, and overall global climate [Martin and Fitzwater, 1988; Martin, 1990; Zhuang *et al.*, 1992; Jickells *et al.*, 2005; Meskhidze *et al.*, 2007; Ito and Kawamiya, 2010]. Based on a significant positive correlation between the atmospheric delivery of mineral dust and phytoplankton growth in the surface waters of the SO it was proposed that the biological productivity in the SO is controlled by Patagonian and southern Australian dust deposition [Gabric *et al.*, 2002; Erickson *et al.*, 2003]. However, recent studies have pointed out that dust-Fe deposition to the surface waters of the SO could be less important for primary productivity than previously estimated [Meskhidze *et al.*, 2007; Blain *et al.*, 2007, 2008; Wagener *et al.*, 2008, Boyd *et al.*, 2010] and that the ocean Fe fertilization alone may not account for atmospheric CO<sub>2</sub> reduction enough to significantly alter the course of climate [e.g., Denman, 2008; Buesseler *et al.*, 2008; Mackie *et al.*, 2008; Strong *et al.*, 2009]. Despite the potentially important role of Fe-laden dust deposition on marine primary productivity and atmosphere-ocean CO<sub>2</sub> fluxes, few studies exist that can help constraining the deposition of bioavailable Fe and subsequent changes in surface ocean chlorophyll concentration and carbon sequestration rates in the polar and sub-polar waters of the SO. To understand the biogeochemical cycling of Fe in both present and past climate regimes and the role of mineral dust in Fe-mediated carbon sequestration in the SO, researchers have looked at the detailed stratigraphic records of mineral dust in Antarctic ice cores and used them as proxies for paleoclimate and paleowinds [e.g., Delmonte *et al.*, 2004; Lambert *et al.*, 2008].

When making connections between past glacial-interglacial fluctuations in dust deposition to Antarctica and carbon dynamics in the SO, in addition to particular sources and deposition processes [e.g., *Petit et al.*, 1999; *Lambert et al.*, 2008], it is important to properly quantify the transport pathways [*Krinner and Genthon*, 2003; *Krinner et al.*, 2010; *Li et al.*, 2008, 2010], labile (or bioavailable) portion of mineral-Fe [*Jickells et al.*, 2005; *Meskhidze et al.*, 2003; 2005; *Solmon et al.*, 2009], and the fraction of fixed carbon sequestered to the deep oceans (>250 m) [e.g., *Buesseler et al.*, 2004].

Several studies that have been conducted to quantify dust transport pathways and deposition fluxes in the Southern Hemisphere (SH) seem to agree that the arid and semi-arid regions of South America and Australia are the major source regions for aeolian dust deposited to the SO [*Fung et al.*, 2000; *Ginoux et al.*, 2001; *Prospero et al.*, 2002; *Zender et al.*, 2003; *Li et al.*, 2008]. Although, there is no definite agreement, modeling and remote sensing studies have also identified distinct horizontal and vertical transport pathways for South American and Australian dust sources over the SO. South American dust has been shown to largely remain at lower elevations (below 6 km), while Australian dust is likely to be elevated to higher levels of the free troposphere [*Krinner and Genthon*, 2003; *Gassó and Stein*, 2007; *Li et al.*, 2008; *Krinner et al.*, 2010; *Gassó et al.*, 2010]. Due to extremely limited observational data the labile fraction of Fe in Southern Hemispheric dust (e.g., South America) remains a topic of active debate [*Cassar et al.*, 2007; *Boyd and Mackie*, 2008]. Quantification of the climatic role of South American dust is further complicated by the fact that the proposed fraction of the fixed carbon sequestered to the deep oceans varies by up to a

factor of ~200 [e.g., *de Baar et al.*, 2008], making the link between marine primary productivity and carbon removal extremely difficult.

Using model simulations and remotely-sensed data, this study attempts to better quantify the role of aeolian dust-Fe supply for marine ecosystem productivity in the SAO domain of the SO. Dust transport pathways and deposition fluxes, resulting changes in ocean ecosystem productivity, and the potential effect of dust-Fe deposition on carbon sequestration in this region are examined based on two large dust advection episodes from South America. Here the labile fraction of dust-Fe is defined as the sum of sol-Fe (produced during atmospheric transport and transformation of mineral-Fe) and leachable-Fe (produced by the slow and sustained leaching of mineral-Fe in the ocean mixed layer). The SAO is roughly outlined as the part of the Atlantic Ocean between the equator and the Antarctic coastline (from north to south) and from 70°W to 20°E, and the possible HNLC region as the portion of SAO south of the Antarctic Circumpolar Current (ACC) (~42°S) [*Boyd et al.*, 2007].

## **4.2. Methods**

### **4.2.1 GEOS-Chem/DFeS**

The 3-D global CTM GEOS-Chem (v8-01-01) was used in this study to simulate Patagonian dust transport and deposition to the SAO. The model uses GEOS-5 meteorological fields [*Bey et al.*, 2001; *Park et al.*, 2004; *Evans and Jacob*, 2005] at a 2° × 2.5° (latitude-longitude) grid resolution and 47 vertical levels. For the prognostic calculations of Fe dissolution, the model is run with a full chemistry configuration, which

includes H<sub>2</sub>SO<sub>4</sub>-HNO<sub>3</sub>-NH<sub>3</sub> aerosol thermodynamics coupled to an O<sub>3</sub>-NO<sub>x</sub>-hydrocarbon-aerosol chemical mechanism [Bey *et al.*, 2001; Park *et al.*, 2004]. The emissions and chemistry of sulfur compounds, carbonaceous aerosols, and sea-salt are described by Park *et al.* [2004], Heald *et al.* [2004], and Alexander *et al.* [2005] respectively. To simulate dust mobilization, GEOS-Chem combines the DEAD scheme [Zender *et al.*, 2003] with the source function used in the GOCART model [Ginoux *et al.*, 2001; Chin *et al.*, 2004]. Principal source regions are deserts or dry lakes and streambeds where alluvial deposits have accumulated. Mineral dust mobilization occurs when turbulent drag forces of the atmosphere overcome gravitational inertia and inter-particle cohesion. Once mineral dust is mobilized from the surface, the model uses four standard dust bins with diameter boundaries of 0.2 - 2.0, 2.0 - 3.6, 3.6 - 6.0 and 6.0 - 12.0 μm to simulate global dust transport and deposition [Fairlie *et al.*, 2007].

In order to determine the influence of mineral dust from Patagonia on biological productivity in the SAO, GEOS-Chem was modified to treat a number of individual dust source regions separately. The terrestrial portion of the globe was divided into seven major dust source regions (i.e., North Africa, South Africa, North America, Asia, Australia, the Middle East, and South America) [Prospero *et al.*, 2002]. Dust emission fluxes, calculated for each source region, were assigned separate tracers. Such treatment allowed dust from each of the seven regions to be independently transported, chemically transformed, and removed from the atmosphere. GEOS-Chem with the modified dust scheme gave us the opportunity to estimate the relative contribution of each of the seven dust regions to total

atmospheric dust and bioavailable Fe fluxes to the SAO domain. The fluxes of sol-Fe to the ocean were calculated using GEOS-Chem with a prognostic dust-Fe dissolution scheme (GEOS-Chem/DFeS model) [Solmon *et al.*, 2009; Johnson *et al.*, 2010]. GEOS-Chem/DFeS simulations of South American dust were shown to be in reasonable agreement with available surface and remotely-sensed data [Johnson *et al.*, 2010].

#### 4.2.2 Labile-Fe and the ocean productivity

Throughout its residence time in the surface ocean dust can become a source of bioavailable Fe due to the slow and sustained leaching of dust-Fe [Boyd *et al.*, 2010]. To calculate the amount of Fe leached from mineral dust we adopt the formulation of Boyd *et al.* (2010):

$$Leachable - Fe = \frac{DST \cdot fFe \cdot fFe_{Leachable}}{r_{Leachable} \cdot t_{residence} \cdot D} \quad (1)$$

where *leachable-Fe* is the amount of Fe leached in the surface ocean for a given quantity of mineral dust deposition ( $\text{g m}^{-3}$ ), *DST* is GEOS-Chem/DFeS-predicted mineral dust deposition during a given dust episode ( $\text{g m}^{-2}$ ), *fFe* is the average mass fraction of Fe in mineral dust (3.5%) [Duce and Tindale, 1991], *fFe<sub>leachable</sub>* is the fraction of Fe in deposited dust that is leachable (0.3), *r<sub>Leachable</sub>* is the rate of Fe leaching ( $30 \text{ day}^{-1}$ ), *t<sub>residence</sub>* is the residence time of dust in the ocean mixed layer (30 day), and *D* is the monthly-mean mixed layer depth (m). The values for *fFe<sub>Leachable</sub>*, *r<sub>Leachable</sub>*, and *t<sub>residence</sub>* are taken from Boyd *et al.* [2010] (all based on measurements made in the Southern Ocean) and the value for *D* was obtained from the global climatological monthly-averaged mixed layer depth data ( $2^\circ \times 2^\circ$ ) [de Boyer Montégut *et al.*, 2004] and regridded to a  $0.25^\circ \times 0.25^\circ$  resolution.

Due to the uncertainty in spatial distributions of leachable-Fe in the dynamic surface waters of the SAO, we only use the model-predicted atmospheric fluxes of sol-Fe as a proxy for the surface ocean primary production [Meredith *et al.*, 2003]. The magnitude of chlorophyll-*a* ([Chl-*a*]) production per unit time (in mg m<sup>-3</sup> day<sup>-1</sup>) can then be calculated as:

$$\frac{d [\text{Chl } a]}{dt} = \frac{12000 \cdot \text{sol-Fe} \cdot (C:\text{Fe}) \cdot (\text{Chl-a}:C)}{D} \quad (2)$$

where the constant of 12000 is used for a unit conversion (from mol C to mg C), *sol-Fe* represents GEOS-Chem/DFeS-predicted atmospheric fluxes of sol-Fe (mol m<sup>-2</sup> day<sup>-1</sup>), *C:Fe* is the carbon to Fe ratio characteristic for the major phytoplankton species found in the enhanced productivity regions of the SAO (mol mol<sup>-1</sup>), and *Chl-a:C* is the chlorophyll-*a* to carbon ratio in phytoplankton (mg mg<sup>-1</sup>). Table 4.1 summarizes the values (with corresponding references) for the parameters used in Eq. (2). This equation implicitly assumes that all of the deposited sol-Fe will contribute to chlorophyll production in the HNLC waters of the SO. Such a provision is supported by past mesoscale Fe enrichment experiments and results from previous studies on marine biota and Fe interactions in HNLC waters [e.g., Hutchins *et al.*, 1999; Tsuda *et al.*, 2003; Jin *et al.*, 2008; Lancelot *et al.*, 2009]. In section 3.3 sensitivity calculations are presented to show the potential contribution of leachable-Fe to atmospheric fluxes of labile-Fe to the SAO.

### 4.2.3 Satellite data

In this study, GEOS-Chem-predicted mineral dust transport during the two dust outbreak episodes of 23 - 30 January 2009 and 11 - 18 February 2009 (from here on J23 and

F11) were compared to real-time imagery and remotely-sensed data obtained from *Terra* and *Aqua* MODIS retrievals [Kaufman *et al.*, 1997; Tanré *et al.*, 1997; Remer *et al.*, 2005] and CALIPSO [Vaughan *et al.*, 2004]. Real-time imagery from MODIS Rapid Response system (<http://rapidfire.sci.gsfc.nasa.gov/gallery/>) was used for the visual confirmation of mineral dust outbreaks from South American continental sources.

The model-predicted vertical profiles of Patagonian dust concentrations were compared to CALIPSO Level 2 (v3.01) data ([http://eosweb.larc.nasa.gov/PRODOCS/calipso/table\\_calipso.html](http://eosweb.larc.nasa.gov/PRODOCS/calipso/table_calipso.html)). The CALIPSO algorithm is distinctive from other satellite algorithms in its capability to discriminate dust aerosols (desert dust and polluted dust) from other subtypes such as clean continental, marine, polluted continental and smoke. To determine the aerosol subtypes the algorithm uses volume depolarization ratio, integrated attenuated backscatter, the earth surface types (land/ocean), and the layer altitude information. The aerosol optical depth (AOD) and extinction/backscatter profile retrievals for different particle subtypes require aerosol extinction-to-backscatter ratio (lidar ratio) specific to the above mentioned six aerosol types [Omar *et al.*, 2009; Young and Vaughan, 2009]. The CALIOP identified features are classified into aerosol and cloud using a CAD algorithm. The CAD algorithm separates clouds and aerosols and provides the cloud-aerosol discrimination score for each layer [Liu *et al.*, 2009]. The standard CAD scores for the level of confidence in the aerosol-cloud classification are ranging from -100 to 0 for aerosol and +100 to 0 for cloud. A larger absolute value of the CAD score indicates higher confidence of the feature classification. To

get relatively high confidence cloud free data, different aerosol types and the corresponding AODs are extracted using CAD scores of -20 to -100 [Yu *et al.*, 2010] for the conditions when initial lidar ratio (selected based on type and subtype of the layer) is equal to the final lidar ratio (derived by applying transmittance correction to the extinction processing) ([http://eosweb.larc.nasa.gov/PRODOCS/calipso/Quality\\_Summaries/](http://eosweb.larc.nasa.gov/PRODOCS/calipso/Quality_Summaries/)).

Daily-averaged Level 3 data for [Chl-*a*] at  $\frac{1}{12}^{\circ} \times \frac{1}{12}^{\circ}$  resolution were obtained from the Sea-viewing Wide Field-of-view Sensor (SeaWiFS) (version 5.1) [O'Reilly *et al.*, 1998] and regridded to  $0.25^{\circ} \times 0.25^{\circ}$ . Previous studies have shown that fluctuations in daily surface [Chl-*a*] retrievals by SeaWiFS compare well with in situ measurements in the SAO, with some possible underestimations in the Drake Passage and Scotia Sea regions of the Antarctic basin [Gregg and Casey., 2004; Dogliotti *et al.*, 2009]. Past studies have shown that the presence of mineral dust may influence optical properties of oligotrophic waters (i.e., [Chl-*a*]  $\leq 0.1 \text{ mg m}^{-3}$ ) and cause anomalous readings in retrievals of phytoplankton biomass [Claustre *et al.*, 2002]. However, we consider such errors to be negligible for the productive waters of the SAO.

### **4.3. Results**

#### **4.3.1 Mineral dust transport from Patagonia**

Dry lake/river beds and low lying regions in Patagonia with little vegetative cover are the predominant source regions of windblown dust emanating from the South American continent and deposited to the surface waters of the SAO [Prospero *et al.*, 2002; Li *et al.*,

2008; Wagener *et al.*, 2008; Johnson *et al.*, 2010]. Patagonian dust plumes have been suggested to travel at low altitudes over the SAO and are accompanied by large amounts of cloud cover [Gassó and Stein, 2007; Li *et al.*, 2008; Krinner *et al.*, 2010], making it difficult to be detected by satellites. On 23 January 2009 and 17 February 2009 clear images of mineral dust transport were captured by *Aqua* MODIS (see Fig. 4.1) allowing for the rare opportunity to carry out model analysis of dust transport for episodes with visual confirmation of mineral dust advection from the South American continent. Figures 4.1a, b indicate that mineral dust emission regions are located near San Antonio Oeste, a region that was previously identified as one of the largest dust sources in Patagonia [Johnson *et al.*, 2010]. This region is located in the northern end of Patagonia and it has recently become an active dust source possibly due to a combination of poor livestock management and drought conditions [Geist and Lambin, 2004; McConnell *et al.*, 2007]. According to Fig. 4.1, GEOS-Chem-predicted transport pathways over the ocean are generally comparable with the satellite images, although the agreement between model-predictions and satellite imagery is somewhat poorer for 17 February 2009, when dust originated from three individual small sources. Model simulations show, that both the J23 and F11 outbreaks had similar transport pathways over the SAO, with daily-averaged vertically-integrated dust concentrations for the F11 dust storm roughly a factor of four higher compared to the J23 dust event (see Fig. 4.1). In addition to horizontal transport, existence of CALIPSO retrievals gives the unique opportunity for examining model-predicted vertical transport pathways of Patagonian dust. Unfortunately, out of the two dust episodes with clear visual evidence of long-range

transport, CALIPSO data is only available for the J23 episode; therefore only the J23 dust storm will be discussed in detail.

In order to examine the impact of synoptic meteorology on mineral dust transport, previous studies have applied sea level pressure anomalies (SLPAs) as a proxy for high and low pressure systems [e.g., *Liang et al.*, 2005; *Yang et al.*, 2007]. Figure 4.2 compares the spatial patterns of the model-predicted column abundance of mineral dust and GEOS-5 SLPAs over the SAO for 23-25 January 2009. This figure indicates that the relative positioning of high and low pressure systems may control the south-eastward transport of the J23 dust plume (Southern Hemispheric low pressure systems rotate clockwise and high pressure systems rotate counter-clockwise). Analyses of model simulations suggest that synoptic flows caused by opposing pressure systems (a high pressure system located to the east/north-east of a low pressure system) produce large-scale southerly advection between 40°S and 60°S. The bulk concentration of mineral dust follows the southerly advection pathway and gets transported over the HNLC waters of the SAO and East Antarctica. The controlling effect of horizontal transport pathways of Patagonian dust by synoptic meteorological patterns found over the SAO is consistent with the results of the recent study by *Li et al.* [2010].

In addition to horizontal transport, the location of high and low pressure systems may also influence the vertical structure of Patagonian dust plumes. Figures 4.3-4.5 compare GEOS-Chem-predicted dust burden and vertical profiles of mineral dust for the J23 dust plume to CALIPSO aerosol type and dust AOD retrievals for 23-25 January 2009. Notice,

that GEOS-Chem outputs are daily-averaged data while CALIPSO results are for a specific overpass time. Figures 4.3 and 4.4 show that near the South American continent, both GEOS-Chem predictions and CALIPSO retrievals position the J23 dust plume at a low altitude (below 2-3 km). Although CALIPSO puts the major portion of the dust plume slightly north to that of GEOS-Chem, the model-simulated vertical structure of the J23 plume compares relatively well with CALIPSO AOD data (Figs. 4.3b, c and 4.4b, c).

Detailed analysis of model simulations reveal that after leaving the continent, the Patagonian dust plume encountered a strong cyclone over the SAO. On 24 January 2009 when the dust plume was about to enter the western sector of the large low pressure system ( $\sim 20^{\circ}\text{W}$ ), the bulk of the dust was still located below 3 km over the SAO (Fig. 4.4b). As the plume entered the cyclone on 25 January 2009 (Fig. 4.5), mineral dust got transported around the low pressure system in a clockwise manner. Although simulations are in poorer agreement with the CALIPSO retrievals on 25 January, both model results (Figs. 4.5c, f) and satellite overpasses (Figs. 4.5b, e) show that over the northern sector of the cyclone ( $\sim 0^{\circ}\text{W} - 5^{\circ}\text{E}$ ) the dust plume was lifted above the marine boundary layer (MBL) and got diluted vertically in the free troposphere (up to  $\sim 6$  km). It should also be noticed that in the 2-3 days of transport time over the SAO the dust plume is significantly depleted and the comparison of remotely-sensed data and the daily-averaged model results become less reliable. Overall, our model simulations suggest that synoptic meteorological conditions played a considerable role in both the horizontal and vertical advection of the J23 storm over the SAO. By using the combination of model and remote sensing techniques, we have shown that low pressure

systems can elevate Patagonian dust to heights suitable for long-range transport over the SAO.

Further analyses of model simulations for the J23 and F11 dust episodes revealed two main transport pathways for mineral dust emitted from the northern end of Patagonia and advected over the SAO. Figure 4.6 shows that when a high pressure system is located to the east/north-east of a low pressure system, it can effectively block the strong easterlies. During such synoptic setup, northern Patagonian dust plume trajectories will go around the low pressure system in a clockwise manner and follow a south-eastward direction. Under such conditions, both model-simulations and CALIPSO retrievals suggest that dust plumes can be uplifted and diluted vertically in the free troposphere creating suitable conditions for the long-range transport towards East Antarctica. A clear example of this southerly advection is seen on 25 January (Fig. 4.6a-c). However, when an intense high pressure system is located north/north-west of a low pressure system over the SAO, northern Patagonian dust follows an anticyclonic circulation and gets transported in an easterly/north-easterly direction. No significant dust uplift is observed for such an advection pathway. Figure 4.6 shows that during the F11 dust episode both transport routes become evident. Between 13-14 February 2009 the Patagonian dust plume is transported to the south-east as the SAO is dominated by a low pressure system with a high pressure system to the east/north-east (Fig. 4.6d, e), while on 15 February 2009 as the low pressure weakens, the dust plume gets entrained into the anticyclonic circulation and gets advected to the east/north-east, following the synoptic flow (Fig. 4.6f). Interestingly, synoptic flow patterns characterized by a high pressure system

located to the west of a low pressure system can even transport Patagonian dust in a north-westerly direction. Figure 4.3a shows a model-predicted “V” shaped horizontal dust burden with two converging dust plumes. Detailed analysis of satellite data and model predictions indicates that the northern portion of the dust plume was emitted from the same source region as the dust from the J23 event, but four days (19 January) prior to it. The initial dust plume was caught in a weak high pressure system with light and variable winds until 23 January, when the low pressure strengthened, transporting the plume to the east/south-east direction. Figure 4.3a shows, that the “V” shaped plume was identified by CALIPSO, but was not retrieved by MODIS due to presence of extensive clouds and sun glint in the region. Although we show dust trajectories for only a few dust episodes, results of this study are consistent with the recent work of *Li et al.* [2010], suggesting that synoptic patterns of high and low pressure systems over the SAO can have considerable influence on Patagonian dust transport trajectories.

The explicit contribution of Patagonian source regions to total dust deposited to the SAO during the J23 and F11 dust episodes were examined using the modified version of GEOS-Chem, with seven specific dust source regions. Figure 4.7 shows that during the J23 and F11 dust episodes Patagonian sources likely accounted for the majority of dust deposited to the South Atlantic Sector of the SO. This result is in agreement with recent studies [e.g., *Li et al.*, 2008; 2010; *Bory et al.*, 2010], suggesting that the transport and deposition of dust from Patagonia represents the major pathways for the atmospheric fluxes of the micronutrient Fe to the HNLC surface waters of the SAO. Model calculations show that during the J23 and

F11 dust episodes a total of ~1.0 and 4.0 Tg of dust was deposited to the SAO oceanic regions, respectively. Roughly ~40% of this mineral dust was deposited to the proposed HNLC region. Figure 4.7 shows that during the austral summer mineral dust from Patagonia can be transported over thousands of kilometers reaching the west coast of South Africa and Australia and the East and West Antarctic continent. However, notice that the considerable contribution of Patagonian sources to mineral dust fluxes to the SAO seen on Fig. 4.7 is largely due to the lack of dust supply from other sources during this time. The contribution of Patagonian sources to dust deposition in the Pacific sector of the SO is quickly declining to near zero values due to the strong contribution from Australian dust.

#### **4.3.2 Response of marine biological productivity to mineral dust deposition**

The potential interactions between mineral dust deposition and marine biological productivity during the J23 and F11 dust events was explored using GEOS-Chem/DFeS-predicted daily- fluxes of sol-Fe (regridded to  $0.25^\circ \times 0.25^\circ$  to match the resolution of remotely-sensed SeaWiFS data). The predicted [Chl-*a*] production due to the atmospheric deposition of sol-Fe was calculated using Eq. (2). Eight-day periods were chosen for each dust event in order to capture the possible biological response to the initial supply of sol-Fe to the SAO. Artificial mesoscale Fe-enrichment experiments revealed that in the SO [Chl-*a*] production responds rapidly to Fe supply (~3-5 days) [e.g., *Boyd et al.*, 2004; 2007], therefore this length of time should be suitable for capturing the initial response of marine biota to sol-Fe deposition. When using average values of the different parameters of Table 4.1, model-predicted fluxes of sol-Fe during the J23 and F11 dust episodes should have

increased surface [Chl-*a*] ( $\Delta[\text{Chl-}a]_{\text{pred}}$ ) between 0.001 and 0.7 mg m<sup>-3</sup> (see Fig. 4.8). Such predicted changes in [Chl-*a*] are small for the SAO, where algal blooms with [Chl-*a*] on the order of several mg m<sup>-3</sup> have often been reported [e.g., *Korb et al.*, 2004; *Romero et al.*, 2006; *Blain et al.*, 2007]. However, as the phytoplankton productivity in surface waters of the SAO are generally considered to be limited by the availability of Fe, even small additions of bioavailable Fe from mineral dust could influence primary productivity in this region. In section 3.3 sensitivity calculations are presented to assess how reasonable variations in the parameters of Table 4.1 can affect estimated biological productivity in the region.

To estimate the potential contribution of model-predicted fluxes of sol-Fe to phytoplankton productivity in the SAO for both the J23 and F11 episodes, we have compared  $\Delta[\text{Chl-}a]_{\text{pred}}$  (Figs. 4.8a, b) to the differences in remotely-sensed 8-day averaged [Chl-*a*] ( $\Delta[\text{Chl-}a]_{\text{obs}}$ ) values (after the storm minus before the storm). Figures 4.9a, b show that there are large areas near the dust deposition regions where  $\Delta[\text{Chl-}a]_{\text{obs}}$  changes by more than 0.5 mg m<sup>-3</sup> (i.e., phytoplankton blooms easily visible from the satellites). From Fig. 4.9 it can be seen that during the individual dust events there is a large spatiotemporal variability in remotely-sensed [Chl-*a*] values. However, this variability may not be related only to dust deposition. Past studies [*Moore and Abbott*, 2000; *Korb et al.*, 2004; *Park et al.*, 2010] show that large changes in [Chl-*a*] can be caused by the dynamic nature of the surface waters in the SAO. Mesoscale physical processes, frontal mixing and topographic effects can cause high-frequency (less than 10 days) eddy variability [*Meredith and Hughes*, 2005], responsible for the upwelling of large amounts of nutrients. Our calculations suggest that the HNLC region

of the SAO had an area-averaged  $\Delta[\text{Chl-}a]_{\text{obs}}$  of  $0.04 \text{ mg m}^{-3}$  and  $0.02 \text{ mg m}^{-3}$  for the J23 and F11 dust events, respectively. These values are above the climatological (1998-2008) mean  $\Delta[\text{Chl-}a]_{\text{obs}}$  in the SAO but within the range ( $-0.04$  to  $0.06 \text{ mg m}^{-3}$  for J23 and  $-0.07$  to  $0.04 \text{ mg m}^{-3}$  for F11) for these respective time periods.

The comparison of Figs. 4.8a, b to Figs. 4.9c, d indicates that the contribution of model-predicted atmospheric sol-Fe deposition to marine productivity in the SAO is disproportionately larger in regions with minimal  $\Delta[\text{Chl-}a]_{\text{obs}}$ . Figure 4.10 shows that for both the J23 and F11 episodes the ratio  $\Delta[\text{Chl-}a]_{\text{pred}}/\Delta[\text{Chl-}a]_{\text{obs}}$ , a proxy for the contribution of model-predicted sol-Fe to biological productivity in the HNLC regions of the SAO, decreases sharply for the larger values of  $\Delta[\text{Chl-}a]_{\text{obs}}$ . This figure suggests that atmospheric fluxes of sol-Fe, while influencing surface ocean productivity in large areas of SAO, played a negligible role in regions with  $\Delta[\text{Chl-}a]_{\text{obs}} > 1.0 \text{ mg m}^{-3}$ . Analysis of data shown on Fig. 4.10 revealed that as much as 50% of all the data points in HNLC waters of the SAO with  $\Delta[\text{Chl-}a]_{\text{obs}} > 0$  had over 20% contribution from mineral dust. This result indicates that a large number of the remotely sensed grid cells with increasing  $[\text{Chl-}a]$  during J23 and F11 dust storms had a sizable contribution from atmospheric fluxes of sol-Fe. However, these grid cells only account for  $< 30\%$  of the total biomass produced in this region. To the extent that carbon export from surface waters of the SAO is believed to be primarily controlled by large, rapidly-sinking diatoms, capable of producing visible blooms [*de Baar et al.*, 1995; 2008], this result suggests that Patagonian dust may have a modest influence on the carbon cycle in the SO.

### 4.3.3 Sensitivity analysis

Uncertainties in reported values of  $C:Fe$  and  $Chl-a:C$  ratios (see Table 4.1) could add a large range to model-predicted changes in marine productivity. When the uncertainties shown in Table 4.1 are considered (with the exception of mixed layer depth), the maximum value of  $\Delta[Chl-a]_{pred}$  increased by roughly a factor of 4. In addition to atmospheric fluxes of sol-Fe associated with the chemically aged mineral dust in the atmosphere it has been suggested that a considerable amount of labile-Fe in mineral dust can be leached during its oceanic mixed layer residence time. This leaching dissolution mechanism comprises processes such as grazer/particle interactions, photo-reductive mechanisms in conjunction with siderophores, and reduction of dust-Fe within particle micro-zones [Boyd *et al.*, 2010]. Calculations using Eq. (1) with GEOS-Chem-predicted dust fluxes over 30 days prior to J23 and F11 episodes indicate that the amount of leachable-Fe would have increased surface  $[Chl-a]$  between 0.001-0.05 and 0.001-0.3  $mg\ m^{-3}$ , respectively, i.e.,  $\sim 50\%$  of  $\Delta[Chl-a]_{obs}$ . Dust deposition rates, dissolution of different Fe-laden minerals, and chemical and mineralogical composition of Patagonian dust could further contribute up to 60% uncertainty in simulated sol-Fe fluxes [Johnson *et al.*, 2010]. Overall, our calculations show that due to the large uncertainties associated with the key parameters used in Eqs. 1 and 2, and the processes for the supply of labile-Fe to the surface waters of the SAO by atmospheric pathways, the role of Patagonian dust in surface biological productivity and carbon dynamics of the SO cannot be fully ascertained. This result highlights the great need for more detailed research of marine biota/mineral-dust interactions in the SAO.

#### 4.4. Conclusions

Two large dust outbreaks from Patagonia (23-30 January 2009, J23 and 11-18 February 2009, F11) were examined in this study to evaluate horizontal and vertical transport pathways of South American dust and quantify the impact of enhanced mineral dust and sol-Fe fluxes on marine biological productivity in the surface waters the SAO. The global chemistry transport model GEOS-Chem/DFeS was used to reveal the processes that define the horizontal and vertical transport pathways of northern Patagonian dust over the SAO and estimate the potential effect of mineral dust and sol-Fe deposition on biological activity in the HNLC waters of the SAO. Retrievals of remotely sensed surface [Chl-*a*] before and after the large summertime outflows of mineral dust allow us to estimate potential contribution of mineral dust to surface ocean primary productivity in the SAO.

Analyses of model results and remotely-sensed data revealed that northern Patagonian dust can travel long distances over the SAO. The long-range transport shown during this study is consistent with recent works of *McConnell et al.* [2007], *Gassó et al.* [2010] and *Li et al.* [2010] which demonstrate that Patagonian dust can travel thousands of kilometers away from the South American continent reaching the coast of South Africa and West and East Antarctica. As the dust outflow off the coast of South America typically occurs below 2 km, for mineral dust to get transported over such long distances, the dust plumes need to be elevated to heights above the marine boundary layer. Model simulations revealed that the horizontal and vertical pathways of northern Patagonian dust are highly dependent on the synoptic meteorological patterns of strong high and low pressure systems over the SAO.

When a high pressure system is located to the east/north-east of a low pressure system, northern Patagonian dust plume trajectories will go around the low pressure system in a clockwise manner and get preferentially transported in a southerly/south-easterly direction. However, when a high pressure system is located to the north/north-west of a low pressure system, northern Patagonian dust follows an anticyclonic circulation and gets transported in an easterly/north-easterly direction. Model simulations and remote sensing also revealed that as the plume enters the cyclonic system rotating in a clockwise manner, the dust plume can be rapidly lifted above the MBL and diluted vertically in the free troposphere (up to ~6 km). A similar process was reported in a satellite observation made by *Gassó and Stein, [2007]* which demonstrated Patagonian dust being uplifted as it encountered a low pressure center over the SAO. Such elevations are suitable for Fe-laden mineral dust to be transported long distances, often reaching the HNLC regions of the SAO and East Antarctica.

The potential effect of bioavailable Fe deposition on phytoplankton dynamics in the SAO during the J23 and F11 dust episodes was explored using model-predicted fluxes of labile-Fe delivered to HNLC waters of the SAO through atmospheric pathways. In addition to GEOS-Chem/DFeS predicted amounts of sol-Fe produced during atmospheric transport and transformation of mineral dust, a dust/biota assessment tool [*Boyd et al., 2010*] was used to estimate the amount of leachable-Fe produced due to the slow and sustained leaching of dust during its residence time in the surface waters of the SAO. Offline calculations of [Chl-*a*] enrichments due to predicted amounts of sol-Fe were compared to remotely-sensed SeaWiFS satellite data and used as an indirect assessment of Patagonian dust contribution to

phytoplankton dynamics in the SAO. Our calculations indicate that on average the atmospheric supply of sol-Fe has a disproportionate effect on surface [Chl-*a*]. The contribution of sol-Fe to biological productivity in the SAO decreases sharply for areas with sizable increases in remotely-sensed [Chl-*a*]. This result implies that in surface waters of the SAO that can sustain large increases in marine primary productivity, the majority of the bioavailable Fe is likely to be delivered through non-atmospheric pathways (e.g., upwelling of deep water, re-suspension of sediments, re-mineralization of sinking material, diffusion from the pore waters, and release of bioavailable Fe from glaciers and icebergs). As the two dust events examined in this study are believed to be representative of strong summertime dust outflow from northern Patagonia, and the supply of bioavailable Fe to the SAO is known to strongly favor production of the larger-size, rapidly-sinking diatoms with highest efficiency of carbon removal from the upper ocean, results of this study suggest that Patagonian dust fluxes should have a lesser effect on the SO carbon cycle. However, calculations also revealed that when large uncertainties in GEOS-Chem/DFeS predicted fluxes of sol-Fe, the amount of leachable-Fe, and reported values for *C:Fe*, *Chl-a:C* ratios are considered, Patagonian dust sources could be responsible for the sizable fraction of remotely-sensed [Chl-*a*] increases in SAO domain. Due to such large uncertainties associated with model-predicted atmospheric fluxes of bioavailable Fe and the parameters used in our offline calculations of [Chl-*a*], further research is needed to better constrain the interactions between Patagonian dust and marine biota in the Fe-limited regions of the SAO.

## **Acknowledgements**

This research was supported by the National Science Foundation through the grant ATM-0826117 and the North Carolina Space Graduate Research Fellowship. Matthew Johnson also acknowledges the opportunity to participate in the Graduate Student Summer Program in Earth System Science at the NASA Goddard Space Flight Center. The authors would like to thank Dr. Yongxiang Hu of the NASA Langley Research Center for his help with the processing and application of CALIPSO data. Thanks are due to Daniel Jacob and the Harvard University Atmospheric Chemistry Modeling Group for providing the base model GEOS-Chem used during our research. We also thank two anonymous reviewers for their thoughtful comments.

## References

- Alexander, B., Savarino, J., Lee, C. C. W., Park, R. J., Jacob, D. J., Thiemens, M. H., Li, Q. B., and Yantosca, R. M.: Sulfate formation in sea-salt aerosols: Constraints from oxygen isotopes, *J. Geophys. Res.*, 110, D10307, 2005.
- Blain, S., Queguiner, B., Armand, L., Sauveur, B., Bombled, B., Bopp, L., Bowie, A., Brunet, C., Brussaard, C., Carlotti, F., Christaki, U., Corbiere, A., Durand, I., Ebersbach, F., Fuda, J., Garcia, N., Gerringa, L., Griffiths, B., Guigue, C., Guillerm, C., Jacquet, S., Jeandel, C., Laan, P., Lefevre, D., Monaco, C. L., Malits, A., Mosseri, J., Obernosterer, I., Park, Y., Picheral, M., Pondaven, P., Remenyi, T., Sandroni, V., Sarthou, G., Savoye, N., Scouarnec, L., Souhaut, M., Thuiller, D., Timmermans, K., Trull, T., Uitz, J., van Beek, P., Veldhuis, M., Vincent, D., Viollier, E., Vong, L., and Wagener, T.: Effect of natural iron fertilization on carbon sequestration in the Southern Ocean, *Nature*, 446, doi:10.1038/nature05700, 1070-1074, 2007.
- Blain, S., Sarthou, G., and Laan, P.: Distribution of dissolved iron during the natural iron fertilisation experiment KEOPS (Kerguelen Island, Southern Ocean), *Deep-Sea Res. Pt. II*, 55, 594-605, 2008.
- Bey, I., Jacob, D. J., Yantosca, R. M., Logan, J. A., Field, B., Fiore, A. M., Li, Q., Liu, H., Mickley, L. J., and Schultz, M.: Global modeling of tropospheric chemistry with assimilated meteorology: Model description and evaluation, *J. Geophys. Res.*, 106(D19), 23073-23095, 2001.
- Bory, A., Wolff, E., Mulvaney, R., Jagoutz, E., Wegner, A., Ruth, U., and Elderfield, H.: Multiple sources supply eolian mineral dust to the Atlantic sector of coastal Antarctica: Evidence from recent snow layers at the top of Berkner Island ice sheet, *Earth Planet. Sc. Lett.*, 291, 138-148, 2010.
- Boyd, P. W. and Mackie, D.: Comment on "The Southern Ocean Biological Response to Aeolian Iron Deposition", *Science*, 319, 159a, 2008.
- Boyd, P. W., Watson, A. J., Law, C. S., Abraham, E. R., Trull, T., Murdoch, R., Bakker, D. C. E., Bowie, A. R., Buesseler, K. O., Chang, H., Charette, M., Croot, P., Downing, K., Frew, R., Gall, M., Hadfield, M., Hall, J., Harvey, M., Jameson, G., LaRoche, J., Liddicoat, M., Ling, R., Maldonado, M. T., McKay, R. M., Nodder, S., Pickmere, S., Pridmore, R., Rintoul, S., Safi, K., Sutton, P., Strzepek, R., Tanneberger, K., Turner, S., Waite, A., and Zeldis, J.: A mesoscale phytoplankton bloom in the polar Southern Ocean stimulated by iron fertilization, *Nature*, 407, 695-702, 2000.

- Boyd, P. W., Law, C. S., Wong, C. S., Nojiri, Y., Tsuda, A., Levasseur, M., Takeda, S., Rivkin, R., Harrison, P. J., Strzepek, R., Gower, J., McKay, R. M., Abraham, E., Arychuk, M., Barwell-Clarke, J., Crawford, W., Crawford, D., Hale, M., Harada, K., Johnson, K., Kiyosawa, H., Kudo, I., Marchetti, A., Miller, W., Needoba, J., Nishioka, J., Ogawa, H., Page, J., Robert, M., Saito, H., Sastri, A., Sherry, N., Soutar, T., Sutherland, N., Taira, Y., Whitney, F., Wong, S-K. E., and Yoshimura, T.: The decline and fate of an iron-induced subarctic phytoplankton bloom, *Nature*, 428, 549-553, 2004.
- Boyd, P. W., Jickells, T., Law, C. S., Blain, S., Boyle, E. A., Buesseler, K. O., Coale, K. H., Cullen, J. J., de Baar, H. J. W., Follows, M., Harvey, M., Lancelot, C., Levasseur, M., Owens, N. P. J., Pollard, R., Rivkin, R. B., Sarmiento, J., Schoemann, V., Smetacek, V., Takeda, S., Tsuda, A., Turner, S., and Watson, A. J.: Mesoscale iron enrichment experiments 1993-2005: Synthesis and future directions, *Science*, 315, 612-617, 2007.
- Boyd, P. W., Mackie, D. S., and Hunter, K. A.: Aerosol iron deposition to the surface ocean: Modes of iron supply and biological responses, *Mar. Chem.*, 120, 128-143, doi:10.1016/j.marchem.2009.01.008, 2010.
- Buesseler, K. O., Andrews, J. E., Pike, S. M., and Charette, M. A.: The effects of iron fertilization on carbon sequestration in the Southern Ocean, *Science*, 30, 414-417, 2004.
- Buesseler, K. O., Doney, S. C., Karl, D. M., Boyd, P. W., Caldeira, K., Chai, F., Coale, K. H., de Baar, H. J. W., Falkowski, P. G., Johnson, K. S., Lampitt, R. S., Michaels, A. F., Naqvi, S. W. A., Smetacek, V., Takeda, S., and Watson, A. J.: Ocean Iron Fertilization-Moving Forward in a Sea of Uncertainty, *Science*, 319, 162, 2008.
- Cassar, N., Bender, M. L., Barnett, B. A., Fan, S., Moxim, W. J., Levy, H. L., and Tilbrook, B.: The Southern Ocean Biological Response to Aeolian Iron Deposition, *Science*, 317, 1067-1070, 2007.
- Chin, M., Chu, A., Levy, R., Remer, L., Kaufman, Y., Holben, B., Eck, T., Ginoux, P., and Gao, O.: Aerosol distribution in the Northern Hemisphere during ACE-Asia: Results from global model, satellite observations, and Sunphotometer measurements, *J. Geophys. Res.*, 109, D23S90, doi:10.1029/2004JD004829, 2004.
- Claustre, H., Morel, A., Hooker, S. B., Babin, M., Antoine, D., Oubelkheir, K., Bricaud, A., Leblanc, K., Queguiner, B., and Maritorena, S.: Is desert dust making oligotrophic waters greener?, *Geophys. Res. Lett.*, 29(10), 1469, doi:10.1029/2001GL014056, 2002.
- Cloern, J. E., Grenz, C., and Videgar-Lucas, L.: An Empirical Model of the Phytoplankton Chlorophyll: Carbon Ratio-the Conversion factor Between Productivity and Growth Rate, *Limnol. Oceanogr.*, 40, 1313-1321, 1995.

- de Baar, H. J. W., de Jong, J. T. M., Bakker, D. C. E., Bettina, M. L., Cornelis, V., Bathmann, U., and Smetacek, V.: Importance of iron for plankton blooms and carbon dioxide drawdown in the Southern Ocean, *Nature*, 373, 412-415, 1995.
- de Baar, H. J. W., Gerringa, L. J. A., Laan, P., and Timmermans, K. R.: Efficiency of carbon removal per added iron in ocean iron fertilization, *Mar. Ecol-Prog. Ser.*, 364, 269-282, 2008.
- de Boyer Montégut, C., Madec, G., Fischer, A. S., Lazar, A., and Iudicone, D.: Mixed layer depth over the global ocean: An examination of profile data and a profile-based climatology, *J. Geophys. Res.*, 109, C12003, doi:10.1029/2004JC002378, 2004.
- Delmonte, B., Petit, J. R., Andersen, K. K., Basile-Doelsch, I., Maggi, V., and Lipenkov, V. Y.: Dust size evidence for opposite regional atmospheric circulation changes over east Antarctica during the last climatic transition, *Clim. Dynam.*, 23, 427-438, 2004.
- Denman, K. L.: Climate change, ocean processes and ocean iron fertilization, *Mar. Ecol-Prog. Ser.*, 364, doi:10.3354/meps07542, 2008.
- Dogliotti, A. I., Schloss, I. R., Almandoz, G. O., and Gagliardini, D. A.: Evaluation of SeaWiFS and MODIS chlorophyll-*a* products in the Argentinean Patagonian Continental Shelf (38°S-55°S), *Int. J. Remote Sens.*, 1, 251-273, 2009.
- Duce, R. A. and Tindale, N. W.: Atmospheric transport of iron and its deposition in the ocean, *Limnol. Oceanogr.*, 36, 1715-1726, 1991.
- Erickson, D. J., Hernandez, J. L., Ginoux, P., Gregg, W. W., McClain, C., and Christian, J.: Atmospheric iron delivery and surface ocean biological activity in the Southern Ocean and Patagonian region, *Geophys. Res. Lett.*, 30(12), doi:10.1029/2003GL017241, 2003.
- Evans, M. J. and Jacob, D. J.: Impact of new laboratory studies of N<sub>2</sub>O<sub>5</sub> hydrolysis on global model budgets of tropospheric nitrogen oxides, ozone, and OH, *Geophys. Res. Lett.*, 32, L09813, doi:10.1029/2005GL022469, 2005.
- Fairlie, T. D., Jacob, D. J., and Rokjin, R. J.: The impact of transpacific transport of mineral dust in the United States, *Atmos. Environ.*, 41, 1251-1266, 2007.
- Fung, I. Y., Meyn, S. K., Tegen, I., Doney, S. C., John, J. G., and Bishop, J. K. B.: Iron supply and demand in the upper ocean, *Global Biogeochem. Cy.*, 14, 281-295, 2000.
- Gabric, A. J., Cropp, R., Ayers, G. P., McTainsh, G., and Braddock, R.: Coupling between cycles of phytoplankton biomass and aerosol optical depth as derived from SeaWiFS time

- series in the Subantarctic Southern Ocean, *Geophys. Res. Lett.*, 29(7), 1112, doi:10.1029/2001GL013545, 2002.
- Gallegos, C. L. and Vant, W. N.: An incubation procedure for estimating carbon-to-chlorophyll ratios and growth-irradiance relationships of estuarine phytoplankton, *Mar. Ecol-Prog. Ser.*, 138, 275-291, 1996.
- Gassó, S. and Stein, A. F.: Does dust from Patagonia reach the sub-Antarctic Atlantic Ocean?, *Geophys. Res. Lett.*, 34, L01801, doi:10.1029/2006GL027693, 2007.
- Gassó, S., Stein, A. F., Marino, F., Castellano, E, Udisti, R., and Ceratto, J.: A combined observational and modeling approach to study modern dust transport from the Patagonia desert to East Antarctica, *Atmos. Chem. Phys.*, in press, 2010.
- Geist, H. J. and Lambin, E. F.: Dynamic Causal Patterns of Desertification, *Bioscience*, 54(9), 817-829, 2004.
- Ginoux, P., Chin, M., Tegen, I., Prospero, J. M., Holben, B., Dubovik, O., and Lin, S.-J.: Sources and distributions of dust aerosols simulated with the GOCART model, *J. Geophys. Res.*, 106, 20255-20273, 2001.
- Gregg, W. W. and Casey, N. W.: Global and regional evaluation of the SeaWiFS chlorophyll data set, *Remote Sens. Environ.*, 93, 463-479, 2004.
- Heald, C. L., Jacob, D. J., Jones, D. B. A., Palmer, P. I., Logan, J. A., Streets, D. G., Sachse, G. W., Gille, J. C., Hoffman, R. N., and Nehr Korn, T.: Comparative inverse analysis of satellite (MOPITT) and aircraft (TRACE-P) observations to estimate Asian sources of carbon monoxide, *J. Geophys. Res.*, 109, D23306, doi:10.1029/2004JD005185, 2004.
- Hutchins, D. A., Witter, A. E., Butler, A., and Luther, G. W.: Competition among marine phytoplankton for different chelated iron species, *Nature*, 400, 858-861, 1999.
- Ito, A. and Kawamiya, M.: Potential impact of ocean ecosystem changes due to global warming on marine organic carbon aerosols, *Global Biogeochem. Cy.*, 24, GB1012, doi:10.1029/2009GB003559, 2010.
- Jickells, T. D., An, Z. S., Andersen, K. K., Baker, A. R., Bergametti, G., Brooks, N., Cao, J. J., Boyd, P. W., Duce, R. A., Hunter, K. A., Kawahata, H., Kubilay, N., LaRoche, J., Liss, P. S., Mahowald, N., Prospero, J. M., Ridgwell, A. J., Tegen, I., and Torres, R.: Global Iron Connections Between Desert Dust, Ocean Biogeochemistry, and Climate, *Science*, 308, 67-71, 2005.

- Jin, X., Gruber, N., Frenzel, H., Doney, S. C., and McWilliams, J. C.: The impact on atmospheric CO<sub>2</sub> of iron fertilization induced changes in the ocean's biological pump, *Biogeosciences*, 5, 385-406, 2008.
- Johnson, M. S., Meskhidze, N., Solmon, F., Gassó, S., Chuang, P. Y., Gaiero, D. M., Yantosca, R. M., Wu, S., Wang, Y., and Carouge, C.: Modeling dust and soluble iron deposition to the South Atlantic Ocean, *J. Geophys. Res.*, 115, D15202, doi:10.1029/2009JD013311, 2010.
- Kaufman, Y. J., Tanré, D., Remer, L. A., Vermote, E., Chu, A., and Holben, B. N.: Operational remote sensing of tropospheric aerosol over land from EOS Moderate Resolution Imaging Spectroradiometer, *J. Geophys. Res.*, 102, 17051-17067, 1997.
- Korb, R. E., Whitehouse, M. J., and Ward, P.: SeaWiFS in the southern ocean: spatial and temporal variability in phytoplankton biomass around South Georgia, *Deep-Sea Res. Pt. II*, 51, 99-116, 2004.
- Krinner, G. and Genthon, C.: Tropospheric transport of continental tracers towards Antarctica under varying climatic conditions, *Tellus*, 53, 54-70, 2003.
- Krinner, G., Petit, J. R., and Delmonte, B.: Altitude of atmospheric tracer transport towards Antarctica in present and glacial climate, *Quaternary Sci. Rev.*, 29, 274-284, 2010.
- Lambert, F., Delmonte, B., Petit, J. R., Bigler, M., Kaufmann, P. R., Hutterli, M. A., Stocker, T. F., Ruth, U., Steffensen, J. P., and Maggi, V.: Dust-climate coupling over the past 800,000 years from the EPICA Dome C ice core, *Nature*, 452, doi:10.1038/nature06763, 2008.
- Lancelot, C., de Montety, A., Goosse, H., Becquevort, S., Schoemann, V., Pasquer, B., and Vancoppenolle, M.: Spatial distribution of the iron supply to phytoplankton in the Southern Ocean: a model study, *Biogeosciences*, 6, 2861-2878, 2009.
- Li, F., Ginoux, P., and Ramaswamy, V.: Distribution, transport, and deposition of mineral dust in the Southern Ocean and Antarctica: Contribution of major sources, *J. Geophys. Res.*, 113, doi:10.1029/2007JD009190, 2008.
- Li, F., Ginoux, P., and Ramaswamy, V.: Transport of Patagonian Dust to Antarctica, *J. Geophys. Res.*, doi:10.1029/2009JD012356, in press.
- Liang, Q., Jaegle, L., and Wallace, J. M.: Meteorological indices for Asian outflow and transpacific transport on daily to interannual timescales, *J. Geophys. Res.*, 110, doi:10.1029/2005JD005788, 2005.

- Liu, Z., Vaughan, M., Winker, D., Kittaka, C., Getzewich, B., Kuehn, R., Omar, A., Powell, K., Trepte, C., and Hostetler, C.: The CALIPSO Lidar Cloud and Aerosol Discrimination: Version 2 Algorithm and Initial Assessment of Performance, *J. Atmos. Ocean. Tech.*, 26, 1198-1213, doi:10.1175/2009JTECHA1229.1, 2009.
- Löscher, B. M., de Baar, H. J. W., de Jong, J. T. M., Veth, C., and Dehairs, F.: The distribution of Fe in the Antarctic circumpolar current, *Deep-Sea Res. Pt. II: Tropical Studies in Oceanography*, 44, 143-187, 1997.
- Mackie, D. S., Boyd, P. W., McTainsh, G. H., Tindale, N. W., Westberry, T. K., and Hunter, K. A.: Biogeochemistry of iron in Australian dust: From eolian uplift to marine uptake, *Geochem. Geophys. Geosys.*, 9, Q03Q08, doi:10.1029/2007GC001813, 2008.
- Martin, J. H. and Fitzwater, S. E.: Iron-deficiency limits phytoplankton growth in the northeast pacific subarctic, *Nature*, 331, 341-343, 1988.
- Martin, J. H. and Gordon, R. M.: Northeast Pacific iron distributions in relation to phytoplankton productivity, *Deep-Sea Res.*, 35, 177-196, 1988.
- Martin, J. H.: Glacial-interglacial CO<sub>2</sub> change: The Iron Hypothesis, *Paleoceanography*, 5, 1-13 1990.
- McConnell, J. R., Aristarain, A. J., Banta, J. R., Edwards, P. R., and Simões, J. C.: 20<sup>th</sup>-Century doubling in dust archived in an Antarctic Peninsula ice core parallels climate change and desertification in South America, *P. Natl. Acad. Sci.*, 104(14), 5743-5748, 2007.
- Meredith, M. P., and C. W. Hughes (2005), On the sampling timescale required to reliably monitor interannual variability in the Antarctic circumpolar transport, *Geophys. Res. Lett.*, 32, L03609, doi:10.1029/2004GL022086.
- Meredith, M. P., Watkins, J. L., Murphy, E. J., Cunningham, N. J., Wood, A. G., Korb, R., Whitehouse, M. J., Thorpe, S. E., and Vivier, F.: An anticyclonic circulation above the Northwest Georgia Rise, Southern Ocean, *Geophys. Res. Lett.*, 30(20), 2061, doi:10.1029/2003GL018039, 2003.
- Meskhidze, N., Chameides, W. L., Nenes, A., and Chen, G.: Iron mobilization in mineral dust: Can anthropogenic SO<sub>2</sub> emissions affect ocean productivity?, *Geophys. Res. Lett.*, 30(21), 2085, doi:10.1029/2003GL018035, 2003.
- Meskhidze, N., Chameides, W. L., and Nenes, A.: Dust and pollution: A recipe for enhanced ocean fertilization?, *J. Geophys. Res.*, 110, D03301, doi:10.1029/2004JD005082, 2005.

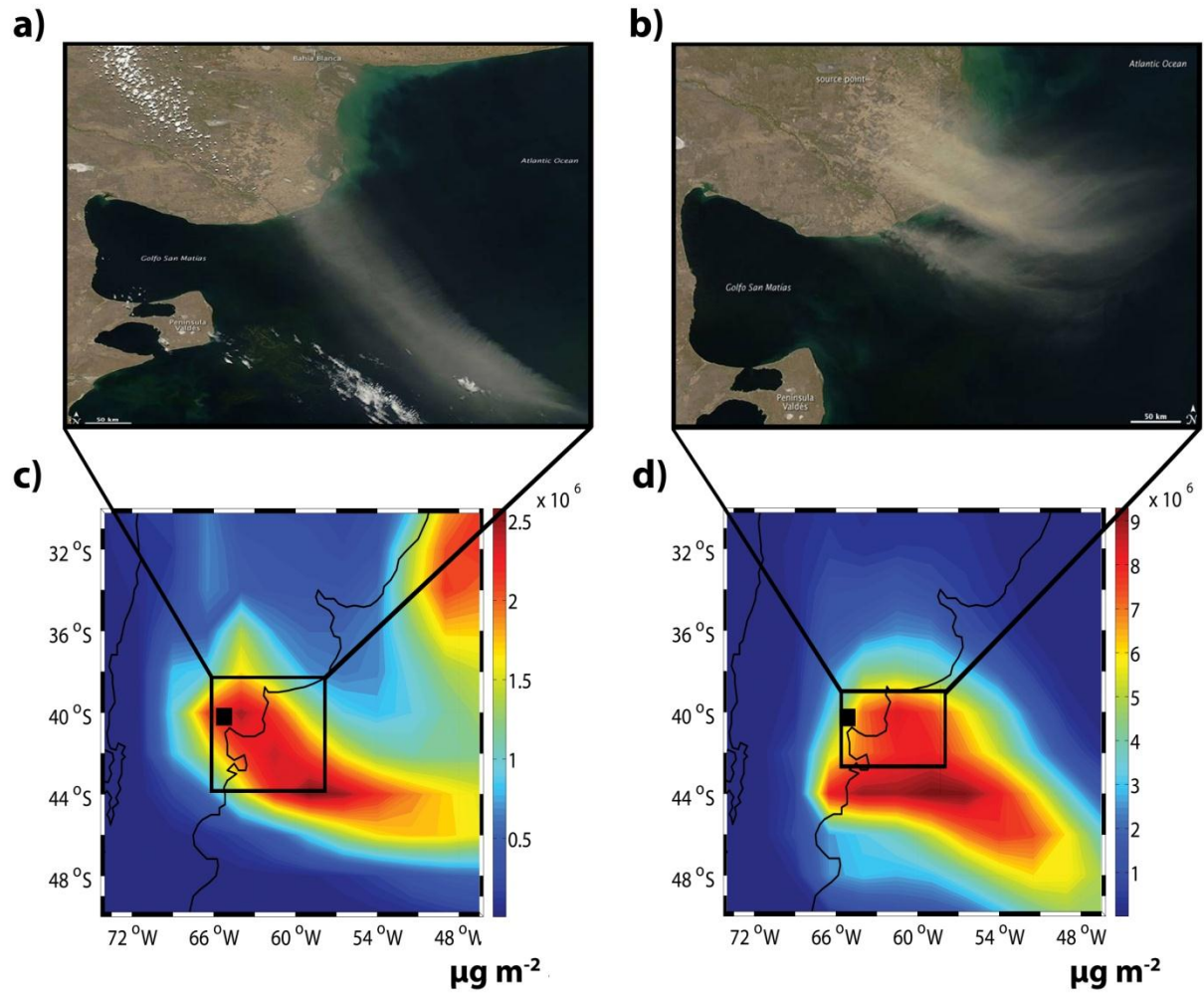
- Meskhidze, N., Nenes, A., Chameides, W. L., Luo, C., and Mahowald, N.: Atlantic Southern Ocean productivity: Fertilization from above or below?, *Global Biogeochem. Cy.*, 21, GB2006, doi:10.1029/2006GB002711, 2007.
- Moore, J. K. and Abbott, M. R.: Phytoplankton chlorophyll distributions and primary production in the Southern Ocean, *J. Geophys. Res.*, 105, 28,709-28,722, 2000.
- Omar, A., Winker, D. M., Kittaka, C., Vaughan, M. A., Liu, Z., Hu, Y., Trepte, C. R., Rogers, R. R., Ferrare, R. A., Lee, K., Kuehn, R. E., and Hostetler, C. A.: "The CALIPSO Automated Aerosol Classification and Lidar Ratio Selection Algorithm", *J. Atmos. Ocean. Tech.*, **26**, 1994-2014, doi:10.1175/2009JTECHA1231.1, 2009.
- O'Reilly, J. E., Maritorena, S., Mitchell, B. G., Siegel, D. A., Carder, K. L., Garver, S. A., Kahru, M., and McClain, C.: Ocean color chlorophyll algorithms for SeaWiFS, *J. Geophys. Res.*, 103(C11), 24937-24953, doi:10.1029/98JC02160, 1988.
- Park, J., Oh, I., Kim, H., and Yoo S.: Variability of SeaWiFS chlorophyll-a in the southwest Atlantic sector of the Southern Ocean: Strong topographic effects and weak seasonality, *Deep-Sea Res. Pt. I*, 57, 604-620, 2010.
- Park, R. J., Jacob, D. J., Field, B. D., Yantosca, R. M., and Chin, M.: Natural and transboundary pollution influences on sulfate-nitrate-ammonium aerosols in the United States: implications for policy, *J. Geophys. Res.*, 109, doi:10.1029/2003JD004473, 2004.
- Petit, J. R., Jouzel, J., Raynaud, D., Barkov, N. I., Barnola, J-M., Basile, I., Bender, M., Chappellaz, J., Davis, M., Delaygue, G., Delmotte, M., Kotlyakov, V. M., Legrand, M., Lipenkov, V. Y., Lorius, C., Pepin, L., Ritz, C., Saltzman, E., and Stievenard, M.: Climate and atmospheric history of the past 420,000 years from the Vostok ice core, Antarctica, *Nature*, 399, 429-436, 1999.
- Prospero, J. M., Ginoux, P., Torres, O., and Nicholson, S. E.: Environmental characterization of global sources of atmospheric soil dust identified with the Nimbus 7 Total Ozone Mapping Spectrometer (TOMS) absorbing aerosol product, *Rev. Geophys.*, 40(3), 1002, doi:10.1029/2000RG000095, 2002.
- Raiswell, R., Benning, L. G., Tranter, M., and Tulaczyk, S.: Bioavailable Iron in the Southern Ocean: The significance of the iceberg conveyor belt, *Geochem. T.*, 9, doi:10.1186/1467-4866-9-7, 2008.
- Remer, L. A., Kaufman, Y. J., Mattoo, S., Martins, J. V., Ichoku, C., Levy, R. C., Kleidman, R. G., Tanré, D., Chu, D. A., Li, R. R., Eck, T. F., Vermote, E., and Holben, B. N.: The MODIS algorithm, products and validation, *J. Atmos. Sci.*, 62, 947-973, doi:10.1175/JAS3385.1, 2005.

- Romero, S. I., Piola, A. R., Charo, M., and Garcia, C. A. E.: Chlorophyll-*a* variability off Patagonia based on SeaWiFS data, *J. Geophys. Res.*, 111, C05021, doi:10.1029/2005JC003244, 2006.
- Sarmiento, J. L., Gruber, N., Brzezinski, M. A., and Dunne, J. P.: High-latitude controls of thermocline nutrients and low latitude biological productivity, *Nature*, 427, 56-60, 2004.
- Sarthou, G., Timmermans, K. R., Blain, S., and Treguer, P.: Growth physiology and fate of diatoms in the ocean: a review, *J. Sea Res.*, 53, 25-42, 2005.
- Solmon, F., Chuang, P. Y., Meskhidze, N., and Chen, Y.: Acidic processing of mineral dust iron by anthropogenic compounds over the north Pacific Ocean, *J. Geophys. Res.*, 114, D02305, doi:10.1029/2008JD010417, 2009.
- Strong, A., Chisholm, S., Miller, C., and Cullen, J.: Ocean fertilization: time to move on, *Nature*, 461(17), 347-348, 2009.
- Tanré, D., Kaufman, Y. J., Herman, M., and Mattoo, S.: Remote sensing of aerosol properties over oceans using the MODIS/EOS spectral radiances, *J. Geophys. Res.*, 102(D14), 16971-16988, 1997.
- Tsuda, A. S., Takeda, S., Saito, H., Nishioka, J., Nojiri, Y., Kudo, I., Kiyosawa, H., Shiimoto, A., Imai, K., Ono, T., Shimamoto, A., Tsumune, D., Yoshimura, T., Aono, T., Hinuma, A., Kinugasa, M., Suzuki, K., Sohrin, Y., Noiri, Y., Tani, H., Deguchi, Y., Tsurushima, N., Ogawa, H., Fukami, K., Kuma, K., and Saino, T.: A mesoscale iron enrichment in the western Subarctic Pacific induces a large centric diatom bloom, *Science*, 300, 958-961, 2003.
- Twining, B. S., Baines, S. B., Fisher, N. S., and Landry, M. R.: Cellular iron contents of plankton during the Southern Ocean Iron Experiment (SOFeX), *Deep-Sea Research I*, 51, 1827-1850, 2004.
- Vaughan, M., Young, S., Winker, D., Powell, K., Omar, A., Liu, Z., Hu, Y., and Hostetler, C.: Fully automated analysis of space-based lidar data: an overview of the CALIPSO retrieval algorithms and data products, *Bba. Lib.*, 5575, doi:10.1117/12.572024, 2004.
- Wagener, T., Guieu, C., Losno, R., Bonnet, S., and Mahowald, N.: Revisiting atmospheric dust export to the Southern Hemisphere ocean: Biogeochemical implications, *Global Biogeochem. Cy.*, 22, GB2006, doi:10.1029/2007GB002984, 2008.
- Watson, A. J., Bakker, D. C. E., Ridgwell, A. J., Boyd, P. W., and Law, C. S.: Effect of iron supply on Southern Ocean CO<sub>2</sub> uptake and implications for glacial atmospheric CO<sub>2</sub>, *Nature*, 407, 730-733, 2000.

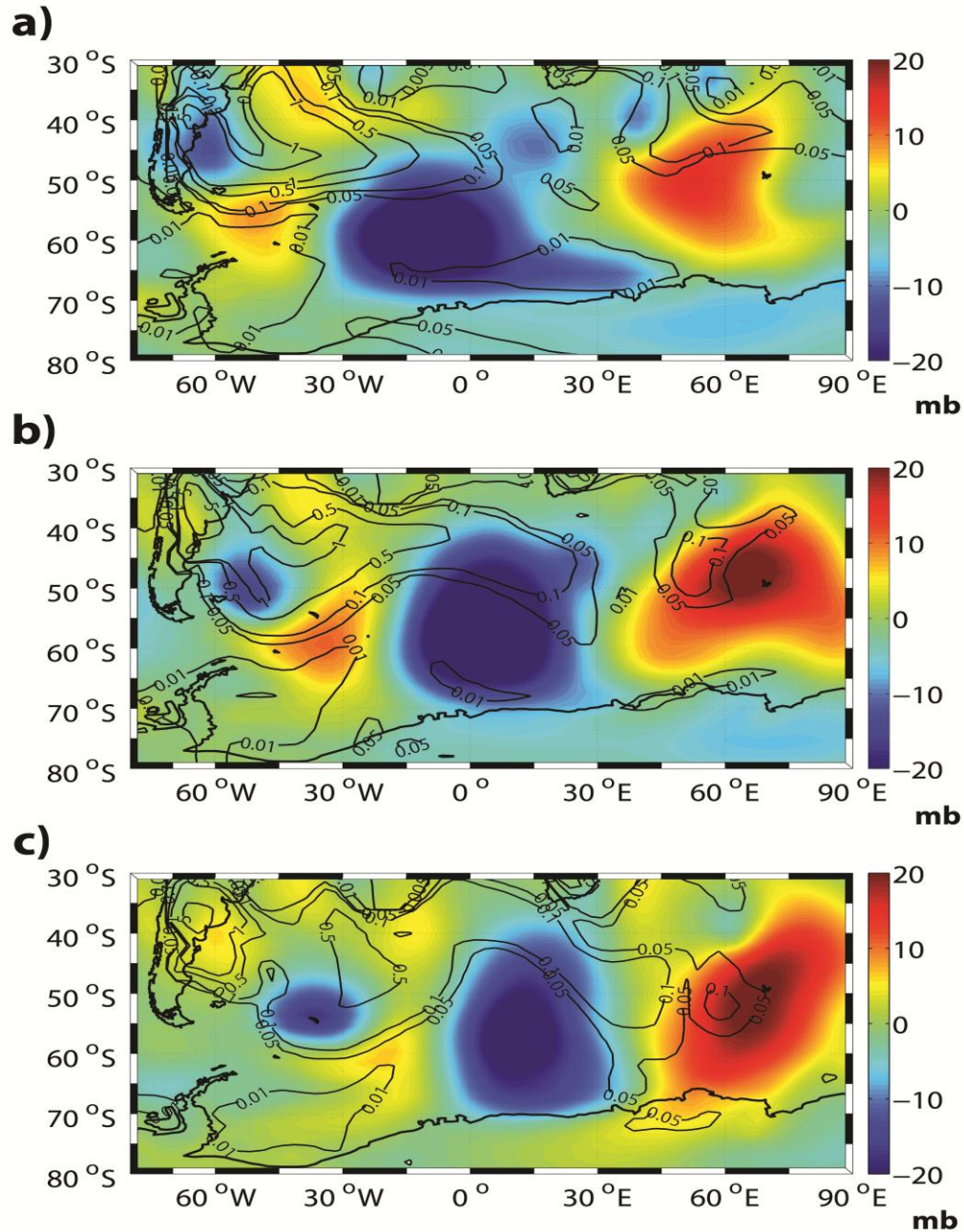
- Yang, Y. Q., Hou, Q., Zhou, C. H., Liu, H. L., Wang, Y. Q., and Niu, T.: Sand/dust storms over Northeast Asia associated large-scale circulations in spring 2006, *Atmos. Chem. Phys. Discuss.*, 7, 9259-9281, 2007.
- Young, S., and Vaughan, M.: The retrieval of profiles of particulate extinction from Cloud Aerosol Lidar Infrared Pathfinder Satellite Observation (CALIPSO) data: Algorithm description. *J. Atmos. Oceanic Technol.*, 26, 1105-1119, 2009.
- Yu, H., Chin, M., Winker, D. M., Omar, A. H., Liu, Z., Kittaka, C., and Diehl, T.: Global view of aerosol vertical distributions from CALIPSO lidar measurements and GOCART simulations: Regional and seasonal variations, *J. Geophys. Res.*, 115, D00H30, doi:10.1029/2009JD013364, 2010.
- Zender, C. S., Newmann, D., and Torres, O.: Spatial heterogeneity in aeolian erodibility: Uniform, topographic, geomorphic, and hydrologic hypotheses, *J. Geophys. Res.*, 108, doi:10.1029/2002JD003039, 2003.
- Zhuang, G., Yi, Z., Duce, R. A., and Brown, P. R.: Link between iron and sulphur cycles suggested by detection of Fe(II) in remote marine aerosols, *Nature*, 355, 537-539, 1992.

Table 4.1. Variables with corresponding values and (uncertainties) used in Eq. (2)

<i>Variable</i>	<i>Value</i>	<i>Source</i>
sol-Fe (mol m <sup>-2</sup> day <sup>-1</sup> )	GEOS-Chem/DFeS	<i>Solmon et al.</i> [2009]
C:Fe (mol mol <sup>-1</sup> )	30,000 (±24,000)	<i>de Baaret et al.</i> [2008]; <i>Sarthou et al.</i> [2005] <i>Twining et al.</i> [2004]
Chl- <i>a</i> :C (mg mg <sup>-1</sup> )	1/30 (1/15-1/100)	<i>Gallegos and Vant,</i> [1996]; <i>Cloern et al.</i> [1995]
Mixed Layer Depth (m)	climatological monthly-average	<i>de Boyer Montégut,</i> [2004]



**Figure 4.1.** *Aqua* MODIS real-time imagery at a) 18:40 UTC 23 January 2009 and b) 18:35 UTC 17 February 2009 and GEOS-Chem-predicted daily-averaged vertically-integrated dust concentration ( $\mu\text{g m}^{-2}$ ) of Patagonian dust plumes advecting off the coast of South America on c) 23 January 2009 and d) 17 February 2009, respectively. The black square indicates the location of San Antonio Oeste (40.8°S, 65.1°W).



**Figure 4.2.** GEOS-Chem-predicted daily dust burden ( $\text{g m}^{-2}$ ) (contour lines) and sea level pressure anomalies (SLPAs) (mb) over the SAO for a) 23 January, b) 24 January, and c) 25 January 2009. Cold colors indicate negative SLPA (low pressure systems) and warm colors display high pressure systems.

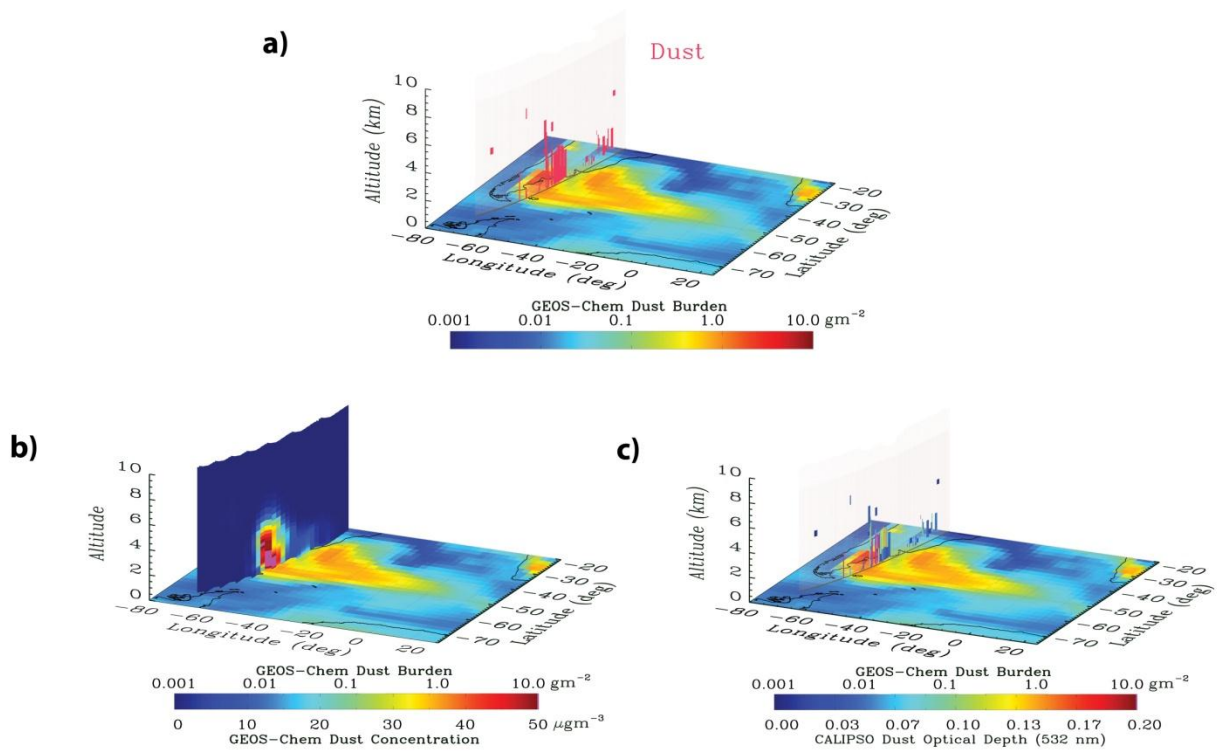


**Figure 4.3.** The GEOS-Chem-predicted dust burden ( $\text{g m}^{-2}$ ) for 23 January 2009 (the background image) with overlaid vertical swaths of a) CALIPSO retrievals of dust aerosol layers, b) model-predicted vertical cross-section of dust concentration ( $\mu\text{g m}^{-3}$ ) along the CALIPSO orbit track and c) CALIPSO dust layer AOD at 532 nm. Modeled vertical cross-section calculations are conducted along the CALIPSO orbital track beginning at 4:28:59 UTC on 23 January 2009 (V3-01.2009-01-23T04-28-59Z).

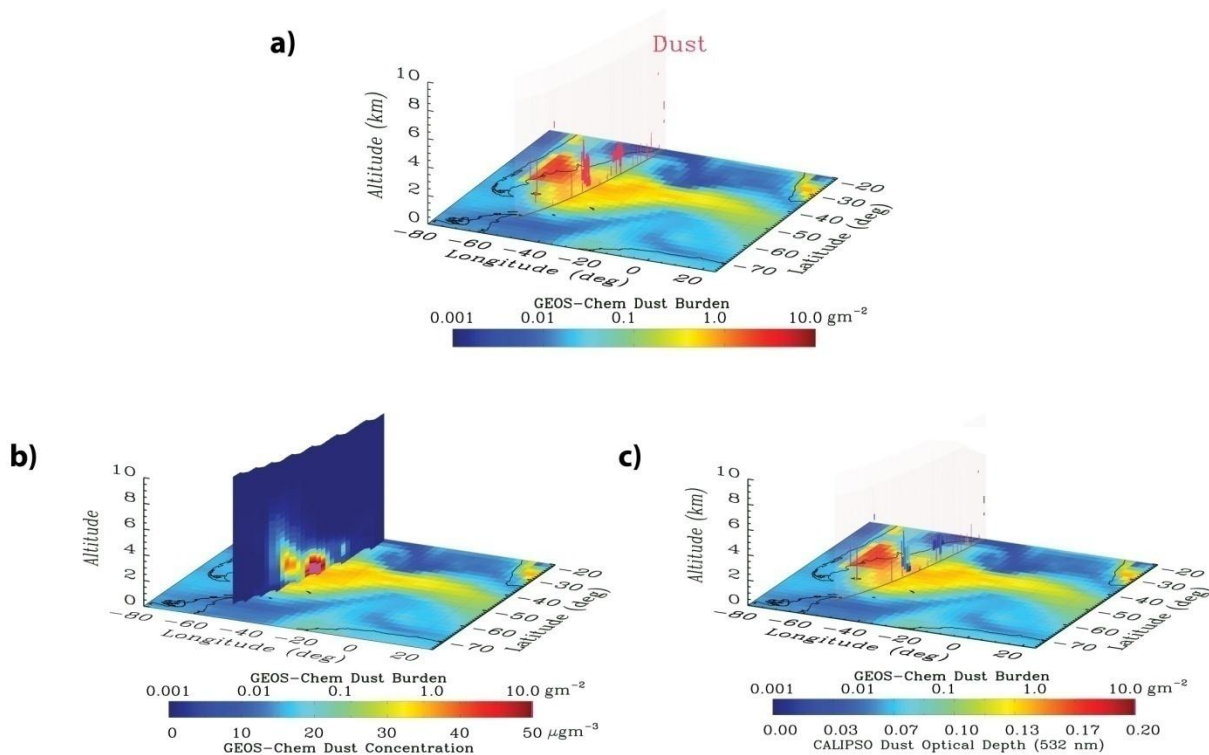


**Figure 4.4.** Same as Fig. 4.3 but for 24 January 2009 and the CALIPSO orbital track beginning at 3:33:27 UTC (V3-01.2009-01-24T03-33-27ZN).

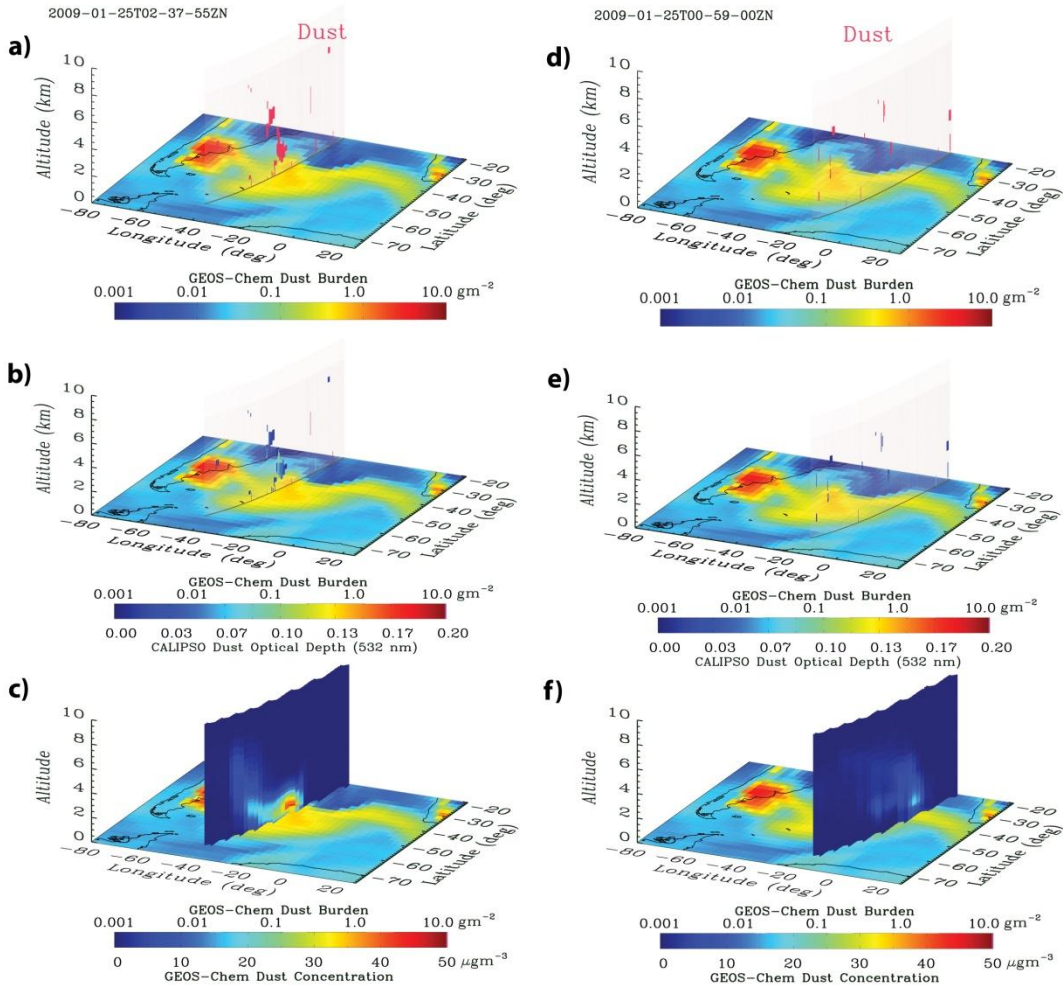


**Figure 4.5.** The background images are the GEOS-Chem-predicted dust burden ( $\text{g m}^{-2}$ ) on 25 January 2009 overlaid with vertical swaths of the CALIPSO orbital track beginning at 2:37:55 UTC (V3-01.2009-01-25T02-37-55ZN) (left column) and 0:59:00 UTC (V3-01.2009-01-25T00-59-00ZN) (right column) displaying the a), d) CALIPSO retrievals of dust aerosol layers, b), e) CALIPSO dust layer AOD at 532 nm, and c), f) model-predicted vertical cross-section of dust concentration ( $\mu\text{g m}^{-3}$ ) along the CALIPSO orbit tracks.

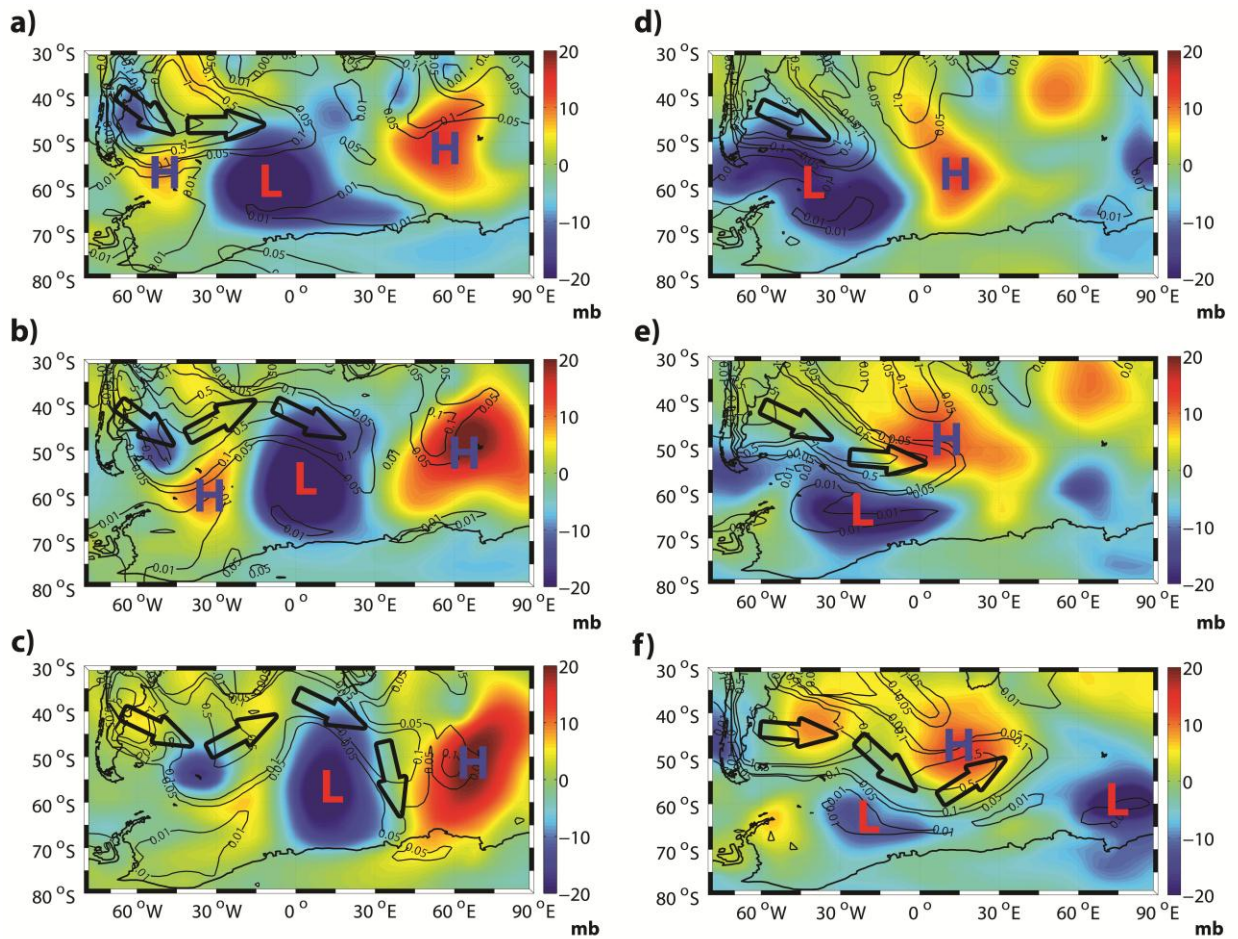


**Figure 4.6.** GEOS-Chem-predicted dust burden ( $\text{g m}^{-2}$ ) (contour lines) and sea level pressure anomalies (SLPAs) (mb) over the SAO for a-c) 23-25 January 2009 and d-f) 13-15 February 2009. Arrows are for the visual aid for the general transport pathway of Patagonian dust. Low and high pressure anomalies are shown by symbols of L and H, respectively.

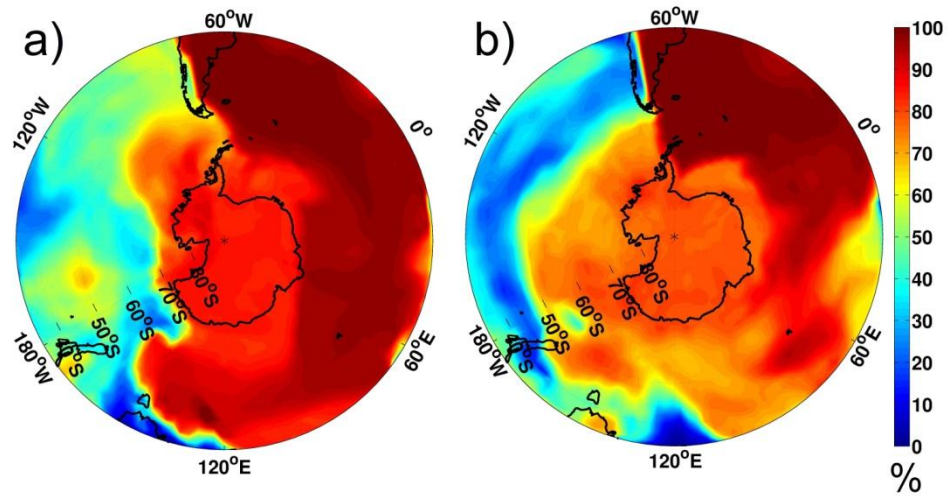


**Figure 4.7.** The 8-day averaged GEOS-Chem-predicted percent contributions of Patagonian dust sources to total mineral dust deposition in the HNLC waters of the SO for the a) J23 and b) F11 dust episodes.

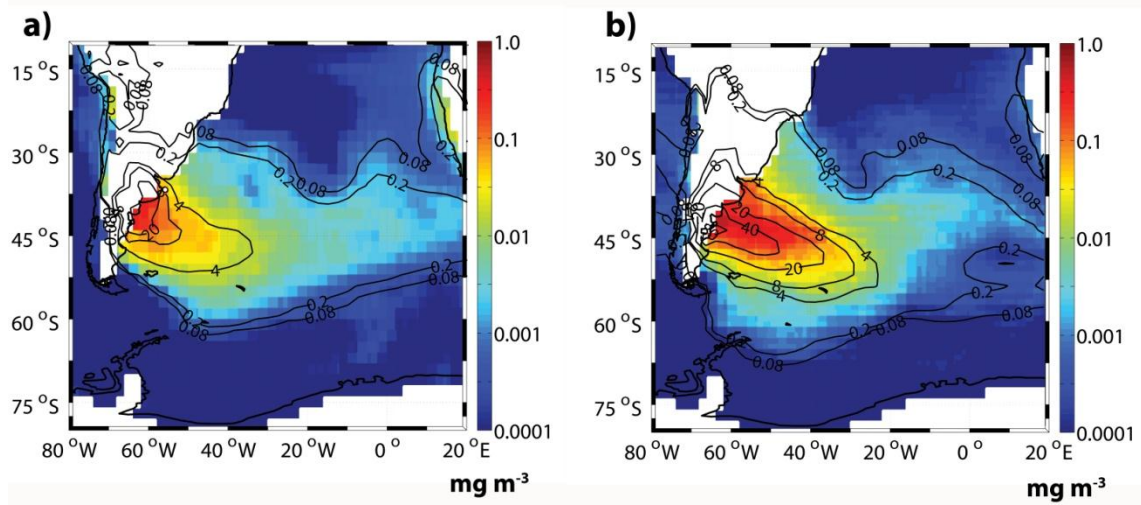


**Figure 4.8.** GEOS-Chem/DFeS-simulated total sol-Fe fluxes ( $\mu\text{g m}^{-2}$ ) (contour lines) and predicted [Chl-*a*] increases ( $\Delta[\text{Chl-}a]_{\text{pred}}$ ) ( $\text{mg m}^{-3}$ ) for the a) J23 and b) F11 dust episodes.

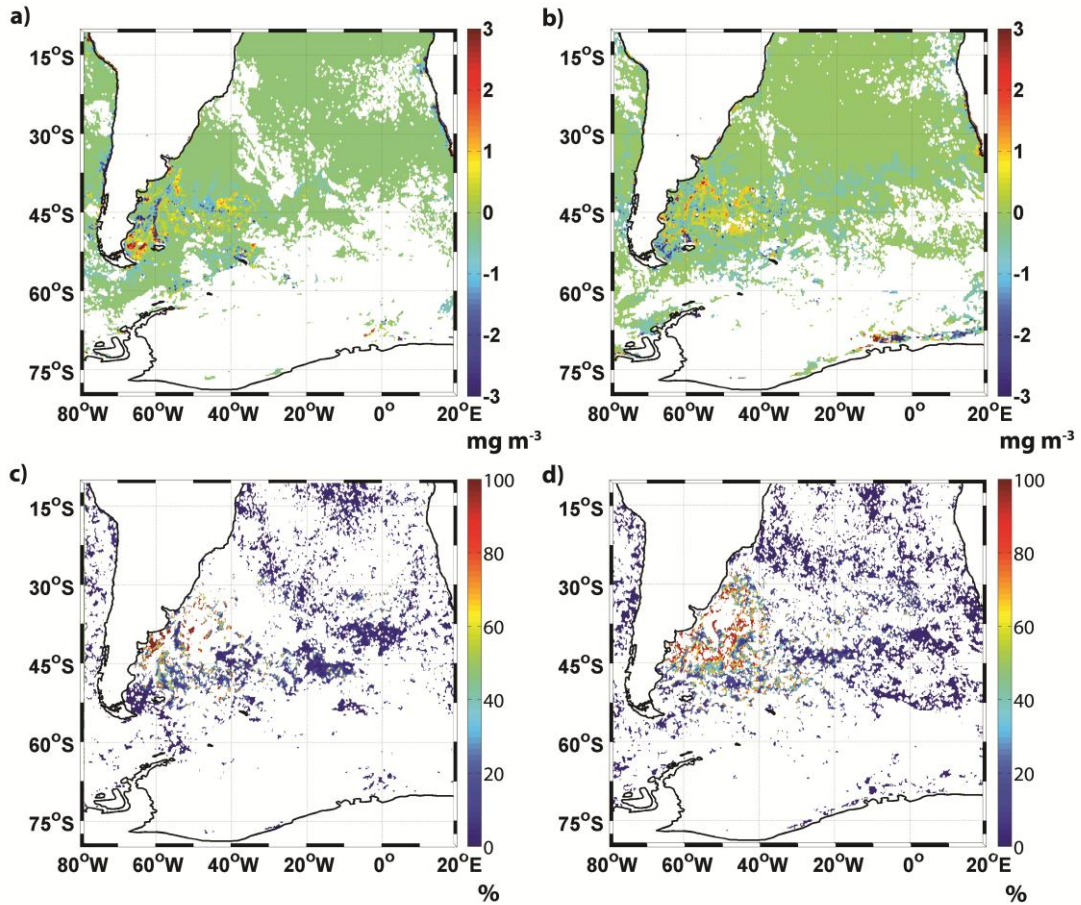


**Figure 4.9.** Differences in SeaWiFS remotely-sensed 8-day averaged [Chl-*a*] ( $\Delta[\text{Chl-}a]_{\text{obs}}$ ) ( $\text{mg m}^{-3}$ ) and the percent ratio of  $\Delta[\text{Chl-}a]_{\text{pred}}/\Delta[\text{Chl-}a]_{\text{obs}}$  for the a), c) J23 and b), d) F11 dust episodes, respectively. The  $\Delta[\text{Chl-}a]_{\text{obs}}$  for J23 and F11 episodes are calculated by subtracting 23-30 January averages from 15-22 January 2009 and 11-18 February averages from 3-10 February 2009, respectively.

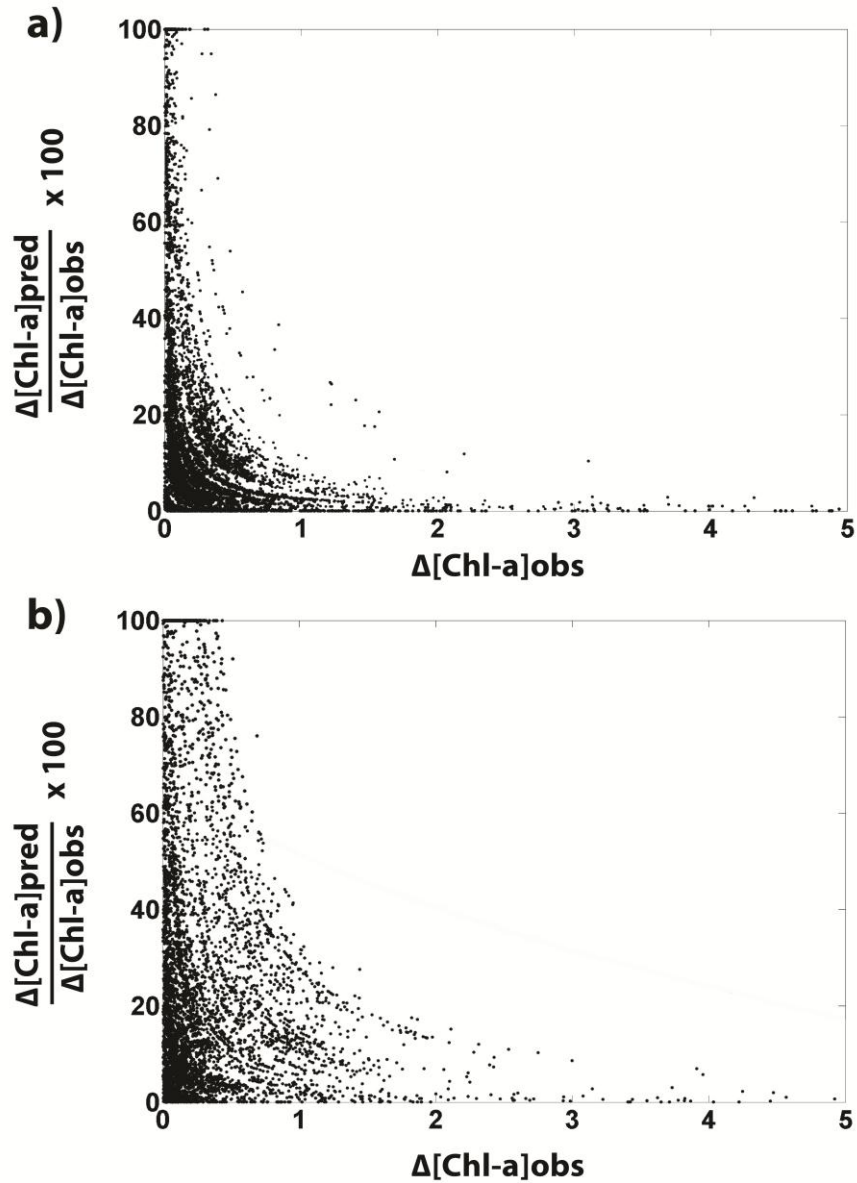


**Figure 4.10.** Percent ratio of  $\Delta[\text{Chl-}a]_{\text{pred}}/\Delta[\text{Chl-}a]_{\text{obs}}$  for the grid cells with positive values of remotely-sensed 8-day averaged [Chl-*a*] differences (after the storm minus before) for the a) J23 and b) F11 dust episodes. Black dots depict the grid cells located in the HNLC regions of the SAO.

## 5. Updated Dust-nutrient Dissolution Mechanism in GEOS-Chem

### Preface

Past studies simulating sol-Fe production within mineral dust, using the 3-D global CTM GEOS-Chem (implemented with a prognostic dust-Fe dissolution scheme), have reported varying degrees of influence that acid mobilization has on atmospheric sol-Fe concentrations. For example, in our past studies [Johnson *et al.*, 2010, 2011] it was shown that a minimal amount of bioavailable Fe is produced within Patagonian dust during atmospheric transport. This differs from the work by Solmon *et al.* [2009] which predicted that acid mobilization could produce large amounts of sol-Fe within Asian dust plumes. The majority of past modeling studies, focused on predicting Fe mobilization within mineral dust, have primarily concentrated on acidity/pH dependent dissolution processes [e.g., Meskhidze *et al.*, 2003, 2005; Cwiertny *et al.*, 2008; Solmon *et al.*, 2009]. However, on average mineral dust does not become acidic; therefore, different chemical and physical processes have been suggested to be important sources of sol-Fe production within mineral dust during atmospheric transport. For example, carboxylic acids commonly found in atmospheric waters [Kawamura and Kaplan, 1989, Zuo and Holgne, 1992] have been shown to increase Fe dissolution rates within mineral dust (ligand-promoted dissolution) [Martin, 2005; Paris *et al.*, 2011]. Additionally, in the presence of organic Fe-complexing ligands and incident solar radiation, Fe-containing mineral dust has been shown to have higher percentages of total sol-Fe in the reduced and more bioavailable Fe(II) form [Cornell and Schwertmann,

1996]. In addition to sol-Fe, mineral dust deposition is an important atmospheric source of bioavailable P and N to remote oceanic surface waters, and have been suggested to play a controlling role in marine ecosystem processes in oligotrophic nutrient depleted surface oceans outside of the global HNLC regions [*Elser et al.*, 2007; *Krishnamurthy et al.*, 2007; *Duce et al.*, 2008; *Mahowald et al.*, 2008; *Okin et al.*, 2011].

Therefore, during this chapter of my dissertation research, we use the 3-D global CTM GEOS-Chem, implemented with a prognostic dust-Fe dissolution scheme (GEOS-Chem/DFeS) [*Solmon et al.*, 2009; *Johnson et al.*, 2010, 2011], which has further been developed to take into account inorganic and organic (oxalic) acid-promoted Fe dissolution processes, photochemical redox cycling between ferric (Fe(III)) and ferrous (Fe(II)) forms of iron, dissolution of three different Fe-containing minerals (hematite, goethite and aluminosilicates), detailed mineralogy of wind-blown dust from the major desert regions, acid-based  $\text{PO}_4^{3-}$  dissolution, and  $\text{NO}_3^-$  production within mineral dust. To simulate global nutrient-laden dust transport and deposition to the surface oceans the model is run between March 2009 and February 2010. The results of this study provide, to date, the most comprehensive dataset of deposition rates of essential micronutrients, associated with mineral dust, to the global oceans.

This chapter of my dissertation is in preparation for submission to Atmospheric Chemistry and Physics Discussion (ACPD). As the figures and values presented in this work are not published please contact Matthew Johnson for finalized work.

# **Updated dust-nutrient dissolution mechanism in GEOS-Chem**

**Matthew S. Johnson and Nicholas Meskhidze**

Marine, Earth, and Atmospheric Science, North Carolina State University, Raleigh, NC,  
USA

*Correspondence to:* Nicholas Meskhidze

([nmeskhidze@ncsu.edu](mailto:nmeskhidze@ncsu.edu))

## Abstract

Many global remote oceanic regions have marine primary productivity limited by essential micronutrients which can be supplied by mineral dust deposition. During this study, mineral dust and bioavailable nutrient deposition rates are predicted for March 2009 to February 2010 using the 3-D chemistry transport model GEOS-Chem implemented with an updated dust-nutrient dissolution scheme. This comprehensive Fe-dissolution scheme simulates sol-Fe production within mineral dust taking into account inorganic and organic (oxalic) acid-promoted Fe dissolution processes, photochemical redox cycling between ferric (Fe(III)) and ferrous (Fe(II)) forms of iron, dissolution of three different Fe-containing minerals (hematite, goethite and aluminosilicates), and detailed mineralogy of wind-blown dust from the major desert regions, acid-based phosphorus/phosphate ( $\text{PO}_4^{3-}$ ) dissolution, and nitrate ( $\text{NO}_3^-$ ) formation during atmospheric transport. During the yearlong simulation, ~0.19, 0.20, and 75 Tg (1 Tg =  $10^{12}$  g) of bioavailable Fe,  $\text{PO}_4^{3-}$ , and  $\text{NO}_3^-$  was deposited to global oceanic regions, respectively. The addition of organic ligand-promoted Fe dissolution proved to be important as total annual model-predicted sol-Fe deposition to global oceanic regions increased by ~25% when compared to simulations only taking into account acid-promoted Fe dissolution. Additionally, the particular speciation of Fe-containing compounds (i.e., hematite, goethite, illite) largely influenced the magnitude of oceanic sol-Fe fluxes. Marine ecosystems with primary productivity limited by sol-Fe, such as the subarctic North Pacific and Southern Oceans, were predicted to receive biogeochemically important sol-Fe fluxes from Asian and Patagonian dust sources with seasonally-averaged deposition rates

exceeding 0.01 to 1.0  $\mu\text{g m}^{-2} \text{day}^{-1}$ . The implementation of Fe(II)/Fe(III) photochemical redox cycling in the model allows for the distinction between different oxidation states of deposited sol-Fe. Our calculations suggest that during the daytime, large fractions of sol-Fe deposited to the global oceans is likely to be in the more soluble Fe(II) form. Surface oceans limited by the essential micronutrients  $\text{PO}_4^{3-}$  and  $\text{NO}_3^-$  are simulated to be supplied with deposition rates exceeding 10 and 100  $\mu\text{g m}^{-2} \text{day}^{-1}$ , respectively. Overall, this study shows the complex and spatiotemporally variable pattern of bioavailable nutrient deposition over the oceans controlled by the mass concentration, mineralogy, the surface area of dust particles, atmospheric chemical composition, cloud processing, relative humidity, and temperature that cannot be easily replicated by the models using fixed, prescribed fractions of nutrient solubility. Specifically, our study suggests that the explicit model representations of individual processes leading to sol-Fe production within dust are needed to improve our understanding of the atmospheric Fe cycle, and quantify the effect of dust-Fe on ocean biological productivity, carbon cycle, and climate.

## 5.1. Introduction

Aeolian dust deposition has been suggested to be a critical source of the micronutrient iron (Fe) to high nitrate-low-chlorophyll (HNLC) oceanic regions where marine primary productivity can be limited by the supply of bioavailable Fe [Martin and Fitzwater, 1988; Coale et al., 1996; Boyd et al., 2000]. HNLC waters comprise ~30% of the world oceans, thus the atmospheric supply of Fe to the surface waters of these regions may play a key role in regulating biological productivity, atmospheric carbon dioxide (CO<sub>2</sub>) concentrations, and climate [Martin et al., 1990; Zhuang et al., 1992; Jickells et al., 2005]. The majority of the Fe mass found in the atmosphere is contained within mineral dust aerosols emitted from continental sources. Fe in atmospheric mineral dust particles is primarily in the form of Fe-(oxyhydr)oxides, such as hematite ( $\alpha$ -Fe<sub>2</sub>O<sub>3</sub>) and goethite ( $\alpha$ -FeO(OH)), and as ferric iron (Fe(III)) substituted into aluminosilicate minerals [Dedik and Hoffmann, 1992; Hoffmann et al., 1996; Arimoto et al., 2002]. In order for Fe, in mineral dust, to be utilized by phytoplankton (i.e., bioavailable Fe), it must be in an aqueous, colloidal, or nanoparticulate form [Raiswell and Canfield, 2012]. Although several pathways such as thermal dissolution, mobilization by organic ligands, photo- and bio-reduction may also be involved in the acquisition of Fe by marine organisms, often directly from particulate sources such as mineral dust [Kraemer, 2005; Barbeau, 2006; Rubin et al., 2011]. The objective of this study is to estimate the supply of bioavailable Fe to different regions of the global oceans through atmospheric pathways. Therefore, here we only consider soluble Fe (hereinafter referred to as sol-Fe) production within mineral dust during its atmospheric transport and do not take

into consideration marine processes leading to the formation of bioavailable Fe in the ocean.

The dissolved iron fraction (DIF) ( $\text{DIF}(\%) = \frac{\text{sol-Fe}}{\text{total Fe}} \times 100$ ) of Fe-containing minerals commonly found in freshly emitted dust particles are typically small (< 1%), however, in situ measurements suggest increased (> 10%) and spatially variable DIFs downwind from the dust source regions [e.g., *Baker and Jickells, 2006; Baker et al., 2006*]. An important goal in present day climate research is to better understand how physical and chemical processes affect the formation of sol-Fe in mineral dust during atmospheric transport from the source regions to surface ocean waters. Fe in mineral dust particles can be mobilized through three different mechanisms: proton-promoted, ligand-promoted, and reductive dissolution [*Schwertmann, 1991*]. Fe dissolution in acidic (low pH) environments commonly occurs due to high proton concentrations destabilizing Fe-oxygen bonds in the crystal lattice of Fe-(oxyhydr)oxides and aluminosilicates [*Wiederhold et al., 2006; Journet et al., 2008*]. During ligand-promoted Fe dissolution, Fe in the crystal lattice structuring is complexed by organic ligand molecules and can be more readily detached in atmospheric and oceanic waters resulting in a soluble form of Fe(III) [*Wiederhold et al., 2006*]. The third process is known as reductive dissolution which involves an electron transfer to Fe(III) resulting in ferrous iron (Fe(II)) formation, which is readily released into solution [*Larsen and Postma, 2001; Fu et al., 2010*].

Past studies focused on predicting Fe mobilization within mineral dust have primarily concentrated on acidity/pH dependent dissolution processes [e.g., *Meskhidze et al., 2003, 2005; Cwiertny et al., 2008; Solmon et al., 2009*]. The acidity/pH of the aqueous solution

surrounding dust aerosols is controlled by the ionic balance between acidic species (e.g., sulfate ( $\text{SO}_4^{2-}$ ) and nitrate ( $\text{NO}_3^-$ )) and the main alkaline buffering agent calcite ( $\text{CaCO}_3$ ). If the concentration of the acidic species becomes abundant enough to overcome the alkalinity of mineral dust, the pH of the aqueous solution surrounding the dust particle will decrease and Fe can be effectively mobilized from the particle through proton-promoted dissolution processes [Meskhidze *et al.*, 2005]. However, due to the large buffering capacity of  $\text{CaCO}_3$ , on average dust particles do not easily become acidic. Therefore, when deliquesced mineral dust particles have near neutral pH values ( $\sim 5$ ), additional chemical processes have been proven as important sources of sol-Fe production. For example, carboxylic acids commonly found in atmospheric waters (i.e., oxalic, acetic, formic, and citric acid) [Kawamura and Kaplan, 1989; Kawamura and Ikushima, 1993] have been shown to increase Fe dissolution rates within mineral dust through organic ligand-promoted dissolution [e.g., Martin, 2005; Paris *et al.*, 2011]. Among the major organic compounds found in the atmosphere, oxalate ( $\text{C}_2\text{O}_4^{2-}$ ) has been extensively measured and suggested to be one of the most abundant and highly effective Fe complexing ligands [Cornell and Schindler, 1987]. Oxalate has been suggested to have both anthropogenic and natural sources of its precursor gases [e.g., Fu *et al.*, 2008; Myriokefalitakis *et al.*, 2008; Sinreich *et al.*, 2010; Volkamer *et al.*, 2010; Rinaldi *et al.*, 2011]. Minor primary emissions have also been identified for oxalate, however, are not expected to be a significant source of carboxylic acids in ambient aerosols [Yamasoe *et al.*, 2000; Huang and Yu, 2007; Myriokefalitakis *et al.*, 2008].

Past laboratory studies have demonstrated that when Fe dissolution experiments are conducted in the absence of UV/visible radiation, minimal amounts of Fe(II) are produced and the majority of sol-Fe is in the form of Fe(III) [e.g., *Cwiertny et al.*, 2009]. However, in the presence of organic Fe-complexing ligands and incoming solar radiation, it has been shown that higher fraction of sol-Fe can exist in the Fe(II) form [*Zuo and Holgné*, 1992; *Cornell and Schwertmann*, 1996]. Organically complexed Fe(III) species produced during the atmospheric transport of mineral dust, strongly absorb UV/visible radiation (with wavelengths between 290-570 nm) and photochemically form Fe(II) [*Zuo and Holgné*, 1992]. As Fe(II) species have been shown to be more soluble than Fe(III), Fe(II) deposited to the ocean surface can effectively increase the amount of bioavailable Fe and enhance phytoplankton growth [*Barbeau et al.*, 2001; *Chen and Siefert*, 2003; *Miller and Kester*, 1994]. Therefore, the accurate characterization of the redox cycling of Fe in atmospheric waters is important for marine biogeochemistry [*Song et al.*, 2005; *Voelker et al.*, 1997].

Although this study focuses on sol-Fe deposition to the global oceans, recent research studies have shown how the deposition of atmospheric sol-Fe can play a role in marine ecosystem processes outside of HNLC waters. For example, some marine organisms in the North Atlantic Ocean are known as nitrogen-fixing species and can transform nitrogen (N) into a bioavailable form as long as there are sufficient oceanic concentrations of sol-Fe and phosphorus (P) [e.g., *Moore et al.*, 2009]. Additionally, the atmospheric deposition of bioavailable P and N can stimulate primary productivity as long as the oceanic concentrations of other essential micronutrients (i.e., sol-Fe) are not a limiting factor. These

recent studies demonstrate how not only a single limiting micronutrient, but multiple co-limiting nutrients, can exert control on marine primary productivity and atmospheric CO<sub>2</sub> uptake to the surface oceans. Therefore, an important topic in present day science is working towards the better understanding of the atmospheric deposition of sol-Fe, P, and N and the direct impact it has on ocean biogeochemistry, the global carbon cycle, and overall climate [Falkowski *et al.*, 1998, Mahowald *et al.*, 2011].

Mineral dust deposition is an important atmospheric source of P and N to remote oceanic surface waters, and has been suggested to play a controlling role in marine ecosystem processes in oligotrophic nutrient depleted surface oceans outside of the global HNLC regions [Elser *et al.*, 2007; Krishnamurthy *et al.*, 2007; Duce *et al.*, 2008; Mahowald *et al.*, 2008; Okin *et al.*, 2011]. Similar to Fe, the majority of P mass found in the atmosphere is contained within mineral dust particles [Mahowald *et al.*, 2008]. Soil-derived-P is primarily found in the apatite mineral group (Ca<sub>5</sub>(PO<sub>4</sub>)<sub>3</sub>(OH, F, Cl)) and can also be absorbed onto Fe-(oxyhydr)oxides [Graham and Duce, 1979; Singer *et al.*, 2004]. Typically, the soluble portion of P (sol-P) within mineral dust is considered to be PO<sub>4</sub><sup>3-</sup> [Mahowald *et al.*, 2008; Nenes *et al.*, 2011], following this fact we refer to bioavailable P formed in mineral dust as sol-P or PO<sub>4</sub><sup>3-</sup>. The soluble fraction of P-containing minerals, within freshly emitted dust particles, are typically small (< 10%), however, downwind from the dust source regions previous modeling/laboratory studies and in situ measurements suggest much higher and spatially variable sol-P fractions (> 90%) [i.e., Baker *et al.*, 2006; Mahowald *et al.*, 2008; Nenes *et al.*, 2011]. These findings imply that chemical processes occurring during

atmospheric transport are increasing the amount of  $\text{PO}_4^{3-}$  formation within mineral dust particles. In situ measurements of the chemical composition of dust particles have shown that  $\text{NO}_3^-$  (bioavailable form of oceanic N) is frequently formed on coarse mode mineral dust aerosols during atmospheric transport [e.g., *Zhuang et al.*, 1999; *Park et al.*, 2004; *Dentener et al.*, 2006; *Sullivan et al.*, 2007]. The major formation pathways of  $\text{NO}_3^-$  on mineral dust are the heterogeneous uptake of nitric acid ( $\text{HNO}_3$ ) and nitrogen dioxide ( $\text{NO}_2$ ) [*Dentener et al.*, 2006; *Usher et al.*, 2003]. It has been suggested that on a global scale the atmospheric deposition of  $\text{NO}_3^-$  is an important supply pathway of  $\text{NO}_3^-$  to remote oceanic regions [i.e., *Paerl and Whittal*, 1999; *Duce et al.*, 2008;]. However, the deposition of  $\text{NO}_3^-$  laden dust particles is an atmospheric supply pathway of bioavailable N that has not been a major focus in previous research evaluating atmospheric nutrient deposition.

In this work the 3-D global chemical transport model (CTM) GEOS-Chem (v8-01-01), implemented with a prognostic dust-Fe dissolution scheme (GEOS-Chem/DFeS) [*Solmon et al.*, 2009; *Johnson et al.*, 2010, 2011] is used to predict sol-Fe deposition rates to the global oceans. The model has been updated to explicitly simulate sol-Fe production during the atmospheric transport of mineral dust taking into account inorganic and organic (oxalic) acid-promoted Fe dissolution processes, photochemical redox cycling between ferric (Fe(III)) and ferrous (Fe(II)) forms of Fe, dissolution of three different Fe-containing minerals (hematite, goethite and aluminosilicates), acid-based  $\text{PO}_4^{3-}$  dissolution, and  $\text{NO}_3^-$  production within mineral dust. The model simulations are carried out between March 2009 and February 2010.

## 5.2. Methods

### 5.2.1 GEOS-Chem

GEOS-Chem is driven by assimilated meteorological fields from the Goddard Earth Observing System (GEOS) of the NASA Global Modeling Assimilation Office [Bey *et al.*, 2001; Park *et al.*, 2004]. During this study the model uses GEOS-5 meteorological fields at a  $2^\circ \times 2.5^\circ$  (latitude-longitude) grid resolution and 47 vertical levels. GEOS-Chem includes H<sub>2</sub>SO<sub>4</sub>-HNO<sub>3</sub>-NH<sub>3</sub> aerosol thermodynamics coupled to an O<sub>3</sub>-NO<sub>x</sub>-hydrocarbon-aerosol chemical mechanism [Bey *et al.*, 2001; Park *et al.*, 2004]. The emissions and chemical transformation of sulfur compounds, carbonaceous aerosols, and sea-salt are accounted for and described by Park *et al.* [2004], Heald *et al.* [2004], and Alexander *et al.* [2005]. To simulate dust mobilization, GEOS-Chem combines the Dust Entrainment and Deposition (DEAD) scheme [Zender *et al.*, 2003] with the source function used in the Goddard Chemistry Aerosol Radiation and Transport (GOCART) model [Ginoux *et al.*, 2001; Chin *et al.*, 2002]. Principal source regions are deserts or dry lakes and streambeds where alluvial deposits have accumulated. Once mineral dust is mobilized from the surface, the model uses four standard dust bins with diameter boundaries of 0.2 - 2.0, 2.0 - 3.6, 3.6 - 6.0 and 6.0 - 12.0  $\mu\text{m}$  to simulate global dust transport and deposition [Fairlie *et al.*, 2007]. The removal of mineral dust occurs through dry deposition processes such as gravitational settling [Seinfeld and Pandis, 1998] and turbulent dry transfer of particles to the surface [Zhang *et al.*, 2001]. Dust removal by wet deposition processes includes both convective updraft scavenging and rainout/washout from large-scale precipitation [Liu *et al.*, 2001]. The

standard GEOS-Chem tropospheric chemical mechanism consists of over 100 species and 300 reactions integrated using the stiff-ordinary first order differential equation solver Sparse Matrix Vectorized GEAR II (SMVGEAR II) [Jacobson and Turco, 1994; Jacobson, 1995, 1998]. The GEOS-Chem model calculates photolysis frequencies using the Fast-J radiative transfer algorithm of Wild *et al.* [2000], with a seven-wavelength quadrature scheme that calculates photolysis rates throughout the troposphere in the presence of an arbitrary mix of cloud and aerosol layers [Olsen *et al.*, 1997; Wild *et al.*, 2000]. In order to simulate the diurnal variations of photochemical processes, photolysis calculations are performed every hour in the model.

Previously, the prognostic physically based dust-Fe dissolution module (DFeS) of Meskhidze *et al.* [2005] was implemented into GEOS-Chem [Solmon *et al.*, 2009; Johnson *et al.*, 2010, 2011]. The original DFeS module explicitly considers a globally uniform mineralogical composition of windblown dust and uses aqueous phase equilibrium and dissolution/precipitation reactions for the following minerals contained in dust: calcite, albite, microcline, illite, smectite, gypsum, and hematite [Meskhidze *et al.*, 2005; Solmon *et al.*, 2009]. The dissolution/precipitation of each mineral is then estimated based on solution pH, temperature, dust mineralogy, and the specific surface area of the individual minerals. An initial Fe solubility of 0.45% (for the most reactive and poorly crystalline pool of Fe in desert top soils) is prescribed based on the synthesis of data from the Saharan and Sahel regions of Northern Africa [Shi *et al.*, 2012]. GEOS-Chem/DFeS-predicted fluxes of mineral dust and sol-Fe to the surface oceans have been shown to be in reasonable agreement with available

observational/remotely-sensed data and past modeling studies [Solmon *et al.*, 2009; Johnson *et al.*, 2010, 2011, 2012].

## 5.2.2 Model developments

### 5.2.2.1 Dust mineralogical composition

The mineralogical composition of dust particles is one of the key factors influencing Fe mobilization during atmospheric transport [e.g., Spokes *et al.*, 1994; Sedwick *et al.*, 2007; Journet *et al.*, 2008]. In the recent study by Nickovic *et al.* [2012] it was shown that top-soil/dust mineralogy is spatially heterogeneous and using a globally constant mass fraction for individual minerals may cause errors in the prediction of the impact of mineral dust on marine biogeochemical processes. Therefore, to account for the spatial heterogeneity of the atmospherically transportable fraction of top soils, the global dust mineralogy database of Nickovic *et al.* [2012] has been implemented in the model. The dataset was re-gridded from the original 30-second resolution (approximately 1 km) to the  $2^\circ \times 2.5^\circ$  grid resolution used by GEOS-Chem/DFeS. The dataset contains percent mass fractions of the following minerals: quartz, illite, kaolinite, smectite, feldspar, calcite, hematite, gypsum, and phosphorus. The mass fraction of Fe in the mineral database of Nickovic *et al.* [2012] is generally less than 1% in the majority of global dust source regions. This mass percentage is noticeably smaller in comparison to past literature [e.g., Taylor and McLennan, 1985; Duce and Tindale, 1991], therefore, the Fe content of mineral dust in GEOS-Chem/DFeS was set to a more widely accepted value of 3.5%.

In order to determine the influence of individual major global dust source regions on atmospheric fluxes of sol-Fe, GEOS-Chem/DFeS was further modified to treat seven different dust source regions separately. Following *Prospero et al.* [2002] the terrestrial portion of the globe was divided into the following dust source regions: North Africa, South Africa, North America, Asia, Australia, the Middle East, and South America. In the model each source region is assigned separate tracers to represent mineralogy as well as chemistry. Such a treatment allows dust from each of the seven major source regions to be independently transported, chemically transformed, and removed from the atmosphere. This model development increased the number of additional tracers in GEOS-Chem/DFeS (by a factor of 7) causing a considerable increase in computational cost. Therefore, the selection of different dust source regions is available as a user-defined option in the updated GEOS-Chem/DFeS.

#### 5.2.2.2 Model-predicted oxalate concentrations

In order to simulate organic ligand-promoted Fe dissolution, a new tracer - oxalate - was implemented into GEOS-Chem/DFeS (see Table 5.1). This organic compound was chosen because of its high affinity to complex with Fe within mineral dust [*Cornell and Schindler*, 1987] and the fact that oxalate has been shown to be one of the most abundant organic constituents detected in tropospheric aerosols [e.g., *Kawamura and Ikushima*, 1993; *Kawamura et al.*, 2005; *Yu et al.*, 2005]. Oxalate has been suggested to have both anthropogenic and natural sources of its precursor gases [e.g., *Fu et al.*, 2008; *Myriokefalitakis et al.*, 2008; *Sinreich et al.*, 2010; *Volkamer et al.*, 2010; *Rinaldi et al.*,

2011]. The in-cloud oxidation of organic compounds such as glyoxylic acid, glycolic acid, glycoaldehyde, glyoxal, and methylglyoxal are suggested to be the dominant precursors of oxalate formation [e.g., *Myriokefalitakis et al.*, 2011] with additional precursor compounds such as aromatic hydrocarbons, cyclic olefins, and aldehydes in highly polluted regions [*Kleindienst et al.*, 1999; *Yu et al.*, 2005]. The explicit calculation of oxalate formation, as in *Myriokefalitakis et al.* [2011], considers a complex system of aqueous and gas phase reactions and is outside the scope of the current study. To estimate oxalate in GEOS-Chem/DFeS we apply the method proposed by *Yu et al.* [2005], in which oxalate concentrations,  $[\text{C}_2\text{O}_4^{2-}]$  in  $\text{nmol m}^{-3}$  are calculated using model-predicted sulfate concentrations ( $[\text{SO}_4^{2-}]$ ):

$$[\text{C}_2\text{O}_4^{2-}] = 0.05 \cdot [\text{SO}_4^{2-}] - 0.273 \quad (1)$$

The linear fit shown in Eq. 1 was derived from aircraft and ground-based measurements of oxalate and sulfate concentrations during the Aerosol Characterization Experiment (ACE)-Asia measurement campaign [*Yu et al.*, 2005]. Measurements from various urban, remote, and coastal regions in Asia also demonstrate high spatial and temporal correlation ( $R^2 = 0.49 - 0.93$ ) [*Yu et al.*, 2005] and comparable size distributions [*Furukawa and Takahashi*, 2011] of oxalate and sulfate in aerosol and cloud water. Such a strong relationship was suggested to be due to the similar locations of emitted precursor species and in-cloud formation pathways [*Yu et al.*, 2005; *Myriokefalitakis et al.*, 2011]. Over the North Atlantic Ocean variable correlation between non-seasalt  $\text{SO}_4^{2-}$  and oxalate was reported from cruise

measurements of *Chen and Siefert* [2004]. The linear correlation coefficient between 0.70 to 0.96 and 0.26 to 0.68 for winter and summer seasons, respectively [*Chen and Siefert*, 2004] suggests that oceanic dimethyl sulfide (DMS) ( $\text{SO}_4^{2-}$  precursor gas) emissions may bias model-predicted oxalate concentrations. Upon the evaporation of cloud droplets and aerosol water both oxalate and sulfate tend to remain in the particulate phase. To avoid the effect of oxalate not associated with mineral dust, the amount of oxalate considered in organic ligand-promoted Fe dissolution is calculated based in dust-sulfate concentrations.

#### 5.2.2.3 Mineral dissolution kinetics

Organic ligand adsorption to mineral surfaces regulates several environmentally significant chemical reactions, including dissolution [*Furrer and Stumm*, 1986] and photochemistry [*Martin et al.*, 1996]. Numerous kinetic and photochemical studies have been carried out to understand dissolution kinetics of Fe-oxyhydr(oxides) and aluminosilicates from hydrometallurgy to aerosol particles in atmospheric liquid phase. Ligands which promote dissolution (e.g., oxalate) are thought to form mononuclear (often bidentate) surface complexes with two single-bonded oxygen atoms each donating electrons to chelate Fe atoms [*Duckworth and Martin*, 2001]. Such ligands, binding as inner-sphere complexes to the surface groups of Fe oxides, increase dissolution rates due to strong electron donation to a surface metal atom, weakening the Fe-O bond of the mineral lattice and lowering the energy barrier for the dissolution [*Cornell and Schwertmann*, 1996]. It has been shown that at pH typical for atmospheric aqueous phase ( $3 < \text{pH} < 6$ ) organic ligand-

promoted Fe dissolution is the major mechanism for the production of sol-Fe [Stumm et al., 1985; dos Santos Afonso et al., 1990; Cornell and Schwertmann, 1996; Taxiarchou et al., 1997]. Out of number of different Fe(III) chelating ligands, dicarboxylic acids - and in particular oxalate - has been widely studied [Cornell and Schindler, 1987; Duckworth and Martin, 2001]. It has been suggested that the presence of oxalate in ambient aerosols can lead to more than an order of magnitude increase in Fe dissolution rates [e.g., Pehkonen et al., 1993; Xu and Gao, 2008; Cwiertny et al., 2009; Paris et al., 2011]. Previous laboratory studies also showed a positive effect of UV radiation on oxalate-promoted dissolution Fe-oxides/hydroxides [Waite, 1986; Cornell and Schindler, 1987]. Light of the appropriate wavelength may promote the reductive dissolution of surface Fe(III) sites by electron-donating Fe(II) complexes [Suter et al., 1991]. A possible mechanism for the dissolution process was suggested to start with photo-reduction of Fe(III)-oxalate complex (released into solution) to an Fe(II)-oxalate. The Fe(II)-oxalate complex then adsorbs on Fe oxyhydr(oxide) where it exchanges electron with a surface Fe(III) atom. This electron exchange at the surface destabilizes the coordination sphere of Fe and increases the rate of dissolution as a result of both loss of charge and larger size of bivalent Fe(II) [Suter et al., 1991; Cornell and Schwertmann, 1996]. Thus, photochemical reduction of Fe(III)-containing aerosols in the presence of oxalate was suggested to increase Fe solubility in atmospheric aerosols [Zuo and Hoigné, 1992; Pehkonen et al., 1993]. In this work oxalate-promoted dissolution of three Fe-containing minerals (hematite, goethite, and illite) was added to GEOS-Chem/DFeS. Illite was chosen as a proxy for all Fe-containing

aluminosilicate minerals. The dissolution rate constant  $K^r$  ( $\text{mol m}^{-2} \text{s}^{-1}$ ) for the Fe-containing mineral “i” in the presence of oxalate is modeled as the sum of proton-promoted and ligand-promoted dissolution rates:

$$K_i^r(T) = K_{p_i}(T) + K_{l_i}(x) \quad (2)$$

where  $K_{p_i}(T)$  and  $K_{l_i}(x)$  are the proton-promoted (see equation 24 in *Meskhidze et al.* [2005]) and the oxalate-promoted mineral dissolution rate constants, respectively and T stands for temperature (K). The  $K_{p_i}$  values for hematite and illite dissolution rates are taken from *Meskhidze et al.* [2005] and  $K_{p_g}$ , the proton-promoted dissolution rate constant for goethite ( $\text{mol m}^{-2} \text{s}^{-1}$ ) is derived from *Cornell* [1976] as:

$$K_{p_g} = 1.4 \times 10^{-11} * \exp \left[ 1.1 \times 10^4 * \left( \frac{1}{298} - \frac{1}{T} \right) \right] \quad (3)$$

The values for  $K_{l_i}(x)$  for three different minerals (hematite, goethite, and illite) are taken from *Paris et al.* [2011]. The study by *Paris et al.* [2011] was selected because it uses oxalate levels typically observed in atmospheric aerosols, several orders of magnitude lower compared to many Fe-hydr(oxide) dissolution experiments [e.g., *Cornell and Schindler*, 1987]. The artificial laboratory light used in *Paris et al.* [2011] study does not allow UV-light emissions and therefore may lead to factor of 2 to 3 underestimation of Fe dissolution rates [e.g., *Waite et al.*, 1986]. However, *Paris et al.* [2011] emphasized that for their experimental conditions, the light-induced reductive dissolution was not the principal process explaining the increase in Fe solubility. For acidic solutions containing various concentrations of oxalate, *Paris et al.* [2011] show a positive linear correlation between sol-

Fe and the oxalate concentration for all of the minerals considered. Using this data one can then calculate (after subtracting out the amount of sol-Fe produced at the absence of oxalate)  $Kl_i(x)$  for different Fe-containing minerals “i” and different oxalate concentrations (x). Coefficients  $a_i$  and  $b_i$  (with corresponding  $R^2$  values) for a linear best fit to *Paris et al.* [2011] data are summarized in Table 5.2.

The proton- and oxalate-promoted dissolution rate constants of the three Fe-containing minerals considered in GEOS-Chem/DFeS are shown in Fig. 5.1. Calculations suggest that out of three Fe-containing minerals illite has the fastest dissolution rate followed by hematite and goethite. The calculated rates for oxalate-promoted dissolution are in agreement with past literature [e.g., *Journet et al.*, 2008; *Sidhu et al.*, 1981; *Schwertmann*, 1991; *Samson and Eggleston*, 2002; *Duckworth and Martin*, 2001]. Figure S1 revealed that dissolution rate constants for all three Fe-containing minerals become relatively constant for pH values greater than 4 (at lower values for higher oxalate concentrations). In order to determine the influence of oxalate on sol-Fe production within mineral dust baseline model simulations are carried out using hematite dissolution rates and the results are compared to the proton-promoted Fe dissolution scheme of *Meskhidze et al.* [2005].

#### 5.2.2.4 Kinetic modeling of Fe photochemistry/chemistry

Past studies have shown that photochemical reactions (for wavelengths  $\lambda < 440$  nm) of Fe(III)-oxalate complexes in atmospheric waters can be an important source of Fe(II) [*Faust and Zepp*, 1993; *Siefert et al.*, 1996; *Balmer and Sulzberger*, 1999]. However, the photolysis of Fe(III)-oxalate complexes may also lead to the reduction of oxygen and

formation of superoxide and its conjugate acid, hydroperoxide radical ( $\text{HO}_2\cdot/\text{O}_2^-$ ), which in turn form hydrogen peroxide ( $\text{H}_2\text{O}_2$ ) [Zuo and Holgné, 1992]. Since sol-Fe and oxalic acid are ubiquitous pollutants in cloud-, fog-, and rainwater, photochemical/chemical redox cycling of oxalate-complexed Fe species could have an important effect on  $\text{H}_2\text{O}_2$  and  $\text{OH}\cdot$  radical formation and removal of atmospheric oxalic acid. In order to simulate the photochemical/chemical cycle of ferric and ferrous complexes, oxalate,  $\text{H}_2\text{O}_2$ , and radical species  $\text{OH}\cdot, \text{HO}_2\cdot, \text{O}_2^-$  additional kinetic, photochemical, and aqueous-phase equilibrium reactions listed in Tables 5.3 and 5.4 (apart from those described in Meskhidze *et al.*, [2005]) were added into SMVGEAR II. The multicomponent activity coefficients for major inorganic species were determined using the method of Bromley [1973]. Ionic strength and pH of the solution are calculated using a modified form of ISORROPIA [Nenes *et al.*, 1998; Meskhidze *et al.*, 2005]. We calculated binary activity coefficients for each new ion pair using the formulation of Kusik and Meissner [1978] and the q-parameters for each relevant salt listed in Table 9 of Meskhidze *et al.* [2005]. Activity coefficients for the following ions  $\text{C}_2\text{O}_4^{2-}, \text{C}_2\text{O}_4^-, \text{FeO}^{2+}, \text{O}_2^-$  have been neglected. To consider a potential salting out effect for electrically neutral species ( $\text{H}_2\text{O}_2, \text{HO}_2, \text{OH}, \text{O}_3, \text{O}_2$ ) activity coefficients were calculated as  $10^{0.1*I}$  [Fischer and Peters, 1970], where  $I$  stands for the ionic strength of the solution.

In addition to Fe, oxalate can readily chelate divalent cations such as  $\text{Ca}^{2+}$ , which is commonly enriched in mineral dust, forming mostly insoluble complexes [e.g., Sullivan *et al.*, 2009]. Technically, the formation of these metal-organic ligand complexes may lower the oxalate concentration available for adsorption onto Fe-(oxyhydr)oxides. However,

reaction of  $\text{Ca}^{2+}$  with oxalate have not been included in Table 5.3, because recent studies of size-fractionated aerosol samples collected in Tsukuba (a city approximately 60 km northeast of Tokyo) showed that on average only 2 to 10% of oxalate is associated with  $\text{Ca}^{2+}$  ions [Furukawa and Takahashi, 2011].

Table 5.5 shows that the primary sources of Fe(II) production are the photochemical reduction of ferric hydroxide ( $\text{Fe}(\text{OH})^{2+}$ ) and Fe(III)-oxalate species and reactions of Fe(III)-hydroxy species with  $\text{HO}_2/\text{O}_2^-$  radicals. The primary destruction pathways of Fe(II) (cycling back to Fe(III)) are the reactions with  $\text{H}_2\text{O}_2$ , ozone ( $\text{O}_3$ ), nitrate ( $\text{NO}_3$ ), and superoxide/hydroperoxide radicals. So based on this reaction mechanism Fe(II) is mainly produced during the day and gets oxidized at night. Since Fe(II) and Fe(III) have very different solubilities in sea water, photochemical/chemical cycling of the two different forms of Fe in ambient aqueous solutions may prove to be important for the effect of dust-deposited Fe on marine ecosystem productivity.

#### 5.2.2.5 Acid-based bioavailable P production and N formation

Soil-derived P is primarily found in the apatite mineral group [Singer *et al.*, 2004; Nenes *et al.*, 2011] and is predominantly insoluble, under alkaline and oxic condition such as oceanic surface waters [Atlas and Pytkowicz, 1977; Nenes *et al.*, 2011], upon emission but has been shown to have increased solubility fractions due to atmospheric processing during transport. Sol-P (i.e., phosphate ( $\text{PO}_4^{3-}$ )) concentrations within mineral dust are predicted in GEOS-Chem/DFeS using the acidity based production method described in the recent work by Nenes *et al.* [2011]. Nenes *et al.* [2011] showed that by combining total dust

concentrations, solution pH, solubility equilibrium of mineral-P, phosphoric acid dissociation equilibrium, and mass balance constraints, the total magnitude of dissolved  $\text{PO}_4^{3-}$  (M) can be accurately calculated with Eq. (4):

$$\frac{d[\text{dust-PO}_4^{3-}]}{dt} = [\text{HPO}_4^{2-}] \left[ \frac{K_3}{[\text{H}^+]} + 1 + \frac{[\text{H}^+]}{K_2} + \frac{[\text{H}^+]^2}{K_1 K_2} \right] \quad (4)$$

where  $[\text{HPO}_4^{2-}]$  is the aqueous concentration of hydrogen phosphate (M),  $[\text{H}^+]$  is the hydronium ion concentration (M), and  $K_1$ ,  $K_2$ ,  $K_3$  (M) represent the ionization constants of phosphoric acid. In order to simulate  $\text{NO}_3^-$  formation on mineral dust we use the methods described in *Meskhidze et al.* [2005] and *Solmon et al.* [2009]. Sources of  $\text{NO}_3^-$  laden dust ( $\mu\text{g m}^{-3}$ ) in GEOS-Chem/DFeS are from the condensation of gas-phase  $\text{HNO}_3$  and the direct absorption of  $\text{NO}_2$  gas on dust particles which is determined by a bulk uptake coefficient shown in Eq. (5) derived from *Solmon et al.* [2009]:

$$\frac{d[\text{dust-NO}_3^-]}{dt} = k_{\text{NO}_2} [\text{dust}] [\text{NO}_2] + S_{eq} \quad (5)$$

where  $k_{\text{NO}_2}$  ( $1 \times 10^{-7} \text{ m}^3 \mu\text{g}^{-1} \text{ s}^{-1}$ ) is the bulk uptake coefficient of  $\text{NO}_2$  [*Herring et al.*, 1996],  $[\text{dust}]$  is the model-predicted concentration of mineral dust ( $\mu\text{g m}^{-3}$ ),  $[\text{NO}_2]$  is the gas-phase concentration of  $\text{NO}_2$  ( $\mu\text{g m}^{-3}$ ), and  $S_{eq}$  represents the deposition/volatilization of  $\text{HNO}_3$  on mineral dust. The concentration of  $\text{NO}_3^-$  deposited/removed from dust particles in GEOS-Chem/DFeS is calculated by invoking thermodynamic equilibrium between the gas-phase and aerosol mode using a modified form of ISORROPIA as described in *Meskhidze et al.* [2005] and *Solmon et al.* [2009].

## 5.3. Results

### 5.3.1 Atmospheric concentrations of oxalate

Past measurement studies have shown that surface level oxalate concentrations range from  $\sim 10$  to  $100 \text{ ng m}^{-3}$  in rural and oceanic locations [Sciare *et al.*, 2009] to greater than  $1000 \text{ ng m}^{-3}$  in urban and highly polluted regions [Kawamura and Ikushima, 1993; Ruellan *et al.*, 1999; Legrand *et al.*, 2007]. In order to determine the relative accuracy of GEOS-Chem/DFeS-predicted surface oxalate concentrations, model-predicted values are compared to a global dataset of oxalate concentration measurements [Myriokefalitakis *et al.*, 2011, and reference within]. Figure 5.2 shows that model-predicted oxalate concentrations compare relatively well to surface measurements and overall can reproduce the majority of measured oxalate concentrations within a factor of 2. However, Fig. 5.2 also shows that when  $\text{SO}_4^{2-}$  is used as a proxy for oxalate, the model tends to over-predict the low concentrations of oxalate measured over the remote oceanic regions. GEOS-Chem/DFeS predictions of oxalate over the remote oceans is a model artifact associated to oceanic dimethyl sulfide (DMS) ( $\text{SO}_4^{2-}$  precursor gas) emissions and is not related to the suggested natural oceanic sources of oxalate precursor gases (e.g., glyoxal) [e.g., Kawamura *et al.*, 1996; Myriokefalitakis *et al.*, 2008; Sinreich *et al.*, 2010; Volkamer *et al.*, 2010]. Nevertheless, it should be noted that model-predicted oxalate concentrations over remote oceanic regions (generally  $< 80 \text{ ng m}^{-3}$ ) have a negligible impact on Fe dissolution kinetics. Therefore, the model-predicted magnitudes of

oxalate concentrations during this study are suitable for the prediction of the effect of organic acids on Fe-dissolution within mineral dust.

### 5.3.2 Sol-Fe deposition

#### 5.3.2.1 Total sol-Fe deposition

Figure 5.3 shows the GEOS-Chem/DFeS-predicted seasonally-averaged sol-Fe deposition rates to the global oceanic regions during each season of the yearlong simulation. Overall, GEOS-Chem/DFeS predicted ~0.17 Tg (1 Tg =  $10^{12}$  g) of sol-Fe was deposited to the global oceans during the entire simulated time period. This magnitude is slightly lower compared to the recent modeling studies of *Luo et al.* [2008] and *Okin et al.* [2011] which predicted total annual sol-Fe deposition to the global surface oceans of 0.21 and 0.36 Tg, respectively. The magnitude of sol-Fe deposition to the North Atlantic Ocean is large year-round with highest fluxes occurring during the spring and fall ( $> 10 \mu\text{g m}^{-2} \text{day}^{-1}$ ). Figure 5.3 also shows that seasonally-averaged sol-Fe deposition rates to the North Pacific Ocean, in close proximity to the Asian continent, are elevated during the spring months (between 0.1 and  $0.5 \mu\text{g m}^{-2} \text{day}^{-1}$ ) when model-predicted mineral dust emissions are at a maximum. According to Fig. 5.3 the highest seasonally-averaged sol-Fe deposition rates to the HNLC waters of the subarctic North Pacific Ocean (north of  $\sim 45^\circ\text{N}$  [*Peterson et al.*, 2005]) also occur during the spring season and could provide an important source of this essential micronutrient.

From Fig. 5.3 it can be seen that in the Southern Hemisphere, the highest rates of sol-Fe deposition to the surface oceans occur downwind from the dust source regions of Australia and South America. According to this figure there is a distinct seasonality in sol-Fe deposition rates to the Southern Ocean. The highest seasonally-averaged sol-Fe deposition rates, associated with Australian dust are predicted to occur during the austral fall and spring, while the highest fluxes from South American sources (predominately the deserts of Patagonia) occurring during the austral summer and fall.

To quantify the importance of the atmospheric transport and transformation of mineral Fe, studies often report either fluxes of sol-Fe or DIFs at the time of mineral dust deposition to the ocean surface. Figure 5.4 shows that DIF values, simulated by GEOS-Chem/DFeS, are highly variable both spatially and temporally. In general DIF values remain low near the dust source regions but increase downwind as acidic trace gases and organic compounds are predicted to initiate Fe mobilization. The highest DIFs are predicted over the regions characterized by low concentration of dust and high amounts of anthropogenic pollution. For example, off the west coast of South America, where dust from the Atacama Desert can be mixed with highly polluted air masses from northern Chile. On the other hand, Fig. 5.4 shows that DIFs remain low over regions frequently influenced by large dust outbreaks. For example, over the North Atlantic Ocean, downwind from the desert regions of North Africa, the concentrations of acidic trace gases are insufficient to overcome the buffering capacity of the  $\text{CaCO}_3$  contained in mineral dust particles. Therefore, Fig. 5.4 shows that DIF values can be used as an indication of the chemical processing of mineral-Fe.

However, when compared to Fig. 5.3, it can be seen that regions characterized by the highest values of DIF also show some of the lowest total fluxes of sol-Fe. Therefore, DIFs alone are poor proxies for the importance of the atmospheric transport pathways for sol-Fe deposition to the ocean. When the biogeochemical cycling of dust-Fe is examined, both fluxes of sol-Fe and DIFs should be presented.

#### 5.3.2.2 Sol-Fe(II) deposition

Since model-predicted Fe(II) is produced primarily through photolytic processes it is expected that Fe(II) deposition rates will be on average much larger during the daytime hours. Figure S5.1 shows GEOS-Chem/DFeS-predicted total sol-Fe and its partition to Fe(II) and Fe(III) species model-predicted sol-Fe(II)% values over Barbados. This figure shows that simulated Fe(II)% values ( $\text{Fe(II)\%} = \frac{\text{sol-Fe(II)}}{\text{total sol-Fe}} \times 100$ ) are in agreement with past studies which suggest that Fe(II)/Fe(III) partitioning varies throughout the day ranging from <2% to 100% [e.g., *Siefert et al.*, 1998; *Zhu et al.*, 1997]. To understand if the model can capture Fe(II)/Fe(III) redox cycling occurring in nature, model-predicted Fe(II) and Fe(III) surface concentrations were evaluated with measurement data obtained during the Barbados Dust Deposition Experiment (BarDEX) [*Trapp et al.*, 2010]. From Fig. S5.2 it can be seen that GEOS-Chem/DFeS can capture the temporal pattern of measured daily-averaged surface concentrations of Fe(III) (correlation coefficient (R) = ~0.70) and Fe(II) (R = ~0.65). However, this figure also shows that the model tends to underestimate the magnitudes of both Fe(II) and Fe(III). These negative biases in model-predicted Fe(II) and Fe(III) surface

concentrations is directly related to the under prediction of mineral dust mass compared to measurements [Trapp *et al.*, 2010] during this time period (NMB =  $\sim -30\%$ ). This result agrees with past studies simulating dust in GEOS-Chem which have shown that the model tends to under predict the concentration of North African dust reaching the Caribbean region due to the under prediction of the westward transport of mineral dust over the N. Atlantic Ocean or the over prediction of depositional fluxes [Generoso *et al.*, 2008].

Figure 5.5 shows GEOS-Chem/DFeS-predicted seasonally-averaged (day and nighttime hours) sol-Fe(II) deposition rates to the global oceanic regions during the yearlong simulation. The comparison of Figs. 5.5 and 5.3 shows that spatial deposition patterns for total sol-Fe and Fe(II) are similar. For example, in the Northern Hemisphere the largest seasonally-averaged deposition rates of Fe(II) (up to  $0.1 - 1.0 \mu\text{g m}^{-2} \text{day}^{-1}$ ) occur over the North Atlantic and North Pacific Oceans associated with mineral dust transport from the Sahara Desert and Asian dust source regions, respectively, while in the Southern Hemisphere, the highest deposition rates of Fe(II) are associated with Australian and Patagonian dust sources. However, the effect of sunlight on sol-Fe partitioning between Fe(II) and Fe(III) species becomes apparent on Fig. 5.6. This figure shows that near the equator, close to 50% of seasonally-averaged fluxes of sol-Fe are in the Fe(II) form. This figure also shows higher Fe(II) fractions over high latitude oceanic regions during the summer season and lower during the winter. As phytoplankton productivity in the HNLC waters of the sub-arctic North Pacific and Southern Ocean intensifies with the availability of sunlight, this finding suggests that the higher fraction of bioavailable Fe can be deposited in

the relatively more soluble Fe(II) form when there is the greatest demand by ocean ecosystems. In addition to sunlight, Fig. 5.6 shows that while the minimal concentrations of oxalate over the remote oceans has little influence on the magnitude of sol-Fe produced, it does however have an effect on the model-predicted Fe(II) fraction. Because in the model oxalate adsorption onto mineral-Fe only occurs for pH values less than 5, over the regions frequently impacted by large magnitudes of mineral dust (e.g., downwind from Sahara Desert), characterized by near neutral aerosol solution pH values, sol-Fe tends to be mainly in the Fe(III) form.

#### 5.3.2.3 *Organic ligand-promoted Fe dissolution*

The influence of organic acids on dust-Fe dissolution is shown on Fig. 5.7 as the percent changes in seasonally-averaged sol-Fe deposition rates. Our calculations suggest that the implementation of organic ligand-promoted Fe dissolution increases global deposition of sol-Fe by ~20% to the global oceans. However, Fig. 5.7 shows that the effect of oxalate on dust-Fe dissolution rates is highly variable. The most noticeable example of the large increases can be seen year-round in regions of the equatorial Pacific Ocean where GEOS-Chem/DFeS sol-Fe deposition rates were increased by over 50% compared to model simulations only taking into account acid mobilization. Figure 5.7 also shows that increases in model-predicted sol-Fe deposition rates due to oxalate were relatively large over the subarctic North Pacific Ocean, reaching up to 30% during the springtime. Such enhanced dissolution of dust-Fe is associated with elevated oxalate concentrations downwind from China. Compared to the Northern Hemisphere, increases in sol-Fe deposition rates to the

HNLC oceanic regions of the Southern Hemisphere were smaller (see Fig. 5.7) largely due to the lower concentrations of oxalic acid over these relatively pristine environments.

#### 5.3.2.4 *Model sensitivity to Fe-containing mineral speciation*

In our baseline GEOS-Chem/DFeS model simulations all the Fe mass was assumed to be contained within hematite. Here we present sensitivity calculations to assess how different Fe-containing minerals (i.e., goethite and illite) can affect model-predicted fluxes of sol-Fe. Simulations are carried out for the months of January and July of the simulation time period and compared to the baseline model results. According to our calculations, when using goethite and illite dissolution rates the amount of sol-Fe deposited to the surface oceans can increase by 15% to 40% during July and 10% to 30% during January, respectively. Figure 5.8 shows the differences in the magnitude of sol-Fe fluxes deposited to the surface oceans when baseline model simulations are subtracted from GEOS-Chem/DFeS calculated sol-Fe production using goethite and illite dissolution rates. This figure shows that Fe-mineralogy can have a large effect on sol-Fe deposition in regions that are commonly characterized by large quantities of dust. These increases in sol-Fe deposition can be directly related to the faster Fe dissolution rates of goethite and illite (see Fig. 5.1) in less acidic environments. This sensitivity study demonstrates how the specific Fe-containing speciation of atmospherically transported dust can have a large impact on the amount of sol-Fe supplied to global oceanic surface waters.

### 5.3.3 PO<sub>4</sub><sup>3-</sup> deposition

Oceanic surface waters are commonly suggested to have marine primary productivity limited by bioavailable P on a geologic timescale [Falkowski, *et al.*, 1998] and in some regions on shorter time scales [i.e., Krishnamurthy *et al.*, 2007]. Therefore, the deposition of PO<sub>4</sub><sup>3-</sup>, associated with mineral dust, is an important parameter to fully understanding marine biogeochemistry. Figure 5.9 shows GEOS-Chem/DFeS-predicted daily-averaged PO<sub>4</sub><sup>3-</sup> deposition rates to the global oceanic regions during each individual season of the yearlong simulation. From this figure it can be seen that the magnitude and spatio-temporal variability of bioavailable PO<sub>4</sub><sup>3-</sup> deposition is similar to sol-Fe and are directly related to model-predicted mineral dust transport pathways. Comparing the solubility fraction of PO<sub>4</sub><sup>3-</sup>-laden dust to sol-Fe it becomes apparent that the dissolution scheme of Nenes *et al.* [2011] produces larger solubility fractions of P compared to model-predicted DIF. Model simulations indicate that the solubility of P within mineral dust generally ranges between ~1 and 75%. The spatial pattern of PO<sub>4</sub><sup>3-</sup> solubility was consistent with DIF values as the solubility fractions of P generally increases with the duration of atmospheric transport of mineral dust. Overall, GEOS-Chem/DFeS predicted ~0.2 Tg of PO<sub>4</sub><sup>3-</sup> was deposited to global surface oceanic regions during the simulated time period. The magnitude of PO<sub>4</sub><sup>3-</sup> simulated to be deposited to the global oceans during this study is similar to recent modeling studies evaluating PO<sub>4</sub><sup>3-</sup> deposition [i.e., Okin *et al.*, 2011].

The seasonal variations in the magnitude and spatial distribution of PO<sub>4</sub><sup>3-</sup> deposition are clearly noticeable in the Northern Hemisphere downwind from the Sahara Desert and

Asian dust sources. The magnitude of  $\text{PO}_4^{3-}$  deposition to the North Atlantic Ocean is large year-round with the maximum fluxes occurring during the spring and fall months ( $\sim 10 \mu\text{g m}^{-2} \text{ day}^{-1}$ ). These large fluxes of mineral dust-laden  $\text{PO}_4^{3-}$  are important due to the fact that the remote regions of the North Atlantic and Pacific Ocean (particularly below  $\sim 40^\circ\text{N}$ ) are considered to have marine primary productivity limited by the supply of bioavailable P. Additionally, in the Southern Hemisphere, mineral dust emissions from Australian dust source regions transported to the north-west provide biogeochemically important fluxes of  $\text{PO}_4^{3-}$  (up to  $\sim 0.5 \mu\text{g m}^{-2} \text{ day}^{-1}$ ) to the P-starved waters of the Indian Ocean.

#### **5.3.4 $\text{NO}_3^-$ deposition**

Past studies have suggested that oceanic surface waters, outside of HNLC regions, have marine primary productivity limited by  $\text{NO}_3^-$  on short time scales [i.e., *Krishnamurthy et al.*, 2007; *Duce et al.*, 2008]. Figure 5.10 shows GEOS-Chem/DFeS-predicted daily-averaged  $\text{NO}_3^-$  deposition rates to the global oceanic regions during each individual season of the simulated time period. From this figure it can be seen that the magnitude and spatio-temporal variability of bioavailable  $\text{NO}_3^-$  deposition is directly related to the regions with large quantities of both mineral dust and gaseous nitrogen species predominantly emitted from anthropogenic sources. Overall, GEOS-Chem/DFeS predicted  $\sim 75 \text{ Tg}$  of  $\text{NO}_3^-$  was deposited to global surface oceanic regions during the simulated time period. This magnitude is similar to recent modeling studies focusing on  $\text{NO}_3^-$  deposition to the global surface oceans [i.e., *Okin et al.*, 2011].

Figure 5.10 shows  $\text{NO}_3^-$  deposition rates to the North Atlantic Ocean, associated with Saharan dust, are the largest global source of this essential micronutrient to N-starved oceanic regions (up to  $\sim 1000 \mu\text{g m}^{-2} \text{day}^{-1}$ ) during times of maximum dust deposition. A similarly large source of  $\text{NO}_3^-$  is provided by dust that originates from the Middle East and is deposited to the Indian Ocean. Model-predicted Asian dust sources are also important supply pathway of bioavailable  $\text{NO}_3^-$  to the N-limited waters of the North Pacific Gyre. Figure 5.10 shows that  $\text{NO}_3^-$ -laden mineral dust deposition rates in the Southern Hemisphere are much smaller in comparison to those predicted in the Northern Hemisphere. This is due to the fact that not only are Northern Hemispheric dust concentrations much larger compared to the Southern Hemisphere, but anthropogenic emissions of nitrogen containing trace gases are also much smaller in the Southern Hemisphere. The largest source of bioavailable  $\text{NO}_3^-$  to N-starved surface waters is from dust deposition off the north-east coast of Australia where fluxes reach up to  $\sim 100 \mu\text{g m}^{-2} \text{day}^{-1}$  in all seasons. Overall, bioavailable  $\text{NO}_3^-$  associated with mineral dust deposition proved to be an important source of this essential nutrient to many global oceanic regions suggested to have marine primary productivity limited by oceanic  $\text{NO}_3^-$  concentrations.

### **5.3.5 Potential biogeochemical impact**

In order to fully understand how model-predicted fluxes of these essential micronutrients may influence marine biogeochemistry, we focus on specific oceanic regions which have marine primary productivity limited by each individual micronutrient. Figure 5.11 shows the daily-averaged deposition rates of sol-Fe,  $\text{PO}_4^{3-}$ , and  $\text{NO}_3^-$  to oceanic regions

which are assumed to be limited by each individual essential micronutrient during the entire simulation period. Fe-,  $\text{PO}_4^{3-}$ -, and  $\text{NO}_3^-$ -starved oceanic regions were approximated from the results of *Okin et al.* [2011] and are shown in Fig. 5.11 as all the un-masked oceanic regions which instead show model-predicted deposition rates. This figure allows the reader to focus on where the deposition of each individual micronutrient is expected to have an impact on marine primary productivity, biogeochemistry, and overall climate.

Figure 5.11a shows that maximum sol-Fe-laden mineral dust deposition rates are predicted to be an important source of bioavailable Fe to surface HNLC oceans directly off the coast of North Africa and the Middle East ( $> 1.0 \mu\text{g m}^{-2} \text{day}^{-1}$ ), in the subarctic North Pacific Ocean (up to  $0.1 \mu\text{g m}^{-2} \text{day}^{-1}$ ), and in the Southern Ocean (up to  $1.0 \mu\text{g m}^{-2} \text{day}^{-1}$ ). A smaller, possibly important, source of sol-Fe up to  $\sim 0.01 \mu\text{g m}^{-2} \text{day}^{-1}$  is also supplied to the equatorial Pacific Ocean through the deposition of mineral dust (see Fig. 5.11a). The atmospheric fluxes of  $\text{PO}_4^{3-}$ -laden-mineral dust are predicted to be an important source of bioavailable  $\text{PO}_4^{3-}$  to the P-starved oceanic regions of the North Atlantic Ocean and Indian Ocean (between  $1.0 - 10.0 \mu\text{g m}^{-2} \text{day}^{-1}$ ). Non-negligible bioavailable  $\text{PO}_4^{3-}$  fluxes up to  $\sim 0.5 \mu\text{g m}^{-2} \text{day}^{-1}$  are also predicted to be deposited to the subarctic South Atlantic and Indian Oceans (see Fig. 5.11b). From Fig. 5.11c it can be seen that bioavailable  $\text{NO}_3^-$  fluxes, associated with mineral dust deposition, are important sources of  $\text{NO}_3^-$  to the N-starved surface waters of the North and South Atlantic, North Pacific, and Indian Ocean with deposition rates ranging between  $1.0$  and  $100 \mu\text{g m}^{-2} \text{day}^{-1}$ . Overall, this study shows the importance of using a fully comprehensive model to predict the magnitudes and highly

spatio-temporal variability of mineral dust and bioavailable nutrient fluxes. The model-predicted micronutrient deposition rates shown during this study are to-date, the most comprehensive data sets of essential micronutrient deposition and are suggested for usage in marine biogeochemical and climate models.

### **5.3.6 Potential error due to a priori assumptions**

During this study it was shown that the GEOS-Chem/DFeS model predicts bioavailable nutrient deposition rates that are highly variable both spatially and temporally. From Fig. 5.4 it was shown that DIF values were highly variable due to the complex Fe dissolution processes simulated within the nutrient dissolution scheme. In this section of the study we focus on the differences in sol-Fe deposition rates to the global oceans between an a priori assumption and applying GEOS-Chem/DFeS to explicitly calculate DIF. Figure 5.12 shows the percent differences between sol-Fe deposition rates when a constant DIF of 1% is prescribed and when DIF values are explicitly calculated by GEOS-Chem/DFeS. From this figure it can be seen that large percent differences occur between sol-Fe deposition when using an a priori assumption of DIF and explicit calculations. For example, when focusing on deposition fluxes to HNLC surface oceans, a priori assumption of DIF will cause under predictions of sol-Fe deposition rates up to 100% in the subarctic North Pacific and equatorial Pacific Oceans. In contrast to the under predictions simulated in the Northern Hemisphere HNLC oceans, a priori assumption of DIF will produce over predictions of sol-Fe deposition rates in the Southern Ocean in comparison to GEOS-Chem/DFeS model predictions. This is due to that fact that on average our model predicts minimal amounts of

sol-Fe production due to atmospheric processing. Overall, from Fig. 5.12 it can be seen that large errors are produced with assuming DIFs in comparison to the explicit calculations of sol-Fe production by GEOS-Chem/DFeS.

#### **5.4. Conclusions**

The atmospheric deposition of mineral dust is a major supply pathway of essential micronutrients for marine primary productivity in many global remote oceanic regions and can be a controlling factor in marine biogeochemistry and overall climate. During this study, bioavailable micronutrient deposition rates were predicted by the global 3-D CTM GEOS-Chem implemented with the newest version of our nutrient dissolution scheme. In order to capture the spatio-temporal variability of these fluxes model runs were conducted for an entire year between March 2009 and February 2010. The advantage of using GEOS-Chem/DFeS is the model's ability to explicitly predict the fraction of individual micronutrients that are bioavailable in mineral dust without making any a priori assumptions. To the best of our knowledge, there are no 3-D global models that can explicitly calculate dissolution-precipitation kinetics of Fe oxides/clay minerals, organic-Fe interactions, Fe photochemistry, acid-based dissolution of  $\text{PO}_4^{3-}$ -laden mineral dust, and bioavailable  $\text{NO}_3^-$  formation on mineral dust during atmospheric transport. Overall, our newest version of GEOS-Chem/DFeS provides the most comprehensive dataset of micronutrient deposition for usage within global atmospheric, marine biogeochemistry, and climate models.

Our updated nutrient dissolution scheme expands on our original Fe dissolution module through the addition of: 1) organic ligand-promoted Fe dissolution, 2) Fe

photochemistry, 3) acid-based  $\text{PO}_4^{3-}$  dissolution, 4) bioavailable  $\text{NO}_3^-$  formation, 5) global mineralogical database, 6) individual Fe-containing mineralogy, and 7) source specific dust/nutrient dissolution treatment. Interesting results due to these model developments include the presence of organic acids significantly increased sol-Fe deposition rates between 10% to well over 50% in regions with large oxalate concentrations. The implementation of Fe photochemistry also allowed for the quantification of the deposition of the more bioavailable form of ferrous Fe (Fe(II)) to marine surface waters. These fluxes of sol-Fe are important as they can be used in marine biogeochemistry models since the different species of Fe(II) and Fe(III) will have highly different chemical pathways in oceanic environments. Additional processes added to the model (e.g., using a global mineralogical database and specifically treating Fe-containing Fe mineralogy) allowed for the explicit calculation of the bioavailable portions of sol-Fe,  $\text{PO}_4^{3-}$ , and  $\text{NO}_3^-$  within deposited mineral dust which achieved the overall goal of allowing GEOS-Chem/DFeS to simulate the atmospheric supply of all the major limiting micronutrients in marine ecosystems.

During this study, GEOS-Chem/DFeS-predicted bioavailable nutrient fluxes were calculated and presented to oceanic regions that have marine primary productivity limited by each individual nutrient (see Fig. 5.11). During the simulation time period, sol-Fe deposition rates are predicted to serve as a biogeochemically important source of Fe to the HNLC oceans such as: directly off the coast of North Africa and the Middle East ( $> 1.0 \mu\text{g m}^{-2} \text{day}^{-1}$ ), in the subarctic North Pacific Ocean (up to  $0.1 \mu\text{g m}^{-2} \text{day}^{-1}$ ), and in Southern Ocean (up to  $1.0 \mu\text{g m}^{-2} \text{day}^{-1}$ ). Additionally, mineral dust also supplied a source of sol-Fe up to  $\sim 0.01$

$\mu\text{g m}^{-2} \text{ day}^{-1}$  to the equatorial Pacific Ocean. Mineral dust deposition also supplied  $\text{PO}_4^{3-}$  to oceanic regions with marine primary productivity limited by P such as: the North Atlantic Ocean and Indian Ocean (between  $1.0 - 10.0 \mu\text{g m}^{-2} \text{ day}^{-1}$ ) and also the subarctic South Atlantic and Indian Oceans (up to  $\sim 0.5 \mu\text{g m}^{-2} \text{ day}^{-1}$ ). Marine ecosystems that are assumed to be limited by the supply of bioavailable N are predicted by GEOS-Chem/DFeS to receive important atmospheric fluxes of  $\text{NO}_3^-$ -laden-dust such as the: North and South Atlantic, North Pacific Ocean, and Indian Ocean with deposition rates ranging between  $1.0$  and  $100 \mu\text{g m}^{-2} \text{ day}^{-1}$ . Overall, our study demonstrates the importance of using a highly comprehensive model in order to simulate the magnitudes and large seasonal and temporal variability of mineral dust and bioavailable nutrient fluxes.

Overall, during the simulation time period, GEOS-Chem/DFeS predicted an annual total of  $\sim 0.17$ ,  $0.20$ , and  $75 \text{ Tg}$  of sol-Fe,  $\text{PO}_4^{3-}$ , and  $\text{NO}_3^-$  was deposited to the global oceans, respectively. These annual totals of micronutrient deposition to the global oceans prove to be consistent with recent modeling studies. However, the advantage of applying our highly comprehensive model in comparison to past modeling studies is GEOS-Chem/DFeS explicitly calculates the bioavailability of all essential micronutrients without making any a priori assumptions. Therefore, our model captures the large spatio-temporal variability of the fraction of bioavailability of these micronutrients within mineral dust that has been measured in nature [i.e., *Baker et al.*, 2006]. This ability to simulate the highly variable fractions of nutrient solubility is important because to-date most marine biogeochemistry and climate models use a priori and constant fraction of solubility to calculate essential micronutrient

deposition rates to drive marine primary productivity. These assumptions can produce large errors in deposition rates used to predict and evaluate marine biogeochemistry and its influence on climate. Therefore, we suggest the usage of our publically available micronutrient deposition flux datasets for further usage in global marine biogeochemistry and climate models.

### **Acknowledgements**

This research was supported by the National Science Foundation through the grant ATM-0826117 and by the National Aeronautics & Space Administration (NASA) through grant no NNX11AG72G. The authors would like to thank Dr. Daniel Jacob and the Harvard University Atmospheric Chemistry Modeling Group for providing the basemodel GEOS-Chem used during our research.

## References

- Alexander, B., J. Savarino, C. C. W. Lee, R. J. Park, D. J. Jacob, M. H. Thiemens, Q. B. Li, and R. M. Yantosca (2005), Sulfate formation in seasalt aerosols: Constraints from oxygen isotopes, *J. Geophys. Res.*, *110*, D10307, doi:10.1029/2004JD005659.
- Arimoto, R., W. Balssam, and C. Schloesslin (2002), Visible spectroscopy of aerosol particles collected on filters: Iron-oxide minerals, *Atmos. Environ.*, *36*, 89-96.
- Baker, A. R., and T. D. Jickells (2006), Mineral particle size as a control on aerosol iron solubility, *Geophys. Res. Lett.*, *33*, L17608, doi:10.1029/2006GL026557.
- Baker, A.R., Jickells, T.D., Witt, M. and Ligne, K.L. (2006) Trends in the solubility of iron, aluminium, manganese and phosphorus in aerosol collected over the Atlantic Ocean. *Marine Chemistry*, *98*(1), 43-58.
- Barbeau, K., E. L. Rue, K. W. Bruland, and A. Butler (2001), Photochemical cycling of iron in the surface ocean mediated by microbial iron(III)-binding ligands, *Nature*, *413*, 409-413.
- Bey, I., D. J. Jacob, R. M. Yantosca, J. A. Logan, B. Field, A. M. Fiore, Q. Li, H. Liu, L. J. Mickley, and M. Schultz (2001), Global modeling of tropospheric chemistry with assimilated meteorology: Model description and evaluation, *J. Geophys. Res.*, *106*(D19), 23,073-23,095.
- Boyd, P. W., Watson, A. J., Law, C. S., Abraham, E. R., Trull, T., Murdoch, R., Bakker, D. C. E., Bowie, A. R., Buesseler, K. O., Chang, H., Charette, M., Croot, P., Downing, K., Frew, R., Gall, M., Hadfield, M., Hall, J., Harvey, M., Jameson, G., LaRoche, J., Liddicoat, M., Ling, R., Maldonado, M. T., McKay, R. M., Nodder, S., Pickmere, S., Pridmore, R., Rintoul, S., Safi, K., Sutton, P., Strzepek, R., Tanneberger, K., Turner, S., Waite, A., and Zeldis, J.: A mesoscale phytoplankton bloom in the polar Southern Ocean stimulated by iron fertilization, *Nature*, *407*, 695-702, 2000.
- Boyd, P. W., Jickells, T., Law, C. S., Blain, S., Boyle, E. A., Buesseler, K. O., Coale, K. H., Cullen, J. J., de Baar, H. J. W., Follows, M., Harvey, M., Lancelot, C., Levasseur, M., Owens, N. P. J., Pollard, R., Rivkin, R. B., Sarmiento, J., Schoemann, V., Smetacek, V., Takeda, S., Tsuda, A., Turner, S., and Watson, A. J.: Mesoscale iron enrichment experiments 1993-2005: Synthesis and future directions, *Science*, *315*, 612-617, 2007.
- Chen, Y., and R. L. Siefert (2003), Determination of various types of labile atmospheric iron over remote oceans, *J. Geophys. Res.*, *108*(D24), 4774, doi:10.1029/2003JD003515.

- Chin, M., P. Ginoux, S. Kinne, O. Torres, B. Holben, B. Duncan, R. Martin, J. Logan, A. Higurashi, and T. Nakajima (2002), Tropospheric aerosol optical thickness from the GOCART model and comparisons with satellite and sunphotometer measurements, *J. Atmos. Sci.*, *59*, 461-483.
- Coale, K. H., et al. (1996), A massive phytoplankton bloom induced by an ecosystem-scale iron fertilization experiment in the equatorial Pacific Ocean, *Nature*, *383*, 495–501, doi:10.1038/383495a0.
- Cornell R. M., A. M. Posner, and J. P. Quirk (1975), The complete dissolution of goethite, *J. Appl. Chem. Biotechnol.*, *25*, 701-706.
- Cornell R. M., and P. W. Schindler (1987), Photochemical dissolution of goethite in acid/oxalate solution, *Clays Clay Miner.*, *35*, 347-352.
- Cornell, R. M., and U. Schwertmann (1996), *The Iron Oxides, Structure, Properties, Reactions, Occurrence and Uses*, 573 pp., John Wiley, Hoboken, N. J.
- Cwiertny, D. M., J. Baltrusaitis, G. J. Hunter, A. Laskin, M. M. Scherer, and V. H. Grassian (2008), Characterization and acid-mobilization study of iron-containing mineral dust source materials, *J. Geophys. Res.*, *113*, D05202, doi:10.1029/2007JD009332.
- Cwiertny, D. M., G. J. Hunter, J. M. Pettibone, M. M. Scherer, and V. H. Grassian (2009), Surface Chemistry and Dissolution of  $\alpha$ -FeOOH Nanorods and Microrods: Environmental Implications of Size-Dependent Interactions with Oxalate, *J. Phys. Chem.*, *113*, 2175-2186.
- Dedik, A. N., and P. Hoffmann (1992), Chemical characterization of iron in atmospheric aerosols, *Atmos. Env.*, *26*, 2545-2548.
- Duce, R. A., and N. W. Tindale (1991), Atmospheric transport of iron and its deposition in the ocean, *Limnol. Oceanogr.*, *36*, 1715-1726.
- Duce, R. A., et al. (2008), Impacts of atmospheric anthropogenic nitrogen on the open ocean, *Science*, *320*(5878), 893–897, doi:10.1126/science. 1150369.
- Elser, J. J., M. E. S. Bracken, E. E. Cleland, D. S. Gruner, W. S. Harpole, H. Hillebrand, J. T. Ngai, E. W. Seabloom, J. B. Shurin, and J. E. Smith (2007), Global analysis of nitrogen and phosphorus limitation of primary producers in freshwater, marine and terrestrial ecosystems, *Ecol. Lett.*, *10*, 1135-1142.
- Fairlie, T. D., D. J. Jacobs, and R. J. Rokjin (2007), The impact of transpacific transport of mineral dust in the United States, *Atmos. Env.*, *41*, 1251-1266.

- Fairlie, T. D., D. J. Jacob, J. E. Dibb, B. Alexander, M. A. Avery, A. van Donkelaar, and L. Zhang (2010), Impact of mineral dust on nitrate, sulfate, and ozone in transpacific Asian pollution plumes, *Atmos. Chem. Phys.*, *10*, 3999-4012, doi:10.5194/acp-10-3999-2010.
- Falkowski, P. G., R. T. Barber, and V. Smetacek (1998), Biogeochemical controls and feedbacks on ocean primary production, *Science*, *281*(5374), 200-206, doi:10.1126/science.281.5374.200.
- Faust, B. C., and R. G. Zepp (1993), Photochemistry of Aqueous Iron(III)-Polycarboxylate Complexes: Roles in the Chemistry of Atmospheric and Surface Waters, *Environ. Sci. Technol.*, *27*, 2517-2522.
- Fu, T. -M., D. J. Jacob, F. Wittrock, J. P. Burrows, M. Vrekoussis, and D. Henze (2008), Global budgets of atmospheric glyoxal and methylglyoxal, and implications for formation of secondary organic aerosols, *J. Geophys. Res.*, *113*, D15303, doi:10.1029/2007JD009505.
- Fu, H., D. M. Cwiertny, G. R. Carmichael, M. M. Scherer, and V. H. Grassian (2010), Photoreductive dissolution of Fe-containing mineral dust particles in acidic media, *J. Geophys. Res.*, *115*, D11304, doi:10.1029/2009JD012702.
- Generoso, S., I. Bey, M. Labonne, and F. M. Breon (2008) Aerosol vertical distribution in dust outflow over the atlantic: Comparisons between Geos-chem and cloud-aerosol lidar and infrared pathfinder satellite observation (calipso), *J. Geophys. Res.*, *113*, D24209, doi:10.1029/2008jd010154.
- Ginoux, P., M. Chin, I. Tegen, J. M. Prospero, B. Holben, O. Dubovik, and S.-J. Lin (2001), Sources and distributions of dust aerosols simulated with the GOCART model, *J. Geophys. Res.*, *106*, 20,255-20,273.
- Graham, W. F., and R. A. Duce (1979), Atmospheric pathways of the phosphorus cycle, *Geochimica et Cosmochimica Acta*, *43*, 1195-1208.
- Guieu, C., and J. Thomas (1996), *The Impact of Desert Dust across the Mediterranean*, Kluwer Acad. Publ., Dordrecht.
- Hand, J. L., et al. (2004), Estimates of atmospheric processed soluble iron from observations and a global mineral aerosol model: Biogeochemical implications, *J. Geophys. Res.*, *109*, D17205, doi:10.1029/2004JD004574.
- Heald, C. L., D. J. Jacob, D. B. A. Jones, P. I. Palmer, J. A. Logan, D. G. Streets, G. W. Sachse, J. C. Gille, R. N. Hoffman, and T. Nehr Korn (2004), Comparative inverse analysis

- of satellite (MOPITT) and aircraft (TRACE-P) observations to estimate Asian sources of carbon monoxide, *J. Geophys. Res.*, *109*, doi:10.1029/2004JD005185.
- Heald, C. L., D. J. Jacob, R. J. Park, B. Alexander, T. D. Fairlie, R. M. Yantosca, and D. A. Chu (2006), Transpacific transport of Asian anthropogenic aerosols and its impact on surface air quality in the United States, *J. Geophys. Res.*, *111*, D14310, doi:10.1029/2005JD006847.
- Hoffmann, P., A. N. Dedik, J. Ensling, S. Weinbruch, S. Weber, T. Sinner, P. Gutlich, and H. M. Ornter (1996), Speciation of iron in atmospheric aerosol samples, *J. Aerosol Sci.*, *27*, 325-337.
- Jacobson, M. Z. (1995), Computation of global photochemistry with SMVGEARII, *Atmos., Environ.*, *29A*, 2541-2546.
- Jacobson, M. Z. (1998), Improvement of SMVGEARII on vector and scalar machines through absolute error tolerance control, *Atmos., Environ.*, *32*, 791-796.
- Jacobson, M. Z., and R. P. Turco (1994), SMVGEAR: A Sparse-Matrix, Vectorized Gear Code for Atmospheric Models, *Atmos. Env.*, *2*, 273-284.
- Jickells, T. D., An, Z. S., Andersen, K. K., Baker, A. R., Bergametti, G., Brooks, N., Cao, J. J., Boyd, P. W., Duce, R. A., Hunter, K. A., Kawahata, H., Kubilay, N., LaRoche, J., Liss, P. S., Mahowald, N., Prospero, J. M., Ridgwell, A. J., Tegen, I., and Torres, R.: Global Iron Connections Between Desert Dust, Ocean Biogeochemistry, and Climate, *Science*, *308*, 67-71, 2005.
- Johnson, M. S., N. Meskhidze, F. Solmon, S. Gassó, P. Y. Chuang, D. M. Gaiero, R. M. Yantosca, S. Wu, Y. Wang, and C. Carouge (2010), Modeling dust and soluble iron deposition to the South Atlantic Ocean, *J. Geophys. Res.*, *115*, D15202, doi:10.1029/2009JD013311.
- Johnson, M. S., N. Meskhidze, V. P. Kiliyanpilakkil, and S. Gassó (2011), Understanding the transport of Patagonian dust and its influence on marine biological activity in the South Atlantic Ocean, *Atmos. Chem. Phys.*, *11*, 2487-2502, doi:10.5194/acp-11-2487-2011.
- Journet, E., K. V. Desboeufs, S. Caquineau, and J.-L. Colin (2008), Mineralogy as a critical factor of dust iron solubility, *Geophys. Res. Lett.*, *35*, L07805, doi:10.1029/2007GL031589.

- Kawamura, K., and I. R. Kaplan (1989), Organic compounds in rainwater. In: Hansen, L.D., Eatough, D.J. (Eds.), *Organic Compounds in Rainwater*, second ed. CRC Press, Boston, 33-284.
- Kawamura, K. and K. Ikushima (1993), Seasonal changes in the distribution of dicarboxylic acids in the urban atmosphere, *Environ. Sci. Technol.*, *27*, 2227-2235.
- Kleindienst, T. E.; D. F. Smith, W. Li; E. O. Edney, D. J. Driscoll, R. E. Speer, and W. S. Weathers (1999), Secondary organic aerosol formation from the oxidation of aromatic hydrocarbons in the presence of dry submicron ammonium sulfate aerosol, *Atmos. Environ.*, *33*, 3669-3681.
- Krishnamurthy, A., J. K. Moore, C. S. Zender, and C. Luo (2007), Effects of atmospheric inorganic nitrogen deposition on ocean biogeochemistry, *J. Geophys. Res.*, *112*, G02019, doi:10.1029/2006JG000334.
- Larsen, O., and D. Postma (2001), Kinetics of reductive bulk dissolution of lepidocrocite, ferrihydrite, and goethite, *Geochim. Cosmochim. Acta*, *65*(9), 1367–1379, doi:10.1016/S0016-7037(00)00623-2.
- Legrand, M., S. Preunkert, T. Oliveira, C. Pio, S. Hammer, A. Gelencser, A. Kasper-Giebl, and P. Laj (2007), Origin of C<sub>2</sub>–C<sub>5</sub> dicarboxylic acids in the European atmosphere inferred from year round aerosol study conducted at a west-east transect, *J. Geophys. Res.*, *112*, D23S07, doi:10.1029/2006JD008019.
- Liu, H., D. J. Jacob, I. Bey, and R. M. Yantosca (2001), Constraints from 210Pb and 7Be on wet deposition and transport in a global three-dimensional chemical tracer model driven by assimilated meteorological fields, *J. Geophys. Res.*, *106*(D11), 12,109-12,128.
- Mahowald, N., Jickells, T. D., Baker, A. R., Artaxo, P., Benitez-Nelson, C. R., Bergametti, G., Bond, T. C., Chen, Y., Cohen, D. D., Herut, B., Kubilay, N., Losno, R., Luo, C., Maenhaut, W., McGee, K. A., Okin, G. S., Siefert, R. L., and Tsukuda, S (2008), Global distribution of atmospheric phosphorus sources, concentrations and deposition rates, and anthropogenic impacts, *Global Biogeochem. Cy.*, *22*, GB4026, doi:10.1029/2008GB003240.
- Mahowald, N., S. Engelstaedter, C. Luo, A. Sealy, P. Artaxo, C. B. Nelson, S. Bonnet, Y. Chen, P. Y. Chuang, D. D. Cohen, F. Dulac, B. Herut, A. M. Johansen, N. Kubilay, R. Losno, W. Maenhaut, A. Paytan, J. M. Prospero, L. M. Shank, and R. L. Siefert (2009), Atmospheric Iron Deposition: Global Distribution, Variability, and Human Perturbations, *Annu. Rev. Mar. Sci.*, 245-278.

- Mahowald, N. (2011), Aerosol Indirect Effect on Biogeochemical Cycles and Climate, *Science*, 334, doi:10.1126/science.1207374.
- Martin, J. H.: Glacial-interglacial CO<sub>2</sub> change: The Iron Hypothesis, *Paleoceanography*, 5, 1-13 1990.
- Martin, J. H. and Fitzwater, S. E.: Iron-deficiency limits phytoplankton growth in the northeast pacific subarctic, *Nature*, 331, 341-343, 1988.
- Martin, S. T. (2005), Precipitation and dissolution of iron and manganese oxides. In: Grassian, V.H. (Ed.), *Environmental Catalysis*, Marcel-Dekker CRC Press, Boca Raton, 61-81.
- Meskhidze, N., W. L. Chameides, A. Nenes, and G. Chen (2003), Iron mobilization in mineral dust: Can anthropogenic SO<sub>2</sub> emissions affect ocean productivity?, *Geophys. Res. Lett.*, 30(21), 2085, doi:10.1029/2003GL018035.
- Meskhidze, N., W. L. Chameides, and A. Nenes (2005), Dust and pollution: A recipe for enhanced ocean fertilization?, *J. Geophys. Res.*, 110, D03301, doi:10.1029/2004JD005082.
- Miller, W. L., and D. R. Kester (1994), Photochemical iron reduction and iron bioavailability in seawater, *J. Mar. Res.*, 52, 325-343.
- Myriokefalitakis, S., M. Vrekoussis, K. Tsigaridis, F. Wittrock, A. Richter, C. Bruhl, R. Volkamer, J. P. Burrows, and M. Kanakidou (2008), The influence of natural and anthropogenic secondary sources on the glyoxal global distribution, *Atmos. Chem. Phys.*, 8, 4965-4981, doi:10.5194/acp-8-4965-2008.
- Myriokefalitakis, S., K. Tsigaridis, N. Mihalopoulos, J. Sciare, A. Nenes, A. Segers, and M. Kanakidou (2011), In-cloud oxalate formation in the global troposphere: a 3-D modeling study, *Atmos. Chem. Phys. Discuss.*, 11, 485-530.
- Nenes, A., S. N. Pandis, and C. Pilinis (1998), ISORROPIA: A new thermodynamic equilibrium model for multiphase multicomponent inorganic aerosols, *Aquat. Geochem.*, 4(1), 123–152.
- Nenes, A., M. D. Krom, N. Mihalopoulos, P. Van Cappellen, Z. Shi, A. Bougiatioti, P. Zarmas, and B. Herut (2011), Atmospheric acidification of mineral aerosols: a source of bioavailable phosphorus for the oceans, *Atmos. Chem. Phys.*, 11, 6252-6272.

- Nickovic, S., A. Vukovic, M. Vujadinovic, V. Djurdjevic, and G. Pejanovic (2012), Technical Note: Minerals in dust productive soils – impacts and global distributions, *Atmos. Chem. Phys.* *12*, 26009-26034.
- Okin, G. S., et al. (2011), Impacts of atmospheric nutrient deposition on marine productivity: Roles of nitrogen, phosphorus, and iron, *Global Biogeochem. Cycles*, *25*, GB2022, doi:10.1029/2010GB003858.
- Olsen, J., M. Prather, T. Berntsen, G. Carmichael, R. Chatfield, P. Connell, R. Derwent, L. Horowitz, S. Jin, M. Kanakidou, P. Kasibhatla, R. Kotamarthi, M. Kuhn, K. Law, J. Penner, L. Perliski, S. Sillman, F. Stordal, A. Thompson, and O. Wild (1997), Results from the Intergovernmental Panel on Climate Change photochemical model intercomparison (PhotoComp), *J. Geophys. Res.*, *102*, 5979-5991.
- Ooki, A., J. Nishioka, T. Ono, and S. Noriki (2009), Size dependence of iron solubility of Asian mineral dust particles, *J. Geophys. Res.*, *114*, D03202, doi:10.1029/2008JD010804.
- Paerl, H. W., and D. R. Whittall (1999), Anthropogenically-derived atmospheric nitrogen deposition, marine eutrophication and harmful algal bloom expansion: Is there a link?, *Ambio*, *28*, 307-311.
- Paris, R., K. V. Desboeufs, and E. Journet (2011), Variability of dust iron solubility in atmospheric waters: Investigation of the role of oxalate organic complexation, *Atmos. Environ.*, *45*, 6510-6517.
- Park, R. J., D. J. Jacob, B. D. Field, R. M. Yantosca, and M. Chin (2004), Natural and transboundary pollution influences on sulfate nitrate-ammonium aerosols in the United States: Implications for policy, *J. Geophys. Res.*, *109*, D15204, doi:10.1029/2003JD004473.
- Pehkonen, S. O., R. Siefert, Y. Erel, S. Webb, and M. R. Hoffmann (1993), Photoreduction of iron oxyhydroxides in the presence of important atmospheric organic compounds, *Environ. Sci. Technol.*, *27*, 2056-2062.
- Prospero, J. M., P. Ginoux, O. Torres, and S. E. Nicholson (2002), Environmental characterization of global sources of atmospheric soil dust identified with the Nimbus 7 Total Ozone Mapping Spectrometer (TOMS) absorbing aerosol product, *Rev. Geophys.*, *40*(3), 1002, doi:10.1029/2000RG000095.
- Ruellan, S., H. Cachier, A. Gaudichet, P. Masclet, and J. P. Lacaux (1999), Airborne aerosols over Central Africa during the experiment for regional sources and sinks of oxidants (EXPRESSO), *J. Geophys. Res.*, *104*, 306730-30690.

- Sciare, J., O. Favez, R. Sarda-Este`ve, K. Oikonomou, H. Cachier, and V. Kazan (2009), Long-term observations of carbonaceous aerosols in the Austral Ocean atmosphere: Evidence of a biogenic marine organic source, *J. Geophys. Res.*, *114*, D15302, doi:10.1029/2009JD011998.
- Schwertmann, U. (1991), Solubility and dissolution of iron oxides, *Plant and Soil*, *130*, 1-25.
- Seinfeld, J. H., and S. N. Pandis (1998), *Atmospheric Chemistry and Physics: From Air Pollution to Climate Change*, Wiley, New York.
- Shi, Z., M. D. Krom, S. Bonneville, A. R. Baker, T. D. Jickells, and L. G. Benning (2009), Formation of Iron Nanoparticles and Increase in Iron Reactivity in Mineral Dust during Simulated Cloud Processing, *Environ. Sci. Technol.*, *43*, 6592-6596.
- Singer, A., S. Dultz, and E. Argaman (2004), Properties of the nonsoluble fractions of suspended dust over the Dead Sea, *Atmos. Environ.*, *38*, 1745-1753.
- Sinreich, R., S. Coburn, B. Dix, and R. Volkamer (2010), Ship-based detection of glyoxal over the remote tropical Pacific Ocean, *Atmos. Chem. Phys.*, *10*, 11359–11371, doi:10.5194/acp-10-11359-2010.
- Solmon, F., P. Y. Chuang, N. Meskhidze, and Y. Chen (2009), Acidic processing of mineral dust iron by anthropogenic compounds over the north Pacific Ocean, *J. Geophys. Res.*, *114*, D02305, doi:10.1029/2008JD010417.
- Song, W., W. Ma, J. Ma, C. H. Chen, and J. Zhao (2005), Photochemical oscillation of Fe(II)/Fe(III) ratio induced by periodic flux of dissolved organic matter, *Environ. Sci. Technol.*, *39*, 3121-3127.
- Spokes, L., and T. D. Jickells (1996), Factors controlling the solubility of aerosol trace metals in the atmosphere and on mixing into seawater, *Aquat. Chem.*, *1*, 355-374.
- Sullivan, R. C., M. J. K. Moore, M. D. Petters, S. M. Kreidenweis, G. C. Roberts, and K. A. Prather (2009), Effect of chemical mixing state on the hygroscopicity and cloud nucleation properties of calcium mineral dust particles, *Atmos., Chem., Phys.*, *9*, 3303-3316.
- Taylor, S. R., and S. M. McLennan (1985), *The Continental Crust: its Composition and Evolution*, Blackwell Scientific, Oxford, England.
- Usher, C. R., A. E. Michel, and V. H. Grassian (2003), Reactions on mineral dust, *Chem. Rev.*, *103*, 4883-4939.

- van Donkelaar, A., R. V. Martin, and R. J. Park (2006), Estimating ground-level PM<sub>2.5</sub> using aerosol optical depth determined from satellite remote sensing, *J. Geophys. Res.*, *111*, D21201, doi:10.1029/2005JD006996.
- Voelker, B. M., F. M. M. Morel, and B. Sulzberger (1997), Iron redox cycling in surface waters: effect of humic substances and light, *Environ. Sci. Technol.*, *31*, 1004-1011.
- Volkamer, R., S. C. Coburn, B. K. Dix, and R. Sinreich (2010), The Eastern Pacific Ocean is a source for short lived atmospheric gases: glyoxal and iodine oxide, *CLIVAR Exchanges*, *15*, 30-33.
- Wiederhold, J. G., et al. (2006), Iron isotope fractionation during proton-promoted, ligand-controlled, and reductive dissolution of goethite, *Environ. Sci. Technol.*, *40*(12), 3787–3793, doi:10.1021/es052228y.
- Wild, O., Q. Zhu, and M. J. Prather (2000), Fast-J: Accurate simulation of in- and below-cloud photolysis in global chemical models, *J. Atmos. Chem.*, *37*, 245-282.
- Wu, S., L. J. Mickley, D. J. Jacob, J. A. Logan, R. M. Yantosca, and D. Rind (2007), Why are there large differences between models in global budgets of tropospheric ozone?, *J. Geophys. Res.*, *112*, D05302, doi:10.1029/2006JD007801.
- Wu, S., L. J. Mickley, E. M. Leibensperger, D. J. Jacob, D. Rind, and D. G. Streets (2008), Effects of 2000–2050 global change on ozone air quality in the United States, *J. Geophys. Res.*, *113*, D06302, doi:10.1029/2007JD008917.
- Xu, N., and Y. Gao (2008), Characterization of hematite dissolution affected by oxalate coating, kinetics and pH, *Appl. Geochem.*, *23*(4), 783-793.
- Yu, J., X. Huang, J. Xu, and M. Hu (2005), When aerosol sulfate goes up, so does oxalate: implication for the formation mechanisms of oxalate, *Environ. Sci. Technol.*, *39*(1), 128-133.
- Zender, C. S., D. Newman, and O. Torres (2003), Spatial heterogeneity in aeolian erodibility: Uniform, topographic, geomorphic, and hydrologic hypotheses, *J. Geophys. Res.*, *108*, doi: 10.1029/2002JD003039.
- Zhang, L., S. L- Gong, J. Padro, and L. Barrie (2001), A Size-segregated Particle Dry Deposition Scheme for an Atmospheric Aerosol Module, *Atmos. Environ.*, *35*(3), 549-560.
- Zhuang, G., Yi, Z., Duce, R. A., and Brown, P. R.: Link between iron and sulphur cycles suggested by detection of Fe(II) in remote marine aerosols, *Nature*, *355*, 537-539, 1992.

Zuo, Y., and J. Holgne (1992), Formation of hydrogen peroxide and depletion of oxalic acid in atmospheric water by photolysis of iron(III)-oxalato complexes, *Environ. Sci. Technol.*, 26, 1014-1022.

## Tables

Table 5.1 Tracers implemented into GEOS-Chem/DFeS and chemical forms allowed

<b>Tracer Symbol</b>	<b>Chemical Forms Allowed for Species</b>
<b>Fe(III)</b>	$(\text{Fe}^{3+})_{\text{aq}}$ , $(\text{Fe}(\text{OH})^{2+})_{\text{aq}}$ , $(\text{Fe}(\text{OH})_2^+)_{\text{aq}}$ , $(\text{Fe}(\text{OH})_3^0)_{\text{aq}}$ , $(\text{Fe}(\text{OH})_4^-)_{\text{aq}}$ , $(\text{FeSO}_4^+)_{\text{aq}}$ , $(\text{Fe}(\text{OH})_3)_s$
<b>Fe(II)</b>	$(\text{Fe}^{2+})_{\text{aq}}$ , $(\text{Fe}(\text{OH})^+)_{\text{aq}}$ , $(\text{Fe}(\text{OH})_2^0)_{\text{aq}}$ , $(\text{Fe}(\text{OH})_2)_s$
<b>Fe(III)-oxalate</b>	$(\text{Fe}(\text{C}_2\text{O}_4^{2-})^+)$ , $(\text{Fe}(\text{C}_2\text{O}_4^{2-})_2^-)$ , $(\text{Fe}(\text{C}_2\text{O}_4^{2-})_3^{3-})$
<b>Oxalate</b>	$(\text{C}_2\text{O}_4^{2-})$
<b>Dust-<math>\text{PO}_4^{3-}</math></b>	$\text{PO}_4^{3-}$
<b>Dust-<math>\text{NO}_3^-</math></b>	$\text{NO}_3^-$

Table 5.2 Coefficients used to derive oxalate-promoted Fe dissolution

<b>Fe-containing mineral</b>	<b><math>a_i</math></b>	<b><math>b_i</math></b>	<b><math>R^2</math></b>
<b>Hematite</b>	$3.5 \times 10^{-12}$	$-1.9 \times 10^{-12}$	0.997
<b>Goethite</b>	$1.3 \times 10^{-11}$	$7.0 \times 10^{-13}$	0.987
<b>Illite</b>	$3.1 \times 10^{-10}$	$5.8 \times 10^{-11}$	0.999

**Table 5.3.** Kinetic and photochemical reactions implemented into SMV-GEAR II

No	Kinetic Equations	Reaction Rates $M^{-n}s^{-1}$	Source
<b>Photolysis of Fe (III) species</b>			
J1	$Fe(OH)^{2+} + hv \rightarrow Fe^{2+} + OH^{\cdot}$	$4.51 \times 10^{-3}$	<i>Benkelberg and Warneck, [1995]</i>
J2	$Fe(C_2O_4)_2^- + hv \rightarrow Fe^{2+} + C_2O_4^{2-} + C_2O_4^{\cdot-}$	$2.47 \times 10^{-2}$	<i>Faust and Zepp [1993]</i>
J3	$Fe(C_2O_4)_3^{3-} + hv \rightarrow Fe^{2+} + 2C_2O_4^{2-} + C_2O_4^{\cdot-}$	$1.55 \times 10^{-2}$	<i>Faust and Zepp [1993]</i>
<b>Fenton reactions</b>			
K1	$Fe^{2+} + H_2O_2 \rightarrow Fe^{3+} + OH^{\cdot} + OH^-$	$5.24 \times 10^1$	<i>Kremer [2003]</i>
K2	$FeC_2O_4 + H_2O_2 \rightarrow FeC_2O_4^{\cdot+} + OH^{\cdot} + OH^-$	$5.24 \times 10^4$	<i>Sedlak and Hoigné [1993]</i>
<b>Fe reduction and oxidation</b>			
K3	$Fe^{2+} + O_2^{\cdot-} + 2H^+ \rightarrow Fe^{3+} + H_2O_2$	$1.0 \times 10^7$	<i>Rush and Bielski, [1985]</i>
K4	$Fe^{2+} + HO_2^{\cdot} + H^+ \rightarrow Fe^{3+} + H_2O_2$	$1.2 \times 10^6$	<i>Rush and Bielski, [1985]</i>
K5	$Fe^{2+} + NO_3 \rightarrow Fe^{3+} + NO_3^-$	$8.0 \times 10^6$	<i>Pikaev et al. [1974]</i>
K6	$Fe^{2+} + NO_2 + H^+ \rightarrow Fe^{3+} + HNO_2$	$3.1 \times 10^4$	<i>Epstein et al. [1982]</i>
K7	$Fe(OH)^{2+} + O_2^{\cdot-} \rightarrow Fe^{2+} + O_2 + OH^-$	$1.5 \times 10^8$	<i>Rush and Bielski, [1985]</i>
K8	$Fe(OH)^{2+} + HO_2^{\cdot} \rightarrow Fe^{2+} + O_2 + H_2O$	$1.3 \times 10^5$	<i>Ziajka et al., 1994</i>
K9	$Fe^{2+} + O_3 \rightarrow FeO^{2+} + O_2$	$8.2 \times 10^5$	<i>Logager et al. [1992]</i>
K10	$FeO^{2+} + H_2O \rightarrow Fe^{3+} + OH^{\cdot} + OH^-$	$1.3 \times 10^{-2}$	<i>Jacobsen et al. [1998]</i>
K11	$FeO^{2+} + OH^{\cdot} + H^+ \rightarrow Fe^{3+} + H_2O_2$	$1.0 \times 10^7$	<i>Jacobsen et al. [1998]</i>
K12	$FeO^{2+} + H_2O_2 \rightarrow Fe^{3+} + HO_2^{\cdot} + OH^-$	$1.0 \times 10^4$	<i>Jacobsen et al. [1998]</i>
K13	$FeO^{2+} + HO_2^{\cdot} \rightarrow Fe^{3+} + O_2 + OH^-$	$2.0 \times 10^6$	<i>Jacobsen et al. [1998]</i>
<b><math>HO_2^{\cdot}/O_2^{\cdot-}</math> reactions</b>			
K14	$HO_2^{\cdot} + HO_2^{\cdot} \rightarrow H_2O_2 + O_2$	$8.3 \times 10^5$	<i>Bielski et al. [1985]</i>
K15	$HO_2^{\cdot} + O_2 + H^+ \rightarrow H_2O_2 + O_2$	$9.7 \times 10^7$	<i>Bielski et al. [1985]</i>
K16	$CO_2^{\cdot-} + O_2 \rightarrow CO_2 + O_2^{\cdot-}$	$2.4 \times 10^9$	<i>Sedlak and Hoigné [1993]</i>
<b>Oxalate reactions</b>			
K17	$Fe(C_2O_4)_n^{3-2n} + O_2^{\cdot-} \rightarrow Fe(C_2O_4)_n^{2-2n} + O_2$	$1.0 \times 10^6$	<i>Sedlak and Hoigné [1993]</i>
K18	$Fe(C_2O_4)_n^{3-2n} + HO_2^{\cdot} \rightarrow Fe(C_2O_4)_n^{2-2n} + O_2 + H^+$	$1.2 \times 10^5$	<i>Sedlak and Hoigné [1993]</i>
K19	$C_2O_4^{2-} + OH^{\cdot} \rightarrow OH^- + C_2O_4^{\cdot-}$	$5.3 \times 10^6$	<i>Getoff et al. [1971]</i>
K20	$C_2O_4^{2-} + NO_3 \rightarrow NO_3^- + C_2O_4^{\cdot-}$	$2.2 \times 10^8$	<i>Raabe [1996]</i>
K21	$C_2O_4^{2-} + O_2 \rightarrow 2CO_2 + O_2^{\cdot-}$	$2.0 \times 10^9$	<i>CAPRAM</i>

**Table 5.4.** Aqueous-phase reactions and equilibrium constants

No	Equilibrium Reaction	Equilibrium Constants	$K_{298}$ (forward) $M^{-n}s^{-1}$	$K_{298}$ (back) $M^{-n}s^{-1}$	Source
E1	$Fe(OH)_3(s) + 3H^+ \leftrightarrow Fe^{3+} + 3H_2O$	$9.1 \times 10^3$			<i>Stumm and Morgan</i> [1981]
E2	$Fe^{3+} + SO_4^{2-} \leftrightarrow FeSO_4^+$	$1.2 \times 10^2$	$3.2 \times 10^3$	$2.7 \times 10^1$	Jayson et al. [1977]
E3	$Fe^{3+} + Cl^- \leftrightarrow FeCl^{2+}$	5.2	4.8	$9.2 \times 10^{-1}$	<i>Xu et al.</i> [1985]; <i>Deguillaume et al.</i> [2005]
E4	$Fe^{3+} + H_2O \leftrightarrow [Fe(OH)]^{2+} + H^+$	$6.0 \times 10^{-3}$	$2.6 \times 10^6$	$4.3 \times 10^8$	<i>Brandt and van Eldik</i> 1995]
E5	$[Fe(OH)]^{2+} + H_2O \leftrightarrow [Fe(OH)_2]^+ + H^+$	$9.8 \times 10^{-4}$	$1.2 \times 10^5$	$1.2 \times 10^8$	<i>Brandt and van Eldik</i> [1995]
E6	$HO_2 \leftrightarrow O_2^- + H^+$	$1.6 \times 10^{-5}$	$8.0 \times 10^5$	$5.0 \times 10^{10}$	<i>Bielski et al.</i> [1985]
E7	$H_2C_2O_4 \leftrightarrow H^+ + HC_2O_4^-$	$6.4 \times 10^{-2}$	$3.2 \times 10^9$	$5.0 \times 10^{10}$	CAPRAM
E8	$HC_2O_4^- \leftrightarrow H^+ + C_2O_4^{2-}$	$5.3 \times 10^{-5}$	$2.6 \times 10^6$	$5.0 \times 10^{10}$	CAPRAM
E9	$Fe^{3+} + C_2O_4^{2-} \leftrightarrow [Fe(C_2O_4)]^+$	$2.5 \times 10^9$	$7.5 \times 10^6$	$3 \times 10^{-3}$	<i>Deguillaume et al.</i> [2005]
E10	$[Fe(C_2O_4)]^+ + C_2O_4^{2-} \leftrightarrow [Fe(C_2O_4)_2]^-$	$6.3 \times 10^6$	$3.0 \times 10^{-3}$	$1.9 \times 10^4$	<i>Deguillaume et al.</i> [2005]
E11	$[Fe(C_2O_4)_2]^- + C_2O_4^{2-} \leftrightarrow [Fe(C_2O_4)_3]^{3-}$	$1.6 \times 10^4$	$4.8 \times 10^1$	$3 \times 10^{-3}$	<i>Deguillaume et al.</i> [2005]

\* Equilibrium constants are given in units of  $mol\ kg^{-1}$ .

\* Fe(II) species such as  $Fe(OH)^+$ ,  $Fe(OH)_3^0$ ,  $Fe(OH)_3^-$  and Fe(III) species such as  $Fe(OH)_3^0$ ,  $Fe(OH)_4^-$  occur at very small concentration and were not considered.

**Table 5.5.** Set of differential equations used in the model

---

$$\begin{aligned}\frac{d\text{Fe(II)}}{dt} &= j_1\text{Fe(OH)}^{2+} + j_2[\text{Fe(C}_2\text{O}_4)_2^-] + j_3[\text{Fe(C}_2\text{O}_4)_3^{3-}] + k_7[\text{Fe(OH)}^{2+}][\text{O}_2^-] \\ &\quad + k_8[\text{Fe(OH)}^{2+}][\text{HO}_2] \\ &\quad + k_{17}[\text{Fe(C}_2\text{O}_4)_n^{3-2n}][\text{O}_2^-] k_{18}[\text{Fe(C}_2\text{O}_4)_n^{3-2n}][\text{HO}_2] \\ &\quad - k_1[\text{Fe}^{2+}][\text{H}_2\text{O}_2] - k_2[\text{FeC}_2\text{O}_4][\text{H}_2\text{O}_2] - k_3[\text{Fe}^{2+}][\text{O}_2^-][\text{H}^+]^2 \\ &\quad - k_4[\text{Fe}^{2+}][\text{HO}_2][\text{H}^+] - k_5[\text{Fe}^{2+}][\text{NO}_3] - k_6[\text{Fe}^{2+}][\text{NO}_2][\text{H}^+] \\ &\quad - k_9[\text{Fe}^{2+}][\text{O}_3]\end{aligned}$$
$$\frac{d\text{Fe(III)}}{dt} = -\frac{d\text{Fe(II)}}{dt}$$
$$\frac{d[\text{FeO}^{2+}]}{dt} = k_9[\text{Fe}^{2+}][\text{O}_3] - k_{10}[\text{FeO}^{2+}][\text{H}_2\text{O}] - k_{11}[\text{FeO}^{2+}][\text{OH}^-][\text{H}^+] - k_{12}[\text{FeO}^{2+}][\text{H}_2\text{O}_2] - k_{13}[\text{FeO}^{2+}][\text{HO}_2]$$
$$\frac{d[\text{C}_2\text{O}_4^{2-}]}{dt} = j_2[\text{Fe(C}_2\text{O}_4)_2^-] + j_3[\text{Fe(C}_2\text{O}_4)_3^{3-}] - k_{19}[\text{C}_2\text{O}_4^{2-}][\text{OH}^-] - k_{20}[\text{C}_2\text{O}_4^{2-}][\text{NO}_3] - k_{21}[\text{C}_2\text{O}_4^{2-}][\text{O}_2]$$
$$\frac{d[\text{H}_2\text{O}_2]}{dt} = k_3[\text{Fe}^{2+}][\text{O}_2^-][\text{H}^+]^2 + k_4[\text{Fe}^{2+}][\text{HO}_2][\text{H}^+] + k_{11}[\text{FeO}^{2+}][\text{OH}^-][\text{H}^+] + k_{14}[\text{HO}_2][\text{HO}_2] + k_{15}[\text{HO}_2][\text{O}_2][\text{H}^+] - k_1[\text{Fe}^{2+}][\text{H}_2\text{O}_2] - k_2[\text{FeC}_2\text{O}_4][\text{H}_2\text{O}_2] - k_{12}[\text{FeO}^{2+}][\text{H}_2\text{O}_2]$$
$$\frac{d[\text{HO}_2]}{dt} = k_{12}[\text{FeO}^{2+}][\text{H}_2\text{O}_2] - k_4[\text{Fe}^{2+}][\text{HO}_2][\text{H}^+] - k_8[\text{Fe(OH)}^{2+}][\text{HO}_2] - k_{13}[\text{FeO}^{2+}][\text{HO}_2] - k_{14}[\text{HO}_2][\text{HO}_2] - k_{15}[\text{HO}_2][\text{O}_2][\text{H}^+] - k_{18}[\text{Fe(C}_2\text{O}_4)_n^{3-2n}][\text{HO}_2]$$
$$\frac{d[\text{OH}^-]}{dt} = j_1\text{Fe(OH)}^{2+} + k_1[\text{Fe}^{2+}][\text{H}_2\text{O}_2] + k_2[\text{FeC}_2\text{O}_4][\text{H}_2\text{O}_2] + k_{10}[\text{FeO}^{2+}][\text{H}_2\text{O}] - k_{11}[\text{FeO}^{2+}][\text{OH}^-][\text{H}^+] - k_{19}[\text{C}_2\text{O}_4^{2-}][\text{OH}^-]$$
$$\frac{d[\text{O}_2^-]}{dt} = k_{16}[\text{CO}_2^-][\text{O}_2] + k_{21}[\text{C}_2\text{O}_4^{2-}][\text{O}_2] - k_3[\text{Fe}^{2+}][\text{O}_2^-][\text{H}^+]^2 - k_7[\text{Fe(OH)}^{2+}][\text{O}_2^-] - k_{17}[\text{Fe(C}_2\text{O}_4)_n^{3-2n}][\text{O}_2^-]$$
$$\frac{d[\text{C}_2\text{O}_4^-]}{dt} = j_2[\text{Fe(C}_2\text{O}_4)_2^-] + j_3[\text{Fe(C}_2\text{O}_4)_3^{3-}] + k_{19}[\text{C}_2\text{O}_4^{2-}][\text{OH}^-] + k_{20}[\text{C}_2\text{O}_4^{2-}][\text{NO}_3] + k_{21}[\text{C}_2\text{O}_4^{2-}][\text{O}_2]$$

---

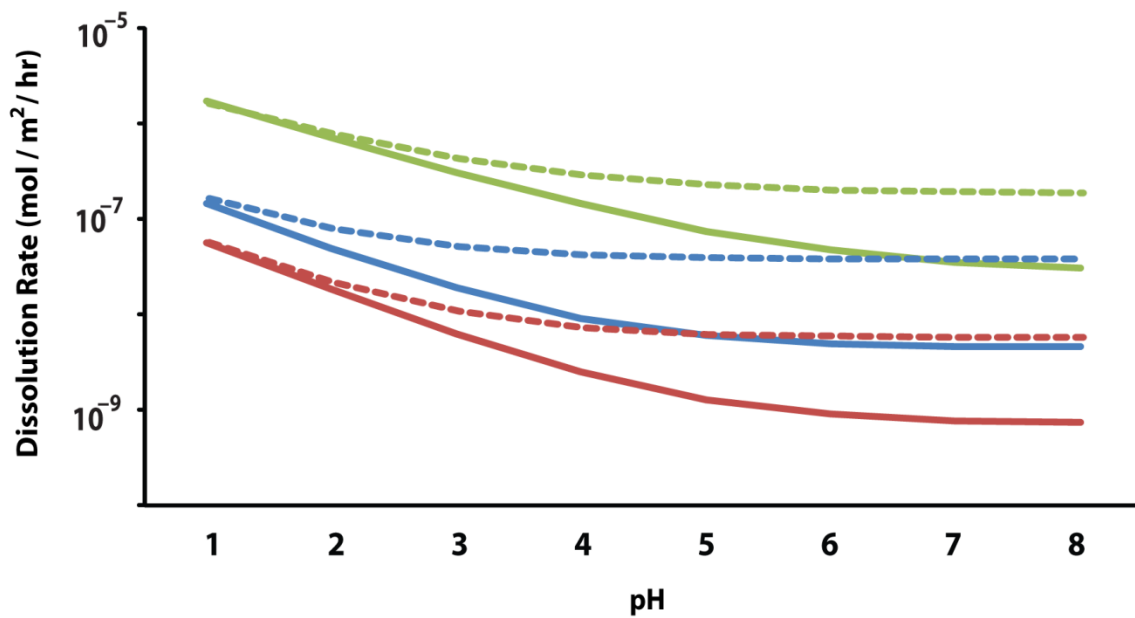


**Figure 5.1.** Fe-containing mineral dissolution rates (mol sol-Fe g total Fe<sup>-1</sup> hr<sup>-1</sup>) used within GEOS-Chem/DFeS simulations for hematite (blue), goethite (red), and illite (green) at 298°K.

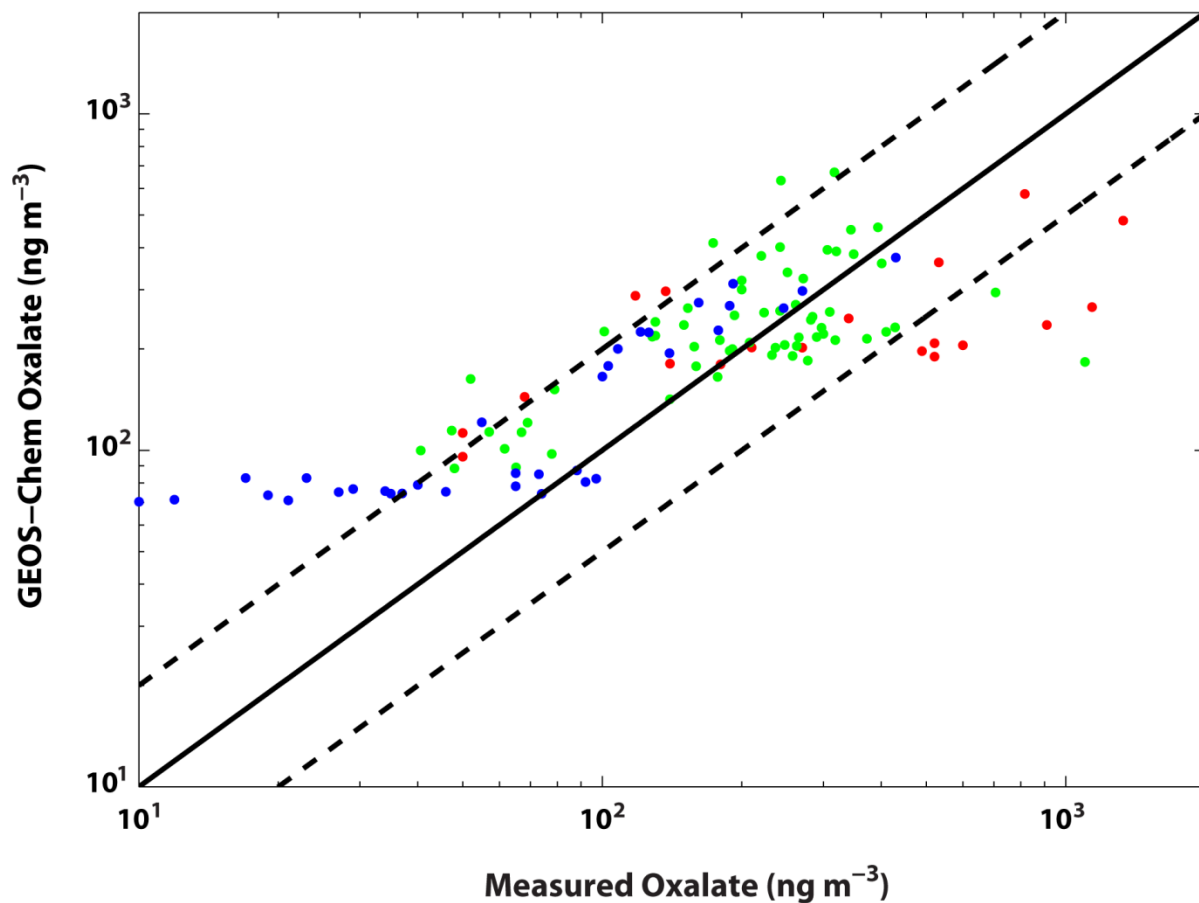


**Figure 5.2.** GEOS-Chem-predicted surface level oxalic acid concentrations (using model-predicted  $\text{SO}_4^{2-}$  concentrations as a proxy, Eq. 1) in comparison to a global data-set of measured oxalic acid concentrations. Urban, rural, and remote oceanic measurements are indicated by red, green, and blue dots, respectively. Observed surface level oxalic acid concentrations are taken from the study of *Myriokefalitakis et al.* [2011] and references within. The solid black line represents the 1:1 comparison of model-predicted and measured oxalic acid and the two dashed lines are the 1:2 and 2:1 comparison lines.

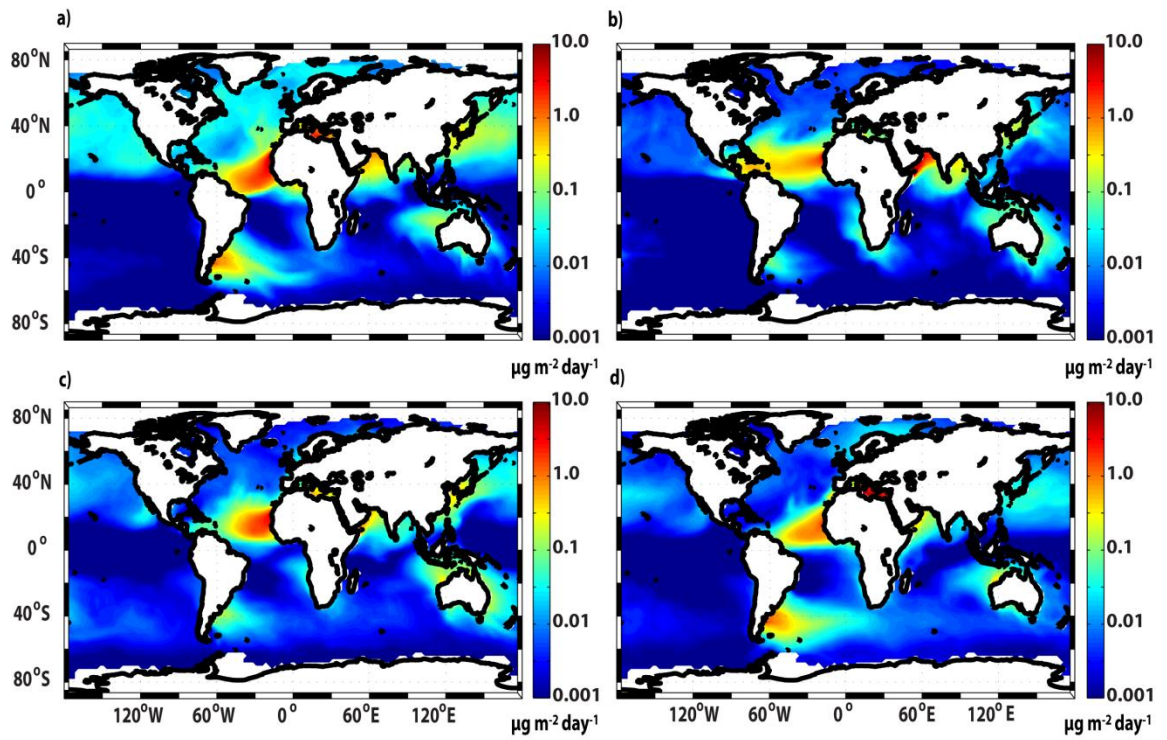


**Figure 5.3.** GEOS-Chem-predicted seasonally-averaged sol-Fe deposition ( $\mu\text{g m}^{-2} \text{day}^{-1}$ ) to the surface oceans between a) March-April (MAM), b) June-August (JJA), c) September-November (SON), and d) December-February (DJF).

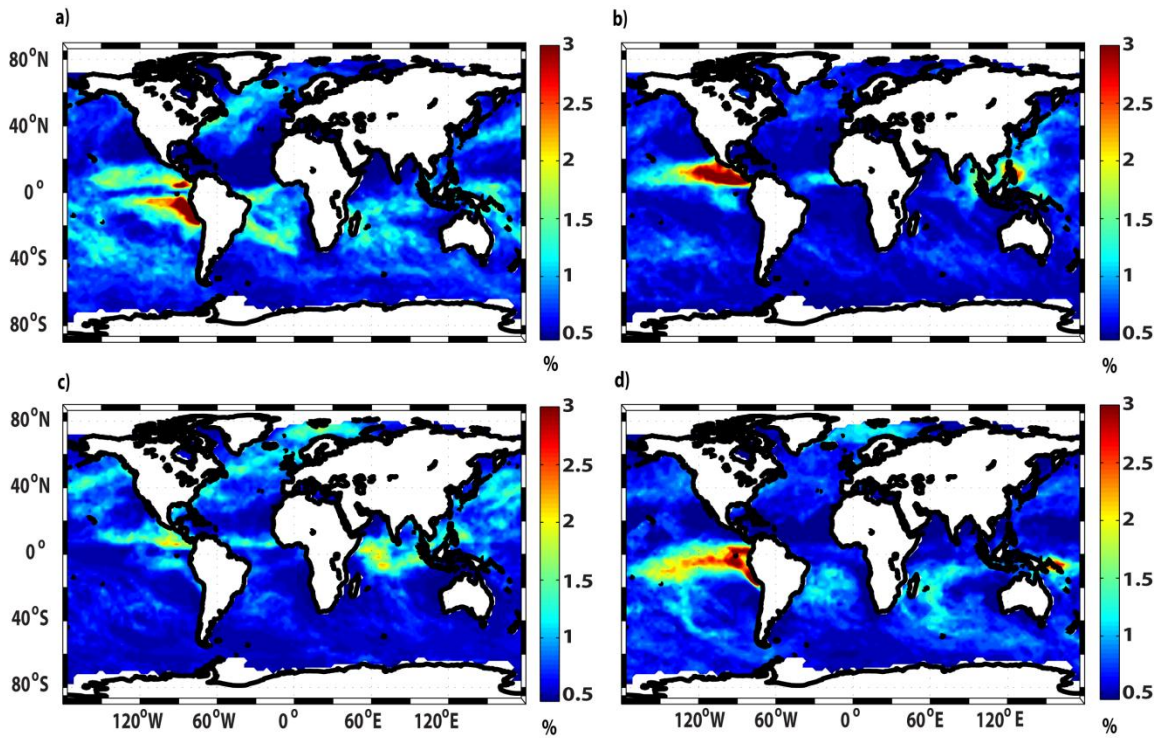


**Figure 5.4.** GEOS-Chem-predicted seasonally-averaged DIF values (%) in mineral dust deposited to the surface oceans between a) March-April (MAM), b) June-August (JJA), c) September-November (SON), and d) December-February (DJF).

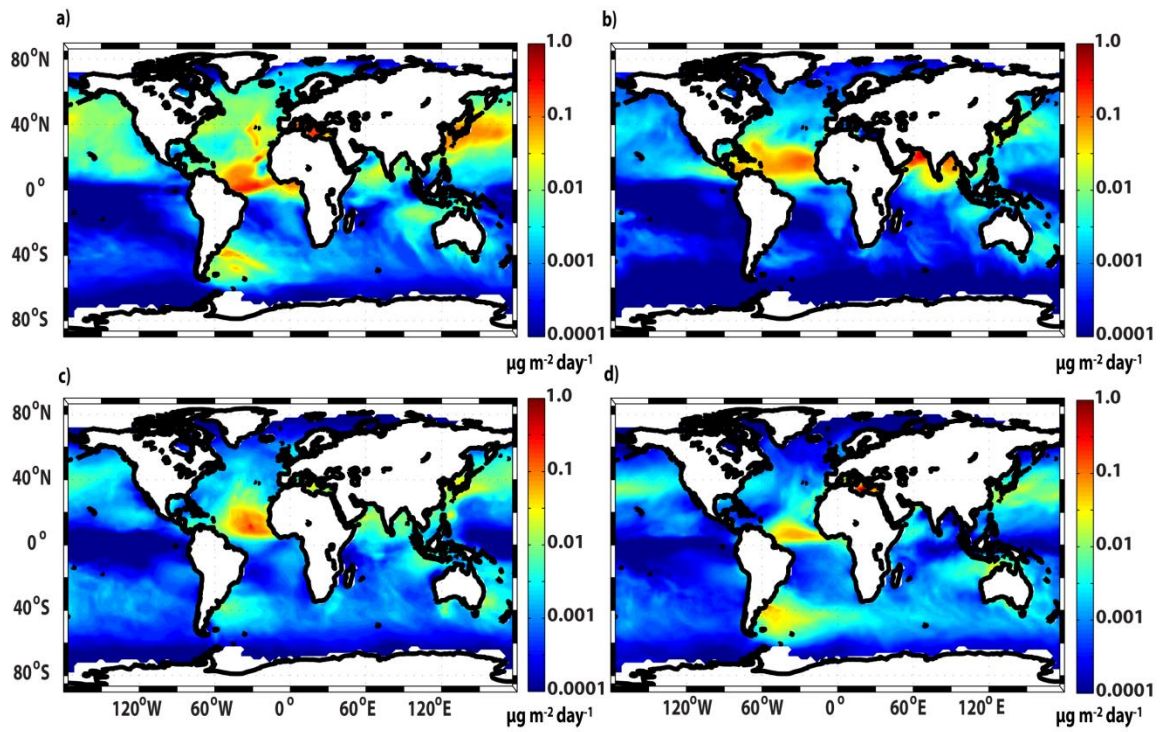


**Figure 5.5.** GEOS-Chem-predicted seasonally-averaged sol-Fe(II) deposition ( $\mu\text{g m}^{-2}\text{day}^{-1}$ ) to the surface oceans between a) March-April (MAM), b) June-August (JJA), c) September-November (SON), and d) December-February (DJF).

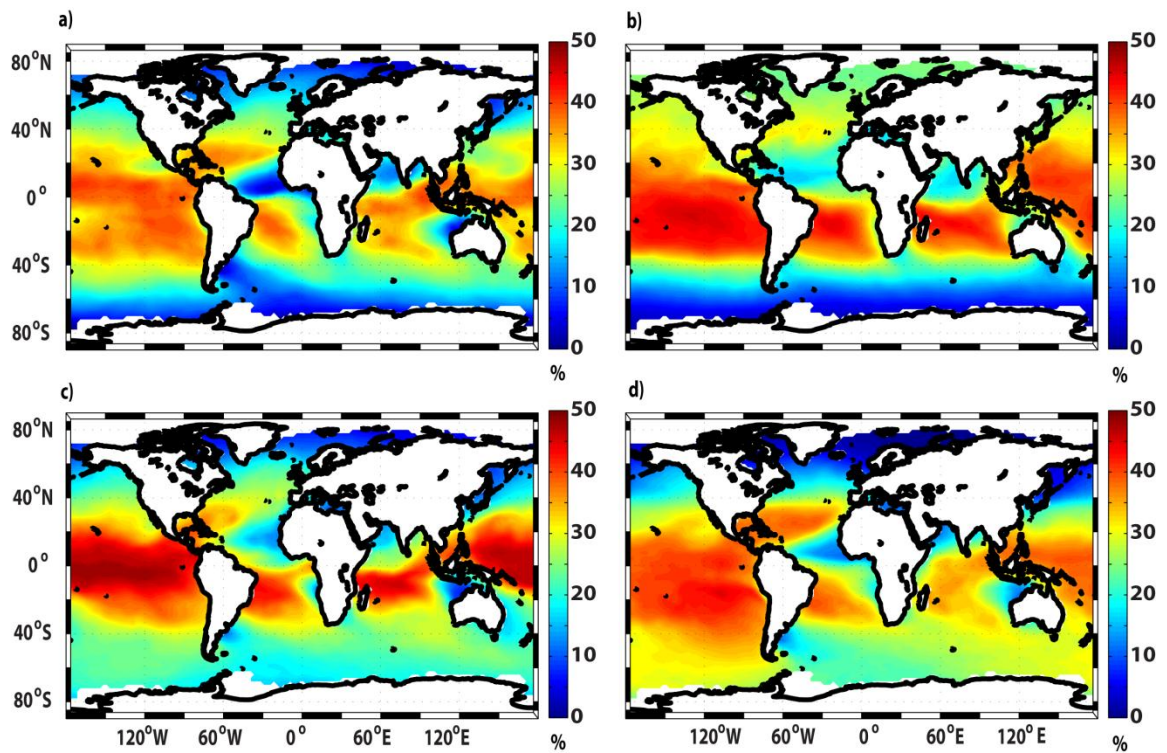


**Figure 5.6.** GEOS-Chem-predicted seasonally-averaged sol-Fe(II)% in deposited dust ( $\mu\text{g m}^{-2} \text{day}^{-1}$ ) to the surface oceans between a) March-April (MAM), b) June-August (JJA), c) September-November (SON), and d) December-February (DJF).

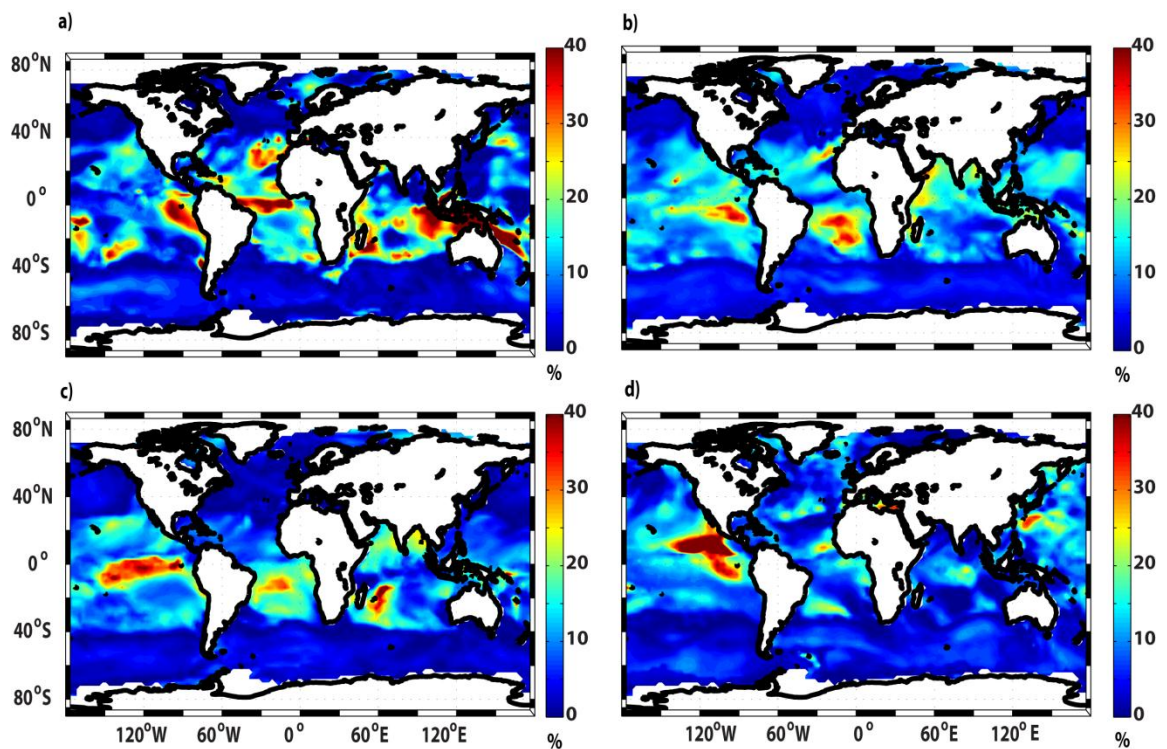


**Figure 5.7.** GEOS-Chem-predicted percent change in seasonally-averaged sol-Fe deposition rates to the surface oceans due to organic ligand-promoted Fe dissolution for a) March-April (MAM), b) June-August (JJA), c) September-November (SON), and d) December-February (DJF).

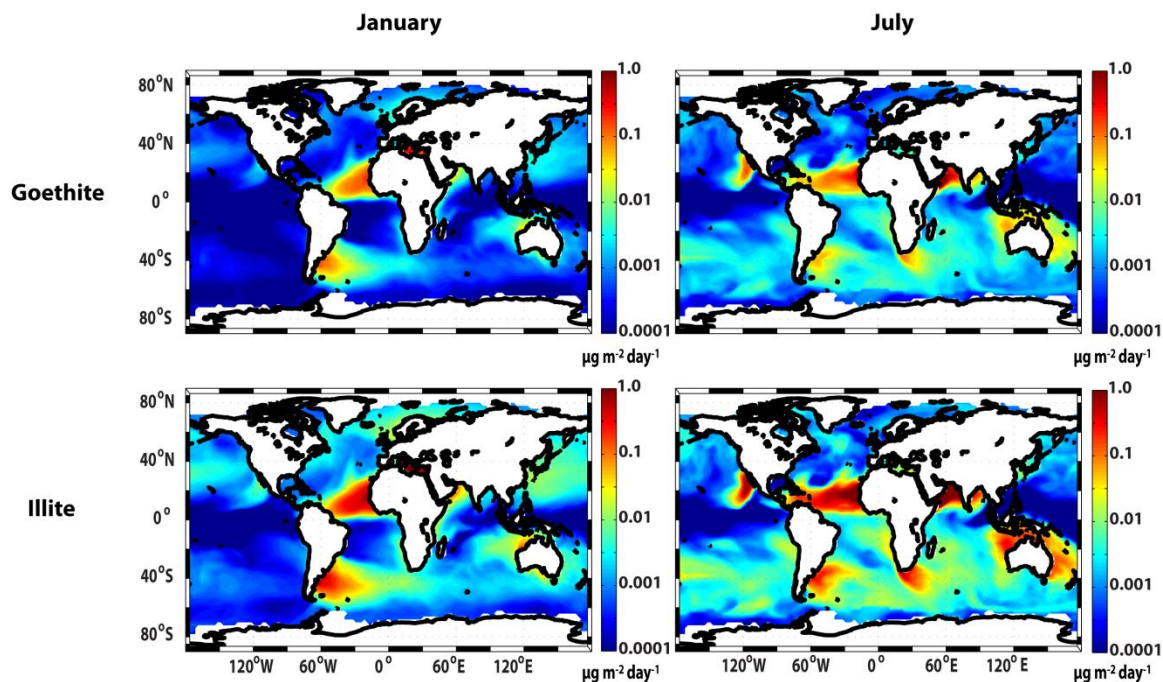


**Figure 5.8.** GEOS-Chem/DFeS-predicted magnitude increases in sol-Fe deposition ( $\mu\text{g m}^{-2}\text{day}^{-1}$ ) for January (left column) and July (right column) of the simulation time period when Fe mobilization is calculated using goethite (top row) and illite (bottom row) dissolution rates compared to baseline model runs applying hematite dissolution rates.

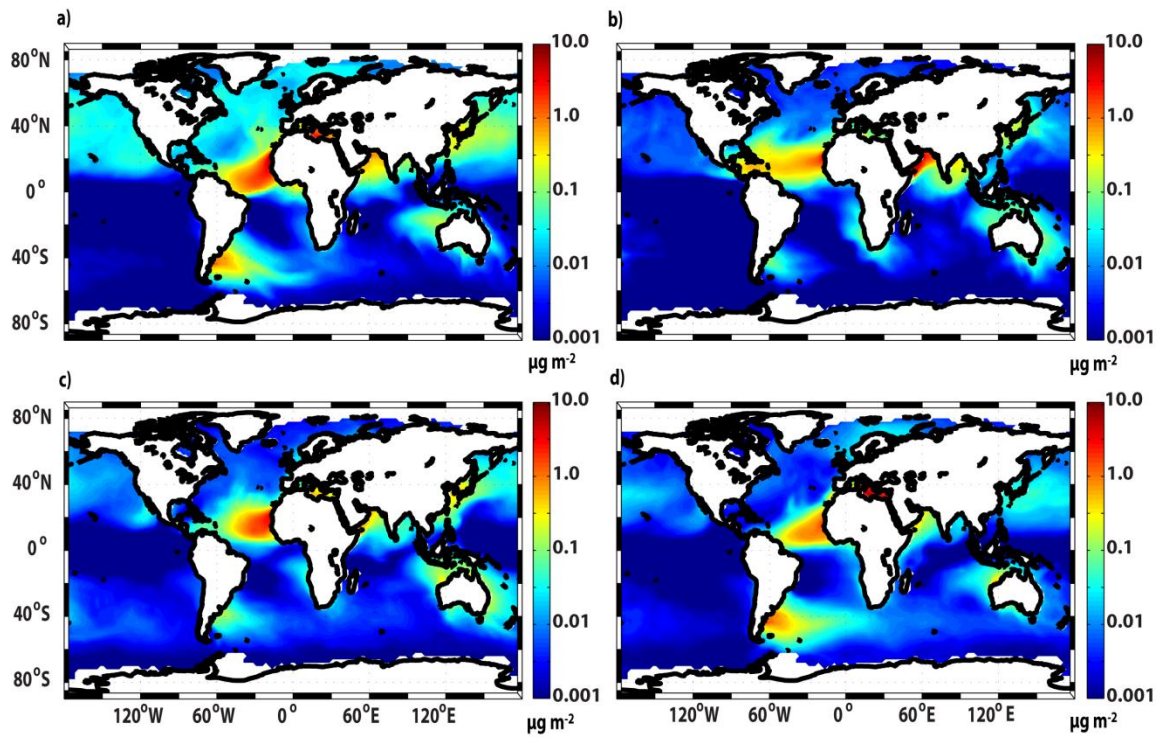


**Figure 5.9.** GEOS-Chem-predicted daily-averaged  $\text{PO}_4^{3-}$  deposition ( $\mu\text{g m}^{-2}$ ) to the surface oceans between a) March-April (MAM), b) June-August (JJA), c) September-November (SON), and d) December-February (DJF).

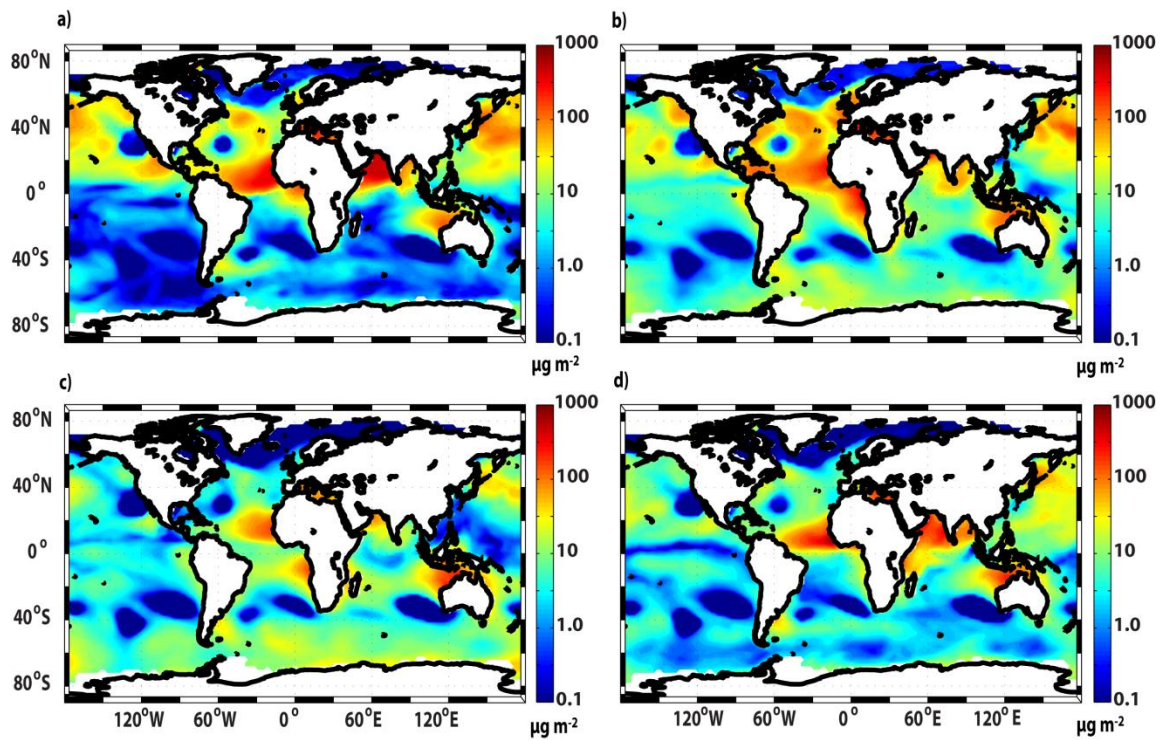


**Figure 5.10.** GEOS-Chem-predicted daily-averaged  $\text{NO}_3^-$  deposition ( $\mu\text{g m}^{-2}$ ) to the surface oceans between a) March-April (MAM), b) June-August (JJA), c) September-November (SON), and d) December-February (DJF).

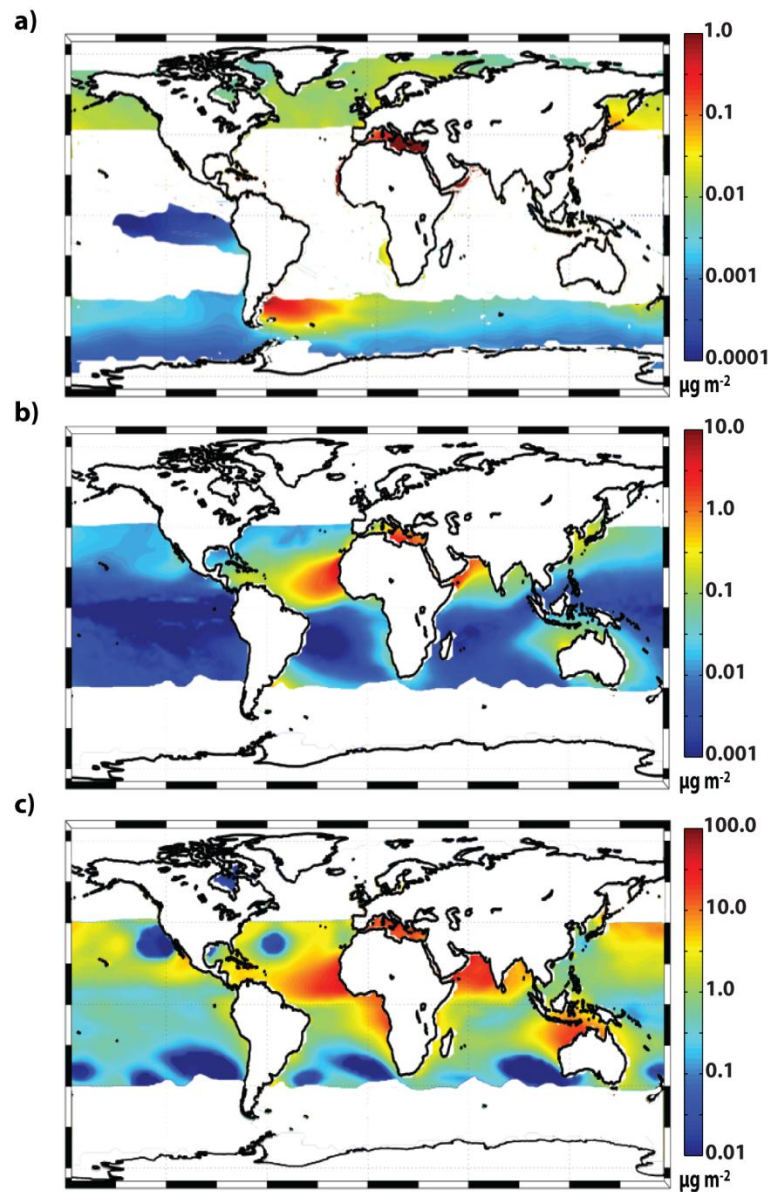


**Figure 5.11.** GEOS-Chem-predicted daily-averaged a) sol-Fe, b)  $\text{PO}_4^{3-}$ , and c)  $\text{NO}_3^-$  deposition rates ( $\mu\text{g m}^{-2}$ ) to the surface oceans which have primary productivity limited by each individual micronutrient during the entire simulation period (March 2009 - February 2010).

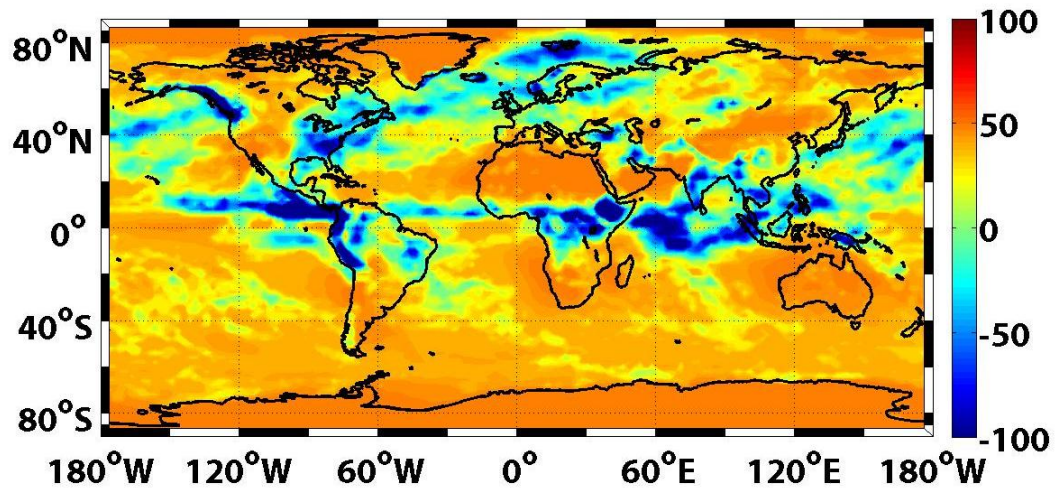


**Figure 5.12.** GEOS-Chem-predicted percent difference between sol-Fe deposition when assuming a constant 1% DIF and explicitly model-predicted DIF during the yearlong simulation period.

## Supplementary Figures

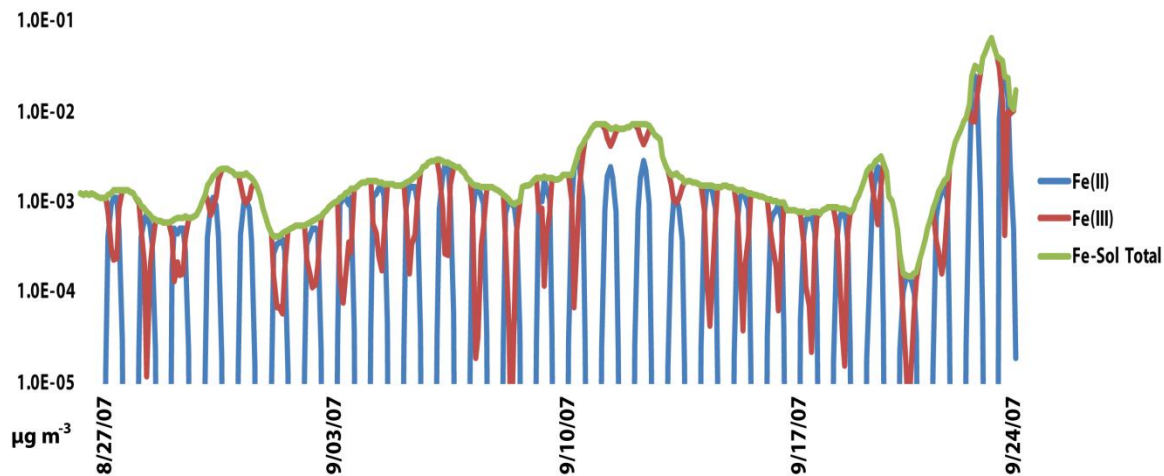


**Figure S5.1.** GEOS-Chem/DFeS-predicted total sol-Fe (green line), Fe(II) (blue line), and Fe(III) (redline) concentrations ( $\mu\text{g m}^{-3}$ ) at the surface of the model grid cell encompassing the dust measurement sites on the island of Barbados ( $13.17^{\circ}\text{N}$ ,  $59.43^{\circ}\text{W}$ ). This figure illustrates the model-predicted diurnal cycle of Fe(II)/Fe(III) redox cycling (2 hour resolution) during the Barbados Dust Deposition Experiment (BarDEX).

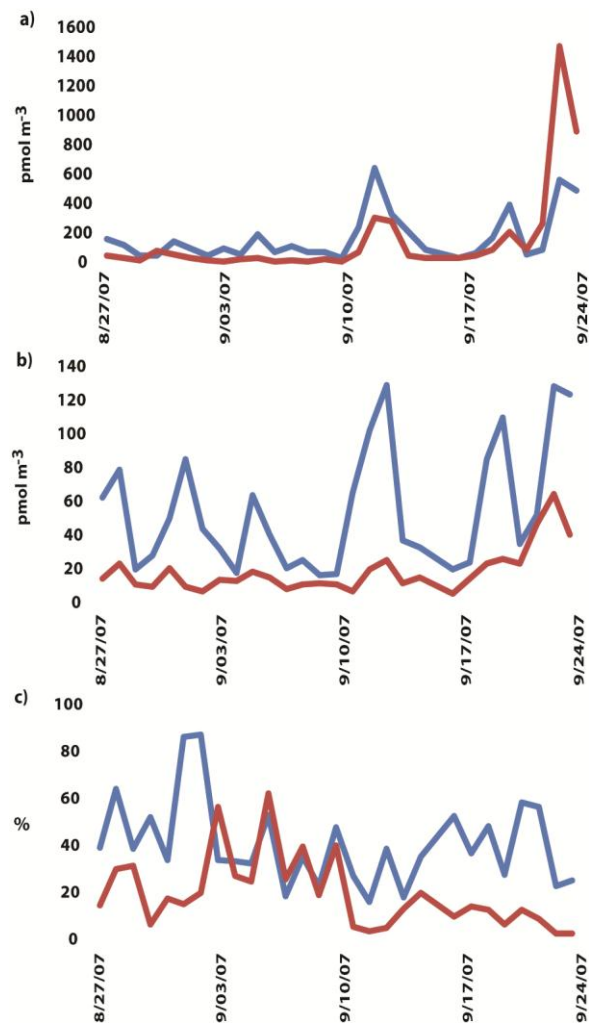


**Figure S5.2.** GEOS-Chem/DFeS-predicted (red line) daily-averaged concentrations of a) Fe(III) ( $\text{pmol m}^{-3}$ ), b) Fe(II) ( $\text{pmol m}^{-3}$ ), and c) Fe(II)% compared to the surface measurement data (blue line) obtained during the Barbados Dust Deposition Experiment (BarDEx) [Trapp *et al.*, 2010].

## **6. Summary and Future Work**

### **6.1 Introduction**

The results from my dissertation demonstrate how using a synergistic approach (combination of model and active/passive satellite data) is beneficial in the effort to better understand the horizontal and vertical transport pathways of global mineral dust, complex chemical transformation processes of nutrients in mineral dust particles, and the influence of mineral dust/sol-Fe deposition on marine primary productivity and biogeochemistry in remote global oceanic ecosystems. The synergistic evaluation performed during this work was designed by combining data from the 3-D global CTM GEOS-Chem and a dust/biota assessment tool with remotely-sensed data from MODIS, MISR, CALIPSO, and SeaWiFS. During this chapter the main results of my dissertation will be summarized and future model developments and evaluation efforts will be suggested.

### **6.2 Main results**

The following is a list of the major results presented within my dissertation encompassing the synergistic evaluation of mineral dust transport and updated model predictions of dust-nutrient dissolution processes and deposition rates:

- GEOS-Chem, MODIS, MISR, and CALIPSO generally produce similar horizontal and vertical dust AOD and aerosol extinction profiles over the major global dust emission and transport regions (“dusty” regions). However, model-satellite comparisons indicate that

over the major “dusty” regions, GEOS-Chem tends to predict higher AOD values compared to remotely-sensed data.

- In comparison with dust aerosol extinction profiles, remotely-sensed by CALIPSO, the model overestimates mineral dust abundances over the major global “dusty” regions primarily below ~4 km. This suggests excessive emissions of mineral dust and/or uncertainties in GEOS-Chem dust optical properties. Additionally, our results suggest that positive/negative biases between satellite and model-predicted aerosol extinction values at different altitudes can sometimes even out, giving a false impression for the agreement between remotely-sensed and model-predicted column-integrated AOD data.

- The implementation of the new *Kok* [2011] dust mass size distribution scheme into GEOS-Chem reduced the yearly-mean positive bias in model-predicted AOD values and generally improved the statistics of the model-satellite intercomparison over major dust emission and transport regions. This improved comparison between model-predicted and remotely-sensed AODs was achieved without having to reduce global dust emission rates. This is important due to the fact that if model-predicted mineral dust emission rates are incorrectly reduced in GEOS-Chem, then dust-nutrient supplies to remote oceanic surface waters will likely be under-predicted.

- GEOS-Chem simulations indicate that the synoptic meteorological patterns of high and low pressure systems are largely accountable for the horizontal and vertical Patagonian dust transport trajectories over the SAO.

- The effect of mineral dust and sol-Fe deposition on surface ocean biomass in the SAO was investigated by comparing model-predicted surface chlorophyll-*a* concentration ([Chl-*a*]) to SeaWiFS [Chl-*a*] data. This comparison suggested that: (1) atmospheric fluxes of mineral dust from Patagonia are not likely to be the major source of bioavailable Fe to oceanic regions characterized by high primary productivity; (2) even if Patagonian dust plumes may not cause visible algae blooms, they could still influence background [Chl-*a*] in the HNLC regions of the SAO.

- During this research, to our knowledge, the first 3-D global model was developed that can explicitly calculate dissolution-precipitation kinetics of Fe oxides/clay minerals, organic acid and mineral-Fe interactions, organic ligand-promoted Fe dissolution, Fe(II)/Fe(III) photochemical redox cycling, and acidity driven  $\text{PO}_4^{3-}$  and  $\text{NO}_3^-$  formation in mineral dust during atmospheric transport. This state-of-the-art dust-nutrient model predicted similar annual total magnitudes of sol-Fe,  $\text{PO}_4^{3-}$ , and  $\text{NO}_3^-$  deposited to the global oceans simulated in past literature studies while capturing the spatially and temporally variable bioavailable fractions of these essential nutrients measured in nature.

- The addition of oxalic acid increased sol-Fe deposition rates and resulted in a total annual global oceanic sol-Fe deposition increase of ~20% (some regions experiencing well over 50% increases in sol-Fe deposition rates compared to model simulations only using acid-based Fe dissolution).

- Different dissolution rates of Fe-containing minerals (hematite, goethite, and illite) were applied to simulate sol-Fe production in mineral dust. When using goethite and illite

dissolution rates in GEOS-Chem/DFeS the magnitude of sol-Fe deposited to the global oceans increased by ~15 and 40% when compared to baseline model simulations (using hematite Fe dissolution rates), respectively.

- Model-predicted seasonally-averaged sol-Fe deposition rates proved to be an important source of atmospheric sol-Fe to the HNLC oceans such as: directly off the coast of North Africa and the Middle East ( $> 1.0 \mu\text{g m}^{-2} \text{day}^{-1}$ ), the subarctic North Pacific Ocean (between  $0.01$  and  $0.1 \mu\text{g m}^{-2} \text{day}^{-1}$ ), and in Southern Ocean (up to  $1.0 \mu\text{g m}^{-2} \text{day}^{-1}$ ).

- The largest seasonally-averaged deposition rates of sol-Fe(II) (up to  $0.1 - 1.0 \mu\text{g m}^{-2} \text{day}^{-1}$ ) are simulated in the North Atlantic and North Pacific Ocean associated with mineral dust transport from the Sahara Desert and Asian dust source regions, respectively. In the Southern Hemisphere the largest atmospheric source of sol-Fe(II) (seasonally-averaged deposition rates between  $0.01$  to  $0.1 \mu\text{g m}^{-2} \text{day}^{-1}$ ) are associated with Patagonian dust deposition in the SAO.

- Mineral dust deposition also supplied a significant amount of  $\text{PO}_4^{3-}$  to oligotrophic oceanic regions with marine primary productivity limited by bioavailable P such as the: North Atlantic and Indian Ocean (seasonally-averaged deposition rates between  $1.0 - 10.0 \mu\text{g m}^{-2} \text{day}^{-1}$ ) and also the subantarctic South Atlantic and Indian Oceans (seasonally-averaged deposition rates up to  $\sim 0.5 \mu\text{g m}^{-2} \text{day}^{-1}$ ). Several marine ecosystems that are assumed to have primary productivity limited by the supply of bioavailable N were predicted by GEOS-Chem/DFeS to receive significant atmospheric fluxes of  $\text{NO}_3^-$ -laden-dust such as the: North

and South Atlantic, North Pacific Ocean, and Indian Ocean (seasonally-averaged deposition rates ranging between 1.0 and 100  $\mu\text{g m}^{-2} \text{day}^{-1}$ ).

- During the yearlong simulation, GEOS-Chem/DFeS predicted annual totals of  $\sim 0.17$ , 0.20, and 75 Tg of sol-Fe,  $\text{PO}_4^{3-}$ , and  $\text{NO}_3^-$  were deposited to the global oceans, respectively. Preliminary results suggest GEOS-Chem/DFeS can capture the temporal variability and overall magnitude of mineral dust, Fe(III), and Fe(III) measured downwind of the Sahara Desert.

- The advantage of using our highly comprehensive dust-nutrient dissolution scheme, in comparison to past parameterizations (typically assuming the bioavailable fraction of individual nutrients), is GEOS-Chem/DFeS explicitly calculates the formation and deposition of each essential micronutrient without making any a priori assumptions. This allows our model to replicate the large spatio-temporal variability of the soluble fractions of these micronutrients within mineral dust that has been measured in nature [e.g., *Baker et al.*, 2006]. Overall, we suggest the application of our publically available micronutrient deposition datasets in global marine biogeochemistry and climate models.

### **6.3 Suggestions for future work**

A highlighted result of my dissertation work is the highly comprehensive data set of bioavailable dust-nutrient deposition rates to the global oceans calculated by our updated dissolution scheme. As present day marine biogeochemistry and climate models generally use atmospheric fluxes of bioavailable nutrients determined by simplified calculations

applying numerous a priori assumptions, we suggest the usage of our explicitly calculated atmospheric nutrient deposition data set in future climate model predictions. The major advantage of using our data sets is they capture the large spatial and temporal variability of the percentage of dust-nutrients that are in a bioavailable form (which cannot be produced using highly simplified a priori/constant bioavailability fractions) that has been measured to occur in nature.

A major suggestion for the improvement of our model is to more realistically simulate the atmospheric deposition of bioavailable nutrients to the global oceans through the addition of nutrient emissions associated with anthropogenic and biomass burning sources. This is due to the fact that recent research has shown that anthropogenic and biomass burning sources can provide significant magnitudes of bioavailable nutrients to the global oceans. For example, *Luo et al.* [2008] obtained the result that the deposition of sol-Fe from anthropogenic combustion and biomass burning sources contribute 20 - 100% of the total bioavailable Fe deposited to some global ocean regions. The DIFs measured in combustion-Fe aerosols are generally higher in comparison to mineral dust aerosols, therefore, the absence of combustion sol-Fe sources may lead to the under prediction of the overall DIF and sol-Fe deposition rates in oceanic regions not downwind from major dust sources. Additionally, anthropogenic emissions have been shown in past literature to be a dominant atmospheric source of aerosol  $\text{NO}_3^-$  deposited to remote global oceanic regions [*Duce et al.*, 2008]. Similar results were presented in the study by *Mahowald et al.* [2008] which demonstrated that anthropogenic sources of  $\text{PO}_4^{3-}$  may be the dominant atmospheric supply

pathway of bioavailable P to oceanic regions not influenced by large magnitudes of mineral dust deposition.

Another suggested improvement to the model would be replacing ISORROPIA [Nenes *et al.*, 1998] with the newest updated version of ISORROPIA II [Fountoukis and Nenes, 2007]. ISORROPIA II is a thermodynamic equilibrium model for the  $K^+$ ,  $Ca^{2+}$ ,  $Mg^{2+}$ ,  $NH_4^+$ ,  $Na^+$ ,  $SO_4^{2-}$ ,  $NO_3^-$ ,  $Cl^-$ , and  $H_2O$  aerosol system in global CTMs. The newest version of the thermodynamic equilibrium model now takes crustal material, such as  $K^+$ ,  $Ca^{2+}$ ,  $Mg^{2+}$ , into consideration without decreasing computational efficiency [Fountoukis and Nenes, 2007]. Presently, when using ISORROPIA, in the current version of GEOS-Chem/DfES, the effects of crustal elements from mineral dust (i.e.,  $Ca^{2+}$ ,  $Mg^{2+}$ , and  $K^+$ ) on chemical properties of the deliquesced aerosol solution are modeled by converting these elements to the equivalent concentration of  $Na^+$  [Meskhidze *et al.*, 2005]. Overall, the implementation of ISORROPIA II will allow for the explicit calculation of the influence of mineral dust elements on aerosol solution pH and acid mobilization processes.

In our model we assume that mineral-Fe, in atmospherically transported dust particles, is the preferential surface for the absorption of oxalic acid. It is unclear if this is a valid assumption due to recent measurement studies determining that oxalic acid, enriched in mineral dust particles, may result in complexes with  $Ca^{2+}$  possibly forming Ca-oxalate species [e.g., Sullivan and Prather, 2007]. Measurement and laboratory studies have demonstrated that oxalic acid reacts with  $Ca^{2+}$ , however, a lack of literature is available that has evaluated the absorption of oxalic acid when mineral-Fe and  $Ca^{2+}$  are both present within

the system. If oxalic acid is absorbed by mineral- $\text{Ca}^{2+}$ , in the presence of Fe-containing minerals, then the model may over estimate the amount of oxalic acid absorbed onto Fe. While this assumption will lead to an over estimation of Fe-oxalate species formation, the enhancement of sol-Fe production caused by oxalic acid concentrations will not be affected by the before mentioned assumption. The reason for this is the organic ligand-promoted Fe dissolution parameterization, implemented in GEOS-Chem/DFeS, is only dependant on aqueous oxalic acid concentrations and not the amount absorbed onto mineral-Fe. However, it is suggested to more realistically simulate the interactions between oxalic acid and all metal cations in mineral dust during future model simulation.

The limited amount of measurement data containing information pertaining to the solubility fraction of nutrients, specifically associated with mineral dust, makes it difficult to evaluate the overall accuracy of our updated dust-nutrient dissolution scheme. The ship measurements of dust-nutrient solubility presented in the work by *Baker et al.* [2006] shows that the solubility fractions of Fe and P range between 1 to 80%. However, from further analysis of this dataset it becomes apparent that the elevated percent solubility fractions of these nutrients are associated with anthropogenic emissions and are not directly comparable to our model calculations. In *Baker et al.* [2006] it is shown that the solubility of mineral-Fe, associated with Saharan dust plumes, were as high as 4% (median value of 1.7%). When focusing on seasonally-averaged DIF values simulated by our model (Chapter 5) it was determined that DIF values in Saharan dust are generally close to the initially prescribed Fe solubility of 0.45%, however, further downwind DIFs can be  $> 1\%$ . Although seasonally-

averaged DIF values are consistently low, when evaluating model-predicted DIF values on a daily basis the model can produce the larger solubility fractions of Fe instantaneously measured in Saharan dust [*Baker et al.*, 2006]. Overall, to fully evaluate model-predicted solubility fractions of micronutrients within mineral dust, long-term and spatially distributed measurements, specifically measuring nutrient solubility in mineral dust particles, are necessary.

This section of the chapter suggests possible locations for nutrient solubility measurements which would significantly benefit our model evaluation:

1. Measurement sites just off the west coast of North Africa, on the island of Cape Verde (similar to the filter measurements of mineral dust performed in *Kandler et al.* [2011]), and far downwind on the islands of Barbados (such as those used in *Trapp et al.* [2010]) would allow for the evaluation of model-predicted nutrient solubility fractions close in proximity to and downwind of a major dust source. The advantage of these sites is that these islands frequently receive large quantities of dust, originating in the Sahara Desert, and are generally assumed to be relatively pristine in nature. These measurements, conducted in unison, would result in a large data base of nutrient solubility measurements which can directly be attributed to mineral dust aerosols. These two sites would allow for the evaluation of the gradient of micronutrient solubility fractions and deposition rates during the long-range transport of mineral dust over the North Atlantic Ocean. Additionally, the model evaluation of the formation of  $\text{PO}_4^{3-}$  and  $\text{NO}_3^-$  on mineral dust at these two sites would be

important due to the North Atlantic Ocean being suggested to have marine primary productivity limited by these nutrients.

2. In past studies, filter sampling has been conducted on the island of Japan at Nagasaki (32°N, 129°E), Okayama (34°N, 133°E), Kofu (35°N, 138°E), and Tokyo (35°N, 139°E) in order to measure mineral dust [e.g., *Kobayashi et al.*, 2006]. These measurement sites would allow for the evaluation of the effect of anthropogenic and naturally emitted acidic trace gases and organic acids on the solubility of nutrients (in particular sol-Fe) within dust aerosols emitted from Asian dust sources. These measurement sites would also be beneficial to evaluate the models ability to calculate the formation of  $\text{NO}_3^-$  on mineral dust. In the model, elevated levels of  $\text{NO}_3^-$  laden dust are simulated downwind from the Asian dust source regions. The reason for this result is the large amount of dust being transported in unison with substantial quantities of nitrogen containing trace gases emitted from the large cities in China. Also, the waters downwind from these measurement sites are assumed to have marine primary productivity limited by  $\text{NO}_3^-$  and sol-Fe supplies which can be supplied through the deposition of Asian dust.

3. It would be highly beneficial, but likely difficult, to have aerosol solubility measurements on buoys in the HNLC oceanic regions of the North Pacific Ocean and Southern Ocean. The dust-nutrient solubility measurements being conducted in the HNLC regions of the North Pacific Ocean, in combination with those on the island of Japan, would allow for the evaluation of the gradient of nutrient solubility and deposition rates during the long-range transport of Asian dust. In addition to buoys, measurement systems on the east

and west coast of Antarctica would allow for the observation of nutrient solubility during the long-range transport of Patagonian and Australian dust. Having these measurement sites would allow for the evaluation of the model, specifically its ability to calculate DIF values, in the oceanic regions which have primary productivity limited by bioavailable Fe supplies.

## References

- Baker, A. R., T. D. Jickells, M. Witt, and K. L. Ligne (2006), Trends in the solubility of iron, aluminium, manganese and phosphorus in aerosol collected over the Atlantic Ocean, *Marine Chemistry*, 98(1), 43-58.
- Duce, R. A., et al. (2008), Impacts of atmospheric anthropogenic nitrogen on the open ocean, *Science*, 320(5878), 893–897, doi:10.1126/science. 1150369.
- Fountoukis, C. and A. Nenes (2007), ISORROPIA II: A Computationally Efficient Aerosol Thermodynamic Equilibrium Model for  $K^+$ ,  $Ca_2^+$ ,  $Mg_2^+$ ,  $NH_4^+$ ,  $Na^+$ ,  $SO_4^{2-}$ ,  $NO_3^-$ ,  $Cl^-$ ,  $H_2O$  Aerosols, *Atmos. Chem. Phys.*, 7, 4639–4659.
- Kandler, K., L. Schutz, S. Jackel, K. Lieke, C. Emmel, D. Muller-Ebert, M. Ebert, D. Scheuven, A. Schladitz, B. Segvic, A. Wiedensohler, and S. Weinbruch (2011), Ground-based off-line aerosol measurements at Praia, Cape Verde, during the Saharan Mineral Dust Experiment: microphysical properties and mineralogy, *Tellus B*, 63(4), 459-474.
- Kobayashi, H., K. Arao, T. Murayama, K. Iokibe, R. Koga, and M. Shiobara (2007), High-Resolution Measurement of Size Distributions of Asian Dust Using a Coulter Multisizer, *J. Atmos. Oceanic Technol.*, 24, 194-205.
- Kok, J. F (2011), A scaling theory for the size distribution of emitted dust aerosols suggests climate models underestimate the size of the global dust cycle, *PNAS*, 108(3), 1016-1021.
- Luo, C., N. Mahowald, T. Bond, P. Y. Chuang, P. Artaxo, R. Siefert, Y. Chen, and J. Schauer (2008), Combustion iron distribution and deposition, *Global Biogeochem. Cycles*, 22, doi:10.1029/2007GB002964.
- Mahowald et al. (2008), Atmospheric Iron Deposition: Global Distribution, Variability, and Human Perturbations, *Annu. Rev. Mar. Sci.*, 1, 245–278.
- Meskhidze, N., W. L. Chameides, and A. Nenes (2005), Dust and pollution: A recipe for enhanced ocean fertilization?, *J. Geophys. Res.*, 110, D03301, doi: 10.1029/2004JD005082.
- Nenes, A., S. N. Pandis, and C. Pilinis (1998), ISORROPIA: A new thermodynamic equilibrium model for multiphase multicomponent inorganic aerosols, *Aquat. Geochem.*, 4(1), 123–152.
- Sullivan, R. C., M. J. K. Moore, M. D. Petters, S. M. Kreidenweis, G. C. Roberts, and K. A. Prather (2009), Effect of chemical mixing state on the hygroscopicity and cloud

nucleation properties of calcium mineral dust particles, *Atmos. Chem. Phys.*, *9*, 3303-3316.

Trapp, J. M., F. J. Millero, and J. M. Prospero (2010), Trends in the solubility of iron in dust-dominated aerosols in the equatorial Atlantic trade winds: Importance of iron speciation and sources, *Geochem. Geophys. Geosyst.*, *11*, Q03014, doi:10.1029/2009GC002651.